DISSERTATION

Sub-daily parameter estimation in VLBI data analysis

carried out in order to obtain the academic degree
"doctor of the technical sciences" under the supervision of

o.Univ.-Prof. Dipl.-Ing. Dr.techn. Harald Schuh

presented at the Vienna University of Technology

Faculty of Mathematics and Geoinformation

Institute of Geodesy and Geophysics

by

MSc. Kamil Teke

Matrikelnummer: 0626624

Rautenstrauchgasse 5/506, 1110, Vienna, AUSTRIA

Vienna, AUSTRIA May 2011

Supervisors

o.Univ.-Prof. Dipl.-Ing. Dr.techn. Harald Schuh

Institute of Geodesy and Geophysics

Vienna University of Technology

Gusshausstrasse 27-29, 1040, Vienna, Austria

Priv.-Doz. Dr.-Ing. Axel Nothnagel

Institute of Geodesy and Geoinformation

University of Bonn

Nussallee 17, 53115 Bonn, Germany

Abstract

The main objective of the work carried out within the scope of this thesis is the contribution to the VLBI2010 project of the International Very Long Baseline Interferometry (VLBI) Service for Geodesy and Astrometry (IVS) by means of developing a parameter estimation module (vie_lsm) of Vienna VLBI Software (VieVS) which is capable of estimating accurate sub-daily VLBI geodetic parameters. The vie_lsm module is based on the classical Gauss Markoff Least-Squares (LS) adjustment method by using continuous piece-wise linear offset (CPWLO) functions which are estimated at unique epochs, e.g. at integer hours, or at integer fractions or integer multiples of integer hours. The interval for CPWLO modelling of the parameters is usually set to values between one day to five minutes.

To investigate the sub-daily tidal motions of the VLBI antennas during IVS-CONT05, hourly CPWLO Terrestrial Reference Frame (TRF) coordinates of the antennas were estimated. Although all tidal displacements are computed from state-of-the-art geophysical models and reduced from the observations a priori to the adjustment, the radial amplitudes from the estimated hourly antenna coordinates can reach up to 1 cm (Kokee, HartRAO, Gilcreek, Westford, Svetloe, and Wettzell). To analyze the high frequency (sub-daily) Earth rotation parameter (HF-ERP) estimates of VieVS during IVS-CONT08, hourly CPWLO ERP were estimated. The Fourier spectra of the hourly VLBI and Global Positioning System (GPS) ERP estimates and the HF-ERP models during IVS-CONT08 are in a good agreement at prograde and retrograde 12 hours both for length of day (LOD) and polar motion. However, at 24 hour prograde polar motion the amplitude from GPS is larger by about 100 μas than VLBI and larger by about 160 μas than HF-ERP models. Additionally, VieVS LOD and polar motion estimates are noisier than from GPS. This may be due to the fact that no relative constraints between the CPWLO ERP estimates in VLBI analysis were introduced. The estimation of hourly source coordinates was rather intended as test study. As long as hourly CPWLO coordinates of two sources are estimated and the remaining sources are fixed to their a priori Celestial Reference Frame (CRF)

coordinates, parametrization of the Earth Orientation Parameters (EOP) is not critical for the estimated source coordinates. However, investigations on this issue need to be carried out in future, e.g. a lot can be learned from correlations between hourly source coordinates and the observation geometry.

The second aim of this thesis, which is also a very good test of the CPWLO estimates of troposphere zenith delays and gradients, is the contribution to combination studies in the framework of the Global Geodetic Observing System (GGOS) of the International Association of Geodesy (IAG) by multi-technique comparison of zenith total delays (ZTD) and troposphere gradients. In the scope of this issue, VLBI VieVS estimates of troposphere ZTD and gradients during IVS-CONT08 were compared with those derived from observations with the GPS, Doppler Orbitography and Radiopositioning Integrated by Satellite (DORIS), and water vapor radiometers (WVR) co-located with the VLBI radio telescopes. ZTD and gradients estimated by space geodetic techniques are compared to those computed by ray-tracing through the profiles of various Numerical Weather Models (NWM), such as the European Centre for Medium-Range Weather Forecasts (ECMWF) (all sites), the Japan Meteorological Agency (JMA) and Cloud Resolving Storm Simulator (CReSS) (Tsukuba in Japan), and the High Resolution Limited Area Model (HIRLAM) (European sites). The best inter space geodetic technique agreement of ZTD during IVS-CONT08 is found between the combined IVS and the International GNSS Service (IGS) solutions with a mean standard deviation of about 6 mm over all sites, whereas the agreement with numerical weather models is between 6 and 20 mm. The standard deviations are generally larger at low latitude sites because of higher humidity, and the latter is also the reason why the standard deviations are larger at northern hemisphere stations during IVS-CONT08 in comparison to IVS-CONT02 which was observed in October 2002. The assessment of the troposphere gradients from the different techniques is not as clear because of different time intervals, different estimation properties, or different observable. However, the best inter-technique agreement is found between the IVS combined gradients and the GPS solutions with standard deviations between 0.2 mm and 0.7 mm. As mentioned before all the comparisons and validation tests on the troposphere products during IVS-CONT08 presented in this thesis provide important information with respect to the planned combination and integration of various observing techniques in the framework of the Global Geodetic Observing System (GGOS) of the International Association of Geodesy (IAG).

Zusammenfassung

Das Hauptziel der Arbeiten, die im Rahmen dieser Dissertation durchgeführt wurden, ist der Beitrag zum Projekt VLBI2010 des International Very Long Baseline Interferometry (VLBI) Service for Geodesy and Astrometry (IVS) mittels Entwicklung eines Moduls zur Parameterbestimmung (vie_lsm) in der Vienna VLBI Software (VieVS), das die präzise Bestimmung der subtäglichen geodätischen Parameter aus VLBI (Very Long Baseline Interferometry) Beobachtungen ermöglicht. Das vie_lsm Modul basiert auf der Methode der kleinsten Quadrate (Gauss-Markoff-Modell) für kontinuierliche stückweise lineare Offset-Funktionen (continuous piecewise linear offsets, CPWLO), wobei die Offsets immer zu eindeutigen Epochen, d.h. ganzen Stunden oder ganzzahligen Teilen bzw. Vielfachen davon, bestimmt werden. Das Intervall für die CPWLO Parametermodellierung liegt üblicherweise zwischen einem Tag und fünf Minuten.

Fr Untersuchungen der subtäglichen Bewegungen der VLBI-Antennen aufgrund der Gezeiten während der CONT05 Kampagne des IVS wurden stündliche CPWLO Stationskoordinaten des terrestrischen Referenzrahmens (TRF) bestimmt. Obwohl alle Gezeitenverschiebungen aus neuesten geophysikalischen Modellen berechnet werden und aus den Beobachtungen vor dem Ausgleich reduziert werden, erreichen die radialen Amplituden der stündlichen Antennenkoordinaten bis zu 1 cm (Kokee Park, HartRAO, Gilcreek, Westford, Svetloe und Wettzell). Für die Untersuchung der hochfrequenten (subtäglichen) Erdrotationparameter (HF-ERP) aus VieVS während der CONT08 Kampagne wurden stündliche CPWLO der Erdrotationsparameter (ERP) bestimmt. Fourierspektren dieser stündlichen VLBI- als auch GPS- (Global Positioning System) ERPs sind in guter Übereinstimmung mit HF-ERP-Modellen während der CONT08 Kampagne, vor allem bei prograden und retrograden Amplituden bei 12 Stunden für Tageslänge (LOD) und Polbewegung. Bei 24 Stunden der prograden Polbewegung ist die Amplitude jedoch aus GPS-Messungen um 100 μas gröer als aus VLBI und um 160 μas gröer im Vergleich zu den ERP-Modellen. Auerdem haben die LOD- und Polbewegungsparameter mit VieVS einen höheren Rausch-Level als jene aus GPS. Der Grund dafür kann sein, dass keine relativen Con-

straints zwischen den CPWLO ERP in der VLBI-Analyse benutzt wurden. Die Bestimmung der stündlichen Quellenkoordinaten war als reine Teststudie gedacht. Solange die stündlichen CPWLO-Koordinaten von zwei Quellen bestimmt wurden und bei den anderen Quellen die a priori CRF-Koordinaten (Koordinaten des himmelsfesten Referenzrahmens) fixiert wurden, war die Parametrisierung der Erdorientierungsparameter (EOP) für die unbekannten Quellenkoordinaten nicht kritisch. Detailliertere Untersuchungen zu diesem Thema sollen jedoch in Zukunft durchgeführt werden. So kann viel aus Korrelationen zwischen stündlichen Quellenkoordinaten und der Beobachtungsgeometrie gelernt werden.

Der zweite Ziel dieser Dissertation, der auch einen sehr guten Test der CPWLO der totalen troposphärischen Laufzeitverzögerungen in Zenitrichtung (ZTD) und der Gradienten darstellt, ist der Beitrag zu Kombinationsstudien im Rahmen des "Global Geodetic Observing System (GGOS)" der "International Association of Geodesy (IAG)". Dabei wurden die ZTD und Gradienten während der IVS-CONT08 Kampagne aus VieVS mit den Parametern an Kolokationsstationen aus GPS, DORIS (Doppler Orbitography and Radiopositioning Integrated by Satellite)- und Wasserdampfradiometer-Messungen verglichen. Auerdem wurden ZTD und Gradienten aus geodätischen Weltraumverfahren mit Ergebnissen des Ray-tracings durch verschiedene numerische Wettermodellen verglichen, wie des Europäischen Zentrums fr Mittelfristige Wettervorhersage (ECMWF) (alle Stationen), der Japanischen Meteorologischen Agentur (JMA), des Cloud Resolving Storm Simulator (CReSS) (Tsukuba in Japan) und des High Resolution Limited Area Model (HIRLAM) (Europäische Stationen). Die beste Übereinstimmung von ZTD während der IVS-CONT08 Kampagne unter den geodätischen Weltraumverfahren wird zwischen der kombinierten IVS- und IGS (International GNSS Service)-Lösung mit der mittleren Standardabweichung von 6 mm für alle Stationen gefunden, wobei die Übereinstimmung mit den numerischen Wettermodellen nur zwischen 6 mm und 20 mm liegt. Die Standardabweichungen sind üblicherweise gröer auf Stationen auf niedrigeren Breiten, was auf den höheren Feuchtegehalt in der Atmosphäre zurückgeführt werden kann. Der Feuchtegehalt war auch der Grund für die höheren Standardabweichungen der Stationen auf der Nordhalbkugel während der IVS-CONT08 Kampagne (August) im Vergleich zur IVS-CONT02 Kampagne, welche im Oktober 2002 durchgeführt wurde. Die Bewertung der troposphärischen Gradienten aus den verschiedenen Verfahren ist schwierig wegen den verschiedenen Zeitintervallen, den verschiedenen Bestimmungseigenschaften oder verschiedenen Beobachtungsgröen. Die beste Übereinstimmung zwischen verschiedenen Verfahren wurde jedoch zwischen den IVS-kombinierten Gradienten und der GPS-Lösung mit der Standardabweichung zwischen 0.2 mm und 0.7 mm gefunden. Wie bere-

its erwähnt liefern alle Vergleiche und Validierungstests der troposphärischen Produkte während der IVS-CONT08 Kampagne, die in dieser Dissertation präsentiert werden, wichtige Informationen für die geplante Kombination und Integration der verschiedenen Beobachtungsverfahren im Rahmen des GGOS der IAG.

Acknowledgements

When I first came to Vienna, Austria as an Erasmus student, it was also the first time that I was abroad. I inspired and fall in love with the city Vienna. I have been acquainted with Dr. Emine Tanır for more than ten years who helped me to get into contact with Prof. Dr. Harald Schuh. I am thankful to Dr. Emine Tanır for her lots of helps and supports. I am grateful to Prof. Dr. Harald Schuh having accepted me to perform PhD at the Institute of Geodesy and Geophysics (IGG) under his supervision when I really needed a helping hand. I will always proud of saying Prof. Dr. Harald Schuh was my PhD supervisor. I profoundly respect and admire him for his kind and tactful attitudes towards people around him. I am also thankful to Prof. Dr. Harald Schuh and Dr. Johannes Boehm for their constant supports, encouragements and motivations on my studies. I have learned too much from Dr. Johannes Boehm in terms of science. I am indeed feeling so lucky that I know such a nice person. I want to forward my special thanks to Dr. Johannes Boehm who helped me on my PhD studies from the beginning to the end. Dr. Tobias Nilsson was always helpful to me on solving lots of unsurmountable scientific problems that I have encountered especially during the last year of my PhD. I am also grateful to Dr. Johannes Boehm and Dr. Tobias Nilsson for reviewing my thesis. Their constructive criticism, suggestions greatly improved this PhD thesis. I am grateful to Dr. Dudy Wijaya for his scientific discussions with me on several issues arising especially during coffee breaks like troposphere, ray-tracing and atmosphere loading that I also learned too much from him and I am thankful to him for the Latex templates of this PhD thesis. I want to express my appreciation to Dipl.-Ing. Lucia Plank and Dipl.-Ing. Hana Spicakova to whom I closely worked with before and after the birth of VieVS, a state-of-the-art VLBI analysis software. I am thankful to Hana Spicakova for translating the English abstract of this thesis to German. I am especially grateful to Dipl.-Ing. Sigrid Boehm, Dipl.-Ing. Michael Schindelegger and Dipl.-Ing. Andrea Pany for their huge scientific support. I want to forward my special thanks to MSc. Mahdi Alizadeh who is my roommate at IGG being always kind and helpful to me. I will never forget all my colleagues working at Advanced Geodesy Research Group being always helpful and

kind to me during my doctorate studies and will always remember them with a smile on my face. I have experienced a great support and joyful working atmosphere with all co-operative people at IGG, TU Wien. I feel very lucky to have been a member of this group, which provided a way to establish my future career. I want to forward my special thanks to Frau Linsmayer who is our Secretary of the IGG. One of the most memorable activities that I will never forget among others is running (for my case it was mostly walking) at Prater each week and having dinner at the restaurants, El Conte and Mehler every week. The other most memorable activities are cottage retreats and cheering for German football team while we were watching the matches at Prof. Schuh's office during World Cup 2010.

I want to forward my special thanks to Karadeniz Technical University, Department of Geomatics Engineering where I graduated from and finished my MSc studies. I want to forward many thanks to Prof. Dr. Mustafa Türker who has supported me when I needed a permanent assistant position for the continuation of my academic studies abroad. I will always be proud of being a member of Hacettepe University and having my PhD from Vienna University of Technology. I want to acknowledge TUBITAK (The Scientific and Technological Research Council of Turkey) for funding my expenses in the first two years of my PhD studies in Vienna. I am grateful to Hacettepe University for its financial support for the remaining years of my doctorate studies and accepting me as a permanent member of Hacettepe University. I want to forward many thanks to IGG, TU Wien for supporting me by paying for my expenses in order to participate many scientific meetings. I cordially acknowledge the International VLBI Service for Geodesy and Astrometry (IVS) and the other International Association of Geodesy (IAG) and International Union of Geodesy and Geophysics (IUGG) services for the data and the numerous authors for their publications that I benefitted from in my doctorate studies.

I am thankful to Dr. Axel Nothnagel and Prof. Dr. Hansjörg Kutterer for doing the external reviews on this thesis and taking the examination.

Finally, I am grateful to my mother and father, and brother for their endless love, patience and support.

Contents

List of Figures

xiii

List of Tables

Symbols

VLBI delay model

c	Velocity of light in vacuum environment
$\vec{k}$	Unit source (quasar) vector defined in a space-fixed, barycentric and equatorial celestial system
$\vec{b}$	Baseline vector of the VLBI antennas defined in Earth-fixed, geocentric, equatorial terrestrial coordinate system
τ	VLBI delay
$\Delta\tau_{retarded\,baseline}$	Delay correction due to the motion of second antenna (in geocentric celestial reference system, GCRS) the during the propagation time of the wavefront between station 1 and station 2
$\Delta\tau_{clock}$	Delay correction due to the synchronization and frequency discrepancies of atomic clocks at station 1 and station 2
$\Delta\tau_{trop}$	Troposphere delay correction
$\Delta\tau_{iono}$	Ionosphere delay correction
t	Observation epoch
X_{ITRS}	ITRS coordinates of the VLBI antenna
X_{GCRS}	GCRS coordinates of the VLBI antenna
$W(t)$	Regardless from "Equinox based" or "CIO based" transformation matrix between ITRS and TIRS (Terrestrial Intermediate Reference System) arising from the motion of the CIP in TRS at the epoch t
y_p	Polar motion coordinate in ITRS along the 270° east meridian
$R_1(y_p)$	Rotation matrix with y_p around the first axis of ITRS
x_p	Polar motion coordinate in ITRS along the Greenwich meridian
$R_2(x_p)$	Rotation matrix with x_p around the second axis of ITRS
s'	Quantity, named as "Terrestrial Intermediate Origin (TIO) locater", which provides

	the position of the TIO on the equator of the CIP at epoch t corresponding to the kinematical definition of the "non-rotating" origin (NRO) in the ITRS
$R_3(s')$	Rotation matrix with s' around the third axis of ITRS
$Q(t)$	CIO based transformation matrix between CIRS (Celestial Intermediate Reference System) and GCRS arising from the motion of the CIP at the epoch t in GCRS
s	Quantity named "CIO locator", which provides the position of the CIO on the equator of the CIP at epoch t corresponding to the kinematical definition of the non-rotating-origin (NRO) in the GCRS
$R_3(s)$	Rotation matrix with s around the third axis of GCRS
$ERA(t)$	Earth Rotation Angle between the CIO and TIO on the equator of the CIP at epoch t
$R_3(-ERA(t))$	Rotation matrix with $-ERA$ at epoch t around the CIP pole or the rotation between TIRS and CIRS around their third axis (CIP axis)
G	Gravitational Constant
M_J	Rest mass of the Jth gravitating body
$M_\oplus$	Rest mass of the Earth
$\vec{R}_{iJ}$	Vector from the Jth gravitating body to the ith antenna
α	Right ascension of a source defined in BCRS
δ	Declination of a source defined in BCRS
ΔT_{gravJ}	Gravitational delay on the signal of the extra-galactic radio source caused by the Jth gravitating body
$\Delta T_{grav\oplus}$	Gravitational delay on the signal caused by the Earth
$\vec{R}_{1J}$	Vector from the the first antenna to the Jth gravitating body
$\vec{R}_{\oplus\odot}$	Vector from the Sun to the geocenter
$\vec{X}_J(t_1)$	Barycentric coordinate vector of the Jth gravitating body at epoch t_1
$\vec{V}_J(t_1)$	Barycentric velocity vector of the Jth gravitating body at epoch t_1
$\vec{X}_\oplus(t_1)$	Barycentric coordinate vector of the geocenter at epoch t_1
ω_i	The geocentric velocity of the ith antenna
$\vec{V}_J(t_1)$	Barycentric velocity vector of the geocenter at epoch t_1
$\vec{X}_i(t_1)$	Barycentric coordinate vector of the ith antenna at epoch t_1
$\vec{x}_i(t_1)$	Geocentric coordinate vector of the ith antenna at epoch t_1
$\vec{V}_\oplus$	Barycentric velocity vector of the geocenter
ΔT_{grav}	Total gravitational delay which is the sum of all gravitating bodies

	including the Earth
γ	Constant according to the general relativity using BCRS equals to 1
U	Gravitational potential at the geocenter, neglecting the effects of the Earth's mass
t_{vi}	"Vacuum" geocentric coordinate time (TCG) of arrival of a radio signal at the ith VLBI receiver including the gravitational bending but neglecting the atmospheric delay and atmospheric bending
δt_{atm1}	Hydrostatic part of the troposphere delay at antenna 1 at the observation epoch t_1
$\Delta L_h^{st(1)}(t_1)$	Troposphere zenith hydrostatic delay at the antenna 1 at epoch t_1
$t_2 - t_1$	Total delay
$t_{g2} - t_{g1}$	Geometric delay
m_h	Hydrostatic mapping function
ε	Elevation angle of the observation from local horizon
$\vec{k}$	Aberrated source vector after transforming to TRF
oc	Observed minus computed vector (reduced observation vector) basically includes clock errors, troposphere zenith wet delays, azimuthal asymmetric parts of the troposphere delays at both antenna of the baseline, and the effect of the errors in the other a priori values used to calculate $t_2 - t_1$
$\frac{\partial \tau}{\partial x_p}$	Partial derivative of the VLBI delay w.r.t. the CIP coordinate in TRF along Greenwich meridian, x_p
$\frac{\partial \tau}{\partial y_p}$	Partial derivative of the delay w.r.t. the CIP coordinate in TRF along 270 east longitude, y_p
$\frac{\partial \tau}{\partial (UT1)}$	Partial derivative of the delay w.r.t. Earth phase of rotation, UT1
$\frac{\partial \tau}{\partial X}$	Partial derivative of the delay w.r.t. the CIP coordinate X in CRF
$\frac{\partial \tau}{\partial Y}$	Partial derivative of the delay w.r.t. the CIP coordinate Y in CRF
$\frac{\partial \tau}{\partial \alpha}$	Partial derivative of the delay w.r.t. right ascension of a source, α
$\frac{\partial \tau}{\partial \delta}$	Partial derivative of the delay w.r.t. declination of a source, δ
$\frac{\partial \tau}{\partial X_{st1}}$	Partial derivative of the delay w.r.t. the TRF coordinate X component of antenna 1
ΔL	Continuous piece-wise linear offset (CPWLO) function
x_1	First CPWLO estimate at integer UTC hour, multiples or fractions of UTC hour
$\frac{\partial \Delta L(t)}{\partial x_1}$	The partial derivative of the CPWLO function w.r.t. the 1st offset x_1 at the observation epoch t
x_2	Second CPWLO estimate at integer UTC hour, multiples or fractions of UTC hour

$\frac{\partial \Delta L(t)}{\partial x_2}$	Partial derivative of the CPWLO function w.r.t. the second offset, x_2 at the observation epoch t
$\frac{\partial \tau(t)}{\partial (X_{st1})_{x_1}}$	Partial derivative of the delay at the observation epoch t w.r.t. the first CPWLO of the X coordinate of the antenna 1

Least-Squares Adjustment

$\phi(x)$	Mathematical model of a phenomena depending on a set of model parameters, x
L_i	i^{th} observation
v_i	Post-fit observational residual of the ith observation
v	Observational residuals vector
K_{ll}	Co-variance matrix of the observations
s_0	A priori standard deviation of unit weight
$v^T P v$	Weighted sum of the squares of the post-fit observational residuals
δx_j	j^{th} reduced unknown parameter, $x_j - x_{0j}$
δx	Reduced unknown parameter vector
l_i	i^{th} reduced observation ('observed'-'computed' with a priori values of estimates, x_0
l	Reduced observation vector
n	Number of observations
u	Number of unknowns
A	Design matrix
P	Weight matrix of the observations
N	Normal equation matrix
b	Normal equation constants (right hand side) vector
m_0	A posteriori standard deviation of unit weight
K	Variance-covariance matrix of the estimated parameters
n_{constr}	Number of constraints as pseudo-observations
v_c	Correction vector the the constraints
H	Jacobian matrix for pseudo-observations
h	'observed' minus 'computed' vector for the constraints
v_c	Residuals vector over the constraints
P_c	Weight matrix for the pseudo-observations
N_{total}	Datum conditions and soft constraints imposed normal equations matrix
b_{total}	Datum conditions and soft constraints imposed normal equations right hand side

	vector
x_c	Unknown parameters of the constrained LS solution
m_{0c}	A posteriori standard deviation of the constrained normal equation system
K_{xx}	Variance-covariance matrix for the unknowns of the constrained
	normal equation system
δx_1	Group of parameters that will be pre-reduced from N and b
δx_2	Group of parameters that will be kept in N and b
N_{reduc}	Reduced normal equation matrix of the parameter set δx_2
b_{reduc}	Reduced normal equation right hand side vector of the parameter set δx_2
$A(i)$	Design matrix of the ith model, e.g. the design matrix of the CPWLO
	TRF coordinates of the antennas
X_i, Y_i, Z_i	New coordinates after LS solution of the ith antenna
X_{0i}, Y_{0i}, Z_{0i}	A priori (catalogue) coordinates of the ith antenna after scaling w.r.t.
	the Earth mean radius
T_X, T_Y, T_Z	Translations in X, Y, Z axes directions between two cartesian coordinate system
α, β, γ	Rotations around X, Y, Z axes between two cartesian coordinate system
μ	Scale factor between two cartesian coordinate system
ζ	Unknown transformation parameters vector
B	Design matrix of the three dimensional cartesian Helmert similarity transformation
δx_c	Unknowns of the conditions
b_c	Constants vector of the condition equations
sc	Scaling factor with the Earth mean radius to the a priori (catalogue) coordinates
m_{dx}	Standard deviation (formal error) of the estimated parameter
m_{v_i}	Standard deviation of the ith post-fit observational residual
Q_{ll}	Cofactor matrix of the observations
$Q_{\hat{l}\hat{l}}^-$	Cofactor matrix of the adjusted observations
Q_{xx}	Cofactor matrix of the estimated parameters
Q_{vv}	Cofactor matrix of the observational residuals

VLBI clock error

$\Delta\tau_{clk}^{POLY}(t)$	One of the clock delay error at the observation epoch t represented by
	the quadratic polynomial
$\Delta\tau_{clk}^{CPWLOF}(t)$	One of the clock delay error at the observation epoch t represented by CPWLO function

β_j	j^{th} order quadratic polynomial coefficient (unknown) of a clock
$\Delta\tau_{clk}(t)$	Total clock error at observation epoch t from quadratic polynomial in addition to CPWLO function
$\frac{\partial\Delta\tau_{clk}(t)}{\partial\beta_j}$	Partial derivative of the clock delay error model w.r.t. j^{th} order polynomial coefficient
$\frac{\partial\Delta\tau_{clk}(t)}{\partial x_1}$	Partial derivative of the clock delay error model w.r.t. the first CPWLO
$\frac{\partial\Delta\tau_{clk}(t)}{\partial x_2}$	Partial derivative of the clock delay error model w.r.t. the second CPWLO
A_{CPWLOF}	Design matrix of CPWLO for the clocks
A_{POLY}	Design matrix of clock polynomial coefficients for the clocks

Troposphere delay

ΔL_{TROP}	Troposphere slant path delay
n	Refractive index
S	Slant radio wave path between the geodetic instrument and the highest part of the troposphere, plus the bending effect
G	Geometric path that can be defined as the path of a signal in vacuum (straight line)
$S - G$	Bending effect
N	Total refractivity
N_h	Hydrostatic refractivity
N_w	Wet refractivity
ρ	Total density of the air
ρ_d	Density of dry air
ρ_w	Density of water vapor
p	Total pressure
e	Water vapor pressure
T	Temperature
R	Universal gas constant
m_d	Molar masses of dry air
m_w	Molar masses of water vapor
Z_d^{-1}	Inverse compressibility factors for dry air
Z_w^{-1}	Inverse compressibility factors for water vapor
ε_1	Initial elevation angle from the site through the troposphere to the source
k	Total number of radio wave path increments through troposphere
s_i	Length of the slant path of the ith increment

ds_{hi}	Slant hydrostatic delay of the ith increment
ds_{wi}	Slant wet delay of the ith increment
P_i	Intersection of the ray with the lower boundary of the ith increment
h_i	the height of P_i
r_0	Earth radius
r_i	Distance from the center of the Earth to the point P_i
$z_{i+1}; y_{i+1}$	2D coordinates of P_i in a plane covering the radio wave path along troposphere
$m_h(\varepsilon, t)$	Hydrostatic mapping function of an observation at elevation the angle ε and the epoch t,
$m_w(\varepsilon, t)$	Wet mapping function of an observation at the elevation angle ε and the epoch t
$a_{h,w}; b_{h,w}; c_{h,w}$	Hydrostatic and wet coefficients of the mapping function
G_N	Troposphere north gradient
G_E	Troposphere east gradient
α	Azimuth angle of the observation)
$\Delta\tau_{trop}^{hyd}(t)$	Zenith hydrostatic delay at the observation epoch t
φ	Latitude of a VLBI site
h	Ellipsoidal height of a VLBI site
$\Delta\tau_{trop}^{wet}(t)$	Wet delay of an observation at epoch t represented by CPWLO function
$\frac{\partial\Delta\tau_{trop}(t)}{\partial(ZWD)_{x_1}}$	Partial derivative of the troposphere wet delay at epoch t
	represented by CPWLO function w.r.t. the first CPWLO
$\frac{\partial\Delta\tau_{trop}(t)}{\partial(ZWD)_{x_2}}$	Partial derivative of the troposphere wet delay at epoch t
	represented by CPWLO function w.r.t. the second CPWLO
$\frac{\partial\Delta\tau_{trop}(t)}{\partial(G_N)_{x_1}}$	Partial derivative of the troposphere north gradient at epoch t
	represented by CPWLO function w.r.t. the first CPWLO
$\frac{\partial\Delta\tau_{trop}(t)}{\partial(G_N)_{x_2}}$	Partial derivative of the troposphere north gradient at epoch t
	represented by CPWLO function w.r.t. the second CPWLO
$\frac{\partial\Delta\tau_{trop}(t)}{\partial(G_E)_{x_1}}$	Partial derivative of the troposphere east gradient at epoch t
	represented by CPWLO function w.r.t. the first CPWLO
$\frac{\partial\Delta\tau_{trop}(t)}{\partial(G_E)_{x_2}}$	Partial derivative of the troposphere east gradient at epoch t
	represented by CPWLO function w.r.t. the second CPWLO

Troposphere tie

H_0	Reference height at the co-located site

H	Height of the geodetic instrument
p_0	Total pressure at the reference height of the co-located site
p	Total pressure at the geodetic instrument
e_0	Water vapor pressure at the reference height of the co-located site
T_0	Temperature at the reference height of the co-located site
T_0	Temperature at the reference height of the co-located site
γ	Average temperature lapse rate
R_L	Specific gas constant
g	Gravity

Analysis of the TRF, EOP, and CRF VLBI estimates

m_{x1}	Formal error of the last CPWLO estimate of the former session
m_{x2}	Formal error of the first CPWLO estimate of the following session
$\bar{x}$	Weighted mean of the CPWLO at the session boundaries
$m(\bar{x})$	Formal error of the new offset
$(X, Y)_{IAU2000A}$	CIP coordinates in GCRS computed from the precession-nutation model e.g. IAU2000A
$(\Delta X, \Delta Y)_{correction}$	Daily corrections to the precession-nutation model derived coordinates of the CIP in GCRS, that can be obtained from e.g. IERS 05 C04 combined daily EOP series (at 0:00 UTC)
$(x_p, y_p)_{predicted}$	Daily TRF coordinates of the rotation pole e.g. distributed with the IERS 05 C04 combined daily EOP series
$\Delta UT1_{predicted}$	Daily values of the Earth phase of rotation e.g. distributed with the IERS 05 C04 combined daily EOP series
$(\Delta x, \Delta y)_{HF-ERP}$	Diurnal and semi-diurnal polar motion variations which can be computed from the sum of high-frequency ERP (HF-ERP) models e.g. ocean tides and libration (Earth's triaxiality)
$\Delta UT1_{HF-ERP}$	Diurnal and semi-diurnal variations on the Earth's absolute rotation angle which can be computed from the sum of high-frequency ERP (HF-ERP) models e.g. ocean tides and libration (Earth's triaxiality)
dx_p, dy_p	CPWLO estimates of polar motion coordinates
$dUT1$	CPWLO estimates of Earth's absolute rotation angle
dX, dY	CPWLO estimates of the CIP coordinates in GCRS

$\bar{\alpha}$	Median of CPWLO right ascension estimates of a source
$\bar{\delta}$	Median of CPWLO declination estimates of a source
$m_{\bar{\alpha}}$	Median formal errors of CPWLO right ascension estimates of a source
$m_{\bar{\delta}}$	Median formal errors of CPWLO declination estimates of a source

Acronyms

VLBI	Very Long Baseline Interferometry
VieVS	Vienna VLBI Software
IVS	International VLBI Service for Geodesy and Astrometry
GNSS	Global Navigation Satellite Systems
CODE	Center for Orbit Determination in Europe
IGS	International GNSS Service
GPS	Global Positioning System
DORIS	Doppler Orbitography and Radio Positioning Integrated by Satellite
IDS	International DORIS Service
IERS	International Earth Rotation and Reference Systems Service
GGOS	Global Geodetic Observing System
IAG	International Association of Geodesy
IAU	International Astronomical Union
IUGG	International Union of Geodesy and Geophysics
AIUB	Astronomical Institute of the University of Bern
IAPG/TUM	Institut für Astronomische und Physikalische Geodäsie of the Technische Universität München
BKG	German Federal Agency for Cartography and Geodesy
TU Wien-IGG	Vienna University of Technology - Institute of Geodesy and Geophysics
IAPG/TUM	Institut für Astronomische und Physikalische Geodäsie of the Technische Universität München
NICT	National Institute of Information and Communications Technology, Japan
NIED	National Research Institute for Earth Science and Disaster Prevention
SMHI	Swedish Meteorological and Hydrological Institute
CNES	Centre National d'Etudes Spatiales

NWM	Numerical Weather Model
NWP	Numerical Weather Prediction Model
ECMWF	European Center for Medium-Range Weather Forecasts
HIRLAM	High Resolution Limited-Area Model
JMA/CReSS	Japanese Meteorological Agency Cloud Resolving Storm Simulator
JMA/KARAT	Japanese Meteorological Agency Kashima Ray-Tracing Tools
JMA/MANAL	Japanese Meteorological Agency Meso-scale Analysis Data

WVR	Water Vapor Radiometer
ZTD	Zenith Total Delay
ZHD	Zenith Hydrostatic Delay
ZWD	Zenith Wet Delay
ΔZWD	Zenith Wet Delay Tie
ΔZHD	Zenith Hydrostatic Delay Tie
VMF1	Vienna Mapping Functions 1
GMF	Global Mapping Functions
NMF	Niell Mapping Functions
IMF	Isobaric Mapping Functions

ICRS	International Celestial Reference System
ICRF	International Celestial Reference Frame
ITRS	International Terrestrial Reference System
ITRF	International Terrestrial Reference Frame
ITRF05	International Terrestrial Reference Frame 2005
VTRF2008	VLBI Terrestrial Reference Frame 2008
NNT	No Net Translation
NNR	No Net Rotation
EOP	Earth Orientation Parameters
ERP	Earth Rotation Parameters
TIO	Terrestrial Intermediate Origin
CIO	Celestial Intermediate Origin
ERA	Earth Rotation Angle between the CIO and the TIO
NRO	Non-rotating Origin

TIRS	Terrestrial Intermediate Reference System
CIRS	Celestial Intermediate Reference System
UTC	Universal Time Coordinated
UT	Universal Time
TAI	Atomic time
TT	Terrestrial Time
J2000	2000 January 1d 12h, named as fundamental or standard epoch
TCB	Barycentric coordinate time
TCG	Geocentric coordinate time
ASD	Allan standard deviation
SET	Solid Earth tide (body tide)
OTL	Ocean tidal loading
ATL	Atmosphere tidal loading
ANTL	Atmosphere non-tidal loading
PT	Pole tide
FES	Finite element solution
HF-ERP	High-Frequency (short period) Earth rotation parameters

1. Introduction

1.1. VLBI Basics

The Very Long Baseline Interferometry (VLBI) is the unique technique observing extra-galactic radio sources whose coordinates define the celestial reference frame (CRF), e.g. ICRF2. VLBI is also unique among other space geodetic techniques in terms of observing Earth orientation parameters (EOP). VLBI antennas cover the globe with intercontinental baselines. Extra-galactic radio sources that are observed by VLBI are also named quasi-stellar radio sources (quasars). Besides, VLBI contributes significantly to the realization of the International Terrestrial Reference System (ITRS), particularly for the scale (Campbell, 1979; Schuh, 1987; Campbell, 2000; Sovers et al., 1998).

Generally, geodetic VLBI observing sessions run for 24 hours and observe a number of different extra-galactic radio sources. VLBI measures the time differences in the arrival of microwave signals τ emitted by extra-galactic radio sources and received at two or more VLBI antennas. VLBI measurements are done at microwave frequencies. Microwaves are less sensitive to weather (clouds, rain) than optical waves. For antennas separated by a few thousand kilometers or less, it is often practical to have all antennas simultaneously observing the same source. At the VLBI sites radio antennas detect weak signals radiating from radio sources and the integration times are typically from 2 to 13 minutes. Presently, the signals recorded at the antenna have the frequencies 2.3 GHz (S-band) and 8.4 GHz (X-band), and the wave-lengths of these signals are 13 and 3.5 cm, respectively. After the signals at each antenna are written to hard disks the signals recorded at all participating antennas in the VLBI session are combined pair-wise at the correlators, thereby producing an interference pattern. The correlation process is carried out in parallel for many frequency channels, with each channel producing average amplitudes and phases every 1-2 seconds. These results are stored for later analyses with post-correlation software. Briefly, post-correlation codes perform many functions in order to prepare the data for the final processing by the modelling/estimation software, e.g. the Vienna VLBI Software,

VieVS. The core task of the post-correlation software is to take the set of phase samples from the various frequency channels and times, and to fit the set with three parameters: the phase, the group delay, and the phase delay rate. To summarize, the interferometer is capable of producing four data types: phase delay, group delay, phase delay rate, and amplitude (Sovers et al., 1998).

VLBI is a part of geodesy for nearly 40 years, and since 1999 it is coordinated by the International VLBI Service for Geodesy and Astrometry (IVS) - a Service of the International Association of Geodesy (IAG) and International Astronomical Union (IAU) (Schuh et al., 2007; Schlüter and Behrend, 2007). IVS provides data and products for the scientific community, the main of which are the Celestial Intermediate Pole (CIP) position in the ITRS (x_p, y_p), the Earth axis absolute rotation angle ($UT1 - UTC(\Delta UT1)$), the Celestial Intermediate Pole (CIP) position in the GCRS (X and Y) (nutation offsets), source coordinates in the BCRS (α, δ), antenna cartesian coordinates and velocities in the TRF, troposphere zenith wet delays (ZWD), troposphere gradients, atomic clock (mostly hydrogen masers) errors due to the synchronization and frequency instabilities, or special parameters, such as tidal Love and Shida numbers (describing the Earth's elastic response to the tidal potential caused by external bodies). The IVS regularly submits a complete set of EOP to the International Earth Rotation and Reference System Service (IERS) which is obtained as a combination of the individual solutions of operational IVS Analysis Centers (AC) (Nothnagel and Steinforth, 2002). The IVS AC also submit datum free normal equation matrices, (N), the right hand side vectors (b) of the antenna TRF positions, and source CRF positions for the realization of CRF on a session-wise basis. All IVS data and products are archived in data centers and are publicly available for research in related areas of geodesy, geophysics and astrometry (Schlüter and Behrend, 2007).

Numerous small periodic and quasi-periodic tidal effects make important contributions to space geodetic observations at the millimeter level. Models of tectonic motions, solid Earth tides, ocean tidal effects, atmosphere pressure loading on antenna TRF positions and alterations of the Earth's surface due to local geological and hydrological processes should be considered in the VLBI observation equations. While high-altitude atmospheric charged-particle (ionospheric) effects are easily modelled for measurements on two well-separated frequencies, the contribution of the neutral atmosphere (troposphere) at lower altitudes is more difficult to remove. In fact, mis-modelling of the troposphere remains the main error source, today.

1.2. Contribution of the thesis and research objectives

In September 2005 the IVS Directing Board accepted the final Working Group 3 report entitled "VLBI2010: Current and Future Requirements for Geodetic VLBI Systems" (Petrachenko et al., 2009). The basic targets for the next-generation VLBI system are envisaged as follows:

- 1 mm VLBI antenna reference point position accuracy in global scale should be achieved.

- Continuous measurements should be done in order to derive uninterrupted time series of station positions and Earth orientation parameters.

- Geodetic products should be available within less than 24 hours.

In related studies of the VLBI2010 project, Monte Carlo simulations were successfully carried out by means of testing several alternatives of simulations, e.g. on the number of observations per session, on the delay observable with different accuracies, on the number of scans per antenna, on the atmosphere estimation intervals, and a priori variance-rates on the atmosphere and clocks (Pany et al., 2008). One of the results of the simulation studies of VLBI2010 was the determination of the need of a future VLBI analysis software. Thus, based on the VLBI2010 project analysis related requirements, the Institute of Geodesy and Geophysics, Vienna University of Technology, has initiated in 2007 a project towards creating a compact VLBI analysis software based on Matlab. It is named Vienna VLBI Software (VieVS). Following the state-of-the-art geodetic and geophysical models, using LS parameter estimation modules for single session and global solutions, adding flexible simulation and scheduling modules VieVS is capable of analyzing future VLBI2010 type sessions. The software is easy to use and flexible options for the models and estimations with graphical user interfaces are available. Basic contributions of this thesis to the VLBI2010 project and to the combination studies of GGOS are as follows:

- **VLBI2010 project:** *Estimating reliable and accurate sub-daily geodetic and geophysical parameters.* The basic pre-requisite of reaching this target is providing the following condition: An adequate number of observations should be dispersed homogenously to each estimation interval of the corresponding parameter in the session.

- **Combination studies:** *Contributing to the combination studies* in the framework of the Global Geodetic Observing System (GGOS) (Rummel et al., 2005) of the International Association of Geodesy (IAG) by multi-technique comparison of ZTD and troposphere

gradients.

The vie_lsm module of VieVS was written for the estimation of geodetic VLBI parameters with the Least-Squares adjustment method (LS), based on the Gauss Markoff model. The development of the vie_lsm module was a major part of this PhD study. The research objectives of this thesis can be itemized as follows:

- *Estimating geodetic parameters with continuous piece-wise linear offset (CPWLO) functions* where rates are represented by offsets. CPWLO are estimated at unique epochs i.e. UTC integer hours or fractions or multiples of integer UTC hours.

- *Estimating the sub-daily CPWLO of VLBI antenna TRF coordinates, and source CRF coordinates.*

- *Analyzing the troposphere estimates of VieVS* i.e. ZTD and troposphere gradients by means of comparing them with the results of other space geodetic techniques such as GNSS, DORIS, WVR, and NWM (ECMWF, HIRLAM, and JMA) during IVS-CONT08.

- *Analyzing the sub-daily (hourly) estimates of VieVS, e.g. antenna TRF coordinate during IVS-CONT05, and hourly EOP during IVS-CONT08.* The sub-daily antenna TRF position estimates are compared with those derived from the tidal motion models e.g. tidal ocean loading displacements based on FES 2004 (Lyard et al., 2006). Hourly ERP estimates are compared with those computed from high frequency (short-period) tidal models (HF-ERP), i.e. ocean tides and libration (McCarthy and Petit (2004), Chapter 5 and 8)).

- *Analyzing the effects of different EOP parametrization on sub-daily (hourly) CRF coordinates of stable sources* during IVS-CONT08. Hourly CPWLO CRF coordinates of some long term stable sources are estimated for different EOP parametrization and compared. Since, source positions do not have any motion this part of the study is just a kind of 'abstract test' without real implication.

- *Determining and eliminating clock breaks in a two step LS approach.* The first LS adjustment includes: Removing large clock errors, correcting outliers, and removing clock breaks. The second LS adjustment includes: Estimating geodetic parameters, preparing datum free normal equation systems for global solution.

- *Detecting outlier observations.* Outlier observations are handled in such a way that the detection and the removal are done in separate analyses. In the first analysis, outlier observations are detected and listed in session-wise ASCII files without removing them. In the second analysis, the outlier observations can be removed. This has the advantage that the analyst can eliminate the same outlier observations through reading the outlier observations from pre-defined files. These two steps in outlier detection give the opportunity to the analyst of performing rigorous comparisons with the same observations and without the same outliers.

- *Forming datum free normal equations for global solutions* including the parameters of antenna TRF coordinates and TRF velocities, EOP, and/or source CRF coordinates.

1.3. Outline of the thesis

The thesis contains nine chapters. Each chapter is outlined in the following:

- *Chapter 2 reviews the VLBI delay model* for the analysis of VLBI observations to extra-galactic objects from the surface of the Earth. In this chapter, the transformation to relate the International Terrestrial Reference System (ITRS) to the Geocentric Celestial Reference System (GCRS) is presented which is based on the concept of the non-rotating-origin (NRO) in the GCRS (McCarthy and Petit, 2004). The VLBI vacuum delay and gravitational delay is explained following the IERS Conventions 2003. The partial derivatives of the VLBI delay model with respect to some of the estimated parameters, e.g. EOP, source CRF coordinates and antenna TRF coordinates are introduced. Continuous piece-wise linear offset (CPWLO) functions for sub-daily parameter estimation are described. It is necessary to state here that similar to estimating continuous piece-wise linear (CPWL) functions where the initial offset and rates are formed, continuous piece-wise linear offset (CPWLO) functions estimate directly the offsets for every UTC integer hour, multiples of integer hours or fractions of integer hours. The implementation of the CPWLO functions and of the partial derivatives of the CPWLO functions in vie_lsm (Least-Squares parameter estimation module of VieVS) is introduced. The partial derivatives of the delay model w.r.t. CPWLO of antenna coordinates and $\Delta UT1$ with their design matrices are presented as an example of showing how the CPWLO can be incorporated into the VLBI observation equations.

- *Chapter 3 describes the Least-Squares (LS) adjustment method based on the Gauss Markoff model.* Furthermore, constraining parameters, free network solutions, stacking of normal equations are briefly introduced. The LS adjustment in the vie_lsm module of VieVS is explained in details: the structure of the sub-design matrices for different parameters to be estimated, constraining parameters in relative or absolute sense, introducing datum conditions, and criteria on detecting outliers.

- *Chapter 4 describes modelling and estimating of VLBI clock errors based on CPWLO functions.* Clock errors are estimated with a new approach in vie_lsm where a two step LS procedure is carried out. In the first LS adjustment a quadratic polynomial is fitted for each clock and one troposphere zenith delay is estimated. Then, this quadratic polynomial is reduced from the observations. In the second LS solution, CPWLO of clocks with a rate and a quadratic term are estimated with all other parameters. The effects of a not corrected clock break on some of the estimated sub-daily parameters, e.g. hourly Earth Rotation Parameters (ERP) and hourly ZWD are investigated. In order to assess the relative frequency stabilities of the clocks during IVS-CONT02, -CONT05, and -CONT08 session-wise Allan standard deviations (ASD) of the clocks are calculated from hourly clock errors using VieVS. The relative clock errors are estimated when Wettzell clock is fixed in all sessions of all IVS-CONT campaigns.

- *Chapter 5 focuses on the estimation of troposphere delays with VieVS.* Troposphere delays can be defined as the integral over the refractive index n along the slant path S between a geodetic station and the highest part of the troposphere. A brief introduction is given on 2D ray-tracing and on troposphere mapping functions. A detailed explanation is provided in this chapter on how the CPWLO of troposphere ZWD and east and north gradients are estimated in the vie_lsm module of VieVS.

- *In Chapter 6 VLBI estimates of troposphere zenith total delays (ZTD) and gradients during IVS-CONT08 are compared with those derived from other techniques.* These techniques are the Global Positioning System (GPS), Doppler Orbitography and Radiopositioning Integrated by Satellite (DORIS), and water vapor radiometers (WVR) co-located with the VLBI radio telescopes. ZTD derived from space geodetic techniques and gradients are compared to those determined by ray-tracing through the profiles of various Numerical Weather Models (NWM) e.g. the European Centre for Medium-Range Weather Forecasts (ECMWF) (at all sites), the Japan Meteorological Agency (JMA) and Cloud Resolving

Storm Simulator (CReSS) (at Tsukuba in Japan), and the High Resolution Limited Area Model (HIRLAM) (at European sites). It should be noted that all the comparisons and validation tests presented within this section provide information with respect to the planned combination and integration of various observing techniques. In fact, such a multitude of different methods to simultaneously determine troposphere parameters from space geodetic techniques and other sources have never been available for comparison before. Thus, the data taken during the IVS-CONT08 campaign will greatly contribute to combination studies in the framework of the Global Geodetic Observing System (GGOS) (Rummel et al., 2005) of the International Association of Geodesy (IAG).

- *In Chapter 7 different troposphere mapping functions and different cut-off elevation angles are investigated w.r.t. the baseline length repeatabilities.* The analysis of IVS-R1 and IVS-R4 sessions are carried out from 4th of January 2002 to 29th of June 2007 for the mapping functions VMF1, GMF, and NMF, and the cut-off angles $3°$, $5°$, $7°$, $10°$, $15°$, $20°$, and $30°$.

- *Chapter 8 presents the analysis of the sub-daily (hourly) TRF, EOP, and CRF estimates of VieVS.* In the first section, sub-daily tidal motions of the VLBI antennas during IVS-CONT05 sessions are analyzed. The hourly CPWLO coordinate estimates of the antennas during IVS-CONT05 are compared with those displacements computed from crustal tidal motion models for the same estimation epochs. In the second section, analysis of the sub-daily ERP estimates of VieVS during IVS-CONT08 are compared to those derived from HF-ERP models (ocean tides and libration (McCarthy and Petit (2004), Chapter 5 and 8) and to those estimated by GPS (Steigenberger et al., 2006, 2007). In the third section, hourly CPWLO source coordinate estimates from VieVS during IVS-CONT08 with different EOP options are analyzed. These sources are selected from the ICRF2 defining sources which have maximum numbers of observations and small structure indices, 1 to 2 (i.e. stable for long time intervals). These sources are 803+784 and 1357+769 (near to the celestial north pole) and 1606+106 and 1749+096 (near to the celestial equator). The reasons of analyzing these sources are to figure out if the long term stable sources have sub-daily harmonic coordinate variations, and if the sub-daily CPWLO source coordinate estimates are sensitive to EOP parametrization. Since, source positions do not have any motion this part of the study is just a kind of 'abstract test' without real implication.

2. VLBI delay model

Very Long Baseline Interferometry (VLBI) is a geometric technique: it measures the time differ-
ence between the arrival at two Earth-based antennas of a radio wavefront emitted by a distant
quasi-stellar radio source (quasar) (Figure 2.1). Using large numbers of time difference mea-
surements from many quasars observed with a global network of antennas, VLBI determines
the inertial reference frame (space fixed frame, e.g. ICRF2) defined by the quasar (source)
coordinates and simultaneously the precise positions of the antennas in the terrestrial frame
(Earth-fixed frame, e.g. VTRF08). The VLBI observation equation (delay model) can be writ-
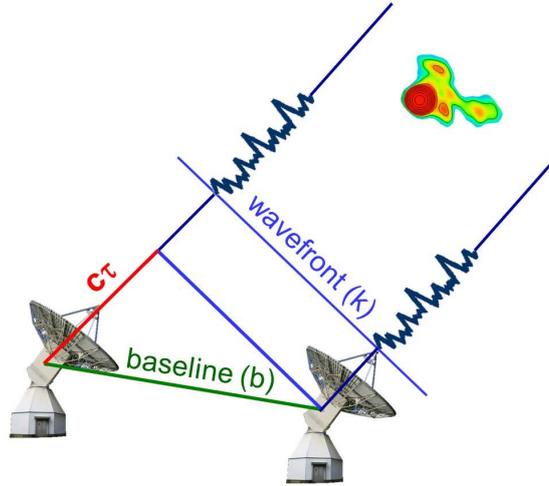
Figure 2.1.: VLBI observation principle.

ten as,

$$-c \cdot \tau = \vec{b} \cdot \vec{k} + \Delta\tau_{retarded\,baseline} + \Delta\tau_{clock} + \Delta\tau_{trop} + \Delta\tau_{iono} + \cdots \qquad (2.1)$$

where c is the velocity of light in vacuum, $\vec{k}$ is the unit source (quasar) vector defined in a space-
fixed, barycentric and equatorial celestial system, $\vec{b}$ is the baseline vector of the VLBI antennas
defined in an Earth-fixed, geocentric, equatorial terrestrial coordinate system. $\Delta\tau_{retarded\,baseline}$
is the delay correction due to the motion of the second antenna (in geocentric celestial reference
system, GCRS) during the propagation time of the wavefront between station 1 and station

2, $\Delta\tau_{clock}$ is the delay correction due to the synchronization and frequency discrepancies of atomic clocks at station 1 and station 2, $\Delta\tau_{trop}$ is the troposphere delay correction, $\Delta\tau_{iono}$ is the ionosphere delay correction. In this chapter, the VLBI delay model is introduced which is known as "consensus model" and proposed in the IERS (International Earth Rotation and Reference Systems Service) Conventions. This chapter basically follows: IERS Conventions 2003, Chapter 5 for the transformation of antenna coordinates from ITRS to GCRS, IERS Conventions 2003, Chapter 11, for the VLBI delay model (McCarthy and Petit, 2004). The partial derivatives of the VLBI delay model w.r.t. the estimated parameters are basically based on Sovers et al. (1998) and Böhm et al. (2010).

The VLBI delay model is designed primarily for the analysis of VLBI observations to extragalactic objects from the surface of the Earth. The observable quantities of the VLBI space geodetic technique are recorded signals measured in the proper time of the station clocks. The VLBI clocks are synchronized to UTC. The ICRF catalogue coordinates of the sources are defined in the Barycentric Celestial Reference Sytem (BCRS) (space-fixed, origin is the center of the mass of the Solar system, equatorial celestial) and the VLBI antenna coordinates are defined in International Terrestrial Reference System (ITRS) (Earth-fixed, origin is the center of the mass of the Earth). There is another coordinate system defined as Geocentric Celestial Reference System (GCRS) which is kinematically not rotating and of which the origin is the center of the mass of the Earth. The delay calculated is the time of arrival at station 2, t_2, minus the time of arrival at station 1, t_1, in GCRS. The UTC time tag of the scan, i.e. t_1, serves as the time reference for the measurement and all scalar and vector quantities are assumed to be calculated at t_1, including e.g. the troposphere delay, tidal corrections on the antenna TRF coordinates, the barycentric velocity of the geocenter. However, t_1 which is in UTC should be transformed to the appropriate timescale corresponding to the time argument to be used to compute each element of the geometric model e.g. terrestrial time, terrestrial time in Julian centuries since the fundamental (standard) epoch, terrestrial time in days since fundamental epoch. First, at the time of the observation, the velocity corrections, eccentricities, tidal effects (i.e. solid Earth tides, tidal ocean loading, tidal and non-tidal atmosphere loading, pole tide) are introduced to the VLBI antenna ITRS catalogue coordinates. Thus, the antenna ITRS coordinates at the epoch of the scan are derived (X_{ITRS}). Then, the transformation to relate the ITRS to GCRS at the epoch the observation (scan) can be written as:

$$X_{GCRS} = Q(t) \cdot R(t) \cdot W(t) \cdot X_{ITRS} \tag{2.2}$$

where $Q(t)$, $R(t)$ and $W(t)$ are the transformation matrices arising from the motion of the

celestial pole in the GCRS, from the rotation of the Earth around the axis of the pole, and from polar motion in the TRS, respectively. More detailed explanations on the procedures for the ITRS and GCRS transformation can be found at Capitaine et al. (2002). In Equation (2.2) the date of the observation, t, is the equivalence of t_1 in Terrestrial Time (TT) in Julian centuries since some reference epoch (in IERS conventions it is J2000, 2000 January 1d 12h, named as fundamental or standard epoch) (McCarthy and Petit (2004), Chapter 5.3):

$$t = (TT - 51544.5)/36525, \tag{2.3}$$

where TT is the terrestrial time given by,

$$TT = UTC + (TT - TAI) + (TAI - UTC)$$
$$TT = t_1 + (32.184 + \text{leap seconds})/86400, \tag{2.4}$$

where $TT - TAI = 32.184$ by definition and TAI-UTC is *leap seconds*. Regardless from "equinox based" or "Celestial Intermediate Origin (CIO) based" transformation procedures, the transformation matrix arising from polar motion (i.e. relating ITRS and Terrestrial Intermediate Reference System, TIRS) can be expressed as:

$$W(t) = R_3(s') \cdot R_2(x_p) \cdot R_1(y_p), \tag{2.5}$$

where x_p and y_p being the "polar coordinates" of the Celestial Intermediate Pole (CIP) in the ITRS. The R_1, R_2, and R_3 denote rotation matrices with positive angle about the first, second, and third axes of the cartesian coordinate system (see Appendix A.1). s' is a quantity, named "Terrestrial Intermediate Origin (TIO) locater", which provides the position of the TIO on the equator of the CIP corresponding the kinematical definition of the "non-rotating" origin (NRO) in the ITRS at date t. The quantity s' is sensitive only to the largest variations in polar motion. Using the current mean amplitudes for the Chandlerian and annual wobbles gives (Capitaine et al., 1986; Lambert and Bizouard, 2002):

$$s' = -47 \cdot 10^{-6} \cdot t. \tag{2.6}$$

The CIO based transformation matrix for the Earth rotation around the axis of the CIP (i.e. relating TIRS and Celestial Intermediate Reference System, CIRS) can be expressed as:

$$R(t) = R_3(-ERA(t_u)) \tag{2.7}$$

where ERA is the Earth Rotation Angle between the CIO and TIO at date t on the equator of the CIP, which provides a rigorous definition of the sidereal rotation of the Earth. The ERA can be derived from UT1 as follows:

$$ERA(t_u) = 2\pi(ERA_0 + ak \cdot t_u). \tag{2.8}$$

In Equation (2.8), ak is 1.00273781191135448 and ERA_0 is 0.7790572732640, and t_u is the observation epoch in days since the fundamental (standard) reference epoch ($UT1 - 51544.5$). UT1 at the observation epoch in MJD can be expressed as:

$$UT1 = t_1 + \Delta UT1/86400. \tag{2.9}$$

The CIO based transformation matrix arising from the motion of the CIP in the GCRS (i.e. relating CIRS and GCRS) can be expressed as:

$$Q(t) = R_3(-E) \cdot R_2(-d) \cdot R_3(E) \cdot R_3(s). \tag{2.10}$$

The quantities E, d, and s can be calculated from the coordinates of the CIP in the GCRS as follows:

$$E = \arctan \frac{Y}{X}, \tag{2.11}$$

$$d = \arccos Z = \arccos \left(\sqrt{1 - X^2 + Y^2} \right), \tag{2.12}$$

$$s = s_0 - \frac{XY}{2}. \tag{2.13}$$

In Equation (2.10) s is a quantity named "CIO locator", which provides the position of the CIO on the equator of the CIP corresponding to the kinematical definition of the non-rotating-origin (NRO) in the GCRS when the CIP is moving with respect to the GCRS, between the fundamental reference epoch and the date t due to precession and nutation (Capitaine et al., 2000, 2002; McCarthy and Petit, 2004). After having the X_{GCRS} coordinates of the VLBI antennas at the observation epoch t_1, $\vec{x}_i(t_1)$, the gravitational and vacuum delays at the corresponding time are calculated. Detailed explanation is given in subsections 2.1 and 2.2.

2.1. Gravitational delay

The gravitational delay on the signal of the extra-galactic radio source caused by the Jth gravitating body can be computed as,

$$\Delta T_{gravJ} = 2\frac{GM_J}{c^3} \ln \frac{|\vec{R}_{1J}| + \vec{K} \cdot \vec{R}_{1J}}{|\vec{R}_{2J}| + \vec{K} \cdot \vec{R}_{2J}}, \tag{2.14}$$

where G is the Gravitational Constant, M_J is the rest mass of the Jth gravitating body, c is the velocity of the light, $\vec{R}_{iJ}$ is the vector from the Jth gravitating body to the ith antenna (receiver), the absolute value sign denotes to the norm of the corresponding vector, $|\vec{x}| = \sqrt{\sum x_i^2}$. $\vec{K}$ is the

unit vector from the barycenter to the source in the absence of gravitational and aberrational bending,

$$\vec{K} = \begin{bmatrix} \cos\delta\cos\alpha & \cos\delta\sin\alpha & \sin\delta \end{bmatrix}, \tag{2.15}$$

where δ denotes to declination and α is right ascension defined in the BCRS. The gravitational delay on the signal caused by the Earth can be computed as follows,

$$\Delta T_{grav\oplus} = 2\frac{GM_\oplus}{c^3}\ln\frac{|\vec{x}_1| + \vec{K}\cdot\vec{x}_1}{|\vec{x}_2| + \vec{K}\cdot\vec{x}_2}, \tag{2.16}$$

where $\vec{x}_i$ denotes to the GCRS coordinates of the ith antenna at epoch t_1 and $M_\oplus$ is the rest mass of the Earth (Kopeikin and Schafer, 1999; McCarthy and Petit, 2004). The $\vec{R}_{iJ}$ vector should be computed at the time (t_{1J}) when the ray is passing closest to the Jth gravitating body. So the time correction to t_1 can be computed as follows,

$$\begin{aligned} t_{1J} &= t_1 - \frac{\vec{K}(\vec{X}_J(t_1) - \vec{X}_1(t_1))}{c}, \\ \vec{X}_J(t_{1J}) &= \vec{X}_J(t_1) + \vec{V}_J(t_{1J} - t_1). \end{aligned} \tag{2.17}$$

where $\vec{X}_J$ and $\vec{V}_J$ denote to the barycentric coordinate and velocity vector of the Jth gravitating body. X_J and t_{1J} can be found by e.g. an iterative approach. The difference vector between the gravitating body to the first antenna can be computed as,

$$\vec{R}_{1J}(t_1) = \vec{X}_1(t_1) - \vec{X}_J(t_{1J}), \tag{2.18}$$

where the barycentric coordinates of the ith antenna $\vec{X}_i$ at epoch t_1 can be derived from the barycentric coordinates of the geocenter $\vec{X}_\oplus(t_1)$ and the GCRS coordinates of the antenna, $\vec{x}_i(t_1)$ as follows,

$$\vec{X}_i(t_1) = \vec{X}_\oplus(t_1) + \vec{x}_i(t_1), \tag{2.19}$$

and the vector between the gravitating body and the second antenna considering the motion of the second antenna during the propagation time between station 1 and station 2 can be derived as follows,

$$\vec{R}_{2J} = \vec{X}_2(t_1) - \frac{\vec{V}_\oplus}{c}(\vec{K}\cdot\vec{b}) - \vec{X}_J(t_{1J}). \tag{2.20}$$

$\vec{V}_\oplus$ denotes to the barycentric velocity vector of the geocenter, and $\vec{b}$ is the GCRS baseline vector at t_1, i.e. $\vec{x}_2(t_1) - \vec{x}_1(t_1)$. The total gravitational delay is the sum of all gravitating bodies including the Earth,

$$\Delta T_{grav} = \sum_j \Delta T_{gravJ}. \tag{2.21}$$

2.2. Vacuum delay and geometric delay

The total geocentric vacuum delay is given by

$$t_{v2} - t_{v1} = \frac{\Delta T_{grav} - \frac{\vec{K}\cdot\vec{b}}{c}[1 - \frac{(1+\gamma)\cdot U}{c^2} - \frac{|\vec{V}_\oplus|^2}{2c^2} - \frac{\vec{V}_\oplus\cdot\vec{\omega}_2}{c^2}] - \frac{\vec{V}_\oplus\cdot\vec{b}}{c^2}(1 + \vec{K}\cdot\vec{V}_\oplus/2c)}{1 + \frac{\vec{K}\cdot(\vec{V}_\oplus + \vec{\omega}_2)}{c}}, \tag{2.22}$$

where $\gamma = 1$ according to the general relativity using BCRS, ω_i is the geocentric velocity of the ith antenna, and U denotes to the gravitational potential at the geocenter, neglecting the effects of the Earth's mass,

$$U = \frac{GM_\odot}{|\vec{R}_{\oplus\odot}|}, \tag{2.23}$$

where $\vec{R}_{\oplus\odot}$ is the vector from the Sun to the geocenter, and $M_\odot$ the rest mass of the Sun, t_{vi} is the "vacuum" geocentric coordinate time (TCG) of arrival of a radio signal at the ith VLBI receiver including the gravitational bending but neglecting the atmospheric delay and atmospheric bending (Kopeikin, 1990; Eubanks, 1991; Treuhaft and Thomas, 1991; Soffel et al., 1991; Sovers and Jacobs, 1994). Some of the vector quantities which are used in the computation of gravitational and vacuum delays e.g. $\vec{X}_\oplus$, $\vec{V}_\oplus$, $\vec{X}_J$, $\vec{V}_J$ can be externally provided from planetary ephemerides e.g. JPL421. The geometric delay can be obtained by adding the geometric part of the troposphere propagation delay to the vacuum delay as follows:

$$t_{g2} - t_{g1} = t_{v2} - t_{v1} + \delta t_{atm1}\frac{\vec{K}(\vec{\omega}_2 - \vec{\omega}_1)}{c}, \tag{2.24}$$

where δt_{atm1} is the hydrostatic part of the troposphere delay at antenna 1 at the observation epoch t_1:

$$\delta t_{atm1} = \frac{\Delta L_h^{st(1)}(t_1)\cdot m_h^{st(1)}(\varepsilon, t_1)}{c}, \tag{2.25}$$

where $\Delta L_h^{st(1)}(t_1)$ denotes to the troposphere zenith hydrostatic delay at antenna 1 at epoch t_1, and m_h is the hydrostatic mapping function, and ε is the elevation angle (see Chapter 5 dedicated for troposphere for further information about these terms). After introducing the corrections which should be applied to the baseline, being elevation and azimuth dependent, i.e. thermal deformation, axis offset correction, and the hydrostatic a priori part of troposphere delay, the total delay $(t_2 - t_1)$ can be derived from the geometric delay, $t_{g2} - t_{g1}$ as:

$$t_2 - t_1 = t_{g2} - t_{g1} + \tau_{therm\,def12} + \tau_{axis\,offset12} + \tau_{trop12}. \tag{2.26}$$

The zenith distance and azimuth of the observation is calculated from the aberrated source vector $\vec{k}$ after transforming to TRF. Thus, the values e.g. for mapping functions, troposphere gradients,

troposphere hydrostatic and wet slant delays are corrected for abberation. The aberrated source vector can be calculated as follows:

$$\vec{k}_i = \vec{K} + \frac{\vec{V}_\oplus + \vec{\omega}_i}{c} - \vec{K}\frac{\vec{K}\cdot(\vec{V}_\oplus + \vec{\omega}_i)}{c}. \tag{2.27}$$

It should be noted that the VLBI observation data include the ionosphere delay (the linear combination of dual frequency measurements is used to calculate the dispersive effect of the ionosphere) in addition to the observed delay. Thus, we assume that the ionosphere delay has already been reduced from the observed delay. The reduced observation (observed minus computed) value (oc) for the corresponding observation can be derived as follows:

$$oc = \tau_{observed} - (t_2 - t_1). \tag{2.28}$$

The oc vector basically includes clock error due to synchronization and frequency instabilities, troposphere zenith wet delays, azimuthal asymmetric parts of the troposphere delay, and the effect of the errors in the other a priori values used to calculate $t_2 - t_1$, (e.g. EOP) which all can be estimated in the parameter estimation stage of the analysis (Sovers et al., 1998; Titov et al., 2004; McCarthy and Petit, 2004; Böhm et al., 2010).

2.3. Partial derivatives of the VLBI delay model with respect to EOP, antenna and source coordinates

For the sake of simplicity a basic delay model is used for the calculation of partial derivatives w.r.t. estimated parameters. In this simple model the retarded baseline due to the motion of the second antenna during the propagation time between station 1 and station 2 is not considered. Besides, the gravitational retardation (delay) and the transformation of station positions between GCRS and BCRS (Lorentz transformation) due to the center of mass (origin) difference is not taken into account. Then, the simple delay model can be written as follows:

$$\tau = \vec{K} \cdot Q \cdot R \cdot W \cdot \vec{b} \tag{2.29}$$

In Equation (2.29) $\vec{K}$ is defined in BCRS, and $\vec{b}$ is defined in TRF. The partial derivative of the simplified VLBI delay model w.r.t. the CIP coordinate in TRF along the Greenwich meridian x_p is:

$$\frac{\partial \tau}{\partial x_p} = \vec{K} \cdot Q \cdot R \cdot \frac{\partial W}{\partial x_p} \cdot \vec{b}, \tag{2.30}$$

where

$$\frac{\partial W}{\partial x_p} = R_3(s') \cdot \begin{bmatrix} -\sin x_p & 0 & -\cos x_p \\ 0 & 0 & 0 \\ \cos x_p & 0 & -\sin x_p \end{bmatrix} \cdot R_1(y_p). \tag{2.31}$$

The partial derivative of the delay model w.r.t. the CIP coordinate in TRF along 270° east longitude y_p is:

$$\frac{\partial \tau}{\partial y_p} = \vec{K} \cdot Q \cdot R \cdot \frac{\partial W}{\partial y_p} \cdot \vec{b}, \tag{2.32}$$

where

$$\frac{\partial W}{\partial y_p} = R_3(s') \cdot R_2(x_p) \cdot \begin{bmatrix} 0 & 0 & 0 \\ 0 & -\sin y_p & cos y_p \\ 0 & -\cos y_p & -\sin y_p \end{bmatrix}. \tag{2.33}$$

The partial derivative of the delay model w.r.t. Earth phase of rotation, UT1, is:

$$\frac{\partial \tau}{\partial (UT1)} = \vec{K} \cdot Q \cdot \frac{\partial R}{\partial (-ERA)} \cdot \frac{\partial (-ERA)}{\partial (UT1)} \cdot W \cdot \vec{b}, \tag{2.34}$$

where

$$\frac{\partial R}{\partial (-ERA)} = \begin{bmatrix} -\sin(-ERA) & cos(-ERA) & 0 \\ -\cos(-ERA) & -sin(-ERA) & 0 \\ 0 & 0 & 0 \end{bmatrix}, \tag{2.35}$$

and

$$\frac{\partial (-ERA)}{\partial (UT1)} = -ak = -1.00273781191135448. \tag{2.36}$$

The transformation matrix arising from the motion of celestial pole in CRS is composed of four transformation matrices given in Equation (2.10). The calculation of E, d, and s, are given in Equations (2.11, 2.12, and 2.13). The partial derivative of the delay model w.r.t. the CIP coordinate X in CRF is:

$$\frac{\partial \tau}{\partial X} = \vec{K} \cdot \frac{\partial Q}{\partial X} \cdot R \cdot W \cdot \vec{b}, \tag{2.37}$$

where

$$\begin{aligned}
\frac{\partial Q}{\partial X} =\ & \frac{\partial R_3(-E)}{\partial (-E)} \cdot \frac{\partial (-E)}{\partial X} \cdot R_2(-d) \cdot R_3(E) \cdot R_3(s) \\
& + R_3(-E) \cdot \frac{\partial R_2(-d)}{\partial (-d)} \cdot \frac{\partial (-d)}{\partial X} \cdot R_3(E) \cdot R_3(s) \\
& + R_3(-E) \cdot R_2(-d) \cdot \frac{\partial R_3(E)}{\partial E} \cdot \frac{\partial E}{\partial X} \cdot R_3(s) \\
& + R_3(-E) \cdot R_2(-d) \cdot R_3(E) \cdot \frac{\partial R_3(s)}{\partial s} \cdot \frac{\partial s}{\partial X}.
\end{aligned} \tag{2.38}$$

15

In Equation (2.38 and 2.43), the rotation matrices around the first, second, and third axis (R_1, R_2, R_3) and the partial derivatives of the rotation matrices w.r.t. corresponding rotation angles are in the form, given in Appendix A.1.

$$\frac{\partial(-E)}{\partial X} = \frac{Y}{X^2 + Y^2}, \tag{2.39}$$

$$\frac{\partial(-d)}{\partial X} = \frac{X}{\sqrt{1 - (X^2 + Y^2)}\sqrt{X^2 + Y^2}}, \tag{2.40}$$

$$\frac{\partial s}{\partial X} = \frac{-Y}{2}. \tag{2.41}$$

The partial derivative of the delay model w.r.t. the CIP coordinate Y in CRF is:

$$\frac{\partial \tau}{\partial Y} = \vec{K} \cdot \frac{\partial Q}{\partial Y} \cdot R \cdot W \cdot \vec{b}, \tag{2.42}$$

where

$$
\begin{aligned}
\frac{\partial Q}{\partial Y} =\ & \frac{\partial R_3(-E)}{\partial(-E)} \cdot \frac{\partial(-E)}{\partial Y} \cdot R_2(-d) \cdot R_3(E) \cdot R_3(s) \\
& + R_3(-E) \cdot \frac{\partial R_2(-d)}{\partial(-d)} \cdot \frac{\partial(-d)}{\partial Y} \cdot R_3(E) \cdot R_3(s) \\
& + R_3(-E) \cdot R_2(-d) \cdot \frac{\partial R_3(E)}{\partial E} \cdot \frac{\partial E}{\partial Y} \cdot R_3(s) \\
& + R_3(-E) \cdot R_2(-d) \cdot R_3(E) \cdot \frac{\partial R_3(s)}{\partial s} \cdot \frac{\partial s}{\partial Y}.
\end{aligned}
\tag{2.43}
$$

In Equation (2.43),

$$\frac{\partial(-E)}{\partial Y} = \frac{-X}{X^2 + Y^2}, \tag{2.44}$$

$$\frac{\partial(-d)}{\partial Y} = \frac{Y}{\sqrt{1 - (X^2 + Y^2)}\sqrt{X^2 + Y^2}}, \tag{2.45}$$

$$\frac{\partial s}{\partial Y} = \frac{-X}{2}. \tag{2.46}$$

The partial derivative of the delay model w.r.t. right ascension of a source is:

$$\frac{\partial \tau}{\partial \alpha} = \frac{\partial \vec{K}}{\partial \alpha} \cdot Q \cdot R \cdot W \cdot \vec{b}, \tag{2.47}$$

where

$$\frac{\partial \vec{K}}{\partial \alpha} = \begin{bmatrix} -\cos\delta\sin\alpha & \cos\delta\cos\alpha & 0 \end{bmatrix}. \tag{2.48}$$

The partial derivative of the delay model w.r.t. declination of a source is:

$$\frac{\partial \tau}{\partial \delta} = \frac{\partial \vec{K}}{\partial \delta} \cdot Q \cdot R \cdot W \cdot \vec{b}, \tag{2.49}$$

where

$$\frac{\partial \vec{K}}{\partial \delta} = \begin{bmatrix} -\sin\delta\cos\alpha & -\sin\delta\sin\alpha & \cos\delta \end{bmatrix}. \tag{2.50}$$

The partial derivative of the delay model w.r.t. the TRF coordinates of the antennas are e.g. for the X component of station 1:

$$\frac{\partial \tau}{\partial X_{st1}} = \vec{K} \cdot Q \cdot R \cdot W \cdot \frac{\partial \vec{b}}{\partial X_{st1}}, \tag{2.51}$$

where

$$\frac{\partial \vec{b}}{\partial X_{st1}} = \begin{bmatrix} 1 \\ 0 \\ 0 \end{bmatrix}. \tag{2.52}$$

2.4. Continuous piece-wise linear offset (CPWLO) functions for sub-daily parameter estimation

Similar to estimating continuous piece-wise linear (CPWL) functions where the initial offset and rates are formed, we directly estimate offsets for every UTC integer hour with the continuous piece-wise linear offset (CPWLO) function given below:

$$x_i = x_1 + \frac{t - t_1}{t_2 - t_1}(x_2 - x_1) \tag{2.53}$$

In the above function x_1 and x_2 are CPWLO estimated at integer UTC hours, fractions or multipliers of UTC integer hours (t_1 and t_2). t is the epoch of the functional value, x_i. The illustration of CPWLO function can be seen in Figure 2.2. In vie_lsm estimated CPWLO are: clock errors, zenith wet delays, troposphere gradients, Earth orientation parameters, station TRF and source CRF coordinates. The partial derivatives of the delay model w.r.t. an unknown parameter, x_i at the observation epoch t can be derived as follows:

$$\frac{\partial \tau(t)}{\partial x_1} = \frac{\partial \tau(t)}{\partial x_i} \cdot \frac{\partial x_i}{\partial x_1}, \tag{2.54}$$

$$\frac{\partial \tau(t)}{\partial x_2} = \frac{\partial \tau(t)}{\partial x_i} \cdot \frac{\partial x_i}{\partial x_2}, \tag{2.55}$$

where the partial derivatives of the CPWLO function given in Equation (2.53) w.r.t. offsets x_1 and x_2 are:

$$\frac{\partial x_i}{\partial x_1} = [1 - \frac{t - t_j}{t_{j+1} - t_j}], \tag{2.56}$$

$$\frac{\partial x_i}{\partial x_2} = [\frac{t - t_j}{t_{j+1} - t_j}]. \tag{2.57}$$

17
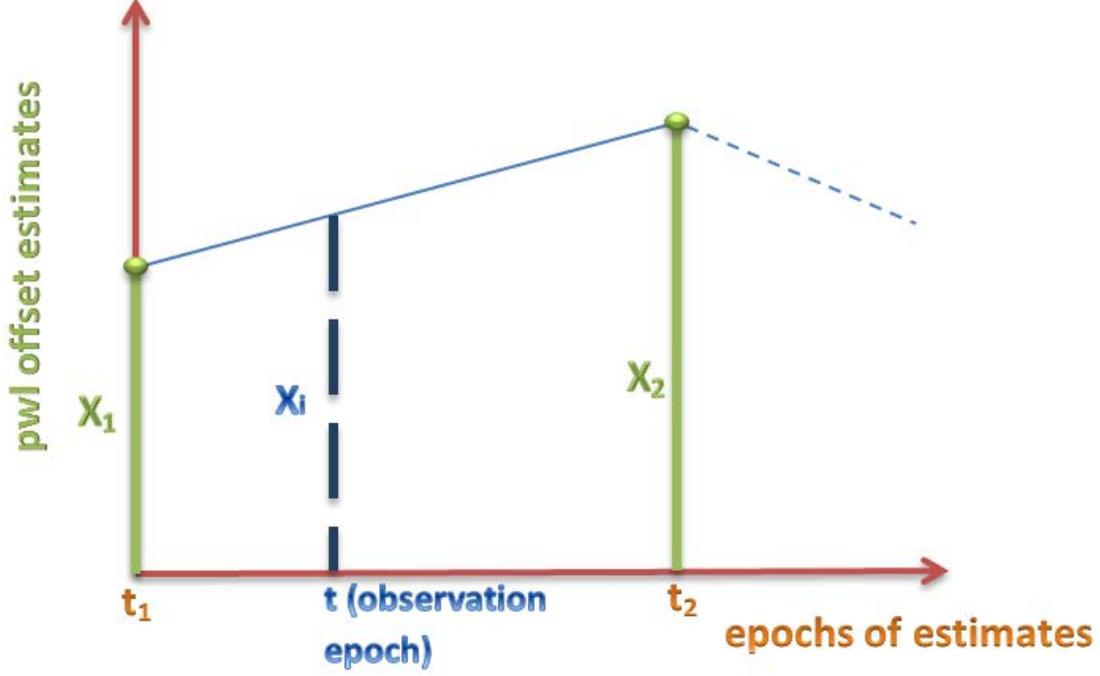
Figure 2.2.: Continuous piece-wise linear offsets (CPWLO).

It should be noted that the epoch of the observation t should provide the condition: $t_j < t < t_{j+1}$ for CPWLO functions. In case, we want to derive the partial derivative of the delay model w.r.t. $UT1$ at epoch t can be derived for two unknown CPWLO (one estimation interval) as follows:

$$\frac{\partial \tau(t)}{\partial (UT1)_{x_1}} = \frac{\partial \tau(t)}{\partial (UT1)} \cdot \frac{\partial (UT1)}{\partial x_1}, \tag{2.58}$$

$$\frac{\partial \tau(t)}{\partial (UT1)_{x_2}} = \frac{\partial \tau(t)}{\partial (UT1)} \cdot \frac{\partial (UT1)}{\partial x_2}, \tag{2.59}$$

In case, we want to derive the partial derivative of the delay model w.r.t. the two TRF CPWLO coordinates of antenna 1, $(st1)$, e.g. for the X component:

$$\frac{\partial \tau(t)}{\partial (X_{st1})_{x_1}} = \frac{\partial \tau(t)}{\partial (X_{st1})} \cdot \frac{\partial (X_{st1})}{\partial x_1}, \tag{2.60}$$

$$\frac{\partial \tau(t)}{\partial (X_{st1})_{x_2}} = \frac{\partial \tau(t)}{\partial (X_{st1})} \cdot \frac{\partial (X_{st1})}{\partial x_2}. \tag{2.61}$$

As an example, the design matrix consisting TRF antenna coordinates X components e.g. for three antennas, three observations carried out at epoch $t1'$, $t2'$, and $t3'$, and one estimation interval (result in two CPWLO unknowns for each antenna) can be written as:

$$\begin{bmatrix} \frac{\partial \Delta\tau(t1')}{\partial (X_{st1})_{x_1}} & \frac{\partial \Delta\tau(t1')}{\partial (X_{st1})_{x_2}} & \frac{-\partial \Delta\tau(t1')}{\partial (X_{st2})_{x_1}} & \frac{-\partial \Delta\tau(t1')}{\partial (X_{st2})_{x_2}} & 0 & 0 \\ 0 & 0 & \frac{\partial \Delta\tau(t2')}{\partial (X_{st2})_{x_1}} & \frac{\partial \Delta\tau(t2')}{\partial (X_{st2})_{x_2}} & \frac{-\partial \Delta\tau(t2')}{\partial (X_{st3})_{x_1}} & \frac{-\partial \Delta\tau(t2')}{\partial (X_{st3})_{x_2}} \\ \frac{\partial \Delta\tau(t3')}{\partial (X_{st1})_{x_1}} & \frac{\partial \Delta\tau(t3')}{\partial (X_{st1})_{x_2}} & 0 & 0 & \frac{-\partial \Delta\tau(t3')}{\partial (X_{st3})_{x_1}} & \frac{-\partial \Delta\tau(t3')}{\partial (X_{st3})_{x_2}} \end{bmatrix}. \tag{2.62}$$

3. Least Squares (LS) Adjustment

3.1. Gauss Markoff model

A physical phenomena or a set of events can be described by mathematical models, $\phi(x)$, depending on some model parameters, x. Since, a model serves a particular purpose, its setup can vary widely from one point of view to another. Thus, the same physical system may be described by more than one model. The model then replaces the physical situation for the purpose of assessing it (Hirvonen, 1971). The mathematical model is often thought of as being composed of two parts: the functional model and the stochastic model. The functional model will in general describe the deterministic properties of the physical situation or event under consideration. On the other hand, the stochastic model designates and describes the nondeterministic or stochastic (probabilistic) properties of the variables involved. Both functional and stochastic models must be considered together. The functional model between observations L_i and unknowns x can be expressed as

$$\phi_i(x) = L_i + v_i \tag{3.1}$$

where v_i are the residuals of the observations L_i. The stochastic model is represented by the variance co-variance matrix of the observations K_{ll}. The elements of K_{ll} are formed by the precision of the observations s_i and correlations between observations r_{ik} as follows

$$K_{ll} = \begin{bmatrix} s_1^2 & r_{12}s_1s_2 & \cdots & r_{1n}s_1s_n \\ r_{21}s_1s_2 & s_2^2 & \cdots & r_{2n}s_2s_n \\ \vdots & \vdots & & \vdots \\ r_{n1}s_1s_n & r_{n2}s_2s_n & \cdots & s_n^2 \end{bmatrix}. \tag{3.2}$$

The weight matrix of the observations is

$$P = s_0^2 K_{ll}^-, \tag{3.3}$$

where s_0 is the a priori standard deviation of unit weight. s_0 can be defined as a measure of the variability or dispersion of a population (e.g. set of observations) over its expected value.

Adjustment is meaningful only in those cases in which the data available exceed the minimum necessary for a unique determination (over determined system). Since the data are usually obtained from observations, which are subject to probabilistic variations (known as errors) redundant data are usually inconsistent in the sense that each sufficient subset yields different results from another subset. To obtain a unique solution and to fit the parameters x to some observations L an additional criterion (such as that of LS) is applied. In LS, the additional criterion is that the sum of the squares of the observational residuals is a minimum,

$$[v^T P v] = minimum \tag{3.4}$$

which is the simplest known mathematical method that can be applied to any complicated case of adjustments. The principle of the least squares sum of residuals has been generally accepted for the adjustments. The principle was published first by *Legendre* in *1806* with the name *"Method of the Least Squares"*. However, *Gauss* had used the same principle already since *1794* and he published several theoretical discourses and practical applications of it in *1809* and later. The method was introduced first for the computation of the orbits of planets and comets but later *Gauss* and *Bessel* applied it to extensive adjustments of various geodetic measurements (Hirvonen, 1971).

In most of the cases the function $\phi(x)$ given in Equation (3.1) is not linear. But for the *Gauss Markoff* model a linear relationship is required. Therefore, the functions $\phi_i(x)$ are linearized around some a priori values using the zero and first-order terms of Taylor series expansion

$$L_i + v_i = \phi_i(x_0) + \sum_j \frac{\partial \phi_i}{\partial x_j} \delta x_j + \frac{1}{2!} \sum_j \sum_k \frac{\partial \phi_i}{\partial x_j \partial x_k} \delta x_j \delta x_k + \dots \ , \tag{3.5}$$

where $\delta x_j = x_j - x_{0j}$ are called the jth reduced unknown parameter. Any term beyond the second on the right hand side of Equation (3.5) is again nonlinear. Therefore, for the purpose of adjustment, only the first two terms (zero and first order) are used to form a linear expression approximating the original true value x_j. The functional model for n observations and u unknown parameters (estimates) can be written as

$$\begin{aligned}
v_1 &= (\tfrac{\partial \phi_1}{\partial x_1})\delta x_1 + (\tfrac{\partial \phi_1}{\partial x_2})\delta x_2 + \dots + (\tfrac{\partial \phi_1}{\partial x_u})\delta x_u - l_1 \\
v_2 &= (\tfrac{\partial \phi_2}{\partial x_1})\delta x_1 + (\tfrac{\partial \phi_2}{\partial x_2})\delta x_2 + \dots + (\tfrac{\partial \phi_2}{\partial x_u})\delta x_u - l_2 \\
&\quad\vdots \\
v_n &= (\tfrac{\partial \phi_n}{\partial x_1})\delta x_1 + (\tfrac{\partial \phi_n}{\partial x_2})\delta x_2 + \dots + (\tfrac{\partial \phi_n}{\partial x_u})\delta x_u - l_n
\end{aligned} \tag{3.6}$$

where l_i is the reduced observation ('observed'-'computed with a priori values of estimates, x_0')
as follows

$$l_i = L_i - \phi_i(x_0) \tag{3.7}$$

Equation (3.6) can be expressed in matrix form as

$$v = A\delta x - l \tag{3.8}$$

where v is the residuals vector of observations, A is the design matrix, and l is the reduced
observation vector. The linearized observation equation system given in Equation (3.8) can be
solved by applying the additional criterion in Equation (3.4) (Koch, 1988; Öztürk and Serbetçi,
1989, 1992; Brockmann, 1997; Wolf and Ghilani, 1997; Niemeier, 2002). Substituting Equation
(3.8) in Equation (3.4) yields

$$\begin{aligned}
v^T P v = (A\delta x - l)^T P (A\delta x - l) = (\delta x^T A^T - l^T) P (A\delta x - l) \\
= \delta x^T A^T P A \delta x - \delta x^T A^T P l - l^T P A \delta x + l^T P l
\end{aligned} \tag{3.9}$$

where $\delta x^T A^T P l$ and $l^T P A \delta x$ are scalar values, thus $\delta x^T A^T P l = l^T P A \delta x$. Equation (3.9) reads
as

$$v^T P v = \delta x^T A^T P A \delta x - 2 l^T P A \delta x + l^T P l \tag{3.10}$$

After introducing partial differentiation to the matrix Equation (3.10) w.r.t. to the vector δx
we get

$$\partial(v^T P v) = \delta x^T A^T P A \partial x + \partial x^T A^T P A \delta x - 2 l^T P A \partial x \tag{3.11}$$

where $\partial d x^T A^T P A \delta x$ and $\delta x^T A^T P A \partial x$ are symmetric matrices and $\partial x^T A^T P A \delta x = \delta x^T A^T P A \partial x$.
After setting (3.11) to zero we get

$$\begin{aligned}
\partial(v^T P v) = 2 \delta x^T A^T P A \partial x - 2 l^T P A \partial x = 0^T \partial x \\
\partial(v^T P v) = 2(\delta x^T A^T P A - l^T P A) \partial x = 0^T \partial x
\end{aligned} \tag{3.12}$$

After dividing both sides of the Equation (3.12) by 2, transposing the matrices in parenthesis,
we finally derive the so called system of normal equations satisfying the condition of LS given
in Equation (3.4).

$$A^T P A \delta x - A^T P A l = 0. \tag{3.13}$$

The resulting unknown parameter can be determined as

$$\begin{aligned}
x = x_0 + \delta x \\
x = x_0 + (A^T P A)^- A^T P l = x_0 + N^- b
\end{aligned} \tag{3.14}$$

where N is

$$N = A^T P A \qquad (3.15)$$

the normal equation matrix and b is

$$b = A^T P l \qquad (3.16)$$

the right hand side vector of the normal equation system. The a posteriori standard deviation is then

$$m_0 = \sqrt{\frac{v^T P v}{n - u}}. \qquad (3.17)$$

The variance-covariance matrix of the estimated parameters is

$$K = m_0 N^-. \qquad (3.18)$$

3.2. Constraining parameters

Constraints can be introduced with linearized observation equations

$$v_c = H \delta x - h \qquad (3.19)$$

where n_{constr} is the number of constraints as pseudo-observations, H is the Jacobian matrix for pseudo-observations, h is the vector 'observed' minus 'computed' vector for the constraints, v_c is residuals vector over the constraints. The LS method leads to the normal equation for the pseudo-observations

$$
\begin{aligned}
H^T P_c H \delta x &= H^T P_c h, \\
N_{constr} \delta x &= b_{constr},
\end{aligned}
\qquad (3.20)
$$

where P_c denotes the weight matrix for the pseudo-observations. The complete normal equation system for the constrained solution can be computed with

$$(A^T P A + H^T P_c H)\delta x = A^T P l + H^T P_c h, \qquad (3.21)$$

where the constrained normal equation matrix is

$$N_{total} = A^T P A + H^T P_c H = N + N_{constr} \qquad (3.22)$$

and the vector of the right hand side of the constrained normal equation system is

$$b_{total} = A^T P l + H^T P_c h = b + b_{constr}. \qquad (3.23)$$

The unknown parameters of the constrained solution can be computed with

$$x_c = x_0 + N_{total}^- b_{total}. \tag{3.24}$$

After computing the residuals over the constraints with the Equation (3.19) the a posteriori variance component of the constrained normal equation system is then

$$m_{0c} = \frac{v^T P v + v_c^T P_c v_c}{n + n_{constr} - u}. \tag{3.25}$$

The variance-covariance matrix for the unknowns of this constrained normal equation system can be computed with

$$K_{xx} = m_{0c} \, N_{total}^-. \tag{3.26}$$

Absolute constraints on parameters: In case, the preferred values of the parameters are known and the parameters (x) are constrained to these preferred values, the observation equation system will be

$$v_c = \delta x - h \tag{3.27}$$

and the normal equation system will be a simplified form of Equation (3.21)

$$(A^T P A + P_c)\delta x = A^T P l + P_c h. \tag{3.28}$$

A special application of Equation (3.27) is constraining parameters to their a priori values. In that case all the elements of h will be 0.

Relative constraints on parameters: In some cases the relation between two parameters δx_i and δx_j is known and this external (additional) condition can be added to the observation equation system. Such a constraint is introduced with the observation equation

$$v = Hdx - h = \begin{bmatrix} 1 & -1 \end{bmatrix} \cdot \begin{bmatrix} \delta x_i \\ \delta x_j \end{bmatrix} - h, \tag{3.29}$$

The standard deviation of the each parameter can be used for weighting them to carry out loosely or tightly constrained solution. Applications for constraining two parameters relative to each other are:

- Estimation of CPWLO of sub-daily parameters: to connect the two parameters which have no observation in an estimation interval. This will keep the normal equation matrix (N) regular. Here, h assigned to 0 means that the two parameters should be identical. In

case the weight of the pseudo-observation equations (the weights of relative constraints) are too small relatively to those of the real observation equations then the estimated parameters will not be defected by the constraints. Besides, the normal equation matrix (N) will always be regular even if more than two sequential estimation intervals have no observation (Kutterer, 2003).

- In VLBI analysis, e.g. when we have two antennas at the same location with a well-known local tie or when inter-technique combination is carried out at observation equation level: to form pseudo-observation equations for local ties. In these cases our h is 'local tie observed by terrestrial surveys' minus '$x_{0i} - x_{0j}$' (Thaller, 2008).

At a co-located site for a combination of two stations at normal equation level assuming the standard deviation of the Equation (3.29) is s_h and substituting the H, h, δx of Equation (3.29) in Equation (3.20) the normal equations for one local tie between two stations is

$$
\begin{aligned}
\begin{bmatrix} 1 \\ -1 \end{bmatrix} \begin{bmatrix} \frac{s_0^2}{s_{h_{ij}}^2} & 0 \\ 0 & \frac{s_0^2}{s_{h_{ij}}^2} \end{bmatrix} \begin{bmatrix} 1 & -1 \end{bmatrix} \begin{bmatrix} \delta x_i \\ \delta x_j \end{bmatrix} &= \begin{bmatrix} 1 \\ -1 \end{bmatrix} \begin{bmatrix} \frac{s_0^2}{s_{h_{ij}}^2} & 0 \\ 0 & \frac{s_0^2}{s_{h_{ij}}^2} \end{bmatrix} \begin{bmatrix} h_{ij} \end{bmatrix}, \\
\begin{bmatrix} \frac{s_0^2}{s_{h_{ij}}^2} \end{bmatrix} \begin{bmatrix} 1 & -1 \\ -1 & 1 \end{bmatrix} \begin{bmatrix} \delta x_i \\ \delta x_j \end{bmatrix} &= \begin{bmatrix} \frac{s_0^2}{s_{h_{ij}}^2} \end{bmatrix} \begin{bmatrix} h_{ij} \\ -h_{ij} \end{bmatrix}.
\end{aligned}
\tag{3.30}
$$

3.3. Free Network Solution

To define the datum for a VLBI network we need to specify the origin and the orientation of the coordinate system. This can be done by introducing absolute constraints on parameters of station coordinates (e.g. fixing some station coordinates to their a priori values) or by adding no-net-translation, (NNT, origin of axis) and no-net-rotation, (NNR, orientation of axis) conditions relative to some set of a priori coordinates. Constraining three translations to zero is called no-net-translation (NNT), or/and constraining three rotations to zero is called no-net-rotation, or/and constraining the scale to one is called as no-net-scale (NNS). The network's datum definition can be provided as full-trace-minimum introducing NNT/NNR conditions over all stations, or as partial-trace-minimum introducing NNT/NNR conditions for certain stations. The transformation between two reference systems e.g. an a priori reference frame and the estimated network (e.g. a daily session), can be formulated as a Helmert transformation. Helmert transformation is used to describe the relation between the internal network solution derived from the observations and the coordinates of the a priori network (e.g. ITRF) that is used as a

reference. Helmert's method as originally presented by Helmert (1872); Rao and Mitra (1971); Prongle and Rayner (1971); Pelzer (1974). The Helmert transformation for each station i of the network with the coordinate estimates X_i, , Y_i, Z_i and the coordinates X_{0i}, , Y_{0i}, Z_{0i} used as a reference, can be formulated given below (when the rotation parameters are small in value):

$$
\begin{bmatrix} X_i \\ Y_i \\ Z_i \end{bmatrix} = (1 + \mu) \begin{bmatrix} 1 & \gamma & -\beta \\ -\gamma & 1 & \alpha \\ \beta & -\alpha & 1 \end{bmatrix} \begin{bmatrix} X_{0i} \\ Y_{0i} \\ Z_{0i} \end{bmatrix} + \begin{bmatrix} T_X \\ T_Y \\ T_Z \end{bmatrix} \tag{3.31}
$$

where T_X, T_Y, T_Z are translations in X, Y, Z axis directions, α, β, γ are rotations around X, Y, Z axes, respectively, and μ is the scale factor. After regrouping the variables Equation (3.31) can be derived as

$$
\begin{bmatrix} X_1 \\ Y_1 \\ Z_1 \\ X_2 \\ Y_2 \\ Z_2 \\ \vdots \end{bmatrix} = \begin{bmatrix} X_{01} \\ Y_{01} \\ Z_{01} \\ X_{02} \\ Y_{02} \\ Z_{02} \\ \vdots \end{bmatrix} + \begin{bmatrix} 1 & 0 & 0 & X_{01} & 0 & -Z_{01} & Y_{01} \\ 0 & 1 & 0 & Y_{01} & Z_{01} & 0 & -X_{01} \\ 0 & 0 & 1 & Z_{01} & -Y_{01} & X_{01} & 0 \\ 1 & 0 & 0 & X_{02} & 0 & -Z_{02} & Y_{02} \\ 0 & 1 & 0 & Y_{02} & Z_{02} & 0 & -X_{02} \\ 0 & 0 & 1 & Z_{02} & -Y_{02} & X_{02} & 0 \\ & & & \cdots & & & \end{bmatrix} \begin{bmatrix} T_X \\ T_Y \\ T_Z \\ \mu \\ \alpha \\ \beta \\ \gamma \end{bmatrix} \tag{3.32}
$$

and can be written in matrix notation:

$$
X - X_0 = B\zeta \tag{3.33}
$$

The unknown transformation parameters ζ can be determined by LS adjustment:

$$
\zeta = (B^T B)^- B^T (X - X_0). \tag{3.34}
$$

The free network solution is asking for the Helmert parameters to be equal to zero. This leads to

$$
\zeta = (B^T B)^- B^T (X - X_0) = 0. \tag{3.35}
$$

Comparing Equation (3.35) with the constraint equation given in Equation (3.19) the Jacobian matrix of the constraints is

$$
H = (B^T B)^- B^T, \tag{3.36}
$$

and the 'observed' minus 'computed' vector for the constraints is a zero vector ($h = 0$). From the normal equation system for constrained solutions given in Equation (3.21), the free-network solution with constraints will be

$$
(A^T P A + H^T P_c H)\delta x = A^T P l, \tag{3.37}
$$

where P_c is the weight matrix of the seven constraint equations.

Another realization of the free network solution is introducing condition equations on the coordinate estimates to the normal equation system. The condition equations B are added to the normal equation matrix as rows and columns:

$$
\begin{bmatrix} A^T P A & B \\ B^T & 0 \end{bmatrix} \begin{bmatrix} \delta x \\ \delta x_c \end{bmatrix} = \begin{bmatrix} A^T P l \\ b_c \end{bmatrix}, \tag{3.38}
$$

$$
N_{total} \cdot dx_{total} = b_{total}, \tag{3.39}
$$

where δx_c is the unknowns of the conditions, b_c is the constants vector of the condition equations which equal to a zero vector for this case, $A^T P A$ includes the relative and absolute constraints on the CPWLO parameters (soft constraints), N_{total} is the datum conditions and constraints imposed normal equation matrix, and b_{total} is the corresponding normal equations constant vector (right hand side vector) (Wolf and Ghilani, 1997; Öztürk and Serbetçi, 1992; Thaller, 2008).

The VLBI antenna TRF coordinates can be estimated as follows (where all the solutions will be regular due to datum definition):

- CRF coordinates of the sources contributing to session can be fixed to the catalogue coordinates, EOP can be estimated and TRF datum conditions can be introduced on the estimated coordinates in such a way that the estimated TRF will have no-net-translation (NNT) and no-net-rotation (NNR) w.r.t. a priori TRF.

- All EOP and CRF can be fixed to their a priori values which will result in fixing rotation of TRF w.r.t. a priori CRF and EOP. Then, only NNT conditions on the antenna TRF coordinates can be applied.

- All EOP and CRF can be fixed to their a priori values which will result in fixing rotation of TRF w.r.t. a priori CRF and EOP. Then, only one antenna TRF coordinates can be fixed to its a priori TRF catalogue coordinates.

- At least three antenna TRF coordinates can be fixed to their a priori values, when EOP is estimated and CRF is fixed.

Estimation of sub-daily antenna TRF CPWLO coordinates (e.g. hourly) with NNT/NNR con-

ditions is not yet available in vie_lsm. Providing the condition of a reasonable parametrization, sub-daily TRF coordinates will be reliable and accurate. An example can be given to a reasonable parametrization as follows:

- Analyze IVS-CONT08 camping of which sessions have partly large number of observations.

- Estimate only one antenna's hourly CPWLO coordinates and fix other antenna's coordinates to their priori TRF coordinates.

- Before the parameter estimation, do not apply e.g. solid Earth tide displacements (derived from the model) to the a priori coordinates of the estimated antenna (do not reduce solid Earth tide displacements from the observations a priori to the adjustment only at the antenna of which hourly CPWLO coordinates are estimated).

- Compare the hourly CPWLO coordinate estimates of the antenna with the solid Earth tide displacements from the model.

A good agreement between the model and the estimates will be provided. The pre-requisite of estimating accurate hourly antenna coordinates is to have homogenously dispersed large numbers of good observations to all contributing antennas and to all coordinate estimation intervals throughout the VLBI session. VLBI antenna coordinate estimation as CPWLO e.g. for 30 minutes or hourly intervals provide the analyst to examine the tidal motion models (i.e. Earth tides, ocean loading, atmosphere loading) and even assess the deficiencies of these aforementioned models in a sub-daily temporal resolution.

3.4. Stacking normal equation systems

In case, we want to perform a global solution of one type of parameter then the other parameters can be reduced from N and b matrices. For instance, if the analyst wants to stack TRF antenna coordinates block of session-wise normal equation matrices then the other blocks of clocks, zenith wet delays, troposphere gradients could be pre-reduced. This will lead to a normal equation system small in size and overcome memory related problems. The pre-reduction algorithm is based on a division of the normal equation system into two parts: δx_1 are the parameters that will be pre-reduced, and δx_2 consisting of the parameters that will be kept. The corresponding

normal equation system is

$$
\begin{bmatrix} N_{11} & N_{12} \\ N_{21} & N_{22} \end{bmatrix} \begin{bmatrix} \delta x_1 \\ \delta x_2 \end{bmatrix} = \begin{bmatrix} b_1 \\ b_2 \end{bmatrix}
\tag{3.40}
$$

or, decomposed into two parts as follows

$$
\begin{aligned}
N_{11}\,\delta x_1 + N_{12}\,\delta x_2 &= b_1 \\
N_{21}\,\delta x_1 + N_{22}\,\delta x_2 &= b_2
\end{aligned}
\tag{3.41}
$$

Solving for δx_1 in the first equation and substituting it in the second equation yields the normal equation system where the parameters δx_1 are pre-reduced:

$$
\begin{aligned}
N_{21}(N_{11}^{-}b_1 - N_{11}^{-}N_{12}\delta x_2) + N_{22}\delta x_2 &= b_2 \\
(N_{22} - N_{21}N_{11}^{-}N_{12})\delta x_2 &= b_2 - N_{21}N_{11}^{-}b_1
\end{aligned}
\tag{3.42}
$$

Finally, the reduced normal equation system of the parameter set δx_2 can be formulated by the following quantities:

$$
\begin{aligned}
N_{reduc} &= N_{22} - N_{21}N_{11}^{-}N_{12} \\
b_{reduc} &= b_2 - N_{21}N_{11}^{-}b_1 \\
v^T P v = l^T P l - \delta x^T b_{reduc} &= \cdots = l^T P l - b_1^T N_{11}^{-}b_1 - \delta x_2^T b_{reduc}.
\end{aligned}
\tag{3.43}
$$

After the reduction procedure, reduced normal equation systems (e.g. of different sessions) can be stacked together. Stacking is a treatment for the common parameters belonging to more than one normal equation systems by merging them into one combined parameter in the resulting combined normal equation system (Helmert, 1872). A sequential LS adjustment leads to the same result with the common adjustment in one step (Brockmann, 1997). From the systems of normal equations, the same set of unknown parameters δx_2 can be derived by combination with the assumption of no correlations between the two sets of observations as

$$
\begin{aligned}
(A_1^T P_1 A_1 + A_2^T P_2 A_2 + \cdots)\delta x_2 &= A_1^T P_1 l_1 + A_2^T P_2 l_2 + \cdots \\
(N_{reduc1} + N_{reduc2} + \cdots)\delta x_2 &= b_{reduc1} + b_{reduc2} + \cdots.
\end{aligned}
\tag{3.44}
$$

3.5. Parameter estimation in vie_lsm

A new VLBI analysis software called Vienna VLBI Software (VieVS) (Böhm et al., 2010) was developed at the Institute of Geodesy and Geophysics of the Vienna University of Technology (in MATLAB programming language). The development of VieVS was not started from the scratch but is based on algorithms used in the software OCCAM (Titov et al., 2004). VieVS

is designed to meet the most probable analysis related requirements of VLBI in the future, in particular the huge amount of observations compared to present sessions. Increasing the number of observations with the new VLBI system, VLBI2010, will provide enough degrees of freedom to determine the sub-daily variations of the VLBI estimates more accurately. The LS parameter estimation module of VieVS is named vie_lsm. In vie_lsm most of the parameters to be estimated are basically modelled with continuous piece-wise linear offset (CPWLO) functions where offsets are estimated at integer hours, integer fractions or at integer multiples of integer hours. In vie_lsm some of the required partial derivatives of observation equations, e.g. w.r.t. antenna coordinates, source coordinates, and Earth orientation parameters are provided from the preceding module, vie_mod. As exchange format between the modules Matlab structure arrays are used.

In vie_lsm VLBI parameters are estimated according to the LS adjustment based on the Gauss Markoff model. The complete functional and stochastic model can be formed as

$$\begin{bmatrix} v \\ v_c \end{bmatrix} = \begin{bmatrix} A \\ H \end{bmatrix} dx - \begin{bmatrix} l \\ h \end{bmatrix}, \tag{3.45}$$

$$\begin{bmatrix} P & 0 \\ 0 & P_c \end{bmatrix} \tag{3.46}$$

where l is the vector of the reduced observations (observed minus computed), h is the vector of the constraint equations formed as pseudo observations, P is the weight matrix of the observations, P_c denotes to the weight matrix of constraints. In Equation (3.45), A is the upper block matrix of the functional model formed by presently 15 horizontally concatenated sub-matrices,

$$A = \begin{bmatrix} A_1 & A_2 & \cdots & A_{15} \end{bmatrix}. \tag{3.47}$$

Up to now the applied models are:

- CPWLO of clocks (A_1),

- rate and quadratic terms of polynomials of clocks (A_2),

- CPWLO of zenith wet delays (A_3),

- CPWLO of troposphere north gradients (A_4),

- CPWLO of troposphere east gradients (A_5),

- CPWLO of polar motion coordinate in TRF along the Greenwich meridian (x_{pol}) (A_6),

- CPWLO of polar motion coordinate in TRF along the 270° east meridian (y_{pol}) (A_7),

- CPWLO of Earth's rotation phase (dUT1) (A_8),

- CPWLO of celestial intermediate pole (CIP) coordinate in CRF (X) (A_9),

- CPWLO of celestial intermediate pole (CIP) coordinate in CRF (Y) (A_{10}),

- CPWLO of right ascensions of sources in CRF (A_{11}),

- CPWLO of declinations of sources in CRF (A_{12}),

- CPWLO or one offset (optional) of VLBI antenna X coordinate in TRF (A_{13}),

- CPWLO or one offset (optional) of VLBI antenna Y coordinate in TRF (A_{14}),

- CPWLO or one offset (optional) of VLBI antenna Z coordinate in TRF (A_{15}).

It is important to emphasize that in the vie_lsm module of VieVS, VLBI antenna TRF coordinates and source CRF coordinates can be estimated as CPWLO. Thus, sub-daily variations on the VLBI antenna TRF and source CRF coordinates can be determined from real VLBI observations. Antenna coordinate estimation as CPWLO e.g. for 30 minutes or hourly intervals will provide the facility to examine the tidal motion models (i.e. Earth tides, ocean loading, atmosphere loading) and may be to refine these models in a sub-daily temporal resolution based on real VLBI measurements. For the case of sources, e.g. all the sources except one can be fixed to their a priori CRF catalogue coordinates and corresponding quasar's right ascension and declination can be estimated as CPWLO. Estimation of one source coordinates as CPWLO e.g. with 30 minutes intervals might provide a handle on systematic effects. In this case, it is obvious that enough observation to that source should be scheduled.

All the CPWLO are estimated at UTC integer hours, integer fractions or integer multiples of integer hours. The length of the estimation intervals of station specific and global CPWLO parameters can be chosen between five minutes and one day. The estimation is performed in units of centimeters and milliarcseconds. In order to avoid singularity problems of the normal

equation matrix caused by an inadequate number of observations within an estimation interval, loose constraints are introduced (Kutterer, 2003). Constraints are introduced to the design matrix as pseudo-observation equations

$$x_{i+1} - x_i = 0 \pm m_{\Delta x},$$ (3.48)

where x_i is the ith CPWLO unknown. $m_{\Delta x}$ denotes the standard deviation of the constraint which can be a function of the estimation interval and a variance rate set before processing vie_lsm. The coefficients of the standard deviations can be selected in order to derive the parameters as tightly, loosely, or 'quasi-tightly' constrained. Singularity of the design matrix, which is treated properly in vie_lsm, occurs mostly when estimation intervals are too short. The constraints given in Equation (3.48) on the offset estimates formed in the lower block Equation (3.45) of the design matrix, H, are made up as follows

$$H = \begin{bmatrix} H_1 & 0 & \cdots & 0 \\ 0 & H_2 \cdots & 0 \\ \vdots & \vdots & \ddots & \vdots \\ 0 & 0 & \cdots & H_{15} \end{bmatrix}$$ (3.49)

where H_i is the sub-constraints matrix of H for the respective model, consisting of the partials of Equation (3.48), simply formed by

$$H_i = \begin{bmatrix} 1 & -1 & 0 & \cdots & 0 & 0 \\ 0 & 1 & -1 & \cdots & 0 & 0 \\ 0 & 0 & 1 & \cdots & 0 & 0 \\ \vdots & \vdots & \vdots & \ddots & \vdots & \vdots \\ 0 & 0 & 0 & \cdots & 1 & -1 \end{bmatrix}.$$ (3.50)

According to the analysis requirements, any model can be excluded from the parameter estimation stage (vie_lsm) processing station-wise or entirely. For instance, troposphere gradients of station Wettzell may not be estimated during one of the IVS-CONT08 sessions or troposphere parameters of the whole stations contributing the session might not be estimated at all. Besides, constraints on the parameters can be omitted for each model separately or for all models. For instance relative or absolute constraints on troposphere parameters may be excluded or both aforementioned constraints (absolute and relative) may be introduced on these parameters.

The datum condition equations on the coordinate estimates (B) given in Equations (3.32 and 3.33) are added to the datum free normal equation matrix according to Equation (3.38). In

Equation (3.32), in B matrix the a priori coordinates are used after scaled with the mean Earth radius (Pelzer, 1974; Öztürk and Serbetçi, 1992):

$$sc = \frac{1}{\sqrt{\sum [(X_i^{apriori})^2 + (Y_i^{apriori})^2 + (Z_i^{apriori})^2]}}, \qquad (3.51)$$

$$X_{0i} = sc * X_i^{apriori} \; ; \; Y_{0i} = sc * Y_i^{apriori} \; ; \; Z_{0i} = sc * Z_i^{apriori}. \qquad (3.52)$$

The overall solution is done with the Equation (3.24) after forming the matrices given in Equations (3.38 and 3.39). The a posteriori variance component (m_{0c}) for the constrained normal equation system is computed with Equation (3.25). The variance-covariance matrix of the unknowns of the constrained normal equation system is computed with the Equation (3.26).

Each estimated value (dx), their standard deviation (m_{dx}), their estimation epoch in MJD, and the column (or row) number of the corresponding estimate in N_{total} (or b_{total}) are some of the results of vie_lsm, thus stored as structure arrays in Matlab. Besides, the N_{total} and b_{total} including the other global parameters e.g. Love and Shida numbers, antenna velocity, and source coordinates are the outputs of vie_lsm and stored with the selected options of LS parameter estimation.

The interval for CPWLO modelling of the parameters is usually set to values between one day to five minutes. Due to the limited number of observations in a session, the estimation intervals should be selected accordingly. Too short estimation intervals for every parameter will cause too many unknowns which will decrease the degrees of freedom of the adjustment and may lead to several singularity problems (as e.g. rank deficiencies). To stabilize the parameter estimation process, constraints (or pseudo-observations) have to be included in intervals with only a small number of observations. The weights of the pseudo-observations have to be chosen according to those of the real observations.

3.5.1. Handling outliers

Two times process of a session is needed in order to eliminate outlier observations in VieVS. In the first process, in vie_lsm module, outlier observations are detected and written in session-wise ASCII files and saved into a user defined directory. In the second process, in vie_init module, the outlier observations are read from the files and eliminated from the observation. These two step process approach is a consistent and easy way to handle outliers. Because, the user may process a set of sessions multiple times with different options. Then, in order to be consistent

with the observations same outliers are eliminated for each run. This approach is easy. Because for a set of specific options the user will have a set of session-wise outlier files and whenever some particular sessions are analyzed these outliers can be directly read from the outlier files and eliminated. Thus, the software would not need to go for outlier detection at each session analyzed.

In the vie_lsm module of VieVS an observation is determined to be an outlier observation in case the condition,

$$v_i => coef \cdot m_0 \tag{3.53}$$

is provided. In Equation 3.53, v_i is the residual of the ith observation, $coef$ is a coefficient that is defined by the user and can be e.g. 3, and m_0 is the a posteriori standard deviation of unit weight given in Equation 3.17 or 3.25. The other criteria for outlier observation detection is: an observation is determined to be an outlier observation in case the condition,

$$v_i => coef \cdot m_{v_i} \tag{3.54}$$

is provided. In Equation 3.54, the standard deviation of v_i is,

$$m_{v_i} = m_0 \sqrt{diag(Q_{vv})}. \tag{3.55}$$

The covariance matrix of the observational residuals (Q_{vv}) given in Equation 3.55 is,

$$Q_{vv} = Q_{ll} - AN^- A^T, \tag{3.56}$$

where Q_{ll} is the inverse of the weight matrix of observations (P_{ll}^-) and $AN^- A^T$ is the inverse of the weight matrix of the adjusted observations ($P_{\hat{l}\hat{l}}^-$).
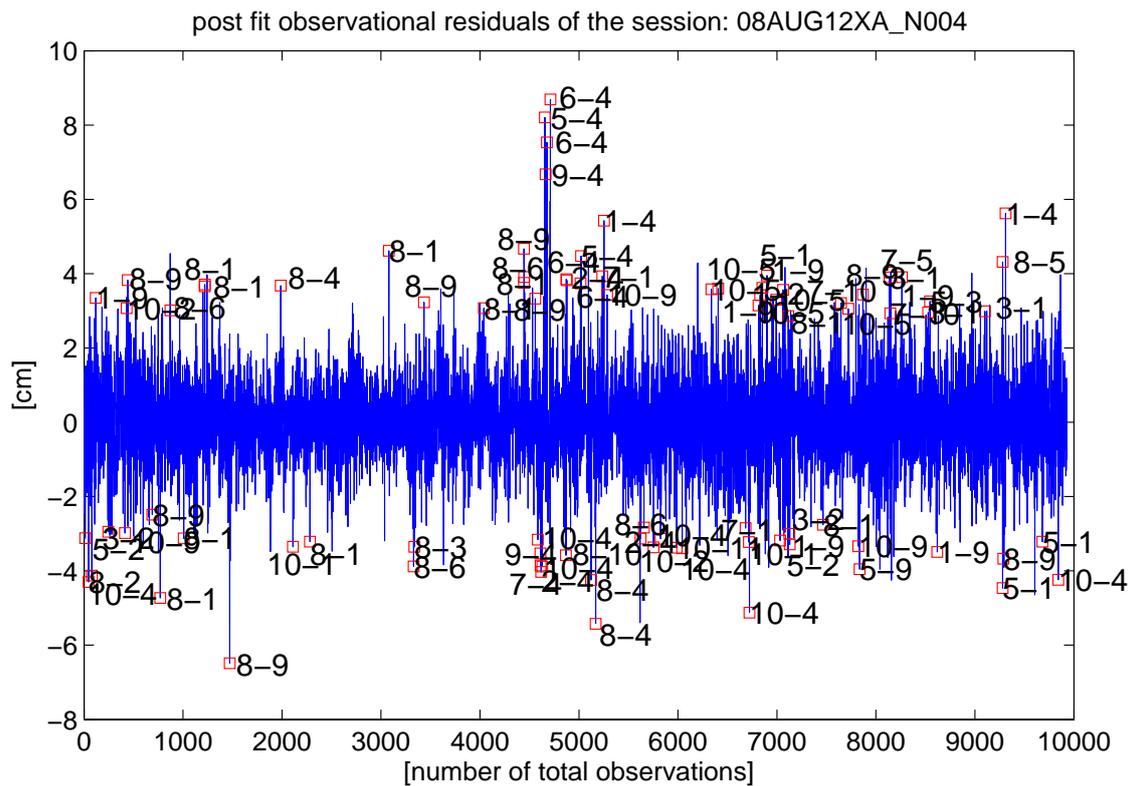
Figure 3.1.: The post-fit observational residuals of the first daily session of IVS-CONT08 (08AUG12XA_N004). The numbers in the plot shows the first and the second antenna of the observation (delay). In total 87 outliers were found out within 9927 observations of 1151 scans. The outlier detection was carried according to the Equation (3.54) with coef = 3.

4. VLBI clock error

In VLBI modelling, all the vector and scalar quantities (e.g. barycentric celestial coordinates of the Jth gravitating body, the geocentric velocity vector of the ith station, the geocentric radius vector of the ith station, barycentric velocity vector of the geocenter) are calculated as a function of time. Here, the most important point is that UTC time tag provided for each scan should be transformed to the appropriate time scale e.g. barycentric coordinate time (TCB), geocentric coordinate time (TCG), terrestrial time (TT) to compute each element of the VLBI model. For that reason time systems and their relations have utmost importance. Basically, time systems can be categorized into two parts: First, *astronomic time systems* consist of *sidereal* and *universal times* which are based on the diurnal rotation of the Earth, and *dynamic time (ephemeris time)* based on the orbital motions of celestial bodies in the solar system following the law of gravitation and independent from the rotation of the Earth. Second is the *atomic time* based on electromagnetic oscillations. For more details about time systems please see Appendix A.2. In this section modelling and estimating of clock errors are introduced, one of the largest constituents of the signal delay in VLBI.

4.1. Modelling and estimating VLBI clock errors based on CPWLO functions

The observable quantities in VLBI technique are recorded signals measured in the proper time of the station clocks. The time scale of the clocks is Universal Time Coordinated (UTC). The quality of a clock is determined by how accurate and stable its frequency is and by its sensitiveness to environmental changes. Two useful measures for the quality of a clock are: frequency accuracy and frequency stability. These measures are not independent. A clock *frequency accuracy* is a measure of how well a clock can realize the defined length of e.g. *second*. *Frequency stability*, on the other hand, indicates the change in frequency from one period of

time to the next. A clock can have a significant frequency error and still be very stable, in other words, the frequency error stays about the same. For example, a clock may have a frequency inaccuracy of gaining one second a day, but if that rate remains the same, it would have perfect frequency stability (Holman, 2005).

The signal delay in VLBI is mainly caused by the differences in the behavior of the frequency standards of the clocks, the geometry of sources in CRF and the geometry of the antennas in TRF. Proper modelling and estimating clock errors caused by frequency instabilities in VLBI measurement analysis has utmost importance. Un-modelled parts of the clock error delay in the observational delay propagate into other estimated parameters. After choosing a reference clock for the entire observing network of a session the remaining clocks show both a constant difference (clock offset) and a linear (clock trend) or even higher rate of change relative to the reference clock. Thus, an appropriate clock with presumably high frequency stability should be chosen as the reference clock for the entire network. Since the clock parameters also 'absorb' physical effects with a similar signature (as e.g. instrumental effects and relativistic effects of higher order) special attention should be paid to this type of parameter (Schuh, 1987; Herring et al., 1990).

4.1.1. Clock error model

Conventionally in VLBI analysis, the time differences between two clocks resulted from being not synchronized are estimated by an offset and the frequency instabilities of the corresponding clocks are fixed by piece-wise offsets with weighted LS adjustment. On the other hand Herring et al. (1990) suggested to use a Kalman Filter for estimating relative clock errors so as to produce more accurate VLBI parameters. In vie_lsm, for VLBI analysis most of the parameters to be estimated are basically modelled with continuous piece-wise linear offset (CPWLO) functions where offsets are estimated at integer hours, integer fractions or at integer multipliers of integer hours with LS. In vie_lsm to describe clock errors a quadratic polynomial was fit with LS to all remaining clocks after fixing one clock. This step is called as first LS adjustment. In this first step the polynomial coefficients of the clocks and a zenith wet delay offset are estimated for each station for the whole session. In order to model clock delay errors in addition to a simple polynomial,

$$\Delta\tau_{clk}^{POLY}(t) = \beta_0 + \beta_1(t - t_0) + \beta_2(t - t_0)^2 \qquad (4.1)$$

a CPWLO function for the second LS adjustment (main solution),

$$\Delta\tau_{clk}^{CPWLOF}(t) = x_1 + \frac{t - t_1}{t_2 - t_1}(x_2 - x_1) \tag{4.2}$$

is used. In Equations (4.1 and 4.2), t is the epoch of the observation. $\Delta\tau_{clk}^{POLY}(t)$ denotes the clock delay error at the observation epoch t represented by the quadratic polynomial. $\Delta\tau_{clk}^{CPWLOF}(t)$ denotes the clock delay error at the observation epoch t represented by the CPWLO function. t_0 denotes the first clock estimation epoch at the first integer or fractions of UTC hours before the beginning of the session (epoch of the first CPWLO clock estimate). β_j are the polynomial coefficients (unknowns) of a clock. x_1 and x_2 are the CPWLO of clocks (unknowns) at integer estimation epochs t_1 and t_2, respectively. Total clock error at t is:

$$\Delta\tau_{clk}(t) = \Delta\tau_{clk}^{POLY}(t) + \Delta\tau_{clk}^{CPWLOF}(t). \tag{4.3}$$

The partial derivatives of the Equation (4.3) with respect to the polynomial coefficients, β_j are:

$$\frac{\partial\Delta\tau_{clk}(t)}{\partial\beta_0} = 1, \tag{4.4}$$

$$\frac{\partial\Delta\tau_{clk}(t)}{\partial\beta_1} = t - t_0, \tag{4.5}$$

$$\frac{\partial\Delta\tau_{clk}(t)}{\partial\beta_2} = (t - t_0)^2. \tag{4.6}$$

The partial derivatives of the Equation (4.3) with respect to the CPWLO (x_1 and x_2) are:

$$\frac{\partial\Delta\tau_{clk}(t)}{\partial x_1} = 1 - \frac{t - t_1}{t_2 - t_1}, \tag{4.7}$$

$$\frac{\partial\Delta\tau_{clk}(t)}{\partial x_2} = \frac{t - t_1}{t_2 - t_1}. \tag{4.8}$$

Since the observation equations are formed based on baselines, the design matrix of CPWLO of the clocks (A_{CPWLOF}) for a scan including three observations at epochs $t1'$, $t2'$, and $t3'$, three clocks (clk_1, clk_2, and clk_3) and one estimation interval (two unknowns for each station) is

$$\begin{bmatrix} \frac{\partial\Delta\tau(t1')}{\partial(clk_1)_{x_1}} & \frac{\partial\Delta\tau(t1')}{\partial(clk_1)_{x_2}} & \frac{-\partial\Delta\tau(t1')}{\partial(clk_2)_{x_1}} & \frac{-\partial\Delta\tau(t1')}{\partial(clk_2)_{x_2}} & 0 & 0 \\ 0 & 0 & \frac{\partial\Delta\tau(t2')}{\partial(clk_2)_{x_1}} & \frac{\partial\Delta\tau(t2')}{\partial(clk_2)_{x_2}} & \frac{-\partial\Delta\tau(t2')}{\partial(clk_3)_{x_1}} & \frac{-\partial\Delta\tau(t2')}{\partial(clk_3)_{x_2}} \\ \frac{\partial\Delta\tau(t3')}{\partial(clk_1)_{x_1}} & \frac{\partial\Delta\tau(t3')}{\partial(clk_1)_{x_2}} & 0 & 0 & \frac{-\partial\Delta\tau(t3')}{\partial(clk_3)_{x_1}} & \frac{-\partial\Delta\tau(t3')}{\partial(clk_3)_{x_2}} \end{bmatrix} \tag{4.9}$$

and the design matrix for the clock polynomial coefficients, A_{POLY} is

$$\begin{bmatrix} \frac{\partial\Delta\tau(t1')}{\partial(clk_1)_{\beta_0}} & \frac{-\partial\Delta\tau(t1')}{\partial(clk_2)_{\beta_0}} & 0 & \frac{\partial\Delta\tau(t1')}{\partial(clk_1)_{\beta_1}} & \frac{-\partial\Delta\tau(t1')}{\partial(clk_2)_{\beta_1}} & 0 & \frac{\partial\Delta\tau(t1')}{\partial(clk_1)_{\beta_2}} & \frac{-\partial\Delta\tau(t1')}{\partial(clk_2)_{\beta_2}} & 0 \\ 0 & \frac{\partial\Delta\tau(t2')}{\partial(clk_2)_{\beta_0}} & \frac{-\partial\Delta\tau(t2')}{\partial(clk_3)_{\beta_0}} & 0 & \frac{\partial\Delta\tau(t2')}{\partial(clk_2)_{\beta_1}} & \frac{-\partial\Delta\tau(t2')}{\partial(clk_3)_{\beta_1}} & 0 & \frac{\partial\Delta\tau(t2')}{\partial(clk_2)_{\beta_2}} & \frac{-\partial\Delta\tau(t2')}{\partial(clk_3)_{\beta_2}} \\ \frac{\partial\Delta\tau(t3')}{\partial(clk_1)_{\beta_0}} & 0 & \frac{-\partial\Delta\tau(t3')}{\partial(clk_3)_{\beta_0}} & \frac{\partial\Delta\tau(t3')}{\partial(clk_2)_{\beta_1}} & 0 & \frac{-\partial\Delta\tau(t3')}{\partial(clk_3)_{\beta_1}} & \frac{\partial\Delta\tau(t3')}{\partial(clk_1)_{\beta_2}} & 0 & \frac{-\partial\Delta\tau(t3')}{\partial(clk_3)_{\beta_2}} \end{bmatrix}.$$

In Figures 4.1 and 4.2, hourly estimates of Westford and Onsala VLBI antenna clock error estimates can be seen when the Gilcreek clock is fixed, during the first session of IVS-CONT05 and during all sessions of IVS-CONT05, respectively. The jumps (discontinuities) of clock estimates between sessions in Figure 4.2 are due to the daily session breaks.
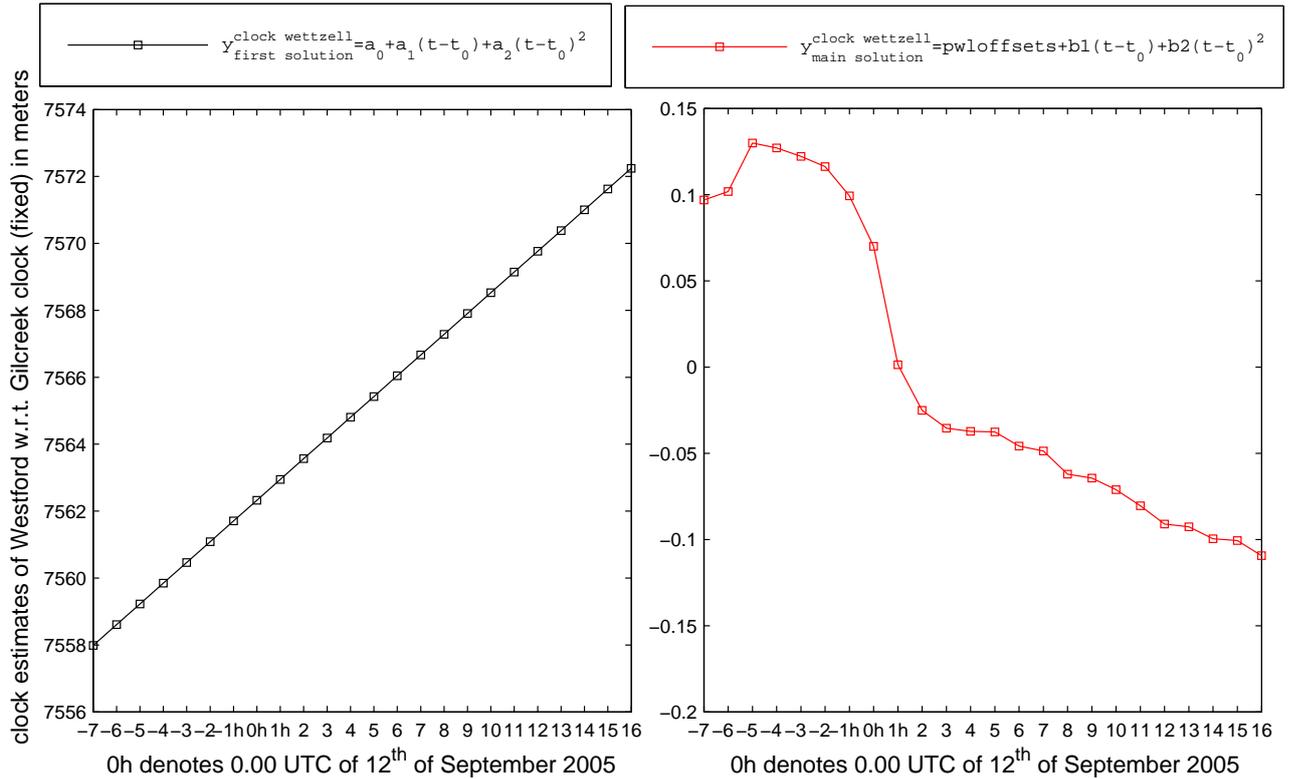
Figure 4.1.: Westford clock errors w.r.t. Gilcreek clock during the first session of IVS-CONT05. The left plot shows the clock polynomial estimated from the first LS solution. The right plot shows the hourly CPWLO estimates plus polynomial with rate and quadratic terms from the main solution. The total clock estimates are the sum of the two plots.

4.1.2. Determining and modelling clock breaks

In VLBI analysis clock breaks (jumps) are encountered. In vie_lsm module of VieVS two step LS adjustment is used. In the first LS adjustment clock breaks are fixed by means of forming a separate clock polynomial for each time segment where the boundaries of the time segments are determined by the epochs of the clock breaks (see Figure 4.4). Optionally, the type of clock polynomial can be selected (only offset or/and rate, ...) in the first LS solution. The basic
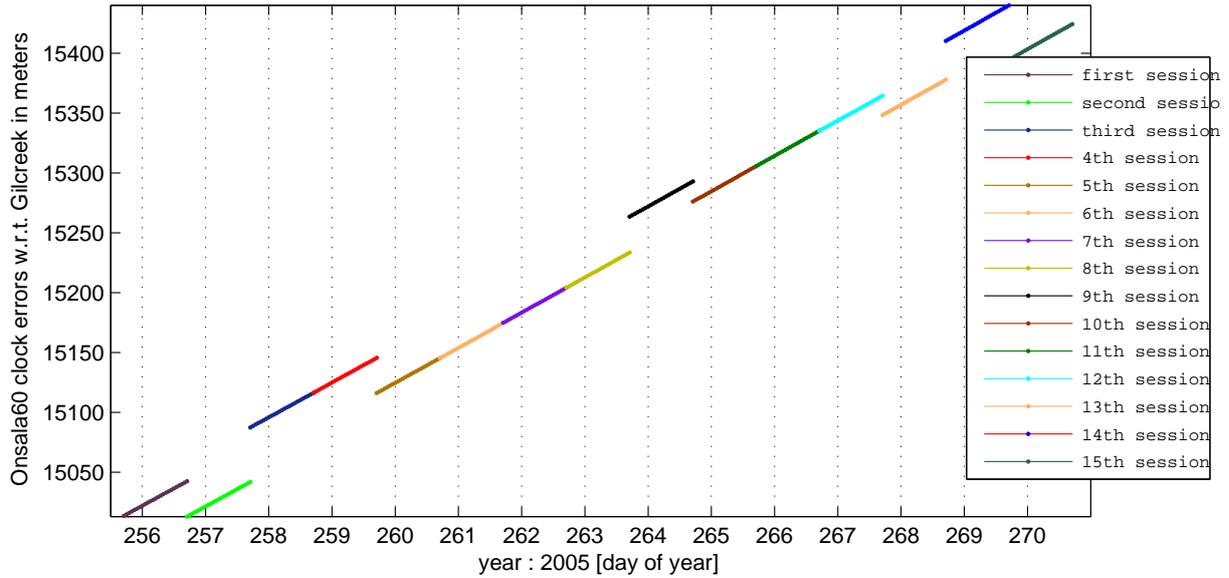
Figure 4.2.: Onsala60 clock errors w.r.t. Gilcreek clock during IVS-CONT05.

reasons for the first LS solution can be itemized as follows:

- To eliminate large clock offsets.

- To fix the corresponding clock breaks that are written in option files. It should be noted that the clock breaks are only corrected in the first LS solution.

- Being a tool for investigating small clock breaks. If the analyst wants to apply only the first LS solution (without main solution), station-wise post-fit observational residuals will be plotted: To detect the clock breaks and the occurrence time.

- To figure out if any large station-wise, source-wise, or/and baseline-wise observational residuals occurred. Then, corresponding station, source, and/or baseline would be excluded from the session by writing them to corresponding session's option file.

At the main LS solution, clock errors are modelled as CPWLO at optional intervals (epochs). Besides, one rate and one quadratic term of a polynomial for the whole session are again included (optional). It should be noted that for the first and the main LS solutions different clocks can be fixed (optional).

As an example for fixing a clock break, we analyze session 08AUG12XA. Station Zelenchukskaya post-fit observational residuals are shown in Figure 4.3 after the first LS solution. When the corresponding clock break was not fixed then the epoch of the break can easily be identified from the post-fit observational residuals plot. The post-fit observational residuals of the station Zelenchukskaya from the first LS solution jump from ~ -20cm to $\sim +40$cm (Figure 4.3). Thus, the analyst can easily identify the epoch of the break, e.g. for this case the clock break occurred at about 54690.406 MJD. After detecting the time (in MJD) of the clock break, the analyst
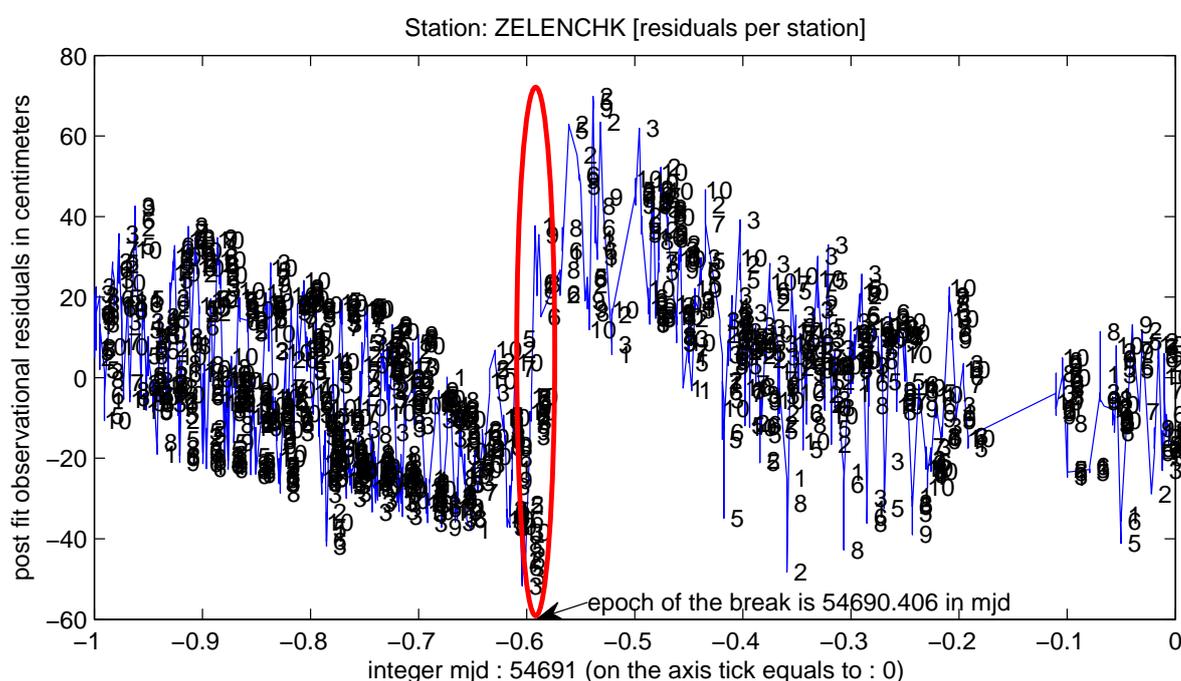
Figure 4.3.: Post-fit residuals of observations of the VLBI station Zelenchukskaya (in Russia) during the session 08AUG12XA (first daily session of IVS-CONT08 campaign). The numbers on the plot, denote to the other stations of the baselines. Red ellipse illustrates the vicinity of the clock break epoch.

should write the station and the time epoch of the break (MJD) in the corresponding option file in VieVS (08AUG12XA.OPT). When a second LS adjustment is carried out of vie_lsm fits a separate polynomial for each segment whose boundaries are defined by clock breaks (Figure 4.4). The post-fit residuals of observations after correcting the clock break are shown in Figure 4.5.
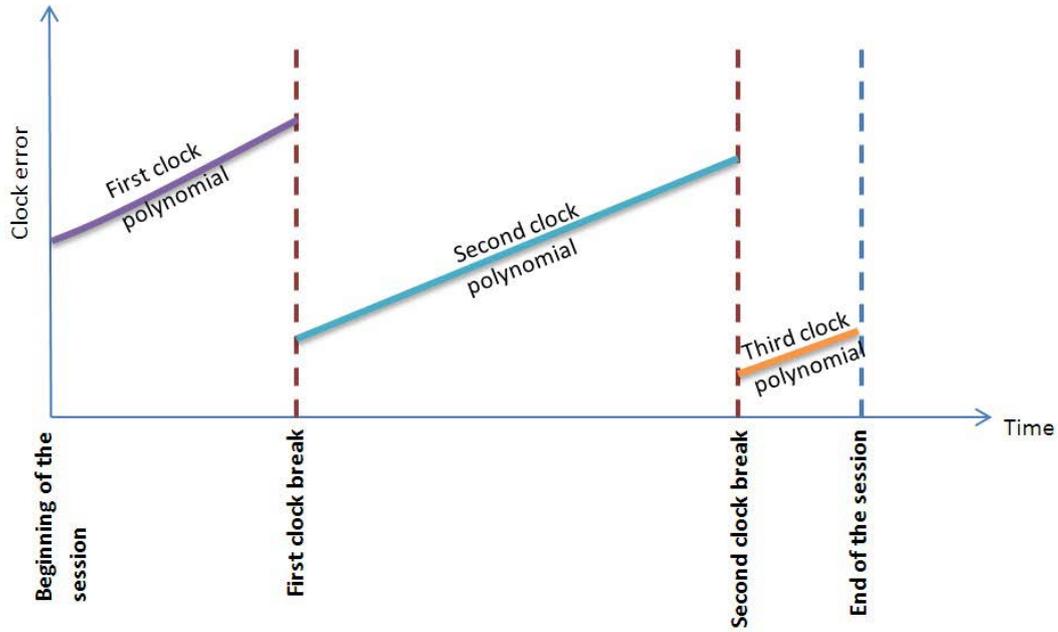
Figure 4.4.: A polynomial is fitted for each interval delimitated by the occurrence time of clock breaks.
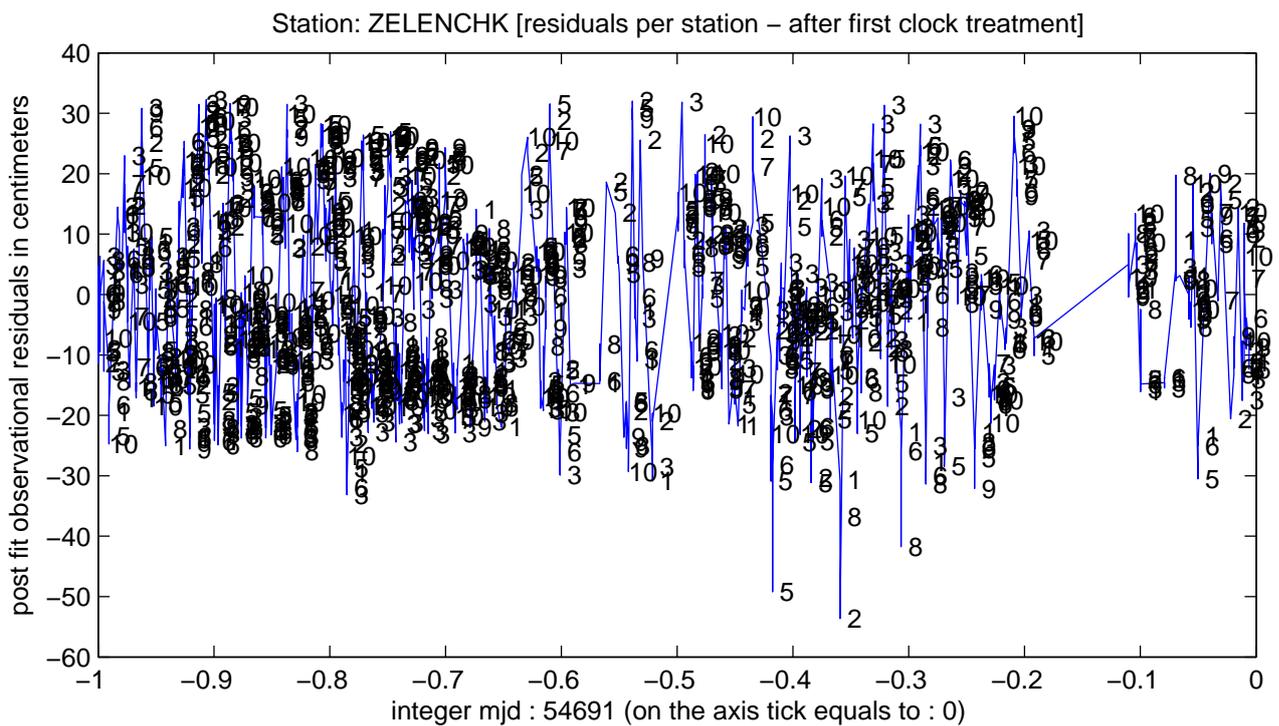
Figure 4.5.: After clock breaks are fixed, post-fit residuals of observations of the VLBI station Zelenchukskaya during the session 08AUG12XA.

4.1.3. Clock break error on the VLBI observations and its propagation on estimated VLBI parameters

In order to show an example on the magnitude of the effects of clock breaks on hourly ERP estimates, and on the hourly zenith wet delays of Zelenchukskaya, Figure 4.6, Figure 4.7, Figure

4.8, and Figure 4.9, are given. The plots show only the ERP estimates without their corresponding a priori values (IERS 05 C04 values (Gambis, 2004; Bizouard and Gambis, 2009) plus the ocean tidal terms as recommended by the IERS Conventions 2003 (McCarthy and Petit, 2004). The clock break at Zelenchukskaya clock occurred at epoch 54690.406 during the session 08AUG12XA is $\sim$ 60 cm. This clock break caused on errors on the estimated ERP as shown in Figure 4.6, Figure 4.8, and Figure 4.9 range up to 5 μs for $\Delta UT1$, 70 μas for x_p, and 200 μas for y_p. The ERP estimates at epochs near by the epoch of the Zelenchukskaya clock break are significantly effected. For the case of the zenith wet delay estimates with and without correcting clock breaks differ significantly during the whole session (see Figure 4.7). Due to this fact that, clock breaks should be modelled and corrected carefully to prevent the propagation of observational errors on the estimates i.e. on station TRF coordinates, on source CRF coordinates and on global parameters.
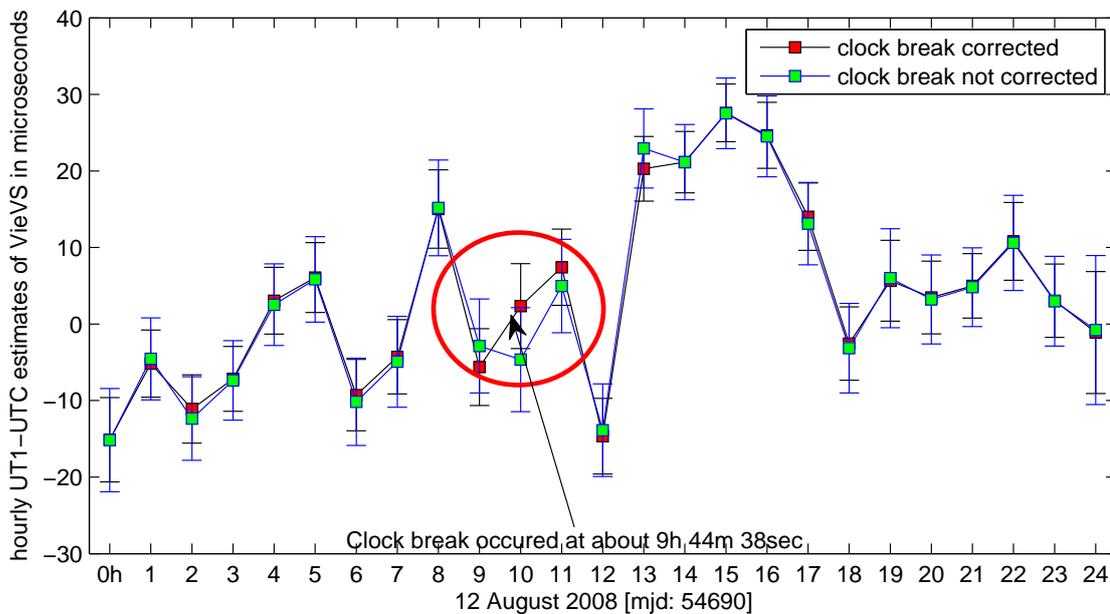
Figure 4.6.: CPWLO of hourly $\Delta UT1$ estimates during the session 08AUG12XA, with and without $\sim$ 60 cm clock break at Zelenchukskaya corrected.

4.2. Frequency stabilities of the VLBI clocks

Clocks have frequency, amplitude, and phase instabilities (fluctuations) (Holman, 2005). In the time domain, sequential average frequency instabilities are called Allan standard deviation
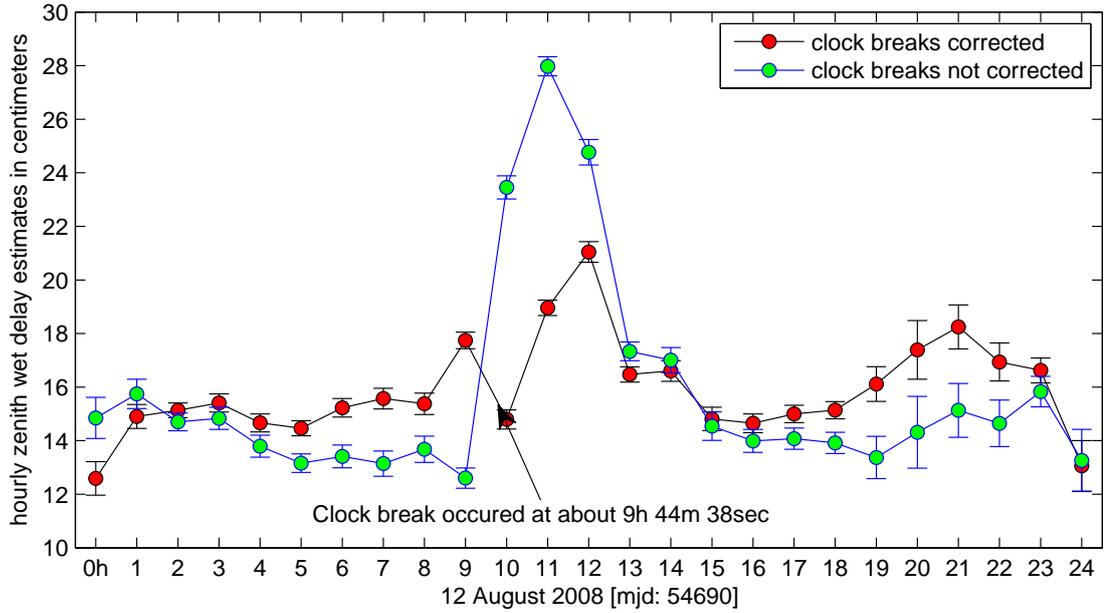
Figure 4.7.: CPWLO of hourly ZWD estimates of Zelenchukskaya VLBI antenna during the session 08AUG12XA, with and without ∼ 60 cm clock break at Zelenchukskaya corrected.
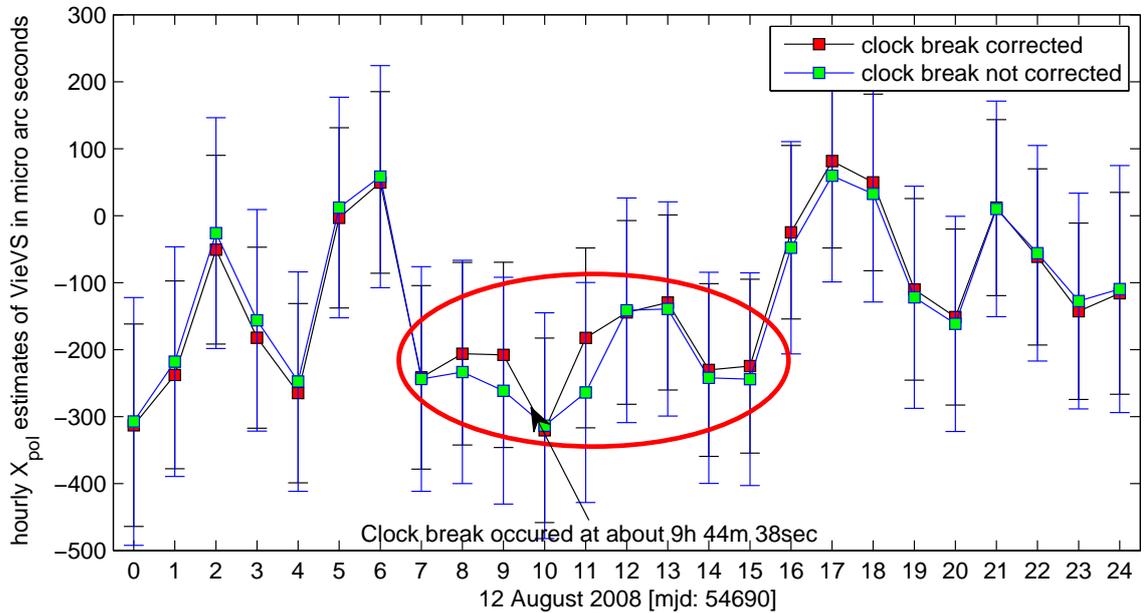
Figure 4.8.: CPWLO of hourly polar motion dx_p coordinate estimates in TRF during the session 08AUG12XA, with and without ∼ 60 cm clock break at Zelenchukskaya corrected.

(ASD) (Allan and Barnes, 1981; Stein, 1985). In the time domain, the ASD can be used as the standard measure of frequency instabilities for clocks. The ASD can be calculated from the
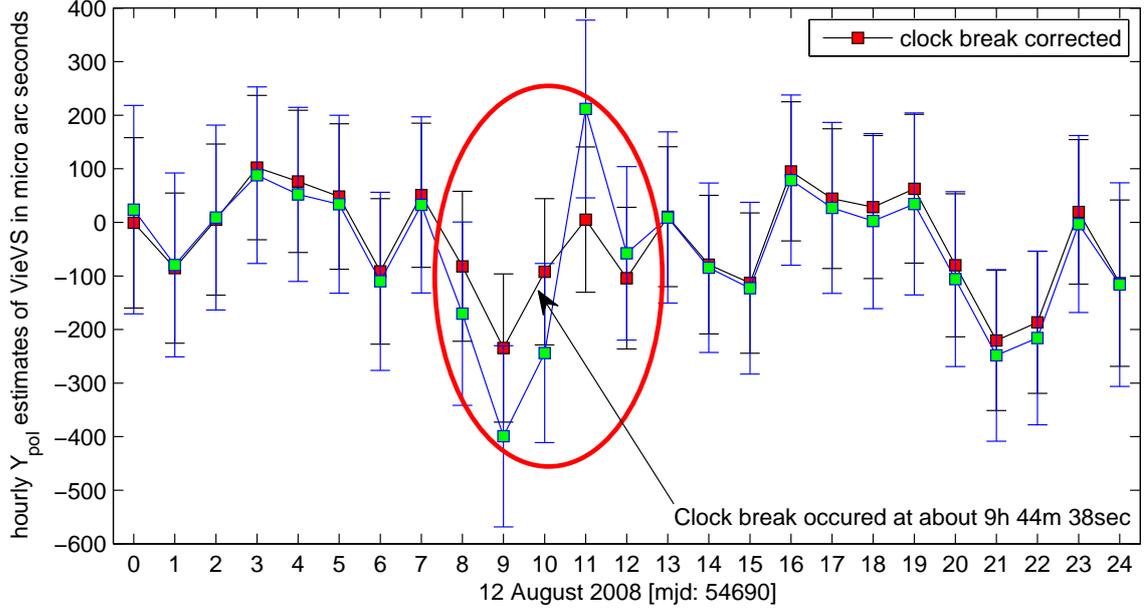
Figure 4.9.: CPWLO of hourly polar motion dy_p coordinate estimates in TRF during the session 08AUG12XA, with and without ~ 60 cm clock break at Zelenchukskaya corrected.

estimated clock errors with respect to a fixed clock as follows,

$$\sigma(\tau) = [\frac{1}{2(N-2m)\tau^2} \sum_{k=1}^{N-2m} (x_{k+2m} - 2x_{k+m} + x_k)^2]^{\frac{1}{2}}, \tag{4.11}$$

where m is

$$m = \frac{\tau}{\triangle t}, \tag{4.12}$$

or for an efficient spacing of sampling intervals in a logarithmic plot

$$m = 2^p \ , \ p = 0, \ 1, \ 2, \ 3, \ldots . \tag{4.13}$$

In Equation (4.11), N is the total number of estimated clock errors, $\triangle t$ is the time interval between the estimated clock errors, τ is the sampling interval e.g. 10 minutes, 1 hour, 3 hours, 11 hours, and/or 1 day. It is necessary to highlight that the sampling intervals (τ), should not be less than the time intervals of the clock error estimates $(\triangle t)$. For example, if the ASD is to be calculated at 30 minutes, clock errors should be estimated at least for 30 minutes intervals. x_k is the kth CPWLO estimate of a clock error when one clock e.g. Wettzell is fixed.

In VLBI analysis clock errors are estimated mainly at 1 hour intervals and one clock is fixed. When one clock is fixed then the ASD of clocks are relative to the fixed clock. In order to investigate and figure out the relative frequency stabilities of the other VLBI clocks w.r.t. Wettzell

44

clock, the continuous IVS-CONT02, -CONT05, and -CONT08 were analyzed and ASD of clocks from CPWLO clock estimates were calculated. In a VLBI session analysis, when one clock is fixed then the ASD of clocks will be relative to the fixed clock. Quadratic polynomial coefficients (offset, rate and quadratic term) for each clock except Wettzell (fixed) were estimated in the first LS solution. In the main LS solution, hourly CPWLO in addition to a rate and a quadratic term were estimated during IVS-CONT02, -CONT05, and -CONT08 sessions. Only the sessions in which none of the clocks have clock breaks were taken into account for computing the ASD of the clocks. The reason for not including the sessions where clock break(s) occurred is: even if a clock break is corrected by means of dividing clock function into pieces, there may be some residual effects of clock breaks which might cause errors on the computed ASD. When the clock frequency stabilities in terms of ASD were computed, four sessions of IVS-CONT08 clock breaks detected: $08AUG12XA$, $08AUG14XA$, $08AUG15XA$, and $08AUG25XA$ were not included in the analysis. For the case of the IVS-CONT02 campaign the sessions: 02OCT25XA and 02OCT27XA include clock breaks. Thus, these sessions were not included in computing ASD. No clock break was detected in the IVS-CONT05 sessions. In order not to be affected from the session jumps session-wise ASD are computed. ASD of the e.g. Onsala60 clock e.g. during IVS-CONT05 sessions, e.g. at 3hour sampling interval, were estimated 15 sessions separately. The mean value of the overall e.g. 15 ASD is considered. The mean value of the overall e.g. 15 ASD is written in the Tables 4.1, 4.2, and 4.3.

In terms of the ASD of clocks from the hourly relative clock error estimates w.r.t. Wettzell during IVS-CONT02, -CONT05, and -CONT08 sessions (Table 4.1, 4.2, and 4.3), the following conclusions can be drawn:

- Range within 10^{-15} to 10^{-14} at 1 hour to 11 hours.

- Slightly getting better for longer sampling time intervals relative to shorter sampling intervals.

- Not a significant ASD improvement (difference) seen of a clock between IVS-CONT02, -CONT05, and -CONT08 sessions.

Table 4.1.: ASD of the VLBI clocks with respect to Wettzell clock, for several sampling intervals, during IVS-CONT02.

	ASD at 1hour	3hour	5hour	7hour	9hour	11hour
Westford	2.4e-15	2.4e-15	2.3e-15	2.0e-15	1.5e-15	8.6e-16

Kokee	4.0e-15	6.8e-15	7.4e-15	6.3e-15	4.6e-15	2.9e-15
Nyales20	4.4e-15	6.4e-15	6.9e-15	6.3e-15	4.8e-15	2.6e-15
Algopark	1.5e-15	2.0e-15	2.1e-15	1.8e-15	1.3e-15	6.8e-16
HartRAO	2.4e-15	4.1e-15	5.1e-15	4.8e-15	3.6e-15	1.8e-15
Gilcreek	2.4e-15	2.9e-15	3.0e-15	2.7e-15	2.1e-15	1.2e-15
Onsala60	2.9e-15	2.5e-15	2.1e-15	1.8e-15	1.4e-15	8.2e-16

Table 4.2.: ASD of the VLBI clocks with respect to Wettzell clock, for several sampling intervals, during IVS-CONT05.

	ASD at 1hour	3hour	5hour	7hour	9hour	11hour
Westford	5.5e-15	4.5e-15	3.2e-15	2.1e-15	1.6e-14	1.1e-14
Kokee	5.1e-15	5.2e-15	4.9e-15	3.9e-15	3.0e-15	1.7e-15
Nyales20	4.2e-15	5.0e-15	4.3e-15	3.6e-15	2.7e-15	1.5e-15
Algopark	2.5e-15	2.8e-15	2.6e-15	2.2e-15	1.6e-15	7.6e-16
HartRAO	2.9e-15	3.7e-15	3.3e-15	2.4e-15	1.9e-15	1.3e-15
Svetloe	5.3e-15	4.9e-15	4.7e-15	4.1e-15	3.2e-15	1.8e-15
Gilcreek	2.7e-15	2.4e-15	2.3e-15	2.0e-15	1.5e-15	9.5e-16
Onsala60	3.8e-15	2.7e-15	2.0e-15	1.5e-15	1.1e-15	7.2e-16
Tsukub32	5.1e-15	3.2e-15	2.1e-15	1.5e-15	1.4e-15	1.1e-15
Tigoconc	1.8e-15	2.8e-15	3.0e-15	2.6e-15	1.8e-15	9.6e-16

Table 4.3.: ASD of the VLBI clocks with respect to Wettzell clock, for several sampling intervals, during IVS-CONT08.

	ASD at 1hour	3hour	5hour	7hour	9hour	11hour
Westford	4.7e-15	3.7e-15	3.4e-15	3.3e-15	2.6e-15	1.4e-15
Kokee	6.4e-15	5.9e-15	4.9e-15	4.5e-15	3.7e-15	2.2e-15
Nyales20	4.7e-15	5.1e-15	4.4e-15	3.2e-15	2.6e-15	1.3e-15
HartRAO	2.9e-15	2.4e-15	2.1e-15	1.7e-15	1.2e-15	7.9e-15
Svetloe	6.7e-15	7.0e-15	5.4e-15	4.7e-15	3.5e-15	2.2e-15
Onsala60	5.3e-15	2.8e-15	2.0e-15	1.4e-15	1.1e-15	8.7e-16
Tsukub32	9.1e-15	9.7e-15	1.0e-14	9.8e-15	7.2e-15	2.9e-15
Tigoconc	2.5e-15	2.2e-15	1.9e-15	1.4e-15	1.1e-15	8.0e-16
Medicina	8.7e-15	1.0e-14	1.1e-14	1.1e-14	8.4e-15	4.1e-15
Zelenchk	5.1e-15	6.0e-15	4.9e-15	4.0e-15	3.6e-15	2.5e-15

In order to figure out the ASD for the short sampling intervals e.g. 10 minutes, IVS-CONT08

second session, 08AUG13XA was analyzed for 10 minutes clock estimation intervals. The results (see Figure 4.10) were compared with those derived from the 1 hour intervals (see Table 4.3). ASD computed from 1 hour clock estimation interval are smaller by one order of magnitude than 10 minutes interval clock estimates.
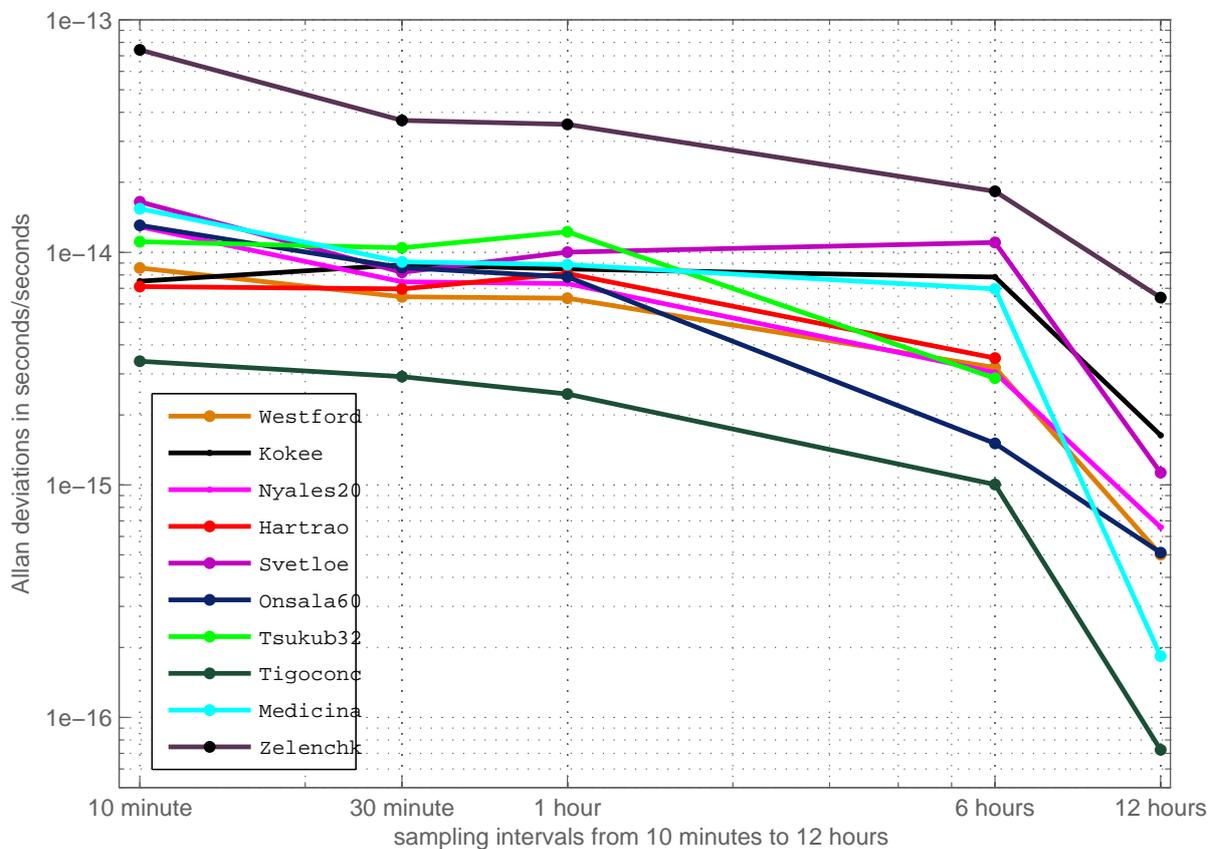
Figure 4.10.: ASD of the clocks w.r.t. Wettzell clock during the second 24h session of IVS-CONT08 (08AUG13XA). The sampling intervals are from 10 minutes to 12 hours (e.g. ASD at 10 minutes).

5. Troposphere delay

Modelling propagation of the electromagnetic microwave signals through the electrically neutral part of atmosphere (troposphere) is a common interest for most of the space geodetic techniques, e.g. VLBI, Global Navigation Satellite Systems (GNSS), and Doppler Orbitography and Radio Positioning Integrated by Satellite (DORIS). Often troposphere is used to refer to the neutral atmosphere. Strictly speaking the neutral atmosphere also consists of other layers, e.g. strato-sphere, mesosphere. Relatively to vacuum environment, retardation and bending cause arrival delays of microwave signals called troposphere slant path delays ΔL_{trop}. The path delay at an arbitrary direction can be defined as the integral over the refractive index, n along the slant path, S between the station and the highest part of the troposphere, plus the bending effect

$$\Delta L_{trop} = \int_s n ds - \int_g dg = \int (n-1)ds + S - G, \tag{5.1}$$

where G is the geometric path that can be defined as the path of a signal in vacuum (straight line), but in neutral atmosphere the electromagnetic signal propagates along the curve S (see Figure 5.1). The bending effect $(S - G)$ has to be included in troposphere modelling. In the following equations the $S - G$ term is dropped for simplicity

$$\Delta L_{trop} = \int_s (n-1)ds = 10^{-6} \int_s N ds = 10^{-6}[\int_s N_h ds + \int_s N_w ds], \tag{5.2}$$

where N is the refractivity. Instead of using N, ΔL_{trop} can be derived by the partial pressure of the dry air, p_d water vapor pressure, e and temperature, T as follows,

$$\Delta L_{trop} = 10^{-6}[\int_s (k_1 \frac{p_d}{T} Z_d^{-1} + k_2 \frac{e}{T} Z_w^{-1} + k_3 \frac{e}{T^2} Z_w^{-1})ds] \tag{5.3}$$

or

$$\Delta L_{trop} = 10^{-6}[\int_s k_1 \frac{R}{m_d} \rho ds + \int_s (k_2' \frac{e}{T} + k_3 \frac{e}{T^2}) Z_w^{-1} ds] \tag{5.4}$$

where $R = 8.314510 \pm 0.00007$ in $\frac{Pa.m^3}{K.mol}$ is the universal gas constant, $k_1 = 77.6 \pm 0.05$ in $\frac{K}{hPa}$, $k_2 = 70.4 \pm 2.2$ in $\frac{K}{hPa}$, $k_3 = 373900 \pm 1200$ in $\frac{K^2}{hPa}$, and $k_2' = k_2 - k_1 \frac{m_w}{m_d}$ are the empirical

"S" is the shortest path in terms of time
"G" is the shortest path in terms of length
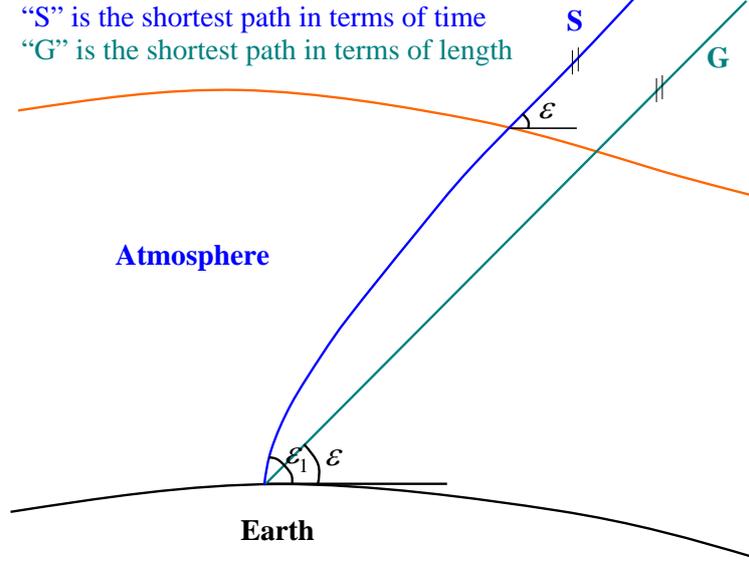
Figure 5.1.: Bending of the ray in the neutral atmosphere. The outgoing (vacuum) elevation angle ε is smaller than the initial elevation angle ε_1 (Böhm, 2004).

coefficients provided by e.g. Bevis et al. (1994). Besides, another estimation of these empirical coefficients can be found in Rüeger (2002). The molar masses of dry air, $m_d = 28.9644 \pm 0.0014$ in $\frac{g}{mol}$ and water vapor, $m_w = 18.015289$ in $\frac{g}{mol}$, stay constant up to 100 km. Z_d^{-1} and Z_w^{-1} are inverse compressibility factors for dry air and water vapor. Formulas accurate to a few ppm were determined by Owens (1967) with the adjustment of thermodynamics data:

$$Z_d^{-1} = 1 + p_d[57.97 \cdot 10^{-8}(1 + \frac{0.52}{T}) - 9\,4611 \cdot 10^{-4}\frac{t}{T^2}], \tag{5.5}$$

$$Z_w^{-1} = 1 + 1650\frac{e}{T^3}[1 - 0.01317t + 1.75 \cdot 10^{-4}t^2 + 1.44 \cdot 10^{-6}t^3], \tag{5.6}$$

where t is the temperature in degree Celsius. In Equation (5.4) we have divided the refractivity into two parts, a hydrostatic part N_h and a wet refractivity part N_w,

$$N_h = k_1\frac{R}{m_d}\rho, \tag{5.7}$$

$$N_w = (k'_2\frac{e}{T} + k_3\frac{e}{T^2})Z_w^{-1}, \tag{5.8}$$

where $\rho = \rho_d + \rho_w$ is the total density. The density of dry air ρ_d and the density water vapor ρ_w are computed as follows:

$$\rho_d = p_d\frac{m_d}{R}\frac{1}{T}Z_d^{-1}, \tag{5.9}$$

$$\rho_w = e\frac{m_w}{R}\frac{1}{T}Z_w^{-1}. \tag{5.10}$$

Nowadays, troposphere delays (hydrostatic and wet) can be determined with ray-tracing through the globally distributed profiles of Numerical Weather Models (NWM) e.g. from the European Center for Medium-Range Weather Forecasts (ECMWF), High Resolution Limited-Area Models (HIRLAM), or the Japan Meteorological Agency (JMA). Each NWM has different horizontal and vertical resolution. E.g. from ECMWF we use 21 pressure levels from 1000 hPa up to 1 hPa. At each pressure level total pressure, water vapor pressure, temperature, relative humidity are provided every 6 UTC integer hours (Böhm, 2009). In order to produce slant/zenith hydrostatic and wet delays via ray-tracing we need to determine hydrostatic, wet, and total refractivities of the ray at all increments (e.g. Table 5.1) from the station up to $\sim$ 100 km. A standard atmosphere model of temperature can be used in order to provide the temperature above the maximum height of the NWM profiles.

Table 5.1.: Increments for ray-tracing (Rocken et al., 2001).

between (km)	0-2	2-6	6-16	16-36	36-136
increment (m)	10	20	50	100	500

Hydrostatic and wet refractivities are used to calculate hydrostatic and wet delays. To compute the total pressure ($p = p_d + e$), and water vapor pressure (e) at all increments along a profile; pressure values provided by e.g. radiosonde or/and numerical weather models (NWM) are interpolated by an exponential function to all height increments as follows:

$$e = e_0 \exp^{(h-h_0)/c},$$

(5.11)

where e_0 is the water vapor pressure of the lower height level at the height h_0. e is the interpolated water vapor pressure at the height h. c is the coefficient of the exponential interpolation calculated for each increment. Temperature values (T) at all height levels can be interpolated linearly to all increments. For each increment the refractivities $N_{h,w}$ can be derived by Equations (5.7) and (5.8). According to Equation (5.2) the zenith troposphere delays can be computed by integration over the sum of the hydrostatic and wet refractivities. Slant delays can also be produced directly by ray-tracing, beginning from a station at an initial elevation angle (ε_1) through the troposphere for k increments when total, hydrostatic and wet refractivities are known at each increment (Figure 5.2) (Böhm (2004); Appendix). If the length of the slant path of each increment (s_i) is known the integral over s_i will provide us the slant delay of the corresponding increment:

$$ds_{hi} = 10^{-6} \sum_{i=1}^{k-1} s_i N_{hi},$$

(5.12)

$$ds_{wi} = 10^{-6} \sum_{i=1}^{k-1} s_i N_{wi}. \tag{5.13}$$

In order to calculate all incremental paths s_i and outgoing elevation angles ε_{i+1} through the troposphere a loop over i can be formed which runs from 2 to $k-1$:

$$s_i = -r_i \sin\theta_i + \sqrt{r_{i+1}^2 - r_i^2 \cos^2\theta_i}, \tag{5.14}$$

where $r_i = r_0 + h_i$ is the distance from the center of the Earth to the point P_i (intersection of the ray with the lower boundary of the ith increment), r_0 denotes the Earth radius, h_i is the height of P_i. Then, geocentric coordinates of P_i can be calculated:

$$z_{i+1} = z_i + s_i \sin\varepsilon_i,$$
$$y_{i+1} = y_i + s_i \cos\varepsilon_i. \tag{5.15}$$

The corresponding angles in the center of the Earth are:

$$\eta_{i+1} = \arctan(y_{i+1}/z_{i+1}),$$
$$\delta_{i+1} = \eta_{i+1} - \eta_i. \tag{5.16}$$

The angles θ_{i+1} and η_{i+1} can be determined as follows:

$$n_i = 1 + (N_{hi} + N_{wi})10^{-6},$$
$$\theta_{i+1} = \arccos(\tfrac{n_i}{n_{i+1}} \cos(\theta_i + \delta_{i+1})),$$
$$\varepsilon_{i+1} = \theta_{i+1} - \eta_{i+1}. \tag{5.17}$$

The geometric bending effect can be computed as follows:

$$S - G = \sum_{i=1}^{k-1} [s_i - \cos(\varepsilon_i - \varepsilon_k)s_i] \tag{5.18}$$

(Böhm (2004); Appendix).

5.1. Troposphere mapping functions

Troposphere mapping functions (MF) project the zenith hydrostatic delay (ZHD) and zenith wet delay (ZWD) at a site from zenith to a slant path at an elevation angle through troposphere assuming the troposphere is azimuthally symmetric. For planar troposphere mapping functions can be represented simply by $\frac{1}{sin\varepsilon}$. In order to provide a more precise model the continued fraction form is used (Marini, 1972):

$$m_{h,w}(\varepsilon) = \frac{1 + \dfrac{a_{h,w}}{1 + \dfrac{b_{h,w}}{1 + c_{h,w}}}}{\sin\varepsilon + \dfrac{a_{h,w}}{\sin\varepsilon + \dfrac{b_{h,w}}{\sin\varepsilon + c_{h,w}}}} \tag{5.19}$$
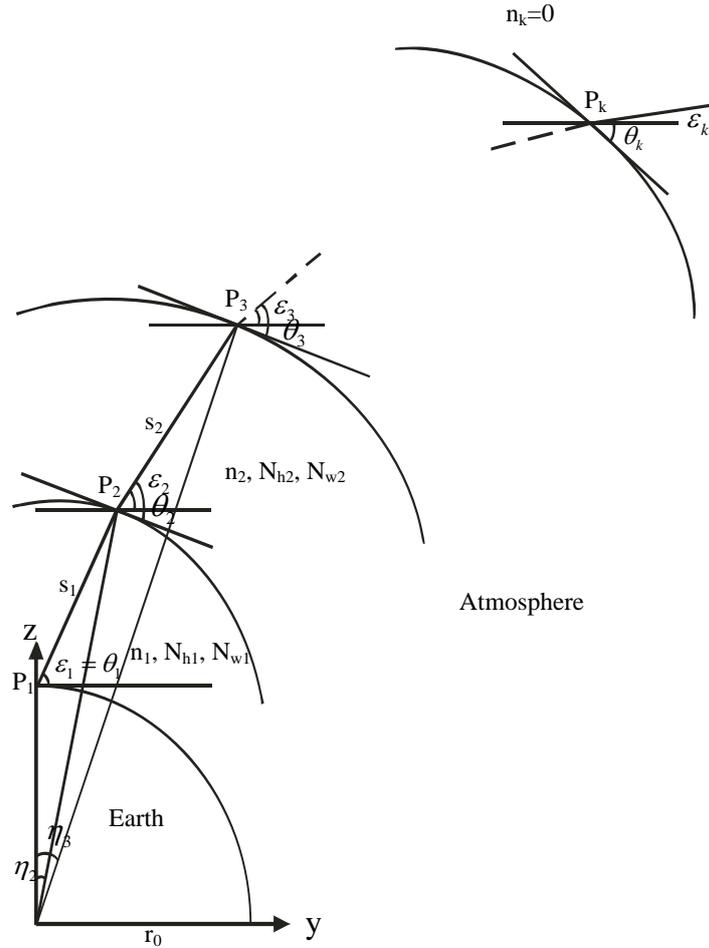
Figure 5.2.: Ray-tracing (Böhm (2004); Appendix)

where $a_{h,w}$, $b_{h,w}$, and $c_{h,w}$ are the hydrostatic and wet coefficients of the mapping function. Niell (1996) found out that three terms are sufficient to keep the error to less then 1 mm for elevations down to 3° if the delays are calculated at eight elevations in addition to zenith direction. Several different mapping functions exist. Below a few commonly used ones are presented.

Niell mapping functions (NMF)

The coefficients of the continued fraction form ($a_{h,w}$, $b_{h,w}$, and $c_{h,w}$) given in Equation (5.19) are functions of day of year, latitude, and height. These functions were determined by standard atmosphere models and validated by radiosonde data at 26 sites for a one year period (1992) with usually two profiles per day, at 00 and 12 UT. The coefficients of NMF are estimated by LS

fit to the "true" mapping functions (ratios of the ray-traced slant delays to the ray-traced zenith delay). The path delays are calculated at 9 different elevation angles from 90° to 3° and for 9 different latitudes (15°, 30°, 45°, 60°, and 75°) and from season-dependent standard atmosphere profiles. For the hydrostatic mapping functions temporal variations of the "a" coefficients are assumed as sinusoidal. The coefficients are modelled as sinusoids in time with a period of 365.25 days (one Julian year). Each of the parameters of NMF is a constant or a function of site latitude (symmetric about the equator which causes biases for example in the Antarctic) and day of year. NMF considers seasonal dependence of the temporal variation of the atmosphere. The details related to NMF (e.g. models of averaged coefficients, amplitude coefficients and height corrections for coefficients) can be found in Niell (1996) and Böhm (2009).

Isobaric mapping functions (IMF)

For the hydrostatic IMF (IMFh) the coefficients of the continued fraction form (a_h, b_h, and c_h) are functions of the height of one pressure level, 200 hPa. The formulas of these functions are based on the radiosonde data to determine the "true" mapping functions for the twenty-eight sites, and the Goddard Space Flight Center (GSFC) Data Assimilation Office (DAO) provided the meteorological parameters on a 2.0° by 2.5° grid in latitude and longitude. All the profiles (~ 730) for each twenty-eight sites were ray-traced for nine elevations from 90° degrees down to 3°. For each profile the coefficients of the mapping function (a, b, $and\, c$) that best fit to the "true" mapping functions at the nine elevations are estimated by LS. Gridded isobaric height data, as used for IMFh, and the corresponding profile information on height and water vapor content needed for IMFw, are publicly available from several meteorological analysis centers at time intervals as short as six hours on a global grid. For the IMFh only one parameter, the height of one isobaric level is needed at each of the grid points. For IMFw several values (geopotential height or pressure, temperature, and a measure of water vapor such as relative humidity) are needed. More details related to IMFh and IMFw can be found in Niell (2000) and Niell and Petrov (2003).

Vienna mapping functions (VMF1)

The functions are relying on empirical equations for the "b" and "c" coefficients of the continued fraction form (Equation 5.19), whereas the "a" coefficients are estimated by LS fit to the ray-traced "true" mapping functions. Ray-tracing is based on the data of European Center for

Medium-Range Weather Forecasts (ECMWF), i.e. pressure level data on 2.5° x 2.0° degrees grids at $0h$, $6h$, $12h$, and $18h$ UT. Ray-tracing is carried out using the profiles data (initial elevation angle, height, temperature and water vapor pressure at 21 pressure levels from 1000 to 1 hPa) at the global grids. The hydrostatic and wet mapping functions as well as the outgoing elevation angles is determined at the initial elevation angle, 3.3°. Hydrostatic VMF1 include geometric bending effect determined by ray-tracing. The Institute of Geodesy and Geophysics at the Vienna University of Technology provides VMF1 global grids (2.5° in longitude times 2.0° in latitude) with a temporal resolution of six hours and for selected IVS, IGS, and IDS sites (Böhm et al., 2006).

Global mapping functions (GMF)

The functions coefficients are obtained from a spherical harmonics expansion of the VMF1 parameters on a global grid. Using 15° x 15° grids of monthly mean profiles for pressure, temperature, and humidity from the ECMWF, the coefficients of "a_h" and "a_w" were determined for the period September 1999 to August 2002 applying the same strategy that is used for VMF1. Taking empirical equations for "b" and "c" (from VMF1) the parameters "a" are derived by ray-tracing of a single 3.3° elevation angle. Thus, at each of the 312 grid points, 36 monthly values were obtained for the hydrostatic and wet "a" parameters. The hydrostatic coefficients were reduced to mean sea level by applying the height correction given by Niell (1996). The mean values of the "a" coefficients, (a_0), and the annual amplitudes A of a sinusoidal function

$$a = a_0 + A \cdot cos(\frac{doy - 28}{365} \cdot 2\pi) \tag{5.20}$$

were fitted to the time series of the "a_h" and "a_w" separately at each grid point, with the phases referred to January 28, corresponding to NMF. Then, the global grid of the mean values $a_{h0,w0}$ and of the amplitudes $A_{h,w}$ for both the hydrostatic and wet coefficients were expanded into spatial spherical harmonics coefficients up to degree and order nine in a LS adjustment. Similar to NMF, input parameters of GMF are *latitude, longitude, height, day of year.* For particular time periods or stations where NWM-based mapping functions are not available (e.g. IMF, VMF), the GMF can be used without introducing systematic biases in the coordinate time series, although the short term precision will suffer (Böhm et al., 2006; Böhm and Schuh, 2007).

Because of the spatial and rapid temporal changes of the troposphere quantities especially wet part troposphere remains the largest error source of space geodetic measurements. Several studies have been performed to determine the accuracy of troposphere parameters e.g. MacMillan

and Ma (1994); Emardson et al. (1998); Haas et al. (1999); Behrend et al. (2000, 2002); Cucurull et al. (2000); Gradinarsky et al. (2000); Niell et al. (2001); Schuh and Böhm (2003); Kouba (2009).

5.2. Troposphere gradients

Since mapping functions model only the azimuthally symmetric part (which depends only on elevation angle), horizontal gradients should be considered additionally. Equation (5.2) can be decomposed into hydrostatic, wet, and gradient delays (Davis et al., 1985, 1993; MacMillan, 1995) as follows:

$$\Delta\tau_{trop} = ZHD \cdot m_h(\varepsilon) + ZWD \cdot m_w(\varepsilon) + m_{h,w}(\varepsilon)cot(\varepsilon)[G_N cos(\alpha) + G_E sin(\alpha)] \qquad (5.21)$$

where ε is the elevation angle from local horizon, α the azimuth (angle from geodetic north), and ZHD the zenith hydrostatic delay, which can be computed from the total pressure and the station coordinates (Saastamoinen, 1972). ZWD is the zenith wet delay, $m_h(\varepsilon)$ and $m_w(\varepsilon)$ are the hydrostatic and wet mapping functions (Marini, 1972; Niell, 1996; Böhm et al., 2006). G_N and G_E are north and east troposphere gradients, respectively. The hydrostatic mapping function account for the bending effect. The gradient model given in Equation (5.21) is illustrated in Figures 5.3 and 5.4.

MacMillan (1995) developed the gradient part of the model given in Equation (5.21). According to the data sets that he analyzed (VLBI sessions from 1990 to 1993 and 12 sessions of IVS-CONT94 R&D experiments) daily averaged gradients can be as large as 50 mm at a 7° elevation and including gradient model in the analysis baseline length repeatabilities can be improved by 1 to 8 mm in an RMS sense. MacMillan and Ma (1997) also investigated the effects of estimating gradients on terrestrial reference frames (TRFs) and celestial reference frames (CRFs). According to their study estimating gradients at the stage of analyzing VLBI sessions can largely reduce the systematic errors of the VLBI reference frames. Chen and Herring (1997) developed two methods for determining the troposphere propagation delay due to the gradients. The first model uses three-dimensional atmospheric pressure, temperature, and relative humidity derived from *National Center for Environmental Prediction* (NCEP), and the other model is based on VLBI data. For a 12-day series of experiments in January 1994, analysis of VLBI sessions and NCEP show common atmospheric gradient delays with amplitudes of up to 30 mm at 10° degree elevation angle. According to Davis et al. (1993) and Böhm and Schuh (2007) linear horizontal
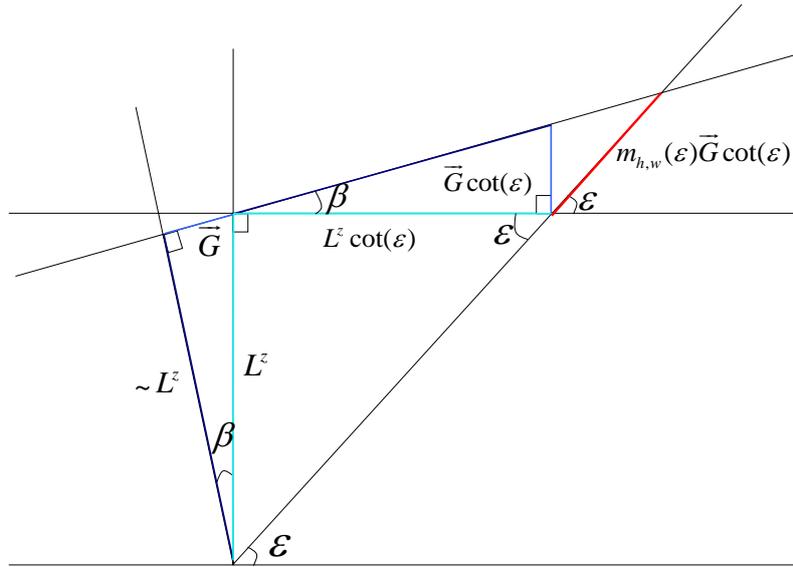
Figure 5.3.: Projecting gradient vector from zenith to slant direction. β is the tilting angle of the mapping function assuming a horizontally stratified atmosphere (Böhm, 2009).
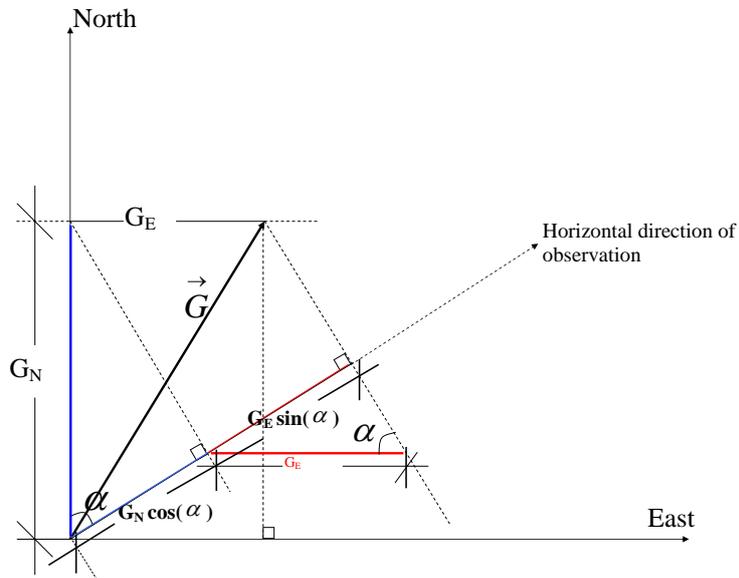
Figure 5.4.: Projecting the gradient vector at the slant direction to the azimuth of observation.

gradients can be obtained from a numerical weather model (NWM) as the vertical integral of the refractivity gradient. They investigated the effects of gradients on baseline length repeatabilities. They analyzed VLBI observables by fixing gradients to zero and not estimating them, when ECMWF model gradients are introduced a priori and/or when they are estimated for 6h

and 24h intervals.

5.3. Troposphere delays in VieVS

In Vienna VLBI Software (VieVS), the hydrostatic delays are introduced a priori to the *oc* given in Equation 2.28. In order to reduce the hydrostatic delay from *oc* for each observation, ZHD are computed according to the function by Saastamoinen (1973) given in the form applied by (Davis et al., 1985).

$$\Delta\tau_{trop}^{hyd}(t) = 0.0022768 \frac{p}{1 - 0.00266\,cos(2\varphi) - 0.28\,10^{-6}h} \tag{5.22}$$

where p in hPa denotes the total surface pressure (e.g. from local surface meteorological measurements, or a numerical weather model (NWM) (Böhm et al., 2006). φ is the latitude, and h is the ellipsoidal height of the site in m. Then, computed ZHD (e.g. shown in Figures 5.5 and 5.6) are mapped according to the mapping functions GMF or VMF1 to the slant direction of the corresponding observations.

In VieVS, estimated troposphere parameters are ZWD e.g. Figures 5.5 and 5.6, and north and east gradients e.g. Figure 5.7. Similar to the other estimates, continuous piece-wise linear offset (CPWLO) functions are used in order to form the sub-design matrices of the adjustment. As an example Equation (5.23) shows the troposphere slant wet delay $\Delta\tau_{trop}^{wet}(t)$ of an observation at epoch t represented by CPWLO function, x_1 and x_2 of the zenith wet delays at epochs t_1 and t_2:

$$\Delta\tau_{trop}^{wet}(t) = m_w(t)\,x_1 + m_w(t)\,\frac{t - t_1}{t_2 - t_1}\,(x_2 - x_1) \tag{5.23}$$

where $m_w(t)$ denotes the wet mapping function of the observation at epoch t which is between t_1 and t_2. The partial derivatives of Equation (5.23) with respect to CPWLO, x_1 and x_2 of zenith wet delays, are:

$$\frac{\partial\Delta\tau_{trop}(t)}{\partial(ZWD)_{x_1}} = m_w(t) - m_w(t)\,\frac{t - t_1}{t_2 - t_1}, \tag{5.24}$$

$$\frac{\partial\Delta\tau_{trop}(t)}{\partial(ZWD)_{x_2}} = m_w(t)\,\frac{t - t_1}{t_2 - t_1}. \tag{5.25}$$

The CPWLO are estimated at integer hours (e.g., at 18 UTC, 19 UTC, ...), at integer fractions of integer hours (e.g. 18:20 UTC, 18:40 UTC, ...) or at integer multiples of integer hours (e.g. 18:00 UTC, 0:00 UTC, 6:00 UTC, ...). This representation is not only used for estimating troposphere
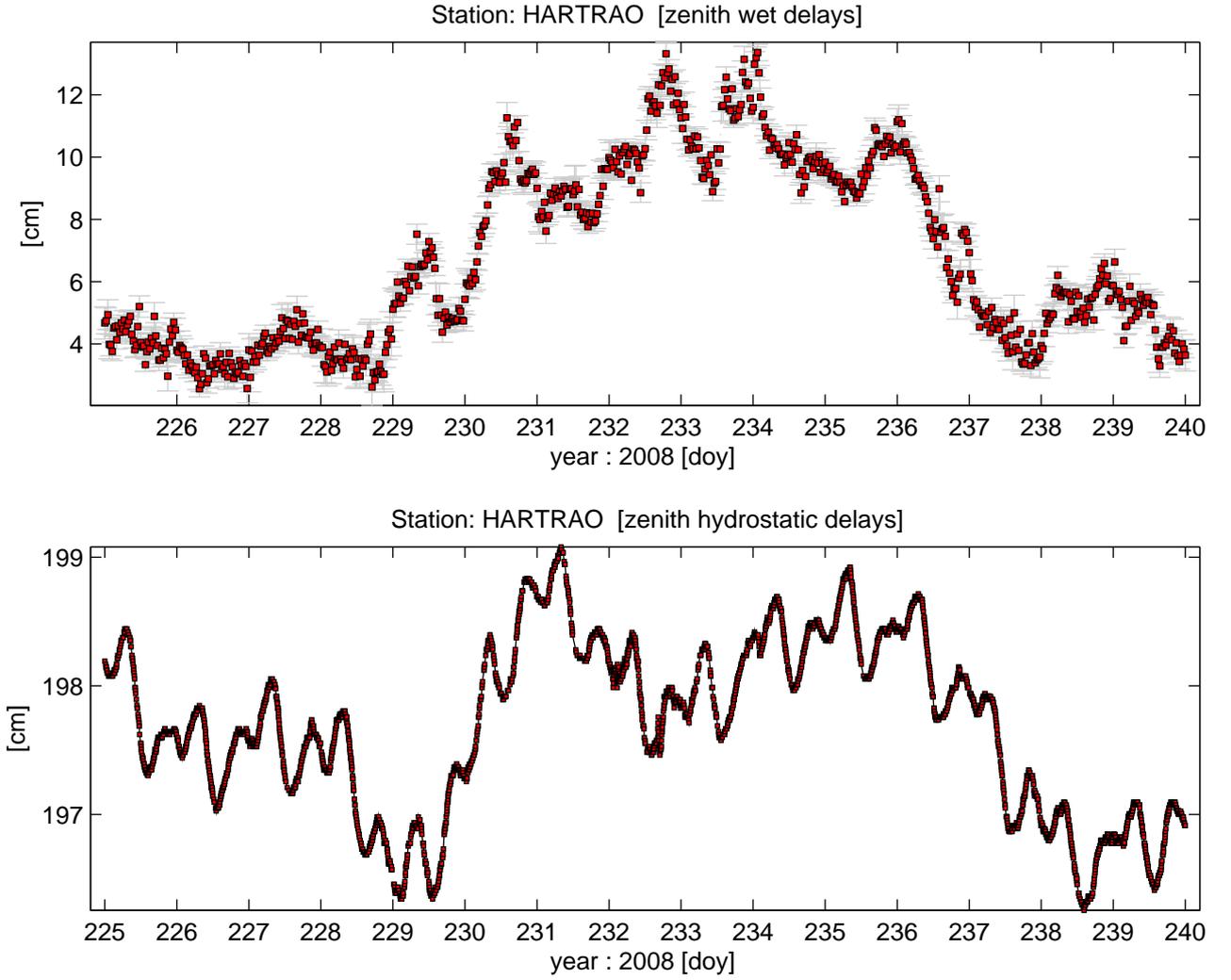
Figure 5.5.: VieVS, ZHD and 30 minutes ZWD estimates of VieVS at Hartebeesthoek VLBI site (Republic of South Africa) during IVS-CONT08. Loose constraints (0.7 $\frac{ps^2}{sec}$ = 11 mm after 30 minutes) are applied.

zenith wet delays and gradients, but also for station clocks, Earth orientation parameters, and station coordinates (Böhm et al., 2010).

Partial derivatives of the troposphere delay model given in Equation (5.21) for the observation at epoch t w.r.t. north gradient CPWLO, x_1 and x_2 results in:

$$\frac{\partial \Delta \tau_{trop}(t)}{\partial (G_N)_{x_1}} = m_w(t) \, \cot \varepsilon \, \cos(\alpha) \, [1 - \frac{t - t_1}{t_2 - t_1}], \tag{5.26}$$

$$\frac{\partial \Delta \tau_{trop}(t)}{\partial (G_N)_{x_2}} = m_w(t) \, \cot \varepsilon \, \cos(\alpha) \, [\frac{t - t_1}{t_2 - t_1}], \tag{5.27}$$
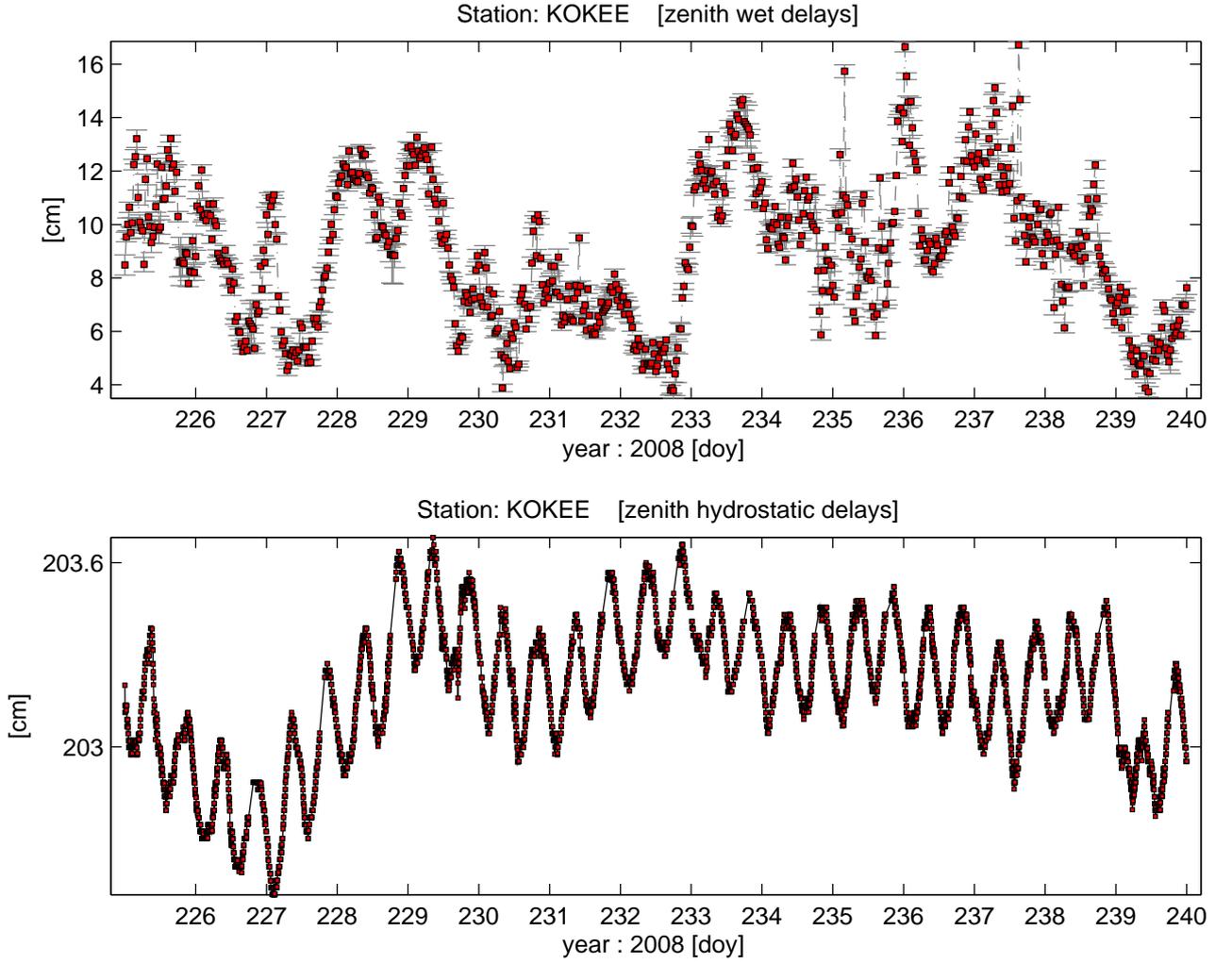
Figure 5.6.: VieVS, ZHD and 30 minutes ZWD estimates of VieVS at Kokee VLBI site - Hawaii, USA during IVS-CONT08. Loose constraints ($0.7 \frac{ps^2}{sec} = 11$ mm after 30 minutes) are applied.

and w.r.t. east gradient CPWLO gives us:

$$\frac{\partial \Delta \tau_{trop}(t)}{\partial (G_E)_{x_1}} = m_w(t) \cot \varepsilon \sin(\alpha) \left[1 - \frac{t - t_1}{t_2 - t_1}\right], \tag{5.28}$$

$$\frac{\partial \Delta \tau_{trop}(t)}{\partial (G_E)_{x_2}} = m_w(t) \cot \varepsilon \sin(\alpha) \left[\frac{t - t_1}{t_2 - t_1}\right]. \tag{5.29}$$

VieVS, CPWLO estimates of north troposphere gradients for 6 hours estimation interval e.g. during IVS-CONT08 are shown in Figure 5.7.
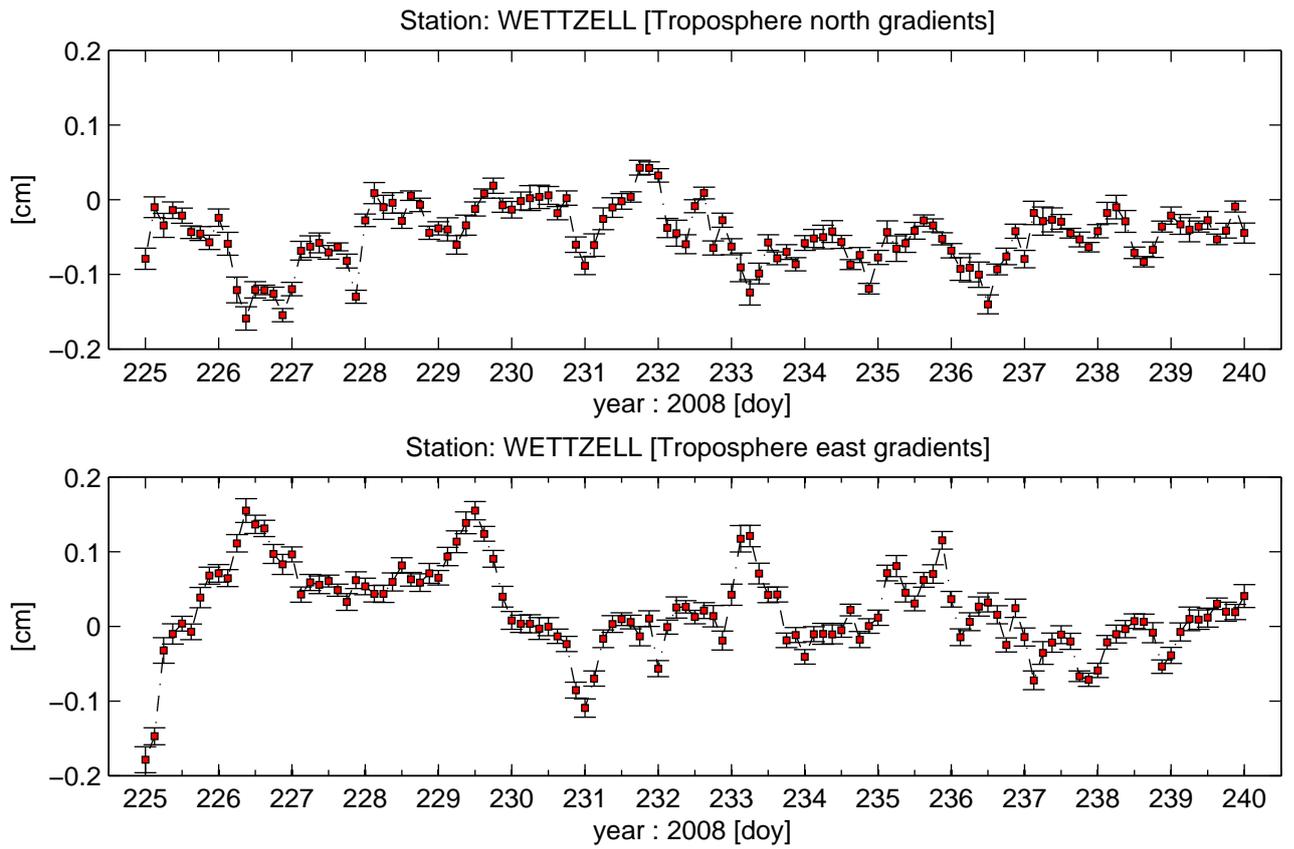
Figure 5.7.: Troposphere north and east gradient estimates of VieVS at Wettzell (Germany), at 6 hour intervals during IVS-CONT08. The a priori north and east gradients are zero. Loose constraints (2 mm/day = 0.5 mm after 6 hours) are applied.

6. Multi-technique comparison of troposphere zenith delays and gradients during IVS-CONT08

In this chapter, VLBI estimates of troposphere zenith total delays (ZTD) and gradients during IVS-CONT08 were compared with those derived from observations with the Global Positioning System (GPS), Doppler Orbitography and Radiopositioning Integrated by Satellite (DORIS), and water vapor radiometers (WVR) co-located with the VLBI radio telescopes. Space geodetic techniques derived ZTD and gradients were also compared to those determined by ray-tracing through the profiles of various Numerical Weather Models (NWM) i.e. the European Centre for Medium-Range Weather Forecasts (ECMWF) (all sites), the Japan Meteorological Agency (JMA) and Cloud Resolving Storm Simulator (CReSS) (Tsukuba in Japan), and the High Resolution Limited Area Model (HIRLAM) (European sites). It should be noted that all comparisons and validation tests presented within this section contribute important information to the planned combination and integration of various observing techniques. In fact, such a multitude of different methods to simultaneously determine troposphere parameters from space geodetic techniques and other sources have never been available for comparison before. Thus, the data taken during the IVS-CONT08 campaign will contribute to combination studies in the framework of the Global Geodetic Observing System (GGOS) (Rummel et al., 2005) of the International Association of Geodesy (IAG).

Troposphere delays are an important error source for space geodetic measurements. Uncertainties in the troposphere delay models propagate into all geodetic estimates, and in particular into the height component of the station positions (Herring, 1986; Davis et al., 1991) due to the high correlations between zenith delays and station heights. The influence of different mapping functions and cut-off elevation angles on geodetic parameters like station heights and baseline lengths has been investigated in several studies, e.g., Davis et al. (1985); Böhm (2004); Böhm

et al. (2006); Tesmer et al. (2007); Steigenberger et al. (2007). Troposphere gradients describe the azimuthally asymmetric delays (Davis et al., 1993). In the analysis of VLBI and GPS observations, they are usually estimated since this improves the accuracy of geodetic estimates. Different studies have been carried out to develop and evaluate troposphere gradient models e.g., Chen and Herring (1997). According to MacMillan (1995), VLBI baseline length repeatabilities can be improved by up to 8 mm if gradients are estimated, thus gradients are important for the realization of terrestrial reference frames (TRFs) and celestial reference frames (CRFs) (MacMillan and Ma, 1997).

Various comparisons of troposphere parameters derived from space geodetic techniques and numerical weather models (NWM) have been performed in order to assess the level of agreement. Behrend et al. (2000, 2002) compared the ZWD derived from the non-hydrostatic numerical weather prediction (NWP) model (MM5) (Cucurull and Vandenberghe, 1999) and a hydrostatic NWP model (HIRLAM) (Cucurull et al., 2000) with the observational results of VLBI, GPS, and a water vapor radiometer (WVR), and they found good agreement for the European geodetic VLBI network during six observing sessions in 1999 in terms of biases, standard deviations, and correlations. Snajdrova et al. (2006) compared ZTD from GPS, VLBI, DORIS, WVR (hydrostatic delays were added), and ECMWF during IVS-CONT02 (a 15 day continuous VLBI campaign in 2002) for co-located sites with VLBI antennas, and the agreement between ZTD from GPS and VLBI was rather good (see Table 6.9); DORIS was fairly compatible with GPS and VLBI, but the agreement for WVR and ECMWF with ZTD estimated from space geodetic techniques was rather low.

6.1. IVS-CONT08 co-located sites, techniques and solutions

IVS-CONT08 was a special campaign of the International VLBI Service for Geodesy and Astrometry (IVS, Schlüter and Behrend (2007)), and it was a follow-on to similar campaigns (IVS-CONT94, -CONT95, -CONT96, -CONT02, and -CONT05). The aim of this campaign was to derive the highest quality geodetic results that VLBI currently can provide. It was a 15 day continuous VLBI observation campaign, carried out during the period August 12 to 26, 2008 with eleven sites on five continents (Figure 6.1).

Unlike previous IVS-CONT campaigns, the IVS-CONT08 sessions were observed from 0 UT
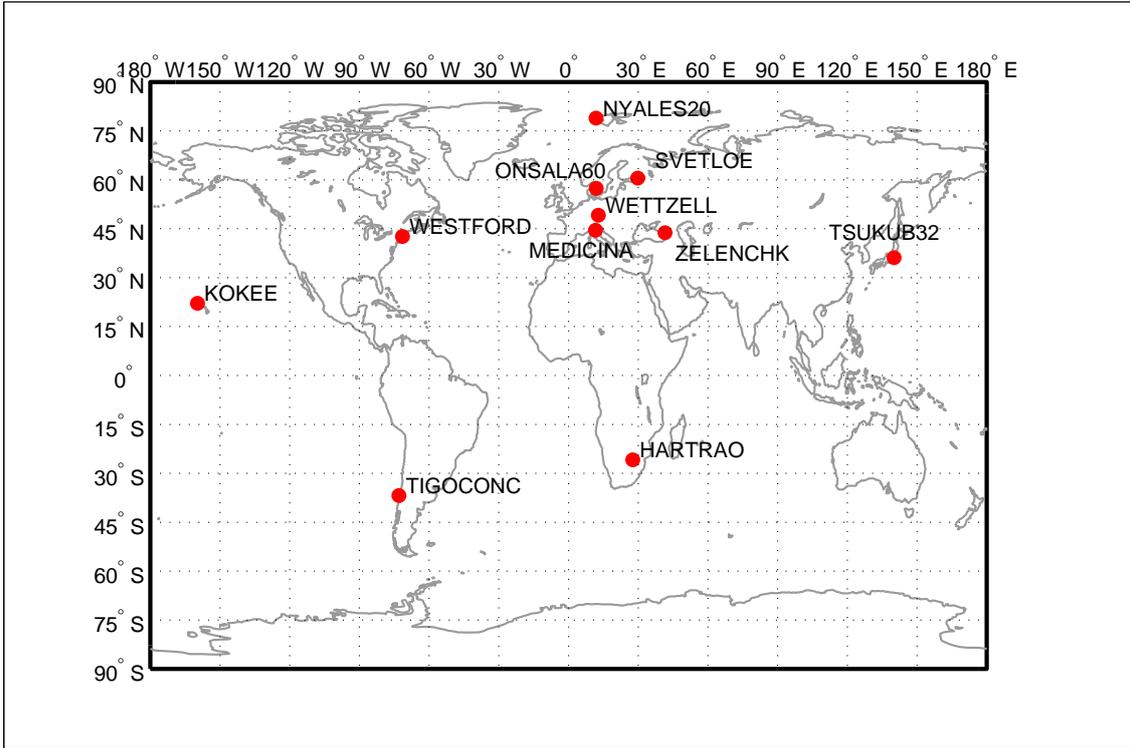
Figure 6.1.: IVS-CONT08 VLBI sites.

to 24 UT, and observational gaps between the single sessions (30 min gaps in the case of IVS-CONT05) were avoided by performing the daily station interrupts at well-coordinated, sequential times for all stations in order not to introduce gaps in the estimated time series, e.g. of Earth orientation parameters (Schuh and Behrend, 2009).

For all eleven sites of IVS-CONT08, troposphere zenith delays and gradients are available from VLBI and GPS. For three sites (Ny-Ålesund in Norway, Hartebeesthoek in The Republic of South Africa, and Kokee Park on Hawaii, U.S.A.) also troposphere estimates from DORIS were available. Profiles through NWM were used to compute zenith total delays and to estimate gradients. When comparing ZTD of different techniques, ZHD computed from surface pressure values were added to the ZWD of the WVR and HIRLAM. In Table 6.1 the acronyms of GPS antennas, DORIS beacons, and WVR names at VLBI co-location sites are listed.

Table 6.1.: Geodetic instruments co-located at the VLBI sites during the IVS-CONT08 campaign.

VLBI Station	Latitudes (°)	IGS acronym	IDS acronym	WVR name
Ny-Ålesund	78.93	NYA1 (CODE + IGS)	SPJB	-
		NYAL (CODE only)		
Svetloe	60.53	SVTL (CODE + IGS)	-	-

Onsala	57.40	ONSA (CODE + IGS)	-		ASTRID
Wettzell	49.14	WTZR (CODE + IGS)	-		RADIOMETRIX
		WTZA (IGS only)			
		WTZJ (IGS only)			
Medicina	44.52	MEDI (CODE + IGS)	-		-
Zelenchukskaya	43.79	ZECK (IGS only)	-		-
Westford	42.61	WES2 (CODE + IGS)	-		-
Tsukuba	36.10	TSKB (CODE only)	-		ROBS
		TSK2 (IGS only)			
Kokee Park	22.13	KOKB (CODE + IGS)	KOLB		-
Hartebeesthoek	-25.89	HRAO (CODE + IGS)	HBMB		-
		HARB (CODE only)			
Tigo Concepcion	-36.84	CONZ (CODE + IGS)	-		-

Table 6.2 shows the ITRF2005 (Altamimi et al., 2007) ellipsoidal heights of the VLBI, GPS, DORIS and WVR reference points as well as the GPS antenna reference point (ARP) eccentricity in the radial direction (the radial distance from the geodetic marker to the phase center of the GPS antenna). GPS ARP eccentricities in radial direction were added to the heights of the GPS reference points when calculating the troposphere ties. In Table 6.2 some of the heights taken from the log file of the stations because not available in ITRF2005. Antenna reference point eccentricities are provided from the station log files at the IGS web sites.

Table 6.2.: ITRF2005 ellipsoidal heights of the co-located VLBI, GPS, and DORIS antennas, and WVR involved in IVS-CONT08. Heights taken from the log file of the stations because not available in ITRF2005. Antenna reference point eccentricities are provided in the station log files at the IGS web site.

VLBI Station	Country	VLBI height (m)	GPS height (m) + up eccentricity (m)	WVR height (m)	DORIS height (m)
Ny-Ålesund	Norway	87.30	84.18 + 0.00 (NYA1)	-	52.60 (SPJB)
			78.45 + 5.22 (NYAL)		
Svetloe	Russia	86.01	77.13 + 0.03	-	-
Onsala60	Sweden	59.28	45.56 + 1.00	46.57	-
Wettzell	Germany	669.13	666.03 + 0.07 (WTZR)	667.56	-
			665.92 + 0.08 (WTZJ)		
			665.91 + 0.07 (WTZA)		
Medicina	Italy	67.17	50.04 + 0.00	-	-
Zelenchukskaya	Russia	1175.43	1167.27 + 0.05	-	-

Westford	USA	86.77	85.02 + 0.00	-	-
Tsukuba	Japan	84.72	67.25 + 0.00 (TSKB)	25.20	-
			70.35 + 0.00 (TSK2)		
Kokee Park	USA	1176.60	1167.37 + 0.06	-	1166.98 (KOLB)
Hartebeesthoek	South Africa	1416.12	1414.16 + 0.08 (HRAO)	-	1560.00 (HBMB)
			1558.09 + 3.05 (HARB)		
Tigo Concepcion	Chile	170.95	180.69 + 0.06	-	-

6.1.1. Space geodetic solutions

VLBI-Vienna VLBI Software: For the analysis of the VLBI observations carried out during IVS-CONT08, the Vienna VLBI Software (VieVS, Böhm et al. (2010)) was used. No cut-off elevation angle or any down weighting of low elevation observations was applied (in IVS-CONT08 no VLBI observation was scheduled and observed below $5°$ elevation and all observations were included in the analysis). The zenith hydrostatic delays were determined from local surface pressure measurements (Saastamoinen, 1972, 1973; Davis et al., 1985), whereas the zenith wet delays were estimated in the LS adjustment as continuous piece-wise linear offsets (CPWLO) at 30 minutes time intervals. In both cases - hydrostatic and wet - the Vienna Mapping Functions 1 (VMF1, Böhm et al. (2006)) were used. Station coordinates were estimated applying no-net-translation (NNT) and no-net-rotation (NNR) condition equations with a priori coordinates from ITRF2005 catalogue (Altamimi et al., 2007), except for the antenna Zelenchukskaya which is not available in ITRF2005. Source coordinates were fixed to ICRF2 (Fey et al., 2009), and atmospheric loading (Petrov and Boy, 2004) as well as tidal ocean loading based on the ocean model FES2004 (Lyard et al., 2006) were introduced a priori. Nutation offsets were estimated once per day in addition to the IAU2000A model plus $IERS\ 05\ C04$ values (Gambis, 2004; Bizouard and Gambis, 2009), and polar motion as well as the Earth's phase of rotation (UT1-UTC) were estimated once per day in addition to the IERS 05 C04 values and the ocean tidal terms as recommended by the IERS Conventions 2003 (McCarthy and Petit, 2004). The estimation interval was 60 minutes for the clocks, 30 minutes for the ZWD and 120 minutes for troposphere gradients. Loose constraints for clocks (0.5 ps^2/s equals to 13 mm after 60 minutes), ZWD (0.7 ps^2/sec equals to 9 mm after 30 minutes) and troposphere gradients (2 mm/day equals to 0.17 mm after 2 hours) were introduced. In addition to the CPWLO for the clocks, a rate and a quadratic term was estimated.

VLBI-International VLBI Service for Geodesy and Astrometry (VLBI-IVS): Like previous IVS troposphere products (Heinkelmann et al., 2007), the combination of troposphere parameters during the 15 day IVS-CONT08 campaign is based on final ZTD and gradient time series by individual groups (and not carried out at the normal equation level). The VLBI-IVS series is a weighted linear combination of the estimates provided by ten IVS Analysis Centers (see Heinkelmann et al. (2011)). It is important to note here that the solution with the Vienna VLBI Software was also part of the IVS combination which was carried out at Deutsches Geodätisches Forschungsinstitut. However, we want to keep both solutions in order to assess the difference between an individual and the combined solution compared to other techniques. Also, it should be noted that the parametrization and the models are not homogeneous for all submissions that were used in the combination. After manual outlier exclusion, the weights for each IVS Analysis Center and parameter (zenith delays, horizontal gradients) were obtained by variance component estimation using the iterative algorithm of Förstner (1979) as outlined in Koch (1997). The details of the submissions, combination procedure and a quality assessment are presented by Heinkelmann et al. (2011)).

DORIS- Institut Géographique National (DORIS-IGN): For the DORIS data analysis, the GIPSY-OASIS software package developed at JPL and modified at IGN (Willis et al., 2010) was used. Instead of the results from the regular IGN solution (ignwd08) submitted to the International DORIS Service (IDS) (Willis et al., 2010), a specific study was performed by using the VMF1 and also daily estimates of horizontal troposphere gradients, following some initial tests of consistency with GPS (Willis et al., 2010). A cut-off elevation angle of 10° was used, as Jason-2 DORIS data were not considered yet in this investigation and as the older DORIS satellites do not provide a large amount of data below this elevation angle. Consequently, during IVS-CONT08, only 4 DORIS satellites were used (Envisat, SPOT-2, SPOT-4 and SPOT-5), all having a sun-synchronous and almost polar orbit. DORIS data were processed in daily batches using a filter approach. Zenith troposphere parameters were estimated at the start of passes, and only if the previous reset was not within 20 minutes. This solution is as close as possible to the IERS Conventions 2003 (McCarthy and Petit, 2004), and it also includes the most recent improvement in DORIS data analysis, in particular in terms of solar radiation pressure modelling (Gobinddass et al., 2009) as well as in terms of atmospheric drag parametrization (Gobinddass et al., 2010). Station coordinates were fixed to their ign09d02 values. This frame is based on the ignwd08 time series, it provides coordinates and velocities for all stations, and it is aligned to ITRF2005 (Willis et al., 2010b). Discontinuities in station coordinates were also properly

handled using information contained in DPOD2005 (Willis et al., 2010).

GPS-International GNSS Service (GPS-IGS): This ZTD product of the IGS (Byun and Bar-Server, 2009) was estimated by using the precise point positioning (PPP) technique as defined in Zumberge et al. (1997). The Earth orientation parameters, orbits, and clocks were fixed to the IGS final combined products. The analyses were carried out with the software GIPSY-OASIS for 24 hour data intervals (Webb and Zumberge, 1993). A cut-off elevation angle of 7° was introduced, and the Niell mapping functions (hydrostatic and wet) (NMF; Niell (1996)) were used. A priori hydrostatic and wet delays were applied based on station altitude (2.3 m at sea level, and 0.1 m, respectively). The estimated parameters were receiver clocks (modelled as white noise), station positions (constant), zenith wet delays (random walk with variance of 3 cm/h, loose) every 5 minutes, atmospheric gradients (random walk with variance of 0.3 cm/h, loose), and phase biases (white noise). The formal errors of the new ZTD product are about 1.5 to 5 mm. However, they are biased by systematic errors in the combined GPS orbits and clocks, as concluded by Byun and Bar-Server (2009).

GPS-Center for Orbit Determination in Europe (GPS-CODE): The Center for Orbit Determination in Europe (CODE, Dach et al. (2009)) is a cooperation of the Astronomical Institute of the University of Bern (AIUB), the Swiss Federal Office of Topography (swisstopo), the German Federal Agency for Cartography and Geodesy (BKG), and the Institut für Astronomische und Physikalische Geodäsie of the Technische Universität München (IAPG/TUM). CODE is one of the global IGS Analysis Centers. The solution used in this paper originated from the CODE contribution to the first IGS reprocessing campaign (Steigenberger et al., 2007). It is based on a global network of 244 GPS tracking stations processed with the current development version 5.1 of the Bernese GPS Software (Dach et al., 2007), and the following models were used: gridded VMF1 and ECMWF a priori delays, non-tidal atmospheric loading model of Petrov and Boy (2004) applied on the observation level, and S1/S2 atmospheric tidal model of Ray and Ponte (2003).

Daily normal equations were combined for the whole IVS-CONT08 time period to get one consistent solution for station coordinates, Earth rotation parameters, troposphere zenith delays and gradients. One set of station coordinates was estimated with an NNT condition of a subset of IGS05 stations w.r.t. the IGS05 reference frame. Troposphere zenith delays and gradients were represented by continuous piece-wise linear (CPWL) functions with a parameter spacing of 2 and 24 hours, respectively. An elevation cut-off angle of 3° and an elevation-dependent

weighting ($\omega = \sin^2 \varepsilon$) were applied.

6.1.2. Water Vapor Radiometer (WVR)

A Water Vapor Radiometer (WVR) infers the wet troposphere delay from measurements of the power of the thermal radiation from the atmosphere at microwave frequencies. Typically two frequencies are used; one more sensitive to water vapor (typically a frequency close to the 22.2 GHz water vapor line) and one more sensitive to liquid water (usually around 30 GHz). By combining these measurements, the respective contributions from water vapor and liquid water to the observed powers can be determined. The water vapor part can then be used to estimate the wet troposphere delay (Elgered, 1993).

During IVS-CONT08 three WVR were operated at VLBI sites: the Astrid radiometer at Onsala (Elgered and Jarlemark, 1998), as well as the Radiometrix radiometers at Wettzell and Tsukuba. The radiometers at Onsala and Wettzell were operated in sky mapping mode, thus providing measurements of the slant wet delays in several different directions. These were used in a LS fit in order to estimate the ZWD and the gradients, using an approach similar to what is presented by Davis et al. (1993). In the LS fit, the ZWD and the gradients were modelled as CPWL functions. The estimation intervals were 30 min for the ZWD and 2 hours for the gradients, i.e. the same as for VLBI-VieVS. The Tsukuba radiometer only measured in the zenith direction, thus only ZWD estimates from this radiometer were available.

One problem with WVR is, that they do not provide reliable results when it is raining. Consequently, all data from rainy periods have been removed (identified by the liquid water content being larger than 0.7 mm). However, it should be noted that since the removal of rain observations was done a posteriori, the remaining observations could still be somewhat affected by rain since all observations were used for example in the tip-curve calibrations. Another problem is, that they cannot measure at low elevation angles ($> 20°$) in order to avoid picking up radiation from the ground. Thus, the gradients estimated from the WVR will be very sensitive to noise, since the effect of gradients is mostly seen for low elevation angles.

6.1.3. Numerical Weather Models (NWM)

European Centre for Medium-Range Weather Forecasts (ECMWF): Operational pressure level data with a 6 hour time resolution were used at 21 levels from 1000 hPa up to 1 hPa (extended up to 136 km with a normal temperature field) with information about the geopotential, temperature, and specific humidity. In particular, four vertical profiles with a horizontal resolution of 0.25° around each station were retrieved and simply the closest profile was used for the determination of the zenith delay. The description of the algorithm for the numerical integration can be found in (Böhm (2004); Appendix). For the calculation of north and east gradients, horizontal refractivity gradients were derived between the four profiles and again used for numerical integration (Böhm and Schuh, 2007).

High Resolution Limited-Area Model (HIRLAM): The High Resolution Limited-Area Model (HIRLAM) is a numerical weather model for short-range forecasting, that is used by several European national meteorological services (Undén et al., 2002). It is a limited area forecasting model that uses ECMWF to provide boundary conditions. Different spatial resolution are available, horizontally 22 km, 11 km or 5 km, and vertically between 16 and 60 levels. The temporal resolution is 6 hours in analysis mode, and predictions are available, for example with 3 and 6 hours resolution.

HIRLAM files with 22 km horizontal resolution and 40 vertical levels and combined analysis and forecast data were used to achieve a temporal resolution of 3 hours. This was done by correcting the 3 hour forecast data by corrections based on a comparison of the 6 hour forecast data with the corresponding analysis data. So-called hybrid-level data of humidity and temperature together with surface pressure and geopotential data were extracted for the four nearest grid points around each station for each 6 hour epoch during IVS-CONT08. Based on these data vertical profiles of pressure, temperature and humidity were constructed for each station and finally vertical integration was used to calculate zenith wet delays.

Japan Meteorological Agency-Kashima Ray-Tracing Tools (JMA-KARAT): At the National Institute of Information and Communications Technology (NICT) the so-called KAshima RAy-tracing Tools (KARAT, Hobiger et al. (2008)) have been developed, which allow one to obtain troposphere slant delays in real-time. Such ray-traced delays can be used as corrections for space geodetic observations (Hobiger et al., 2008) and remote sensing applications. The Japanese Meteorological Agency (JMA) provides a variety of weather models, whereas the meso-scale 4D-

Var model (Meso-scale Analysis Data, MANAL, Ishikawa (2001)) with its horizontal resolution of about 10 km is usually taken for KARAT processing. This model covers large parts of the East Asian region, including Japan, Korea, Taiwan, and East China. The 3 hour time resolution of the data sets make the appliance of this model for positioning applications feasible.

Cloud Resolving Storm Simulator (CReSS): Other than regional numerical weather models, fine-mesh models allow to study smallest structures in the atmosphere and some models even try to resolve clouds. Thereby, the model space is limited to a few hundred kilometers, which requires some modifications of the ray-tracing code (Hobiger et al., 2010), in order to ensure that rays are not leaving the model domain laterally. Dedicated model runs of the Cloud Resolving Storm Simulator (CReSS; Tsuboki and Sakakibara (2002)) at the Japanese National Research Institute for Earth Science and Disaster Prevention (NIED) provided 1 km fine-mesh model data with a temporal resolution of one hour during the IVS-CONT08 period, which were used for the ray-tracing. Thereby, the CReSS model is embedded within the 10 km JMA MANAL field to ensure that rays at lower elevations are not cut-off due to the spatial limitations of the fine-mesh model.

The gradients of JMA/KARAT and CReSS numerical weather model solutions were calculated as follows: The mean ray-traced slant delays, one for each elevation angle, were calculated from $3°$ to $90°$ elevation angle for the case of JMA/KARAT and $4°$ to $90°$ for the case of CReSS. I.e., for each elevation angle the mean values over the 360 ray-traced slant delays (every degree in azimuth) were determined, which were then subtracted from the individual ray-traced slant delays at all azimuths and elevation angles. The north and east gradients every 3 hours for JMA/KARAT and every hour for CReSS were estimated by a classical LS adjustment fitting the gradient model suggested by MacMillan (1995).

6.2. Agreement criteria for the comparisons and troposphere ties

We applied basic statistics techniques to assess the agreement between the various estimates of ZTD and gradients. Mean biases of the differences between time series, the standard deviations as well as the Pearson correlation coefficients were used. As statistical test for the correlation coefficients, p-values with a critical value of 0.05 were computed. Strictly speaking, the p-value is the probability of making a Type 1 error (the error of rejecting a null hypothesis when it

is actually true) where a null hypothesis is formed with no correlation between two data sets (Schervish, 1996).

Before the comparisons "troposphere ties" were introduced with respect to a reference height, which was chosen as the height of the VLBI reference point. The atmosphere in the layer between two instruments causes biases of the troposphere ZTD which can be called "troposphere ties". Troposphere tie corrections were introduced to account for the height differences between the antennas of geodetic techniques at the co-located sites before determining the difference ($\triangle$), and they were derived as the sum of the hydrostatic (Saastamoinen, 1972, 1973) and the wet part (Brunner and Rüeger, 1992), as shown in Equations (6.1) to (6.3).

$$p = p_0 (1 - \frac{\gamma(H - H_0)}{T_0})^{\frac{g}{\gamma R_L}}, \tag{6.1}$$

$$\triangle ZHD = \frac{0.0022768(p - p_0)}{1 - 0.00266 \cos{(2\varphi_0)} - 0.28 * 10^{-6} H_0}, \tag{6.2}$$

$$\triangle ZWD = \frac{-2.789\, e_0}{T_0^2}(\frac{5383}{T_0} - 0.7803)\gamma(H - H_0), \tag{6.3}$$

H_0 denotes the reference height (in our case the height of the VLBI reference point) in meters. The parameters e_0, p_0, and T_0 are the water vapor pressure in hPa, total pressure in hPa, and temperature in Kelvin, at the reference height, and they are derived from data of the ECMWF; H and p are the height and total pressure at the co-located site. The other parameters are the average temperature lapse rate $\gamma = -0.0065\ Km^{-1}$, the gravity g in ms^{-2} at the site, and $R_L \approx 287.058\ m^2 s^{-2} K^{-1}$ is the specific gas constant.

In Table 3, the height differences between VLBI, GPS, DORIS antennas as well as WVR are shown. The troposphere ZTD ties were calculated at each common epoch from the Equations (6.1) to (6.3) based on the meteorological parameters e_0, p_0, T_0 and from the ECMWF, interpolated linearly to the ZTD epochs of the corresponding techniques. Since the variability of the ZTD ties is significant - especially for the sites where the weather is humid - we subtracted the ZTD ties calculated for each common epoch from the ZTD of the techniques before comparisons. In Figure 6.2, the troposphere ties between the GPS antenna TSKB and the VLBI antenna TSUKUB32 during IVS-CONT08 are shown. Red and black dotted lines illustrate total and hydrostatic ties, respectively, and the negative sign of the ties is due to the fact that the lower GPS antenna TSKB has more troposphere above the station than the VLBI antenna TSUKUB32. As can be seen in Figure 6.2, the ZHD ties vary only slightly around the value of -4.5 mm at Tsukuba within the 15 days, but after adding the ZWD ties, the ZTD ties have significantly more variability, which is due to the fact that the atmosphere at Tsukuba is very

humid in August. In Tables 6.3, 6.4, and 6.5, the mean ZTD, ZHD, and ZWD ties of the whole
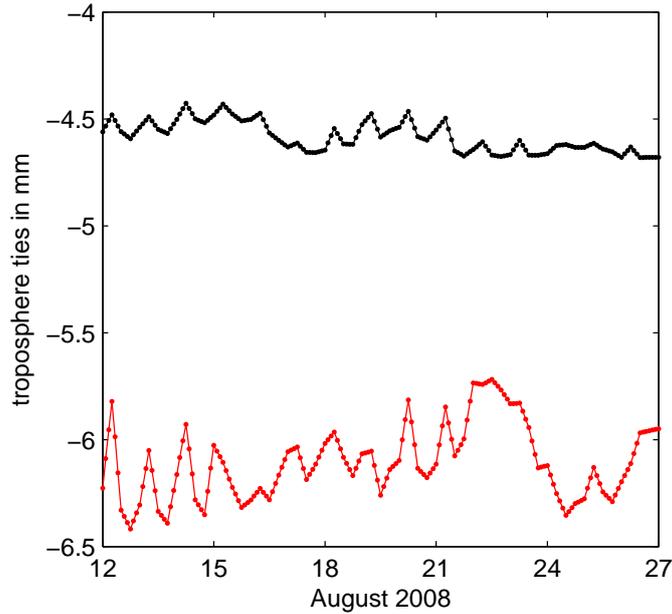
Figure 6.2.: Troposphere ties between the GPS antenna TSKB and the VLBI antenna TSUKUB32 during IVS-CONT08, calculated for all common epochs. Red and black dotted lines illustrate total and hydrostatic ties, respectively.

IVS-CONT08 duration are shown. The ZHD ties of the WVR are zero since the ZHD from VLBI were used (Table 6.5).

The mean ZTD biases between the VLBI antennas and the DORIS beacons at Ny-Ålesund ($H_{VLBI} - H_{DORIS} = 34.70$ m) and at Hartebeesthoek ($H_{VLBI} - H_{DORIS} = -143.88$ m) were reduced to 0.79 mm (from -9.98 mm) and to 4.62 mm (from 41.80 mm), respectively, after introducing the mean troposphere ties. At the IGS site HARB ($H_{VLBI} - H_{GPS} = -145.02$ m) the mean ZTD bias of 37.52 mm was reduced to 0.14 mm after introducing the ZTD tie (37.39 mm), whereas at the DORIS co-located site at Kokee Park ($H_{VLBI} - H_{DORIS} = 9.62$ m) the mean bias increased from 2.32 mm to 5.16 mm after introducing the mean troposphere tie (-2.84 mm); however, this difference is comparably small. It should also be mentioned here that the distances between VLBI antennas and the DORIS beacons are rather large so that the DORIS signals (in particular at 2 GHz) do not disturb the VLBI observations. This can also be a reason for the worse agreement.

Table 6.3.: Height differences and troposphere ties between the co-located VLBI and GPS antennas involved in IVS-CONT08.

72

VLBI Station	VLBI-GPS height difference (m)	Mean GPS troposphere ties ZTD=ZHD+ZWD (mm)
Ny-Ålesund	3.12 (NYA1)	-0.97=-0.88+(-0.09)
	3.63 (NYAL)	-1.13=-1.02+(-0.11)
Svetloe	8.85	-2.92=-2.38+(-0.54)
Onsala60	12.72	-4.16=-3.43+(-0.73)
Wettzell	3.03 (WTZR)	-0.94=-0.79+(-0.15)
	3.13 (WTZJ)	-0.97=-0.82+(-0.15)
	3.15 (WTZA)	-0.97=-0.82+(-0.16)
Medicina	17.13	-5.52 = -4.51+(-1.01)
Zelenchukskaya	8.11	-2.35=-1.91+(-0.44)
Westford	1.75	-0.56 = -0.46+(-0.10)
Tsukuba	17.47 (TSKB)	-6.11=-4.58+(-1.52)
	14.37 (TSK2)	-5.02=-3.77+(-1.25)
Kokee Park	9.17	-2.72 = -2.21+(-0.52)
Hartebeesthoek	1.88 (HRAO)	-0.51=-0.46+(-0.05)
	-145.02 (HARB)	37.39=33.40+3.99
Tigo Concepcion	-9.80	3.07=2.66+0.40

Table 6.4.: Height differences and troposphere ties between the co-located VLBI and DORIS antennas involved in IVS-CONT08.

VLBI Station	VLBI-DORIS height difference (m)	Mean DORIS troposphere ties ZTD=ZHD+ZWD (mm)
Ny-Ålesund	34.70	-10.77=-9.78+(-0.99)
Kokee Park	9.62	-2.84=-2.30+(-0.54)
Hartebeesthoek	-143.88	37.18=33.19+(3.99)

Table 6.5.: Height differences and troposphere ties between the co-located VLBI and WVR involved in IVS-CONT08.

VLBI Station	VLBI-WVR height difference (m)	Mean WVR troposphere ties ZTD=ZHD+ZWD (mm)
Onsala60	$\sim$ 12.71	-0.73=0.00+(-0.73)
Wettzell	$\sim$ 1.57	-0.08=0.00+(-0.08)
Tsukuba	59.52	-5.30=0.00+(-5.30)

Data types and epochs for comparisons

In order to ensure a consistent comparison similar geophysical models were used for the analysis of space geodetic data, whereas the parametrization for the LS adjustment of the space geodetic techniques was optimized for each solution. In Table 6.6, an overview of the solutions, types of the estimates, and intervals for both zenith delays and gradients are listed. GPS-IGS and HIRLAM solutions do not provide gradients. All gradients from the techniques except WVR are total gradients.

Table 6.6.: Summary of the data used for the comparisons

Technique	Zenith total/wet delay	Estimation interval of zenith delays	Estimation interval of gradients
VLBI-VieVS	ZWD, ZTD	30 minutes	2 hours (total gradients)
VLBI-IVS	ZWD, ZTD	1 hour	1 hour (total gradients)
GPS-IGS	ZTD	5 minutes	-
GPS-CODE	ZTD	2 hours	1 day (total gradients)
DORIS-IGN	ZTD	per satellite pass	1 day (total gradients)
WVR	ZWD	30 minutes	2 hours (wet gradients)
ECMWF	ZWD, ZTD	6 hours	6 hours (total gradients)
JMA-KARAT	ZTD,	3 hours	3 hours (total gradients)
CreSS	ZTD	1 hour	1 hour (total gradients)
HIRLAM	ZWD	3 hours	-

The total number of common epochs of ZTD (first line) and of gradients (second line) between VieVS and the other techniques during IVS-CONT08 can be found in Table 6.7. The reliability of the mean biases, standard deviations, and correlations increases and the vulnerability to outliers decreases in direct proportional to the total number of ZTD and gradients available (degrees of freedom). Due to the small number of gradients provided by CODE and DORIS solutions (16 estimates at maximum for the whole 15 days duration) biases, standard deviations, and correlations involving these solutions have to be interpreted with care.

The estimates from DORIS correspond to distinct epochs of actual measurements during the DORIS satellite passes. For the whole IVS-CONT08 campaign, the DORIS station at Ny-Ålesund (SPJB) provided 243 ZTD with a gap (no observation) every day between 2 to 5 UT. The DORIS station KOLB at KOKEE Park provided in total 82 ZTD, and each day is observed in two separate intervals between 7 to 10 and 20 to 23 UT. HBMB at Hartebeesthoek provided in total 77 ZTD in IVS-CONT08 observed between 6 to 10 and 19 to 22 UT. In a first step,

the zenith delays from DORIS were linearly interpolated to adjacent 2 hour intervals at UT integer hours. This interpolation was only performed for those integer hours when the time differences between the last observation before and the first observation after the integer hours is less than 6 hours. This is not optimum for DORIS ZTD, as DORIS data are scarce and DORIS troposphere solutions are then provided using some interpolation. However, in this study, the current capability of all techniques was tested, so it is important to know the performances of all techniques over the complete period of observations and not only during DORIS satellite passes.

Table 6.7.: ZTD (first line) and troposphere gradients (second line) common epochs of VieVS with the other techniques during IVS-CONT08.

Site	IVS	IGS	CODE	DORIS	WVR	ECMWF	HIRLAM
Ny-Ålesund	357	714 (NYA1)	180 (NYA1)	149	-	60	120
	179	-	16 (NYA1)	15	-	60	-
Svetloe	360	672	181	-	-	60	121
	180	-	16	-	-	60	-
Onsala60	360	623	181	-	593	60	121
	180	-	16	-	181	60	-
Wettzell	360	662 (WTZR)	181 (WTZR)	-	548	60	121
		616 (WTZJ)					
		670 (WTZA)					
Medicina	360	720	181	-	-	60	121
	180	-	16	-	-	60	-
Zelenchukskaya	326	552	-	-	-	55	110
	163	-	-	-	-	55	-
Westford	360	672	169	-	-	60	-
	180	-	15	-	-	60	-
Tsukuba	360	719 (TSK2)	181 (TSKB)	-	560	60	-
	180	-	16 (TSKB)	-	-	60	-
Kokee Park	360	720	181	66	-	60	-
	180	-	16	15	-	60	-
Hartebeesthoek	360	720 (HRAO)	181 (HRAO)	60	-	60	-
	180	-	16 (HRAO)	15	-	60	-
Tigo Concepcion	242	192	122	-	-	39	-
	121	-	11	-	-	39	-

6.3. Intra-technique comparisons of ZTD

The intra-technique biases at the co-located sites between VieVS and the IVS combined solution are between -1.6 mm and 1.9 mm with standard deviations between 2.3 mm (Wettzell) and 5.7 mm (Zelenchukskaya) (Table 6.8). This is similar to what is found for the differences between the CODE and the IGS solution, where the standard deviations are between 2.4 mm (Hartebeesthoek, HRAO) and 4.9 mm (Medicina). The biases between the GPS solutions are slightly larger with values between -4.5 (Wettzell, WTZR) and 2.9 (Medicina) mm, but it has to be clearly stated that the VieVS series is part of the IVS combined solution, whereas the IGS Kalman filter solution differs from the CODE solution in many aspects, e.g. PPP vs. network approach, NMF vs. VMF1, or different frames.

At Wettzell, we have IGS ZTD solutions for three different receivers from three different manufacturers which are only separated by a few meters and thus observe the same troposphere (WTZA, WTZJ, and WTZR). The mean biases between the ZTD series are -1.1 mm (WTZA - WTZJ) or smaller, and all standard deviations are at about 1.5 mm, which is significantly smaller than the standard deviation between the IGS and the CODE solution for WTZR (3.4 mm). Similar results are found at Ny-Ålesund, where we have two solutions from CODE (NYAL and NYA1) with no bias and a standard deviation of 1.0 mm. The standard deviation between the ZTD at NYA1 from CODE and IGS is 2.7 mm. This discrepancy shows that the choice of analysis strategies is critical for the estimation of ZTD whereas the hardware (antenna, receiver) or effects like multipath or antenna phase center variations only add a smaller fraction to the total uncertainty of ZTD. This is also confirmed by the fact that at many sites the standard deviations between IGS and CODE is nearly as large as the standard deviations between VLBI and GPS solutions.

At Tsukuba, the best agreement of two weather models is between JMA and CReSS. This can be expected because the high-resolution CReSS model is embedded in and initialized with the JMA model. On the other hand, this agreement is slightly worse than between ECMWF and HIRLAM for European stations, but it has to be mentioned, that the latter stations are not as humid as Tsukuba. More details about biases and standard deviations can be found in Table 6.8.

In order to find out the amount of shared variances (degree of linear relationship) between the

estimates/products of each pair of techniques, correlation coefficients were calculated. Correlation coefficients with $p > 0.05$ are assumed to be statistically insignificant. The intra-technique correlations of ZTD between VieVS and the IVS combined solution are between 0.96 and 1.00 (Table 6.12), between CODE and the IGS solution between 0.99 and 1.00, and between ECMWF and HIRLAM they range from 0.55 (Zelenchukskaya) to 0.96 (Ny-Ålesund, and Svetloe). The correlations between the weather models ECMWF, JMA, and CReSS at Tsukuba are at about 0.9. The correlations of ZTD between VieVS and other solutions (and their p-values in parentheses) are shown in Table 6.12.

6.4. Inter-technique comparisons of ZTD

As an example Figure 6.3 show the ZTD at Hartebeesthoek, Wettzell, and Onsala during IVS-CONT08. Inter-technique ZTD biases and standard deviations w.r.t. the VieVS and the CODE solutions can be found in Table 6.8 and the mean values are also shown in Figure 6.4. The biases between different space geodetic techniques are mostly smaller than 5 mm after the application of troposphere ties, with the largest value remaining between the IVS combined and the CODE solution at Medicina (Italy) with 6.2 mm. In terms of standard deviation, the best inter space geodetic technique agreement of ZTD is found between the IVS combined solution and the IGS Kalman filter solution, in particular at Ny-Ålesund with 2.7 mm. Slightly worse is the agreement between VieVS solution and the IGS Kalman filter solution, between CODE and the IVS combined solution, and between CODE and VieVS.

Generally, for all sites the median standard deviation between ZTD from GPS and VLBI is about 4 to 5 mm. The agreement of ZTD from DORIS with those from GPS and VLBI is rather good at Ny-Ålesund with a standard deviation of about 6 mm (there is a large number of common epochs), but it is worse at Kokee Park and Hartebeesthoek with more than 12 mm.

As far as the standard deviations of ZTD differences WVR and the space geodetic techniques are concerned, the best agreement can be found at Onsala with about 5 mm. This is significantly better than for Wettzell ($\sim$ 11 mm) or Tsukuba ($\sim$ 20 mm). Also the biases of ZTD from WVR are larger at Tsukuba. It should be noted, that during IVS-CONT08 rainy weather contaminated most of the measurements of the WVR (Robs) at Tsukuba although obvious outlier observations due to rain were eliminated.
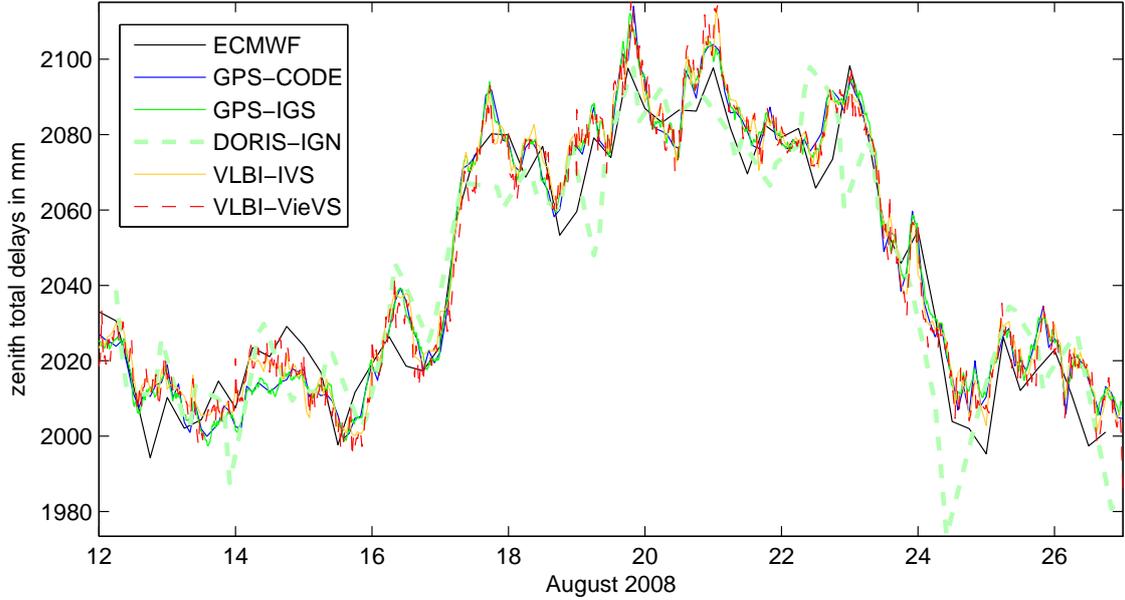
Figure 6.3.: Troposphere ZTD of the co-located site HartRAO during IVS-CONT08. Troposphere ZTD of the other co-located sites that contribute IVS-CONT08 can be found in Appendix A.6.

The standard deviations of ZTD from numerical weather models compared to ZTD from space geodetic techniques are between 6 mm at Ny-Ålesund and $\sim$ 20 mm at Tsukuba. It seems that CReSS data is closer to the space geodetic results than the JMA. The CReSS model sometimes has differences w.r.t. VLBI at 0 UT similar to the JMA model. This comes from the fact that the CReSS model is initialized with the JMA model and needs some time to settle to its own physics. From Table 6.8 no conclusions can be drawn whether ECMWF or HIRLAM agrees better with ZTD from space geodetic techniques, because this varies w.r.t. station and solution.

As a general trend, the standard deviations of the differences between ZTD from the different techniques and NWM decrease with increasing latitude, that is, the minimum standard deviations are at the site Ny-Ålesund (see Table 6.1 for the latitudes). On the other hand, the low latitude sites like Kokee Park and Tsukuba have significantly larger standard deviations of ZTD. Most of the correlations between the ZTD of different techniques are larger than 0.9 and statistically significant .

78

Table 6.8.: Mean biases and standard deviations. [1]: NYA1, [2]: NYAL, [3]: WTZR, [4]: TSKB, [5]: TSK2, [6]: HRAO.

	Ny-Ålesund	Svetloe	Onsala	Wettzell	Medicina	Tsukuba	Kokee	HartRAO	Tigoconc
VLBI/VieVS-VLBI/IVS	−1.6±2.8	0.3±3.3	−0.4±2.6	−0.4±2.3	−1.0±4.7	−0.1±4.8	−0.2±4.7	−0.7±3.2	−1.0±4.0
VLBI/VieVS-GPS/IGS	−2.0±3.9[1]	1.2±5.5	1.0±4.5	2.2±4.1[3]	2.3±7.0	−6.0±11.1[4]	0.8±8.3	−0.2±4.7[6]	−4.0±5.1
VLBI/VieVS-GPS/CODE	0.0±3.9[2]	1.0±6.1	3.1±5.0	−2.1±4.6[3]	5.1±7.9	1.4±11.6[5]	1.9±9.5	0.1±5.2[6]	−4.5±5.0
VLBI/VieVS-DORIS/IGN	0.8±6.4	-	-	-	-	-	5.2±14.7	4.6±12.7	-
VLBI/VieVS-WVR	-	-	−0.4±5.1	−14.3±10.3	-	−24.8±22.2	-	-	-
VLBI/VieVS-ECMWF	−3.4±6.5	0.9±10.9	3.4±11.2	−2.1±11.8	−2.1±19.8	−0.3±20.2	2.9±18.1	3.0±8.4	0.9±11.2
VLBI/VieVS-JMA/KARAT	-	-	-	-	-	7.8±25.7	-	-	-
VLBI/VieVS-CreSS	-	-	-	-	2.4±18.0	6.0±20.0	-	-	-
VLBI/VieVS-HIRLAM	0.6±11.1	0.8±16.2	6.4±11.0	2.5±10.1	-	-	-	-	-
GPS/CODE-VLBI/IVS	−1.4±2.9[1]	−0.7±5.1	−3.3±4.5	1.8±4.2[3]	−6.2±8.7	−1.5±9.7	−2.0±7.3	−0.9±4.0[6]	2.4±7.3
GPS/CODE-GPS/IGS	−1.9±2.7[1]	0.5±4.1	−2.0±4.0	4.5±3.4[3]	−2.9±4.9	-	−1.0±4.5	−0.2±2.4[6]	1.2±2.6
GPS/CODE-DORIS/IGN	0.7±5.4[1]	-	-	-	-	-	3.2±13.0	4.1±13.1[6]	-
GPS/CODE-WVR	-	-	−3.1±5.7	−12.5±11.6[3]	-	−26.1±20.2	-	-	-
GPS/CODE-ECMWF	−3.4±5.9[1]	0.1±10.6	−0.1±11.1	−0.8±11.5[3]	−8.8±18.4	0.2±20.6	1.9±16.5	2.0±8.3[6]	4.4±9.7
GPS/CODE-JMA/KARAT	-	-	-	-	7.1±20.6	7.1±20.6	-	-	-
GPS/CODE-CreSS	-	-	-	-	5.3±18.9	5.3±18.9	-	-	-
GPS/CODE-HIRLAM	1.2±10.2[1]	0.4±14.6	3.6±9.6	2.5±9.4[3]	−3.2±16.7	-	-	-	-
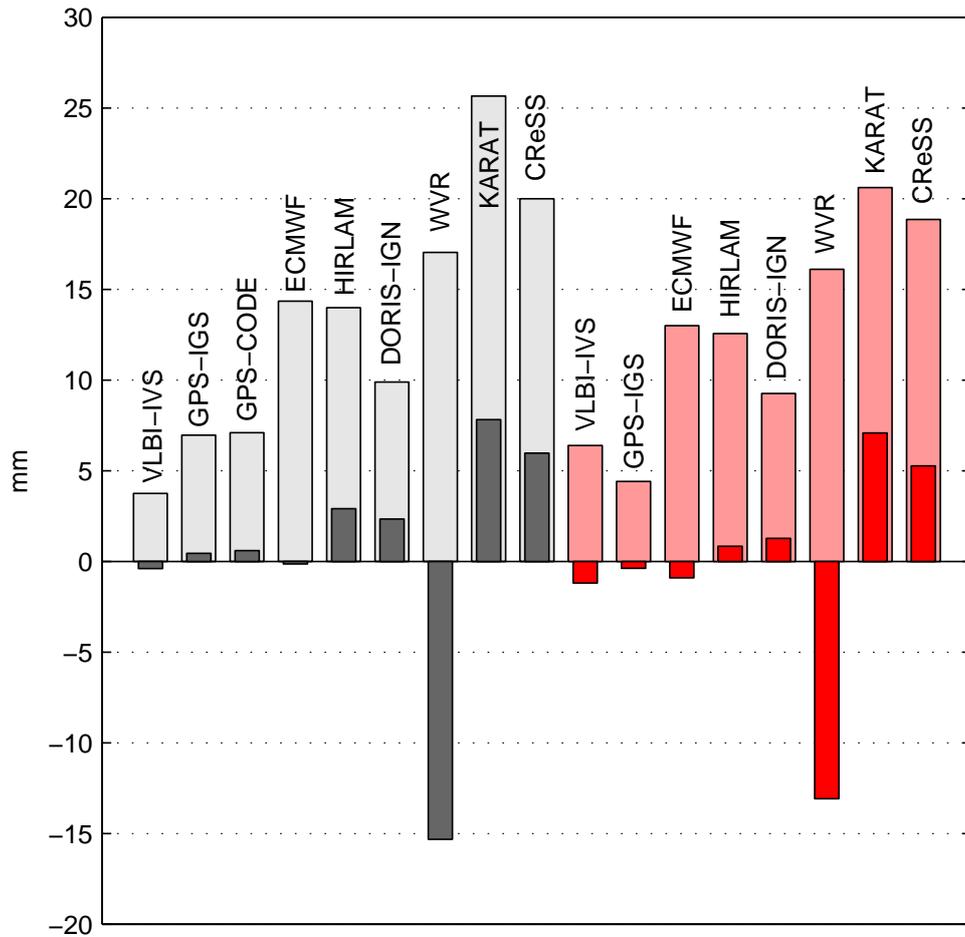
Figure 6.4.: Mean biases and standard deviations of all ZTD during IVS-CONT08 w.r.t. VLBI-VieVS (bias: dark grey, std. dev.: light grey) and GPS-CODE (bias: dark red, std. dev.: light red).

6.5. Comparison with IVS-CONT02

Comparing the level of agreement of ZTD in this study (IVS-CONT08) with the findings for IVS-CONT02 by Snajdrova et al. (2006) the following conclusions can be drawn (see also Table 6.9): the biases between VLBI and GPS decrease by several mm for IVS-CONT08 except for Onsala60 (see Table 6.9). This might be due to a better agreement of the underlying models like the terrestrial reference frames used for the analyses and improved troposphere ties. On the other hand the standard deviations between VLBI and GPS increase for all stations except Hartebeesthoek (South Africa). This is certainly caused by the fact that IVS-CONT08 was observed in August, corresponding to northern hemisphere summer, which is a more humid period for stations in the northern hemisphere compared to October when IVS-CONT02 was observed.

A similar increase in standard deviations for IVS-CONT08 (except for Hartebeesthoek) can be found for the comparison of ZTD between ECMWF and space geodetic techniques, probably caused by the same reason. On the other hand, there is a better agreement between DORIS and GPS/VLBI for IVS-CONT08, which is due to improved DORIS data processing for this investigation.

Table 6.9.: Comparison of mean biases and standard deviations of the ZTD difference vectors from IVS-CONT02 (Snajdrova et al., 2006) and IVS-CONT08 (this study) for the common sites. At those sites, where more than one IGS antenna was situated the following antennas were used for the comparison: NYAL, WTZR, and HRAO. IVS-CONT08 results were derived from GPS-CODE and VLBI-VieVS solutions.

	Ny-Ålesund		Onsala		Wettzell	
	CONT02	CONT08	CONT02	CONT08	CONT02	CONT08
VLBI-GPS	0.1 ± 3.3	0.0 ± 3.9	0.7 ± 4.1	3.1 ± 5.0	-2.1 ± 4.5	-2.1 ± 4.6
VLBI-ECMWF	7.1 ± 4.7	-3.4 ± 6.5	8.1 ± 5.7	3.4 ± 11.2	13.2 ± 8.8	-2.12 ± 11.8
VLBI-DORIS	1.5 ± 7.9	0.8 ± 6.4	-	-	-	-
VLBI-WVR	-	-	-2.8 ± 6.7	-0.4 ± 5.1	-17.2 ± 9.0	-14.3 ± 10.3
GPS-ECMWF	6.6 ± 3.5	-3.8 ± 6.0	7.6 ± 5.5	-0.1 ± 11.1	15.1 ± 7.8	-0.8 ± 11.4
GPS-DORIS	1.2 ± 8.1	0.5 ± 5.2	-	-	-	-
GPS-WVR	-	-	-3.7 ± 5.4	-3.1 ± 5.7	-14.7 ± 8.1	-12.5 ± 11.6
ECMWF-DORIS	-6.8 ± 8.5	4.1 ± 7.7	-	-	-	-
ECMWF-WVR	-	-	-11.7 ± 10.2	-3.1 ± 10.9	-26.2 ± 7.5	-11.9 ± 15.6

	Westford		Kokee		HartRAO	
	CONT02	CONT08	CONT02	CONT08	CONT02	CONT08
VLBI-GPS	-6.5 ± 3.5	-3.7 ± 6.4	-5.7 ± 6.6	1.9 ± 9.5	-3.4 ± 5.8	0.1 ± 5.2
VLBI-ECMWF	-16.2 ± 5.9	-3.8 ± 16.6	-8.8 ± 21.0	2.9 ± 18.1	-4.8 ± 19.4	3.0 ± 8.4
VLBI-DORIS	-	-	-7.2 ± 32.1	5.2 ± 14.7	2.7 ± 14.0	4.6 ± 12.7
GPS-ECMWF	-9.1 ± 7.1	-1.7 ± 14.7	-1.9 ± 17.4	1.9 ± 16.5	-0.3 ± 18.6	2.0 ± 8.3
GPS-DORIS	-	-	2.7 ± 34.7	3.2 ± 13.0	5.5 ± 14.5	4.1 ± 13.1

6.6. Troposphere gradients comparisons

Unlike the ZTD, there are not as many north and east gradient series from the individual techniques available for comparison. We do not have gradients from the IGS Kalman filter solution, nor do we have gradients from HIRLAM or the WVR at Tsukuba. It has to be

stressed again, that the gradients from the WVR at Wettzell and Onsala are wet-only gradients and do not contain hydrostatic parts. All other gradients are gradients of the total delays. As an example, the troposphere north and east gradients at Tsukuba and Wettzell, respectively are shown in Figure 6.5 and 6.6. The best agreement of gradients is found between VieVS and the IVS combined series which was expected because VieVS is part of the IVS combination (Heinkelmann et al., 2007). The gradients provided by CODE have a daily resolution only (one offset estimate from the observations over the 24 hours). Whereas the gradients from VLBI describe the mean asymmetry over two hours (one offset estimate from the observations over 4 hours). Thus, the comparison of the VLBI and GPS (CODE) gradients at the common epochs (at exactly 0:00 UTC) is not so equitable. The biases are as large as 0.5 mm and the standard deviations are mostly in 0.4-0.8 mm. This is pretty big compared to the gradient estimates which are mostly less than 1 mm (see Table 6.10 and 6.11).
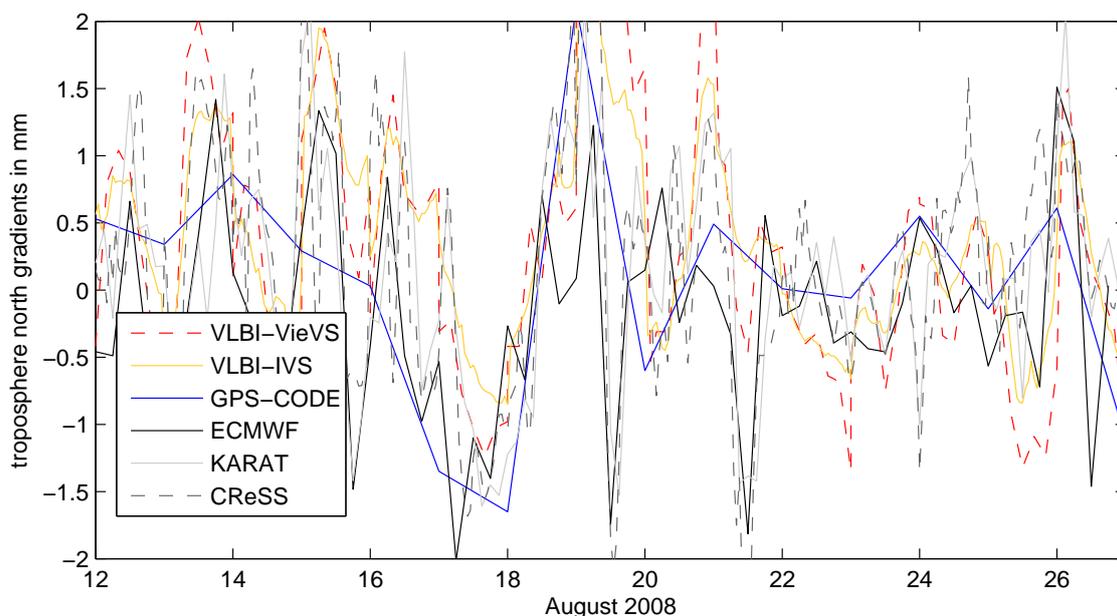
Figure 6.5.: Troposphere north gradients of the co-located site Tsukub32 in Japan during IVS-CONT08. Troposphere north gradients of the other co-located sites that contribute IVS-CONT08 can be found in Appendix A.7.1.

The standard deviations of DORIS gradients w.r.t. gradients from VieVS are rather large, in particular at Hartebeesthoek (South Africa) with 1.8 mm and 0.9 mm in the east and north direction, and at Kokee Park (Hawaii, U.S.A.) with 1.2 mm in east and 0.9 mm in north direction. It can also be noted here, that there is a large north gradient bias of ~ 1 mm for the DORIS station at Hartebeesthoek with respect to VLBI. This could come from the fact that at this high latitude the tracks of the DORIS satellites (all sun-synchronous, as Jason-2 was not used
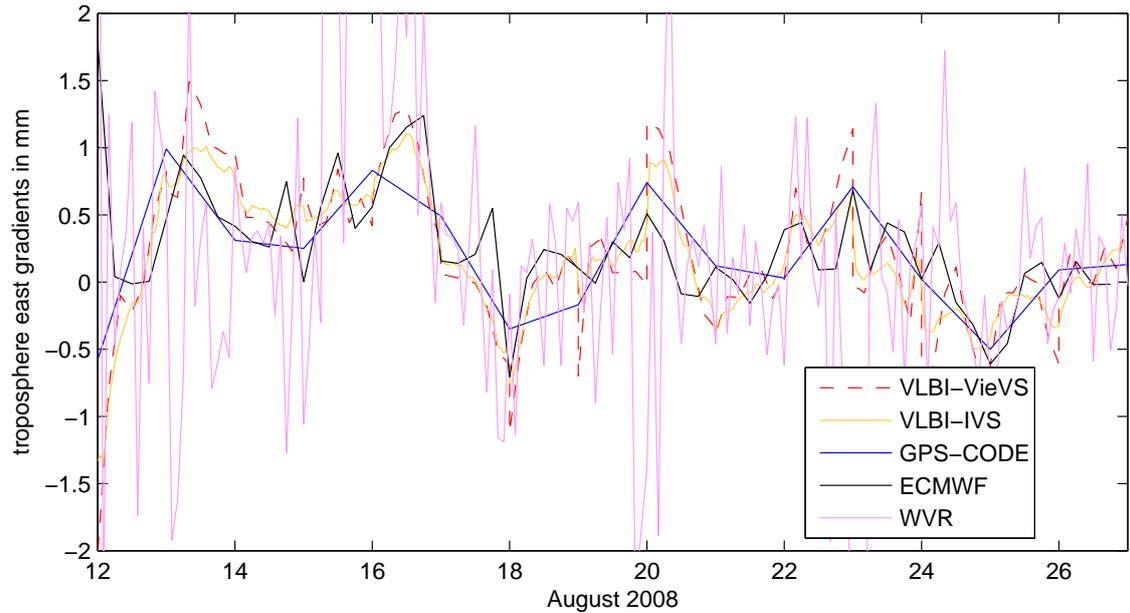
Figure 6.6.: Troposphere east gradients of the co-located site Wettzell in Germany during IVS-CONT08. Troposphere east gradients of the other co-located sites that contribute to IVS-CONT08 can be found in Appendix A.7.2.

here) are mostly east-west oriented, i.e. perpendicular to the north gradient. Willis et al. (2010) see a similar problem for the other stations (equatorial or mid-latitude), when the tracks are north-south oriented and the east-west gradient is only loosely determined. However, since the standard deviation is of about the same size, this bias is not very significant.

There is a large standard deviation of more than 1 mm for the gradients from the WVR at Wettzell, which might be due to a tilting of the instrument. In general the wet gradients from WVR are noisier because they are only derived from slant delays above 20° elevation (Figure 6.6). On the other hand, the biases should be disregarded because they might be caused from the neglected hydrostatic part.

The best intra-NWM agreement of north and east gradients is found between JMA and CReSS, which could be expected because the CReSS model is initialized with the data from the larger JMA model. One has to keep in mind that the gradients from the weather model are a snap-shot of the troposphere at a certain epoch, whereas the gradients from the space geodetic techniques are averaged over a certain period, which is related to the way how the temporal resolution of the gradients is parameterized. The gradients from VLBI are estimated from very sparse spatial sampling, i.e. one direction at a given epoch. Scan lengths are between 20 seconds to a

few minutes (depending on the source flux density) for IVS-CONT08 but there are also several minutes slew times between on-source times. Thus, VLBI scans the sky with only about 25 scans per hour.

In order to find out the amount of shared variances (degree of linear relationship) between the gradients of each pair of techniques, Pearson correlation coefficients were calculated. In Table 6.13, the correlations of gradients between VieVS and the other solutions (and their p-values in parentheses) are shown. Correlation coefficients with $p > 0.05$ are assumed to be statistically insignificant and are written in italic. The correlation coefficients of north and east gradients between VieVS and the IVS combined solutions are above 0.85 except for the east gradient at Hartebeesthoek (0.70), and all are significant. The correlation coefficients between the gradient estimates from VieVS and CODE are mostly below 0.7 and some of them are insignificant.

Table 6.10.: Mean biases and standard deviations of the troposphere east gradient difference vectors between VLBI-VieVS and other solutions for the co-located sites during IVS-CONT08. All the gradients except those derived from WVR (wet gradients) are total gradients. (^{1}) : NYA1, (^{2}): WTZR, (^{3}): TSKB, (^{4}): HRAO.

	Ny-Ålesund	Svetloe	Onsala	Wettzell	Medicina	Tsukuba	Kokee	HartRAO	Tigoconc
VLBI/VieVS-VLBI/IVS	0.0±0.2	0.0±0.2	0.0±0.2	0.0±0.2	0.0±0.2	0.1±0.4	0.0±0.2	−0.1±0.3	0.1±0.3
VLBI/VieVS-GPS/CODE	0.2±0.5(^{1})	0.2±0.5	−0.1±0.5	−0.3±0.6(^{2})	0.0±0.5	0.2±1.1(^{3})	0.1±0.7	0.0±0.5(^{4})	0.1±0.8
VLBI/VieVS-DORIS/IGN	0.2±0.7	-	-	-	-	-	−0.2±1.2	0.2±1.8	-
VLBI/VieVS-WVR	-	-	0.3±0.8	0.0±1.3	-	-	-	-	-
VLBI/VieVS-ECMWF	0.0±0.4	0.2±0.5	0.0±0.4	−0.1±0.6	0.0±0.5	−0.3±0.9	−0.2±0.6	0.1±0.4	0.2±0.5
VLBI/VieVS-JMA/KARAT	-	-	-	-	-	0.1±0.9	-	-	-
VLBI/VieVS-CreSS	-	-	-	-	-	0.1±0.9	-	-	-

Table 6.11.: Mean biases and standard deviations of the troposphere north gradient difference vectors between VLBI-VieVS and other solutions for the co-located sites during IVS-CONT08. All gradients except those derived from WVR (wet gradients) are total gradients. (^{1}): NYA1, (^{2}): WTZR, (^{3}): TSKB, (^{4}): HRAO.

	Ny-Ålesund	Svetloe	Onsala	Wettzell	Medicina	Tsukuba	Kokee	HartRAO	Tigoconc
VLBI/VieVS-VLBI/IVS	0.0±0.2	0.0±0.2	0.0±0.2	0.0±0.2	0.0±0.3	0.0±0.4	0.0±0.3	0.3±0.4	0.0±0.3
VLBI/VieVS-GPS/CODE	0.0±0.4(^{1})	−0.2±0.5	0.3±0.6	−0.1±0.4(^{2})	−0.1±0.8	0.3±1.1(^{3})	0.2±1.1	0.5±0.5(^{4})	0.3±0.5
VLBI/VieVS-DORIS/IGN	0.4±0.7	-	-	-	-	-	−0.3±1.2	1.2±0.9	-
VLBI/VieVS-WVR	-	-	−0.4±0.8	−0.6±1.1	-	-	-	-	-
VLBI/VieVS-ECMWF	0.0±0.4	−0.1±0.5	0.0±0.5	−0.1±0.4	0.0±0.8	0.5±1.0	−0.2±0.8	0.3±0.6	0.3±0.5
VLBI/VieVS-JMA/KARAT	-	-	-	-	-	0.2±1.0	-	-	-
VLBI/VieVS-CreSS	-	-	-	-	-	0.2±1.0	-	-	-

Table 6.12.: Correlation coefficients and their p-values between the ZTD estimates of VLBI-VieVS and other solutions for the co-located sites during IVS-CONT08. Correlations written in italic are statistically insignificant ($p > 0.05$). [1]: NYA1, [2]: WTZR, [3]: HRAO.

	Ny-Ålesund	Svetloe	Onsala	Wettzell	Medicina	Tsukuba	Kokee	HartRAO	Tigoconc
VLBI/VieVS-VLBI/IVS	1.00 (0.00)	1.00 (0.00)	1.00 (0.00)	1.00 (0.00)	0.99 (0.00)	1.00 (0.00)	0.98 (0.00)	1.00 (0.00)	0.99 (0.00)
VLBI/VieVS-GPS/IGS	0.99 (0.00) [1]	0.99 (0.00)	0.99 (0.00)	0.99 (0.00)	0.98 (0.00)	0.98 (0.00)	0.95 (0.00)	0.99 (0.00)	0.99 (0.00)
VLBI/VieVS-GPS/CODE	0.99 (0.00) [1]	0.99 (0.00)	0.98 (0.00)	0.99 (0.00) [2]	0.98 (0.00)	0.98 (0.00)	0.94 (0.00)	0.99 (0.00) [3]	0.99 (0.00)
VLBI/VieVS-DORIS/IGN	0.98 (0.00)	-	-	-	-	-	0.83 (0.00)	0.93 (0.00)	-
VLBI/VieVS-WVR	-	-	0.98 (0.00)	0.97 (0.00)	-	0.98 (0.00)	-	-	-
VLBI/VieVS-ECMWF	0.98 (0.00)	0.96 (0.00)	0.90 (0.00)	0.93 (0.00)	0.84 (0.00)	0.94 (0.00)	0.77 (0.00)	0.97 (0.00)	0.96 (0.00)
VLBI/VieVS-HIRLAM	0.95 (0.00)	0.92 (0.00)	0.92 (0.00)	0.95 (0.00)	0.86 (0.00)	-	-	-	-
VLBI/VieVS-JMA/KARAT	-	-	-	-	-	0.89 (0.00)	-	-	-
VLBI/VieVS-CreSS	-	-	-	-	-	0.94 (0.00)	-	-	-

Table 6.13.: Correlation coefficients and their p-values between the troposphere gradient estimates of VLBI-VieVS and other solutions for the co-located sites during IVS-CONT08. Correlations written in italic are statistically insignificant ($p > 0.05$). Troposphere north gradients are in first line and east gradients are in second line. ([1]): NYA1, ([2]): WTZR, ([3]): TSKB, ([4]): HRAO.

	Ny-Ålesund	Svetloe	Onsala	Wettzell	Medicina	Tsukuba	Kokee	HartRAO	Tigoconc
VLBI/VieVS-VLBI/IVS	0.93 (0.00)	0.94 (0.00)	0.93 (0.00)	0.89 (0.00)	0.91 (0.00)	0.92 (0.00)	0.89 (0.00)	0.87 (0.00)	0.86 (0.00)
	0.93 (0.00)	0.89 (0.00)	0.93 (0.00)	0.95 (0.00)	0.88 (0.00)	0.93 (0.00)	0.91 (0.00)	0.70 (0.00)	0.85 (0.00)
VLBI/VieVS-GPS/CODE	0.74 (0.00)[1]	0.75 (0.00)	0.69 (0.00)	*0.39 (0.13)*[2]	0.54 (0.03)	*0.49 (0.05)*[3]	*-0.19 (0.48)*	0.68 (0.00)[4]	*0.58 (0.06)*
	0.57 (0.02)[1]	*0.34 (0.20)*	0.70 (0.00)	0.80 (0.00)[2]	0.56 (0.02)	*0.55 (0.03)*[3]	*0.34 (0.20)*	*0.25 (0.35)*[4]	*0.23 (0.50)*
VLBI/VieVS-DORIS/IGN	*0.19 (0.49)*	-	-	-	-	-	*-0.06 (0.83)*	*0.16 (0.57)*	-
	-0.16 (0.56)	-	-	-	-	-	*0.41 (0.13)*	*0.40 (0.14)*	-
VLBI/VieVS-WVR	-	-	0.49 (0.00)	0.31 (0.00)	-	-	-	-	-
	-	-	0.57 (0.00)	*0.11 (0.14)*	-	-	-	-	-
VLBI/VieVS-ECMWF	0.62 (0.00)	0.51 (0.00)	0.52 (0.00)	0.51 (0.00)	0.28 (0.03)	0.40 (0.00)	*0.01 (0.94)*	*0.24 (0.06)*	0.34 (0.04)
	0.61 (0.00)	*0.21 (0.10)*	0.76 (0.00)	0.31 (0.02)	0.48 (0.00)	0.28 (0.03)	*0.10 (0.43)*	*0.14 (0.28)*	0.60 (0.00)
VLBI/VieVS-JMA/KARAT	-	-	-	-	-	0.39 (0.00)	-	-	-
	-	-	-	-	-	0.50 (0.00)	-	-	-
VLBI/VieVS-CreSS	-	-	-	-	-	0.45 (0.00)	-	-	-
	-	-	-	-	-	0.41 (0.00)	-	-	-

The space geodetic techniques VLBI, GPS, and DORIS, including co-located WVR and the use of NWM (ECMWF, HIRLAM, KARAT, CReSS during IVS-CONT08) allowed to perform a comprehensive comparison of simultaneously determined troposphere parameters. The comparisons done in this study are essential to combine estimates from different techniques in the sense of GGOS, the Global Geodetic Observing System of the IAG.

These are the main findings of this part of the PhD study: ZTD estimates of space geodetic techniques generally agree at the sub-centimetre level during IVS-CONT08. For ZTD, the best agreement is found from the intra-technique comparisons between VieVS and the IVS combined solution as well as CODE and the IGS Kalman filter solution with median standard deviations of 3-4 mm and 4-5 mm, respectively. The best inter space geodetic technique agreement of ZTD during IVS-CONT08 is slightly worse and it can be found between IVS and IGS with a median standard deviation of about 5 mm over all sites. Since the standard deviation between ZTD for co-located GPS receivers from one solution (IGS at Wettzell, CODE at Ny-Ålesund) is at about 1.0 to 1.5 mm and the standard deviation between IGS and CODE is nearly as large as w.r.t. VLBI solutions, it can be argued that the choice of the analysis options adds a major part to the total uncertainty of ZTD from GPS.

As far as the overall agreement of ZTD is concerned between the techniques/solutions, two groups can be formed. GPS and VLBI form a group with the best agreement. The second group consists of the other models/techniques which are DORIS, ECMWF, HIRLAM, KARAT, CReSS, and WVR. Correlation coefficients of ZTD are typically larger than 0.9 and all of the correlations are statistically significant.

There is a latitude- and season-dependence of the standard deviations between the techniques. The standard deviations generally decrease with increasing northern and southern latitudes, which is due to the lesser amount of humidity at higher latitudes. Additionally, the comparison with the results from the IVS-CONT02 campaign in October 2002 showed, that standard deviations are generally larger during IVS-CONT08, which was observed in August 2008. In particular observations at Tsukuba are affected by the humid conditions in August.

The best intra-technique agreement of north and east gradients are found between VieVS and the IVS combined solution, which was not surprising because VieVS was part of the IVS combination for IVS-CONT08. The inter-technique biases are as large as 0.5 mm and the standard deviations are mostly in 0.4-0.5 mm. This is pretty big since the gradient estimates are mostly less than 1

mm. In general it has to be stressed, that the results of the comparison of gradients have to be used with care. Not only because of different time intervals but also due to basic differences in the observed quantities and setups.

Organizing further inter-technique comparison campaigns with consistent analysis models dedicated to the investigation of the troposphere would help to investigate the weaknesses of the individual space geodetic techniques (e.g. low degrees of freedom, inadequacy of gradient models) and the weaknesses of NWM in terms of conventions on data assimilation, time and spatial resolution of the profiles, and the ray-tracing technique.

7. VLBI Baseline Length Repeatability Tests of IVS-R1 and -R4 Sessions

VLBI has reached sub-centimeter precision for baseline lengths and station coordinates determined in a global terrestrial reference frame from 24 hour sessions (Schlüter and Behrend, 2007). However, future expectations are to improve the precision of these parameters to millimeter level. The baseline length and station coordinate repeatabilities depend on the amount of observables, the lengths of the baselines, but also on the accuracy of mathematical models, e.g. the troposphere delay model including the mapping functions that are used to describe the relation between the troposphere delay at zenith direction and at an arbitrary angle above the horizon. Due to the longer path through the atmosphere when decreasing the elevation angle, difficulties in troposphere delay modelling increase. From this point of view observations should be made near the zenith zone. On the other hand, including observations that are widely separated over all elevation and azimuth angles allows us to decrease the observational correlations (Malkin, 2008). Thus, there is a trade-off between smaller correlations of zenith delays and station heights as well as larger mapping function errors when using low elevation observations. Baseline length repeatabilities can be considered as important accuracy criteria for VLBI analysis, since baseline lengths are independent of rotations of the polyhedron formed by several VLBI stations (Niell, 2006). For each baseline, the repeatability can be determined as the standard deviation,

$$\sigma = \sqrt{\frac{\sum_{i=1}^{n} v_i^2}{n-2}} \tag{7.1}$$

of the n post-fit baseline length residuals (v) come up after the regression of polynomial of first order to the baseline lengths. In the analysis stage IVS-R1 and IVS-R4 sessions, baseline length repeatabilities were derived from several troposphere parametrization: with the troposphere mapping functions NMF, GMF, and VMF1, and with the cut-off elevation angles $3°$, $5°$, $7°$, $10°$, $15°$, $20°$, and $30°$.

7.1. IVS-R1 and -R4 sessions

The major purpose of the IVS-R1 and -R4 sessions is to provide twice-weekly EOP (Figure 7.1). The "1" and "4" indicate that in general the sessions are on Mondays and Thursdays, respectively. The "R" stands for rapid turnaround because the stations, correlators, and analysts have taken the commitment to make the time delay from the end of recording to results as short as possible. For the IVS-R1 and -R4 sessions the latency in order to make available the end products should not exceed 15 days (Schlüter and Behrend, 2007).
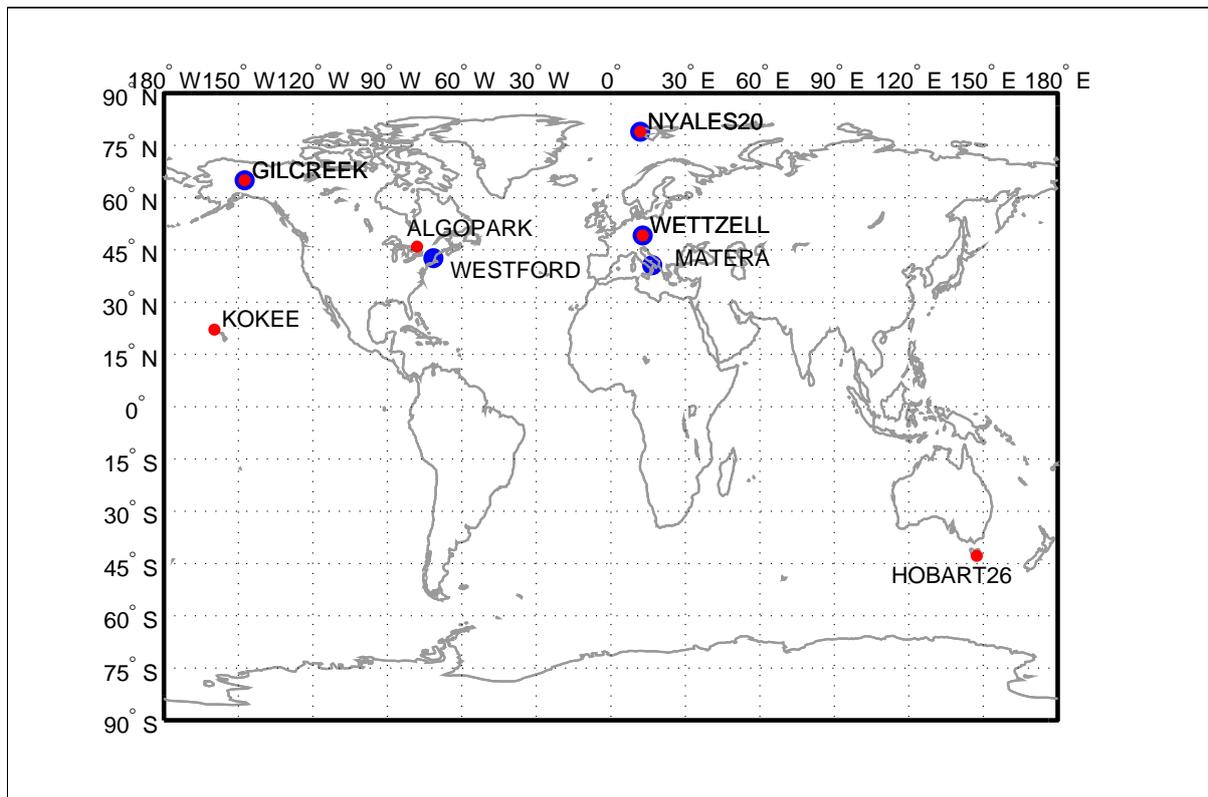
Figure 7.1.: VLBI antennas which contributed to 02APR02XA (IVS-R1 session) are shown as blue circles, and to 02APR04XE (IVS-R4 session) are shown as red circles.

7.2. Comparison of baseline length repeatabilities derived from different mapping functions and cut-off angles

To determine the baseline length repeatabilities of the IVS-R1 and -R4 sessions from 04/01/2002 (MJD:52278 begin with -R4) to 29/06/2007 (MJD:54280 end with IVS-R4) a linear function was fitted to the baselines in order to eliminate the effect of e.g. crustal motion on the baseline length time series as follows,

$$B_i(t_j) = a_{i(1)} + a_{i(2)}(t_j - t_0) \qquad (7.2)$$

where $B_i(t_j)$ is the length of the baseline i for session j and t_j is the estimation epoch of the coordinates on the each side of the baseline. $a_{i(1)}$ and $a_{i(2)}$ are the unknown parameters of the linear regression function. The RMS value of each fit Equation (7.1) is considered as the baseline length repeatability. The baseline length repeatabilities of the IVS-R1 and -R4 sessions were determined using three mapping functions: Niell Mapping Functions (NMF, Niell (1996)), Global Mapping Functions (GMF, Böhm et al. (2006)), and Vienna Mapping Functions 1 (VMF1, Böhm et al. (2006)). Brief introductions to troposphere mapping functions given in Section 5.1. Two regression functions were formed before and after the Earthquake for the baselines with station Gilcreek (e.g. Figure 7.2), because of the Denali Earthquake (03/11/2002). For more details relevant to the motion of Gilcreek Heinkelmann et al. (2008) is refered.

After having the repeatabilities for all baselines of IVS-R1 and -R4 sessions of a mapping function e.g. VMF1 and a cut-off angle of e.g. 7° a quadratic polynomial was fitted to the repeatabilities (without linear term) as follows

$$r_n = k_{m(1)} + k_{m(2)}B_n^2 \qquad (7.3)$$

where B_n is the mean length (no need to be known precisely) of the baseline n, and r_n is the repeatability value of the corresponding baseline; $k_{m(1)}$ and $k_{m(2)}$ are the unknown parameters of the regression function, m denotes the selected mapping function and the cut-off elevation angle (e.g. $m = 1$ denotes VMF1, cut-off angle 3°). The unknown parameters were estimated by a LS adjustment. Figures 7.3 and 7.4 show the repeatabilities of the baseline lengths for different mapping functions and cut-off angles.

The mapping functions yield similar baseline repeatabilities for cut-off angles 3°, 5°, 7°, and 10°, but from 15° onwards, the repeatabilities grow significantly. VMF1 gives the best repeatabilities
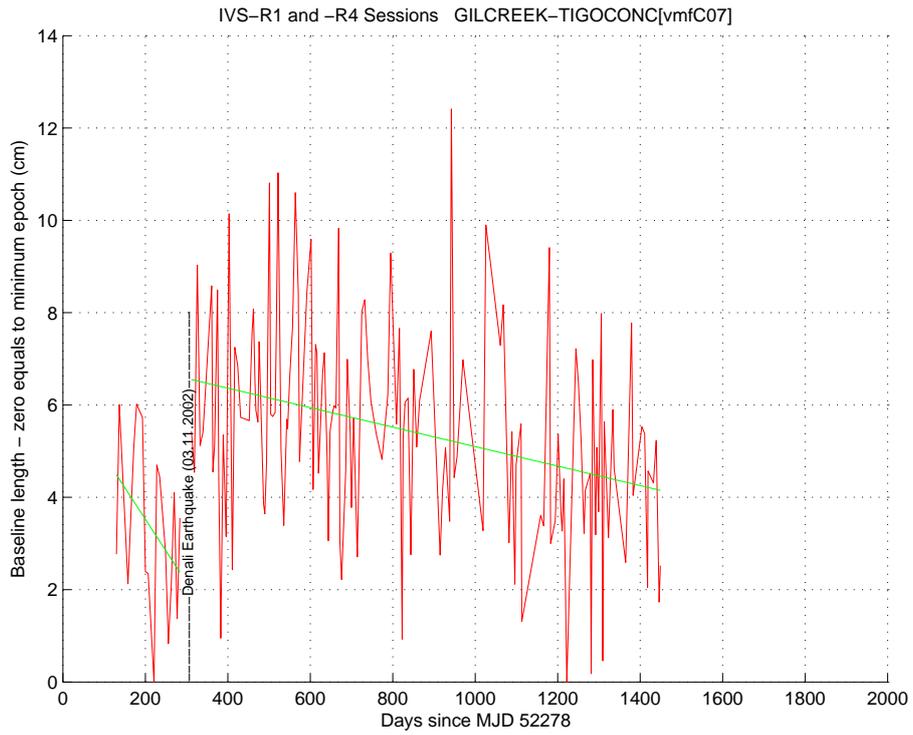
Figure 7.2.: Baseline lengths between the Gilcreek, USA - TIGO Concepcion, Chile VLBI stations and linear LS fit to the series.
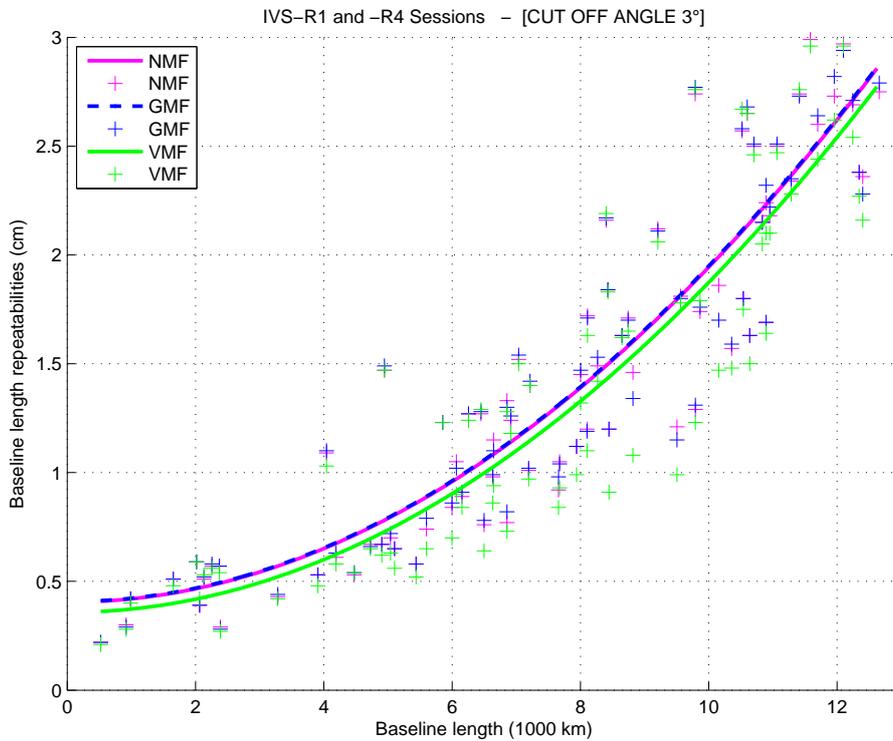
Figure 7.3.: Baseline length repeatabilities with VMF1, GMF, and NMF for a cut-off angle 3°.
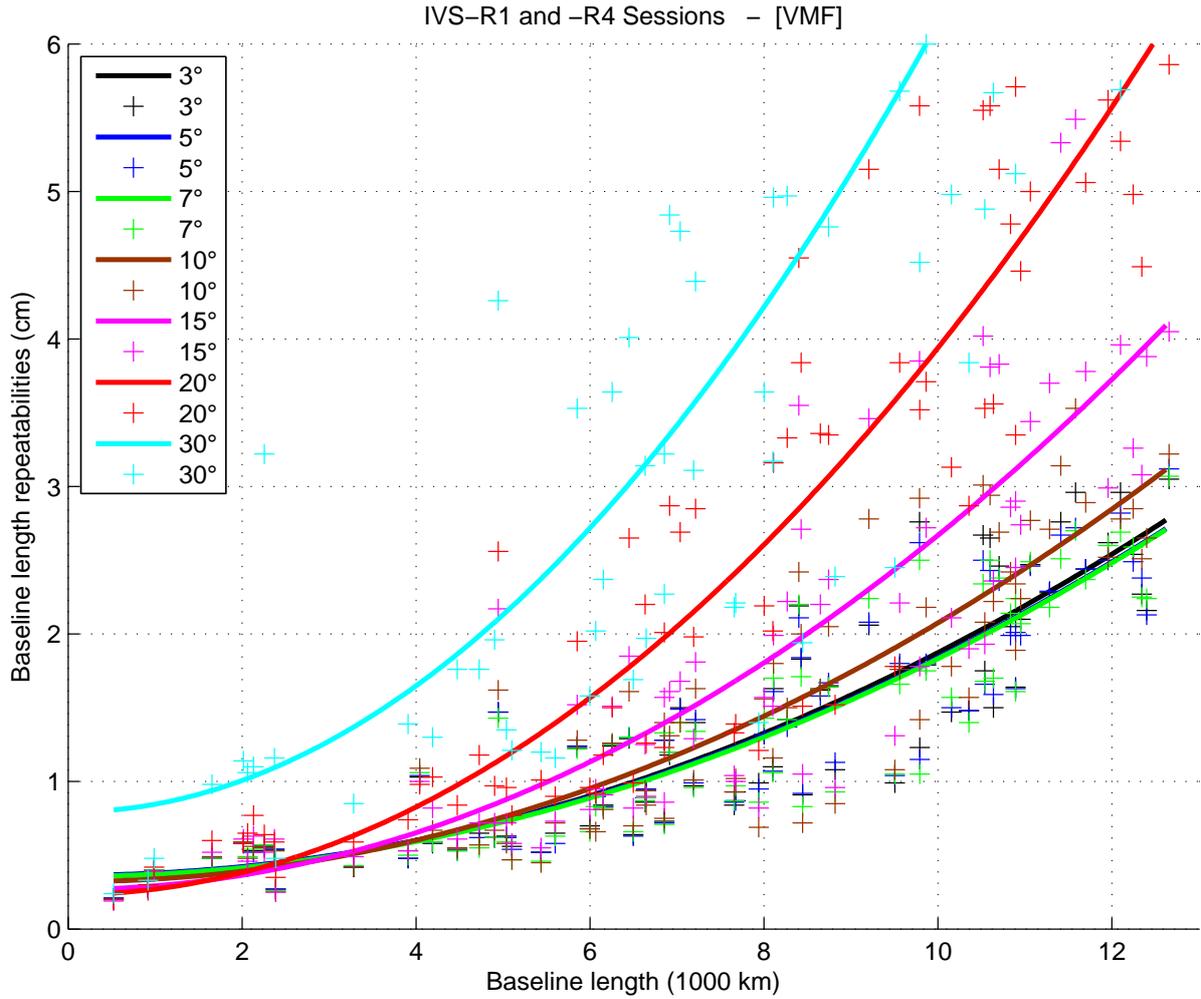
Figure 7.4.: Baseline length repeatabilities with VMF1 for the cut-off angles 3°, 5°, 7°, 10°, 15°, 20°, and 30°.

in the interval ([3° to 10°]) with the lowest value at 7°. Above 10° all three mapping functions more or less yield the same repeatabilities. Figure 7.5 shows the sum of the repeatabilities for each mapping function and cut-off elevation angle.

The sum of the repeatabilities with VMF1 is smaller than with NMF or GMF, at least below 10°. Above 10° all mapping functions produce approximately the same sum of repeatabilities. In Table 7.1, the total number of observations of IVS-R1 and IVS-R4 Sessions from 04/01/2002 to 29/06/2007 and the mean number of observations per session is given for each cut-off elevation angle. In this time span, 277 sessions of IVS-R1 and 268 sessions of IVS-R4 were analyzed.

Table 7.1.: Total number of observations for all sessions from 04/01/2002 to 29/06/2007 and the number of observations per session.

cut-off	total obs. (IVS-R1)	mean obs. (IVS-R1)	total obs. (IVS-R4)	mean obs. (IVS-R4)
3^0	519259	1875	350536	1308
5^0	515212	1860	348347	1300
7^0	492457	1778	337583	1260
10^0	451846	1631	313850	1171
15^0	380012	1372	267530	998
20^0	312135	1127	220201	822
30^0	193116	697	139688	521

From the investigations of IVS-R1 and IVS-R4 sessions baseline repeatabilities for the mapping functions VMF1, GMF, and NMF and the cut-off angles 3°, 5°, 7°, 10°, 15°, 20°, and 30° the following conclusions can be drawn:

- VMF1 gives the best repeatabilities for low cut-off elevation angles [3° to 10°] compared to other mapping functions.

- The repeatabilities are smallest with a cut-off elevation angle of 7°. For cut-off elevation angles above 10°, VMF1, NMF, and GMF yield approximately the same baseline length repeatabilities.

- There is no significant difference in repeatabilities between NMF and GMF.

Using different cut-off elevation angles means in this study that not the same number of observations is used. Thus, these tests should be repeated removing observations randomly when a low cut-off elevation angle is applied so that the number of observations will be identical for all cut-off angles. Investigations with down weighting of low elevation observations should be carried out, too.
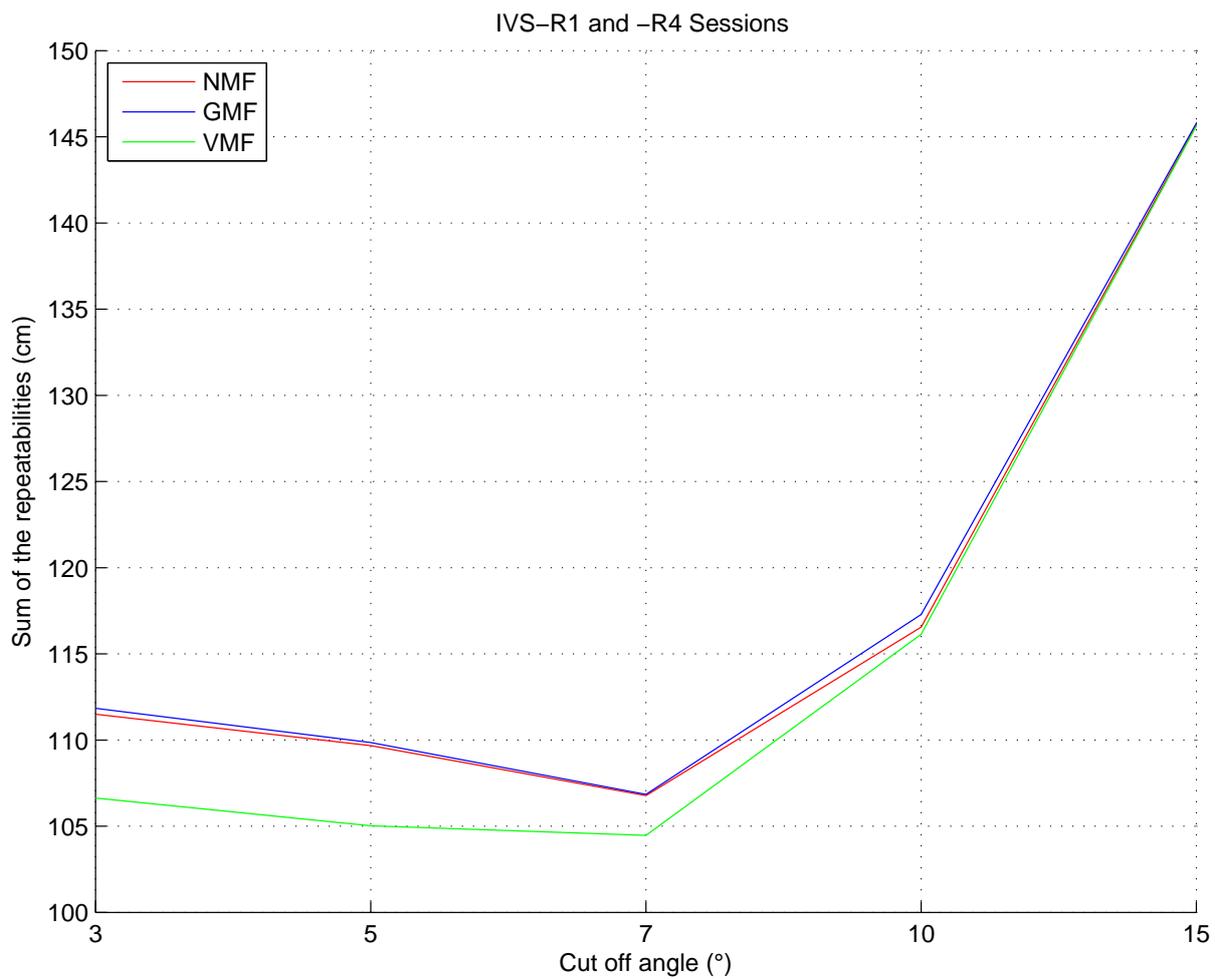
Figure 7.5.: Sum of the baseline length repeatabilities with VMF1, GMF, and NMF for the cut-off angles 3°, 5°, 7°, 10°, and 15°.

8. Analyses of the TRF, EOP, and CRF VLBI estimates

8.1. Analysis of the tidal motions at VLBI antennas: Sub-daily CPWLO coordinate estimates versus tide models during IVS-CONT05

In this section, *tidal motions* of VLBI antennas during IVS-CONT05 sessions are analyzed in such a way that the sub-daily CPWLO coordinate estimates of the antennas during IVS-CONT05 are compared with those computed from crustal tidal motion models. The reason for using VLBI observations during IVS-CONT05 sessions is the good global geographical coverage and the improved sub-daily precision (Schlüter and Behrend, 2007). IVS-CONT05 is a special 15 days continuous VLBI campaign composed of daily sessions. IVS-CONT05 was scheduled and carried out by IVS during the period September 12 to 27, 2005 where 11 globally distributed VLBI sites were allotted (Figure 8.1). Three crustal tidal motion models are basically considered in order to clarify the discrepancies between the models and the VLBI observations (VLBI antenna hourly CPWLO TRF coordinate estimates from VieVS): Solid Earth tide model according to the IERS conventions (McCarthy and Petit (2004), Chapter 7.1.1), ocean tidal loading model based on Finite Element solution, FES 2004 (Lyard et al., 2006), and atmosphere tidal loading (ATL) and atmosphere non-tidal loading (ANTL) model (Petrov and Boy, 2004). Before the analysis of each tidal motions a brief introduction on the corresponding tide or load will be presented.

One of the tidal motions of crust fixed VLBI antennas are generated by *solid Earth tides (body tides)* (SET). Sun and Moon periodic orbits induce time-varying displacements of the Earth's crust. SET can be defined as the elastic responses of the Earth crust to the frequency dependent tidal potential on the Earth caused by Sun and Moon. The tide generating potential due to the gravitational attraction of Sun and Moon can be described by an expansion into a set of tidal
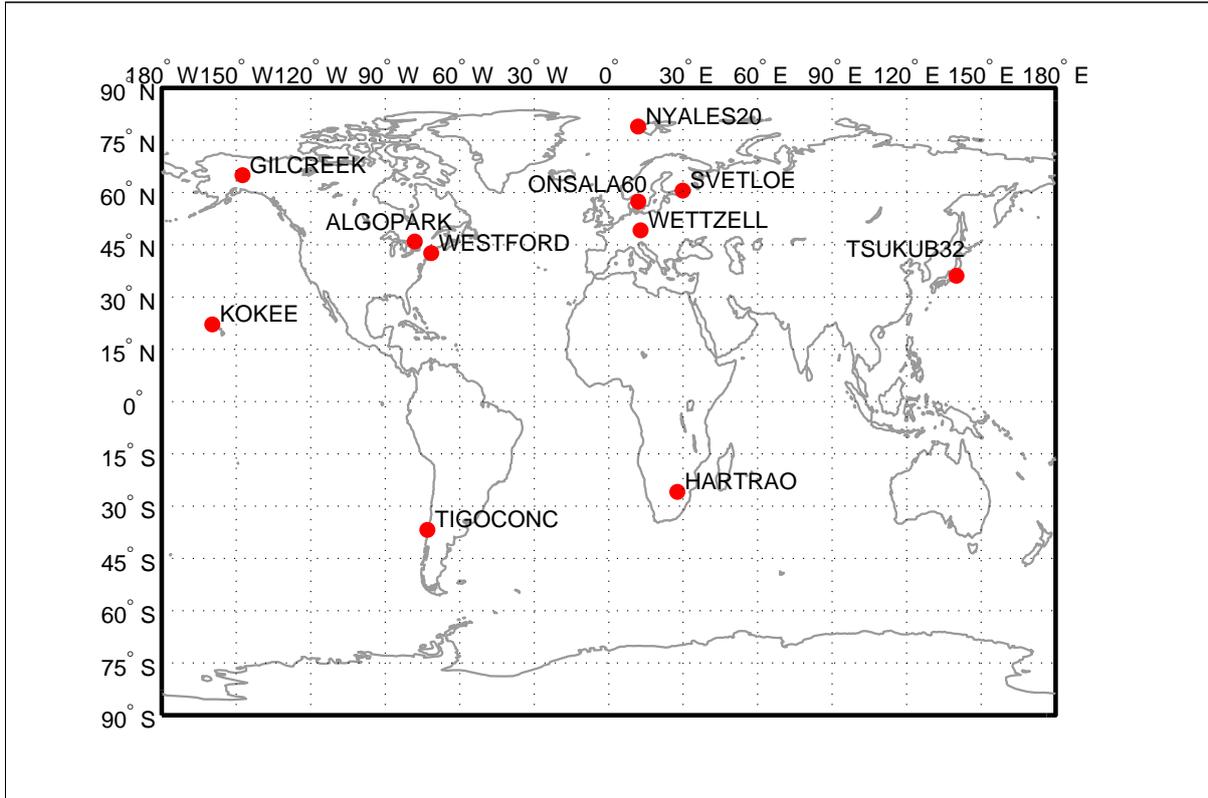
Figure 8.1.: IVS-CONT05 VLBI sites.

harmonics e.g. Cartwright and Tayler (1971); Cartwright and Edden (1973); Tamura (1987); Hartmann and Wenzel (1995). Site displacements caused by tides of spherical harmonic degree and order (nm) are characterized by the tidal Love number h_{nm} and the tidal Shida number l_{nm} (McCarthy and Petit (2004), Chapter 7.1.1). The effective values of these numbers depend on station latitude and tidal frequency (Wahr, 1981). Periodicities of the tidal motions range from hours to years. The basic semidiurnal tides are named as: M_2, S_2, N_2, K_2, and the basic diurnal tides are: O_1, P_1, Q_1, K_1, Φ_1, Ψ_1, and S_1. Long term tides are: M_m (Moon monthly tide) has a period of 27.555 solar days, M_f tide has a period of 13.661 solar days, and S_{sa} (Solar semi-annual tide) has a period of 0.5000 year. It should be mentioned that there are many significant body tides in the vicinity of the semi-diurnal and diurnal frequencies. SET produce station displacements that can reach up to half meter in radial direction.

In order to study the agreement of the displacements computed from the SET model (McCarthy and Petit (2004), Chapter 7.1.1) with the VLBI hourly CPWLO antenna coordinates, IVS-CONT05 sessions were analyzed. The parametrization for the estimation of hourly CPWLO antenna coordinates with VieVS during IVS-CONT05 are given in Table 8.1. Hourly CPWLO

coordinate estimates of VieVS when only the SET model is not reduced a priori to the adjustment from the observations were compared to those from the model. The VLBI antennas Wettzell (Germany), HartRAO (Republic of South Africa), and Kokee (Hawaii, USA) were studied. In Figure 8.2, the time series of the displacements due to SET at Wettzell (Germany) during IVS-CONT05 is shown (see also the displacements due to SET at the antenna HartRAO in Figure A.9.1 and at the antenna Kokee in Figure A.9.2).

Table 8.1.: Parametrization for the estimation of hourly CPWLO antenna coordinates with VieVS during IVS-CONT05 sessions. *For each analysis of a tidal motion in one particular solution this motion was not reduced from the observations a priori to the adjustment at this station.

a priori CRF	ICRF2 (all sources fixed).
a priori TRF	VTRF2008.
a priori ERP	IERS 05 C04 series plus high frequency ERP models**
	(**ocean tides and libration (McCarthy and Petit (2004), Chapter 5 and 8)).
a priori nutation offsets	IAU2000A precession-nutation model plus
	IERS 05 C04 corrections (McCarthy and Petit, 2004).
corrections to the	
antenna TRF coordinates	*solid Earth tides (McCarthy and Petit (2004), Chapter 7.1.1),
	*ocean tidal loading (FES 2004, Lyard et al. (2006)),
	*tidal and atmosphere non-tidal loading (Petrov and Boy, 2004),
	*pole tide (McCarthy and Petit (2004), Chapter 7.1.4).
corrections to the baselines	Thermal deformation of the antennas (Nothnagel, 2009).
	Antenna axis offset corrections.
Troposphere MF	VMF1 (Böhm et al., 2006)
handling observations	Outliers ($v_i \geq 3m_{v_i}$) were eliminated.
	No down-weighting of the observations was introduced.
	No cut-off elevation angle to the observations was introduced.
Estimated parameters	
clocks	Quadratic clock function coefficients (first LS).
	Hourly CPWLO of clocks plus rate and quadratic term (second LS).
	Loose constraints were used between the hourly
	CPWLO of clocks (0.5 $ps^2/s = 13$ mm after one hour).
zenith wet delays	CPWLO of zenith wet delays (ZWD) for 30 minutes intervals.
	Loose constraints were used between
	CPWLO of ZWD (0.7 $ps^2/s = 10.6$ mm after 30 minutes).
troposphere gradients	CPWLO of troposphere total gradients for 6 hours intervals.
	Loose constraints were used between gradients.
	2 mm/day = 0.5 mm after 6 hours.

Earth orientation parameters	CPWLO of EOP were estimated for 1 day interval. Tight constraints were used between the CPWLO of EOP (10^{-4} mas/day for all EOP).
antenna TRF coordinates	Hourly CPWLO of antenna coordinates were estimated. For each analysis of all IVS-CONT05 sessions, hourly CPWLO coordinates of one antenna were estimated. Others were fixed to VTRF2008. Loose constraints were used between CPWLO antenna coordinates (4 mm/hour and 3 cm/hour and 21 cm/hour.)
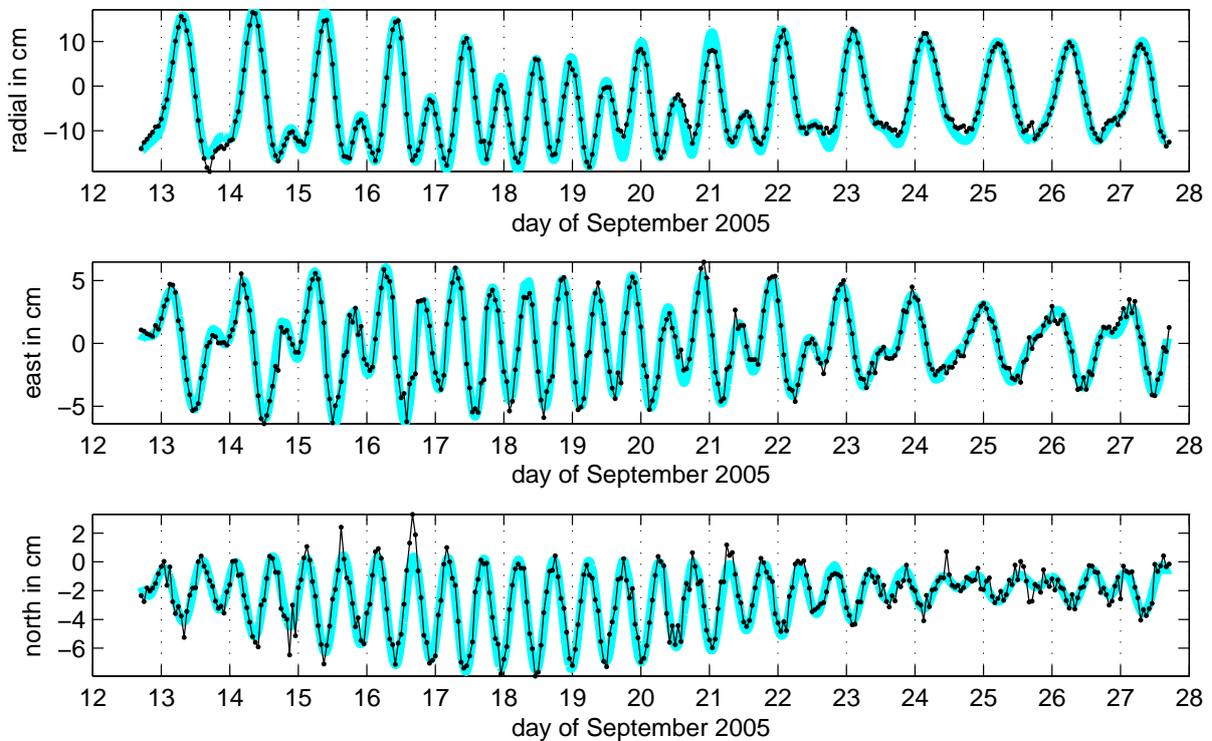
Figure 8.2.: The cyan line shows the *solid Earth tide* model (McCarthy and Petit (2004), Chapter 7.1.1) displacements at *Wettzell (Germany)* during IVS-CONT05. Black dotted lines are the hourly CPWLO coordinate estimates of VieVS when the solid Earth tide model for Wettzell was not reduced a priori to the adjustment from the observations. Zero ticks on the Y axes of the plots denote to the VTRF2008 coordinates of the antennas including all the model corrections introduced a priori except solid Earth tide. The IVS-CONT05 sessions analysis options are given in Table 8.1.

The sub-daily time series of the CPWLO estimates overlaps at the session boundaries at 0:00 UTC. Instead of stacking normal equations at the session boundaries, the weighted mean ($\bar{x}$) of

the offsets: (x_1, x_2) was calculated as follows,

$$\bar{x} = \frac{\sum_{i=1}^{2} \frac{x_i}{m_{xi}^2}}{\sum_{i=1}^{2} \frac{1}{m_{xi}^2}} = \frac{\frac{x_1}{m_{x1}^2} + \frac{x_2}{m_{x2}^2}}{\frac{1}{m_{x1}^2} + \frac{1}{m_{x2}^2}}, \tag{8.1}$$

and used instead of the overlapping offsets. In Equation (8.1), m_{x1} and m_{x2} denote the formal errors of the overlapping offsets. The formal error of the new offset was derived by calculating the weighted root mean square (WRMS) error as follows,

$$m(\bar{x}) = \sqrt{\frac{1}{\sum_{i=1}^{2} \frac{1}{m_{xi}^2}}} = \sqrt{\frac{1}{\frac{1}{m_{x1}^2} + \frac{1}{m_{x2}^2}}}. \tag{8.2}$$

In order to compare the displacements in the frequency domain, spectra of the displacements caused by SET were plotted for the sites Wettzell, HartRAO, and Kokee. The spectra plots of the radial components are shown in Figure 8.3. The spectra plots of all components (including east and north) of the VLBI antennas Wettzell, HartRAO and Kokee are given in Figure A.9.3. Basically, semi-diurnal and diurnal tidal effects on the antenna positions can clearly be seen on these plots. However, the Fourier spectra between model and the estimates cannot be distinguished from the Figures 8.3 and A.9.3. In order to see the spectral differences more clearly, hourly solid Earth tide displacements from the model were subtracted from the hourly coordinate estimates at the same epochs. The spectra plots of the radial components differences between the estimates and the model are shown in Figure 8.4. Maximum radial amplitudes of the differences range within [5,8] mm and some of the significant amplitudes are in the vicinity of semi-diurnal and diurnal periods. Wettzell has a radial amplitude of 5 mm at 25.8 hours. HartRAO has radial amplitudes of 6 and 7 mm at 21 and 23.8 hours, respectively. Kokee has the radial amplitudes of 8, 6, 6 mm at 12.0, 13.9, 24.1 hours, respectively (Figure 8.4). If we assume our observations and all other models used in the parameter estimation are perfect except the solid Earth tide model, then someone could assume that these differences were inferred as the solid Earth tide model deficiencies at the corresponding VLBI sites. More likely, these signals could be artefacts caused by errors in the modelling of troposphere, clocks, sources, antenna deformation or any systematic effect on the observations. These signals also may be resulted from the deficiencies of tidal motion models which are reduced from the observations a priori to adjustment (see also Figure A.9.3).

Loading effects

Another tidal effect on the positions of the VLBI antennas is *ocean tidal loading* (OTL). The response of the oceans to the gravitational attraction of Moon and Sun is manifested as periodic
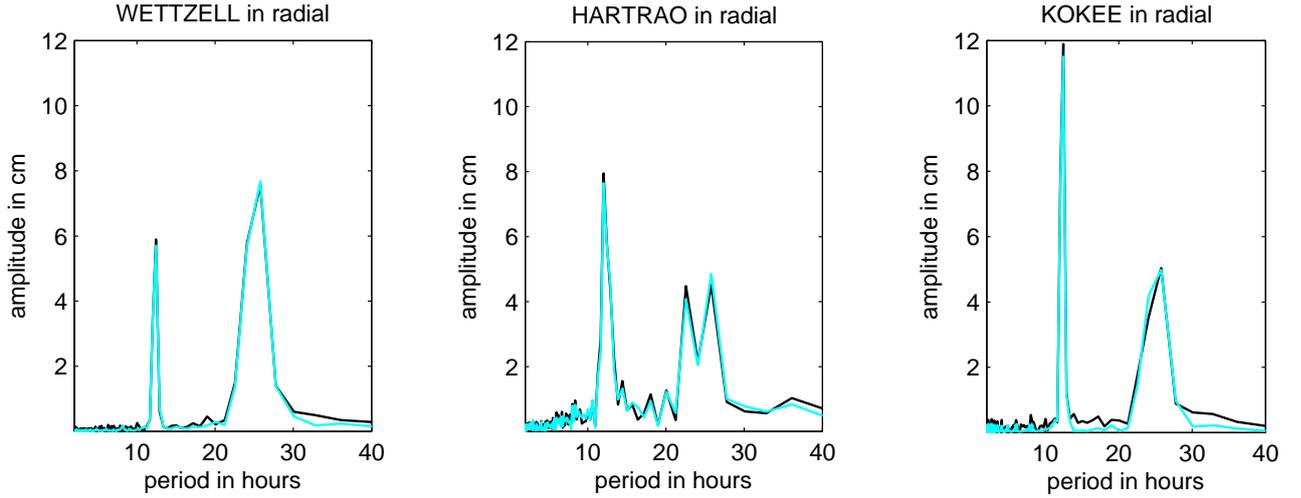
Figure 8.3.: Cyan lines show the Fourier spectra of hourly radial displacements computed from the *solid Earth tide* model (McCarthy and Petit (2004), Chapter 7.1.1). Black lines show the spectra of the radial components of the hourly CPWLO coordinate estimates when only the solid Earth tide model displacements were not reduced a priori from the observations during IVS-CONT05. The analysis options of the IVS-CONT05 sessions are given in Table 8.1.

movements of the fluid masses. The periodic changes of the fluid masses deform the solid Earth (crust) which results in periodic site motions. In the words, the response of the oceans to the tide generating potential has a temporal variation of the ocean mass distribution and the associated load on the crust, and time-varying deformations of the Earth crust are produced that can reach up to 100 mm especially on the areas near ($\sim$ 100 km) oceans. The ocean response, unlike the solid Earth, is strongly dependent on local and regional conditions. Most modern models assimilate sea surface height measurements carried out by altimetry satellites in addition to numerical models (McCarthy and Petit (2004), Chapter 7.1.2). For each VLBI site, the OTL models provide amplitudes and phases of 11 tidal waves at semi-diurnal periods: M_2, S_2, N_2, K_2, at diurnal periods: K_1, O_1, P_1, Q_1 and at longer periods: M_m, M_f, and S_{sa}.

The OTL displacements derived from the model FES 2004, Lyard et al. (2006) and the CPWLO hourly coordinate estimates of VieVS from the analysis of the IVS-CONT05 sessions were compared for the VLBI antennas Wettzell, HartRAO, and Kokee. In Figure 8.5, the time series of the displacements due to OTL at HartRAO VLBI antenna during IVS-CONT05 is shown (see also the displacements due to OTL at the antenna Wettzell in Figure A.9.4 and at the antenna Kokee in Figure A.9.5). In order to compare the displacements in the frequency domain, spectra of the radial displacements due to OTL were plotted for the sites Wettzell, HartRAO, and Kokee.
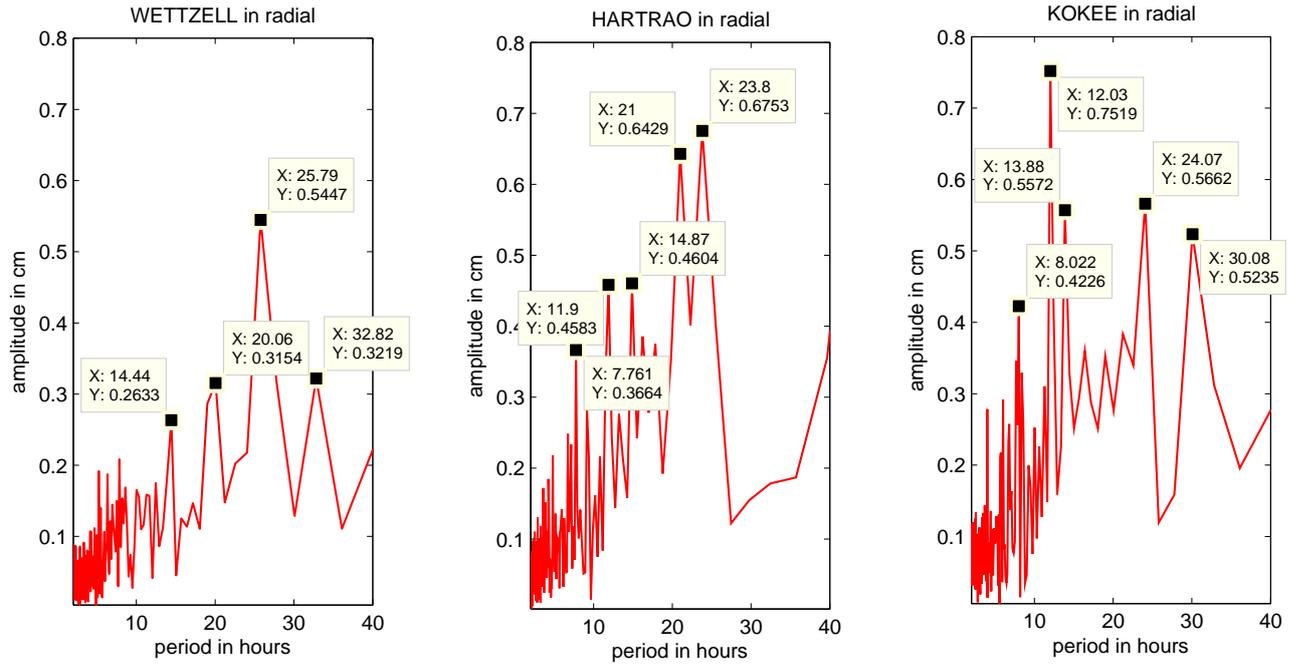
Figure 8.4.: Fourier spectra of the radial components difference vector between hourly CPWLO coordinate estimates during IVS-CONT05 (when solid Earth tide model displacements were not reduced from observations a priori to the adjustment) and the hourly model displacements computed from the *solid Earth tide* model (McCarthy and Petit (2004), Chapter 7.1.1). The analysis options of the IVS-CONT05 sessions are given in Table 8.1. In the plots, X values refer to the periods in hours and Y values refer to the amplitudes in centimeters of the hourly coordinate time series Fourier spectra.

The spectra plots of the radial components are shown in Figure 8.6. From Figure 8.6 it is clearly seen that for the antennas Wettzell, HartRAO, and Kokee the semi-diurnal amplitudes of the OTL model are in a good agreement with the estimated coordinates (OTL model is not reduced from observations a priori to the adjustment). At Wettzell there is a radial amplitude of 6 mm from the estimates and 5 mm from the OTL model at 12.45 hours that reveals a good agreement between the estimates and the OTL model at semi-diurnal periods. This good agreement at semi-diurnal periods is also valid for the antennas HartRAO and Kokee. The spectra of the radial components from the OTL model and from the estimates also agree at the diurnal period for the antenna Kokee. However, at Wettzell and at HartRAO the discrepancies between radial amplitudes at diurnal period are about 5 mm (Figure 8.6). These differences are significant and probably partly caused by the deficiency of the OTL model for these sites. The spectra plots of the north and east components from the estimates and from the OTL model are given in Figure A.9.6.
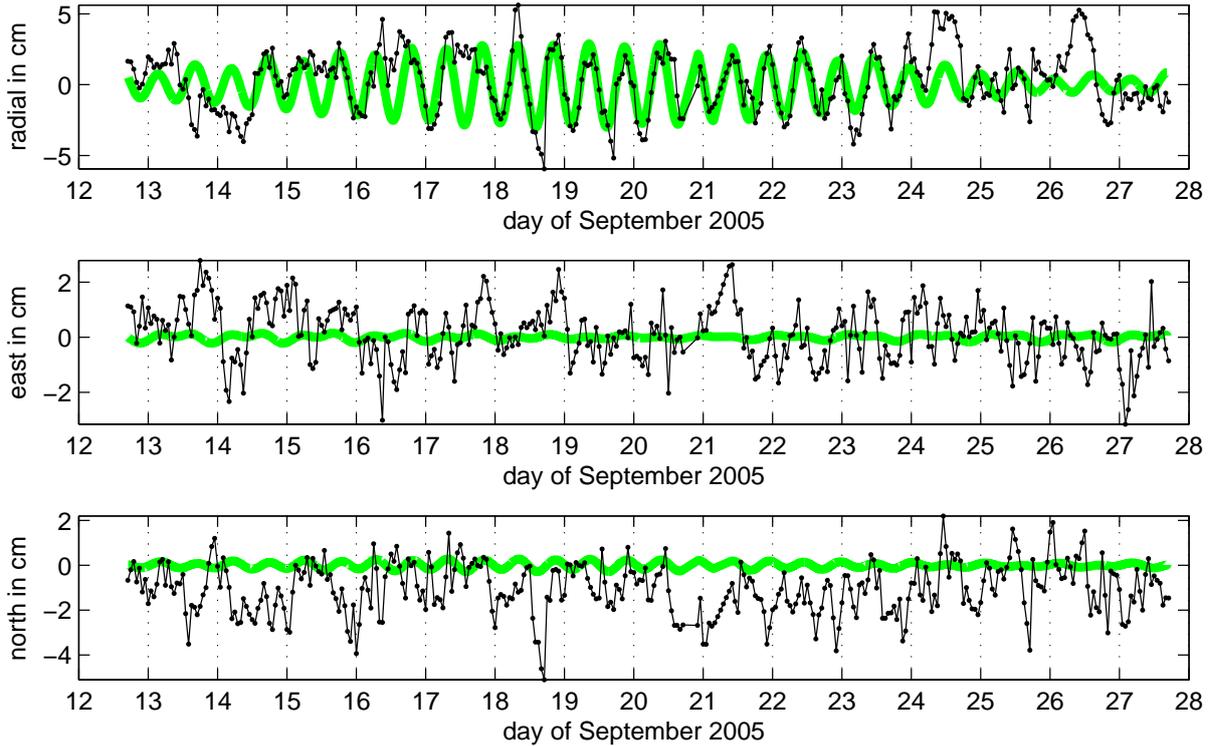
Figure 8.5.: Green lines show the *ocean tidal loading* (OTL) model (FES 2004, Lyard et al. (2006)) displacements at *HartRAO* during IVS-CONT05. Black dotted lines show the hourly CPWLO coordinate estimates of VieVS when only the OTL model displacements were not reduced a priori to the adjustment from the observations. Zero ticks on the Y axes of the plots denote the VTRF2008 coordinates of the antennas including all the model corrections introduced a priori except OTL. The analysis options of the IVS-CONT05 sessions are given in Table 8.1.

The changes of the surface pressure variations cause displacements up to 20 mm in radial and 3 mm in horizontal directions (Rabbel and Schuh, 1986; vanDam and Herring, 1994; Petrov and Boy, 2004). Surface pressure variations consist of tidal and non-tidal parts. The tidal part consists of diurnal S_1 and semi-diurnal S_2 periods and induces periodic motions of the VLBI antennas less than 2 mm in radial direction. The non-tidal part is approximately one order of magnitude larger than the ATL displacements (Ray and Ponte, 2003). In VLBI analysis, atmosphere loading corrections at the stations should be introduced to all observations a priori to the parameter estimation similar to other tidal and loading corrections. Neglecting atmospheric loading corrections at the observation level results in propagation of these displacements to the positions of other VLBI stations, especially to height components (Böhm et al., 2009).

The atmosphere loading displacements computed from the model (Petrov and Boy, 2004), and the hourly CPWLO coordinate estimates of the VLBI antennas, Wettzell (non-tidal part) and
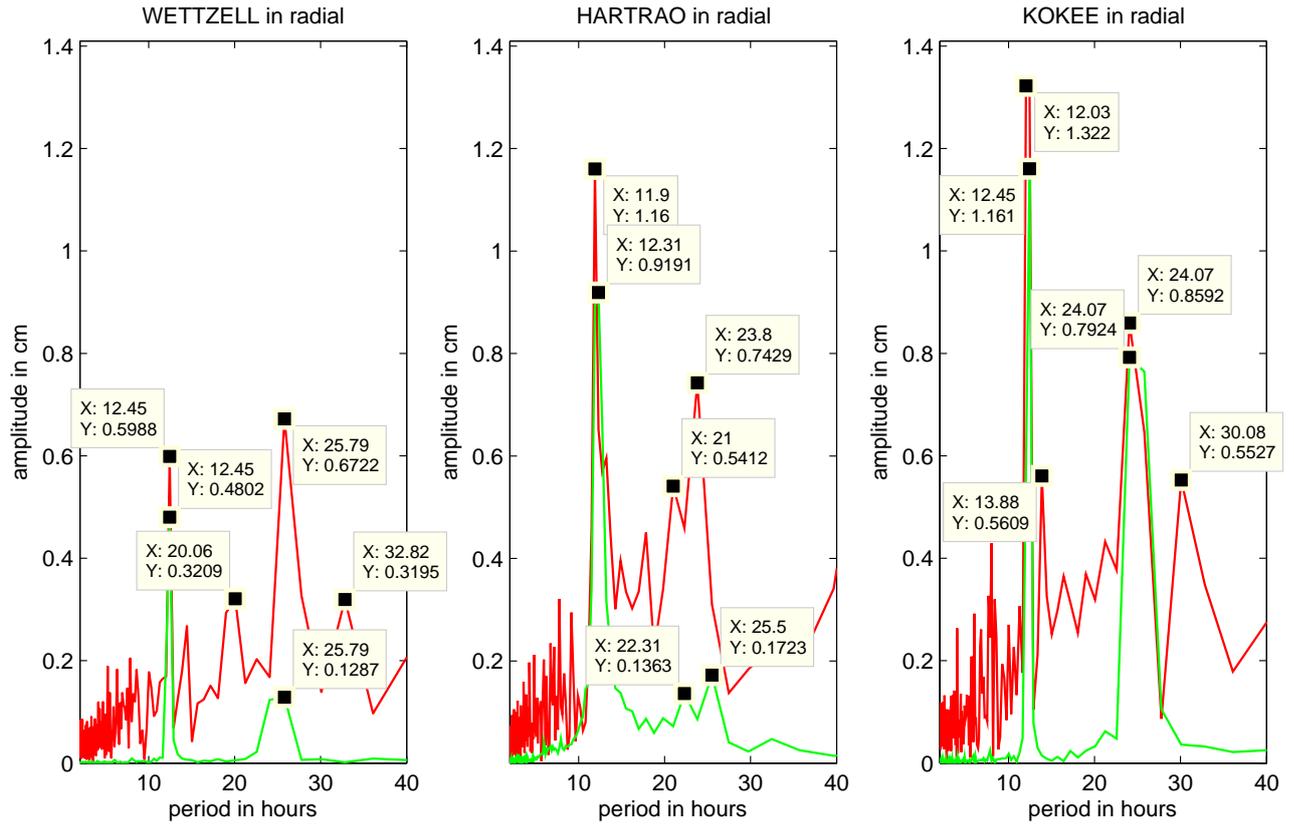
Figure 8.6.: Green lines show the Fourier spectra of the radial components of the hourly displacements computed from the *ocean tidal loading* (OTL) model (FES 2004, Lyard et al. (2006)). Red lines show the spectra of radial components of the hourly CPWLO coordinate estimates of VieVS when only the OTL model displacements were not reduced a priori from the observations during IVS-CONT05. The analysis options of the IVS-CONT05 sessions are given in Table 8.1. In the plots, the X values refer to the periods in hours and the Y values refer to the amplitudes in centimeters of the hourly coordinate time series Fourier spectra.

Kokee (tidal part) are shown in Figures A.9.7 and A.9.8, respectively. In order to compare the ATL displacements in frequency domain between the hourly values of the model and the VieVS CPWLO coordinate estimates (when the model tides are not reduced a priori from the observations), spectra of the radial components were plotted for the VLBI antennas: Wettzell, HartRAO, and Kokee (Figure 8.7). In Figure 8.7 blue line shows the Fourier spectra of the radial components of the hourly displacements computed from the ATL model (Petrov and Boy, 2004). The red line shows the spectra of the CPWLO coordinate estimates when only the ATL model values are not reduced from the observations a priori to the parameter estimation. The amplitudes of S_1 (diurnal) and S_2 (semi-diurnal) ATL model tides rather small (less than 1 mm) for the antennas Wettzell, HartRAO, and Kokee VLBI sites (Figure 8.7). Reducing ATL

model displacements from the observations a priori to the adjustment, as recommended in Böhm et al. (2009), resulted in about 1 mm accuracy improvement on the height components for the aforementioned VLBI sites. However, there are clear peaks of about 6 to 7 mm at diurnal periods for all three antennas and 5 to 6 mm amplitudes in semi-diurnal periods of the antennas HartRAO and Kokee. These significant tidal displacements should be investigated further. The spectral plots of all components (including east and north) of the VLBI antennas: Wettzell, HartRAO and Kokee are shown in Figure A.9.9.
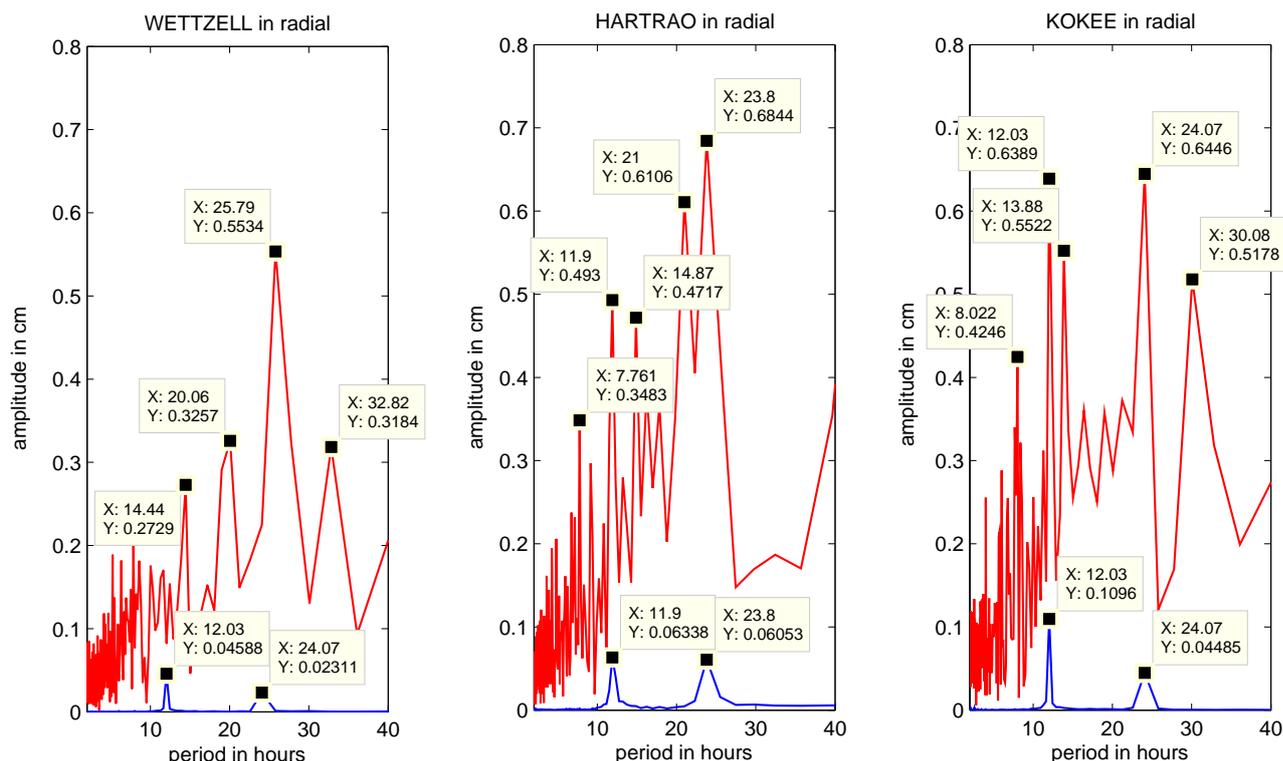
Figure 8.7.: Blue lines show the Fourier spectra of the radial components of the hourly displacements computed from the *atmosphere tidal loading* (ATL) model (Petrov and Boy, 2004). Black lines show the spectra of the CPWLO coordinate estimates when only the ATL model values were not reduced a priori from the observations. The analysis options of the IVS-CONT05 sessions are given in Table 8.1. In the plots, the X values refer to the periods in hours and the Y values refer to the amplitudes in centimeters of the hourly coordinate time series Fourier spectra.

One of the tidal displacements of the antennas is named *pole tide*. The pole tide is caused by the centrifugal potential generated by the deviations of the Earth rotation axis from the figure axis. The pole tide should be reduced from the VLBI observations a priori to the paramater estimation. The pole tide motions computed from the model (McCarthy and Petit (2004), Chapter 7.1.4) during IVS-CONT05, and VieVS hourly CPWLO coordinate estimates of the

Wettzell antenna (when the pole tide model was not reduced a priori from the observations) is given in Figure A.9.10.

The hourly coordinate estimates of the VLBI antenna TRF positions, during IVS-CONT05, reveals several significant peaks at sub-daily and daily periods. The significant peaks are basically seen at semi-diurnal and diurnal periods. The radial amplitudes can reach up to 1 cm except Tigoconc (more than 2 cm due to not enough observation). The significant periods and amplitudes of the hourly radial CPWLO coordinate estimates from VieVS are shown in Figure 8.9. It should be mentioned that all the tidal models are reduced a priori to the parameter estimation from the observations during IVS-CONT05.

Similar to clocks, relative constraints should be applied to the CPWLO coordinates to prevent singularity problems of the normal equation matrix. In Figure 8.9 black lines show the spectra of the radial components of the hourly CPWLO coordinate estimates which are constrained with 4 mm/hour (black line), 3 cm/hour (red line), and 21 cm/hour (cyan line). In order to assess the influence of bad observations, the peaks of the cyan line in Figure 8.8, which seem to be unrealistic hourly coordinates, should be treated as outliers and eliminated from the set before further analysis. The reason of this spurious peaks in the hourly coordinates may be due to small number or bad observations in the corresponding estimation intervals. VieVS hourly CPWLO TRF coordinate estimates of all VLBI antennas contributing to IVS-CONT05 are given in Figures A.8.1 to A.8.10.

For the antennas participating in IVS-CONT05, except Tigoconc, and Algopark, no significant radial amplitude difference is seen between the spectra of the sub-daily coordinates illustrated in red and cyan in Figure 8.9. These differences of the radial amplitudes, especially at Tigoconc are too large (1 to 1.5 cm), when very loose constraints are introduced and not enough observations per estimation interval were carried out. From the analysis of the hourly CPWLO coordinate estimates in terms of applying loose constraints of different magnitudes the following conclusions can be drawn:

- Even when very loose constraints (e.g. 21 cm/hour) are introduced between the CPWLO coordinate estimates many of the hourly coordinate estimates are not affected because of a sufficient number of observations per estimation interval (see time series of hourly estimates during IVS-CONT05 in Figure 8.8 and Figures A.8.1 to A.8.10).
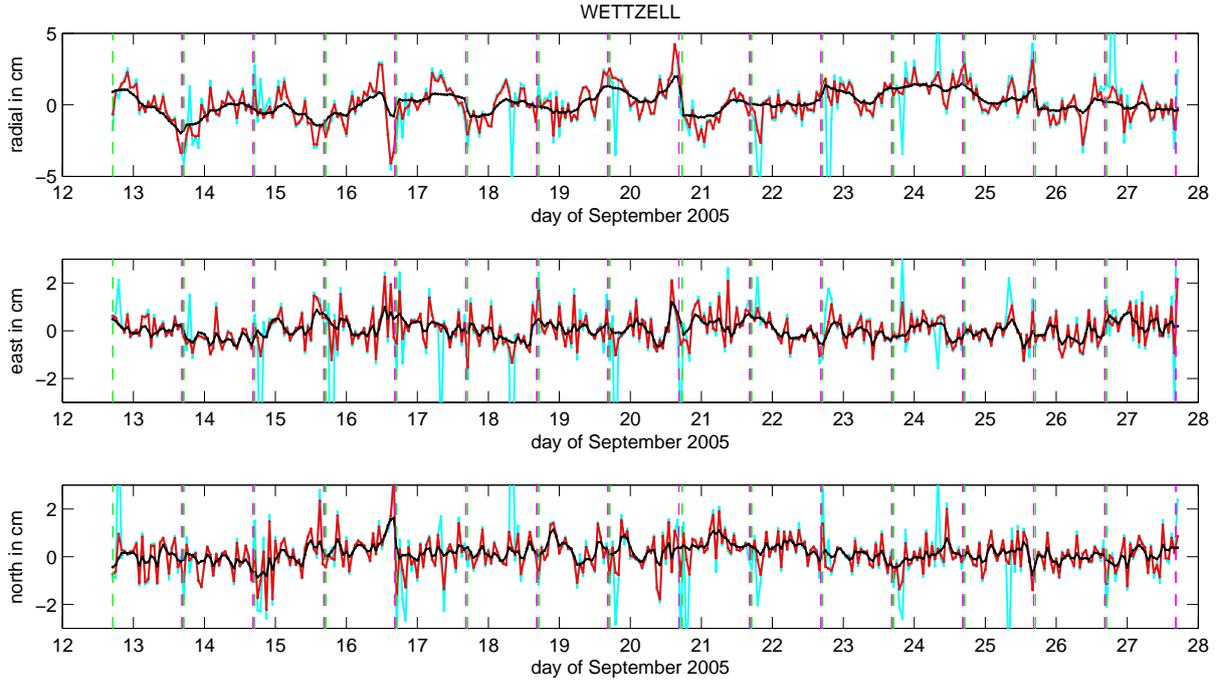
Figure 8.8.: Black, red and cyan dotted lines show VieVS hourly (at UTC integer hours) CPWLO coordinate estimates of the VLBI antenna Wettzell during IVS-CONT05. The estimates are illustrated with black dotted lines if constraints of 4 mm/hour are used, and red dotted lines if loose constraints of 3 cm/hour and cyan lines when very loose constraints of 21 cm/hour are used. Zero ticks on the Y axes of the plots denote to the VTRF2008 coordinates of the antennas including all the model corrections introduced a priori to the parameter estimation. Vertical green dashed lines show the beginning of the sessions and vertical magenta dashed lines show the end of the sessions. The analysis options are given in Table 8.1.

- Some of the hourly CPWLO coordinate estimates seem unrealistic when very loose constraints, e.g. 21 cm/hour, are introduced. This is most likely due to few observations in the corresponding coordinate estimation intervals. Very loose constraints cannot constrain the offsets if a few or bad observations are included in the corresponding estimation intervals.

- The number of observations should be homogenously distributed over all estimation intervals of all antennas within the session to prevent outliers of sub-daily offsets.

From the analysis of significant amplitudes and their periods of the hourly CPWLO coordinate estimates the following conclusions can be drawn. It should be mentioned that the following results are based on loose constraints of 3 cm/hour between the CPWLO coordinate estimates. Other analysis options are given in Table 8.1:

- The spectra of the sub-daily CPWLO coordinate estimates (Figure 8.9) may not only result from the deficiencies of the tidal models but also from un-modelled troposphere delays and other systematic error sources of the observations, e.g. a priori EOP.

- Most probably, spectra of the hourly coordinate estimates is due to the propagation of the un-corrected parts of the antenna positions at each observation epoch (e.g. due to the inadequacies of the tidal and loading models) to the estimates.
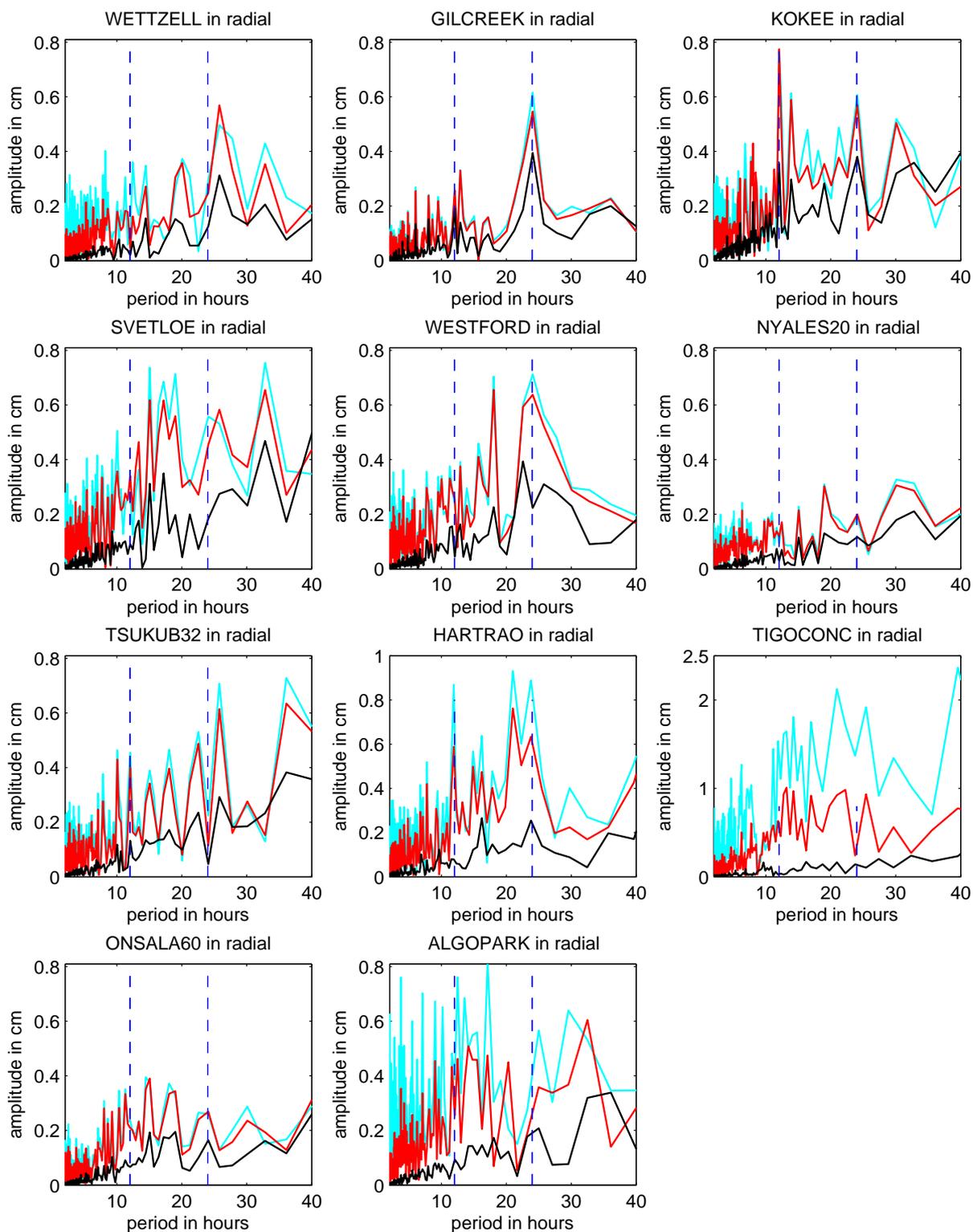
Figure 8.9.: Spectra of radial components of the hourly CPWLO coordinate estimates during IVS-CONT05 when all the tidal models were reduced a priori from the observations during IVS-CONT05. Black lines show the spectra when constraints of 4 mm/hour were applied to hourly CPWLO coordinate estimates. Red lines show the spectra for 3 cm/hour and cyan lines show the spectra for 21 cm/hour constraints. The other analysis options are given in Table 8.1.

8.2. Analyses of the sub-daily ERP during IVS-CONT08: model versus observations

The Earth's rotation axis in space i.e. Celestial Intermediate Pole (CIP) and its equatorial plane have secular (smoothly varying) and periodic (oscillatory) rotations relatively in time. In other words, the Earth rotation axis is rotating relatively to a non-rotating inertial system (celestial coordinate system, e.g. quasi-inertial, ICRS) (Mathews, 2009). The motion of the CIP in space is driven by mainly the gravitational attraction of Sun and Moon. The total motion in space is composed of a mean secular component: precession, and a periodic component: nutation. Completion of the precession circle takes about 26000 years. Nutation has several periods varying from 18.6 years to 2 days. The Celestial Intermediate Pole (CIP) is an intermediate Earth rotation pole of which motion in ITRS and GCRS are separated by convention (IAU 2000 Resolution B1.7) into terrestrial and celestial parts. The celestial motion of the CIP (precession-nutation) includes all terms with periods greater than 2 days (frequencies between -0.5 and +0.5 cycles per sidereal day, cpsd) in the GCRS. The variations in rotation axis corresponding to motions with periods more than two days in GCRS (Chao et al., 1991) that are not part of the nutation models e.g. IAU 2000A precession-nutation model (Capitaine et al. (2002), and McCarthy and Petit (2004), Chapter 5) are provided in the IERS 05 C04 daily combined series as $(\Delta X, \Delta Y)_{correction}$. The CIP coordinates in the GCRS (X and Y) can be derived from e.g.:

$$(X, Y) = (X, Y)_{IAU2000A} + (\Delta X, \Delta Y)_{correction} \tag{8.3}$$

where $(X, Y)_{IAU2000A}$ are the CIP coordinates in GCRS computed from the precession-nutation model e.g. IAU2000A. $(\Delta X, \Delta Y)_{correction}$ are the daily corrections to the precession-nutation model derived coordinates of the CIP in GCRS, that can be obtained from e.g. IERS 05 C04 combined daily EOP series (at 0:00 UTC) of the International Earth Rotation and Reference Systems Service (IERS) (Bizouard and Gambis, 2009).

In order to compare between daily nutation corrections at 0:00 UTC epochs from IERS 05 C04 EOP combined series and the VieVS CPWLO estimates at the same epochs (0:00 UTC) during IVS-CONT08, the options given in Tables 8.2 and 8.3 were selected in VieVS.

Table 8.2.: Common parametrization for the analysis on EOP estimates during IVS-CONT08.

a priori CRF	ICRF2 (all sources fixed).
a priori TRF	VTRF2008 (NNT and NNR conditions imposed on the coordinate estimates with a priori coordinates from VTRF2008).

a priori ERP	Specified in the following tables.
a priori nutation offsets	Specified in the following tables.
corrections to the	
antenna TRF coordinates	Solid Earth tides (McCarthy and Petit (2004), Chapter 7.1.1),
	ocean tidal loading (FES 2004, Lyard et al. (2006)),
	tidal and atmosphere non-tidal loading (Petrov and Boy, 2004),
	pole tide (McCarthy and Petit (2004), Chapter 7.1.4).
corrections to the baselines	Thermal deformation of the antennas (Nothnagel, 2009).
	Antenna axis offset correction.
Troposphere MF	VMF1 (Böhm et al., 2006).
handling observations	Outliers ($v_i \geq 3m_{v_i}$) were eliminated.
	No down-weighting of the observations was introduced.
	No cut-off elevation angle to the observations was introduced.
Estimated parameters	
Clocks	Quadratic clock function coefficients (first LS).
	Hourly CPWLO of clocks plus rate and quadratic term (second LS).
	Loose constraints were used between the hourly
	CPWLO of clocks (0.5 ps^2/s = 13 mm after one hour).
zenith wet delays	CPWLO of zenith wet delays (ZWD) for 30 minutes intervals.
	Loose constraints were used between ZWD.
	(0.7 ps^2/s = 10.6 mm after 30 minutes).
troposphere gradients	CPWLO of troposphere total gradients for 6 hours intervals.
	Loose constraints were used between gradients.
	2 mm/day = 0.5 mm after 6 hours.
Earth orientation parameters	Specified in the following tables.
antenna TRF coordinates	One offset was estimated per session (day). Condition equations
	were introduced to the normal equation system providing the new TRF
	of the estimated coordinates have NNT and NNR w.r.t. VTRF2008.

The agreement between the daily CPWLO estimates of nutation (dX, dY) from the VieVS analysis of IVS-CONT08 sessions with the nutation corrections of IERS 05 C04 combined EOP series, $(\Delta X, \Delta Y)_{IERS}$ are shown in Figure 8.10 and 8.11. The formal errors of the daily (at 0:00 UTC) nutation dX estimates of VieVS are found out within [10,19] μas and the IERS 05 C04 series ΔX formal errors are within [27,60] μas. The formal errors of the dY estimates of VieVS range within [11,20] μas and the IERS 05 C04 series ΔY formal errors are within [54,109] μas. The daily (at 0:00 UTC) nutation $dX - \Delta X$ differences (nutation estimates minus IERS 05 C04 series nutation correction) range within [-54,+57] μas and $dY - \Delta Y$ are within [-94,+32] μas

(Figures 8.10 and 8.11).

Table 8.3.: Parametrization for the estimation of the daily CPWLO coordinates of the CIP in GCRS (dX, dY) with VieVS during IVS-CONT08 to analyze daily corrections to the IAU2000A precession-nutation model.

a priori ERP	IERS 05 C04 ERP series plus high-frequency ERP (HF-ERP) models*
	(*ocean tides and libration (McCarthy and Petit (2004), Chapter 5 and 8)).
a priori nutation offsets	IAU2000A precession-nutation model (McCarthy and Petit, 2004).
Earth orientation parameters	CPWLO of EOP were estimated for 1 day interval.
	Tight constraints were used between the CPWLO of EOP
	(10^{-4} mas/day for all EOP).
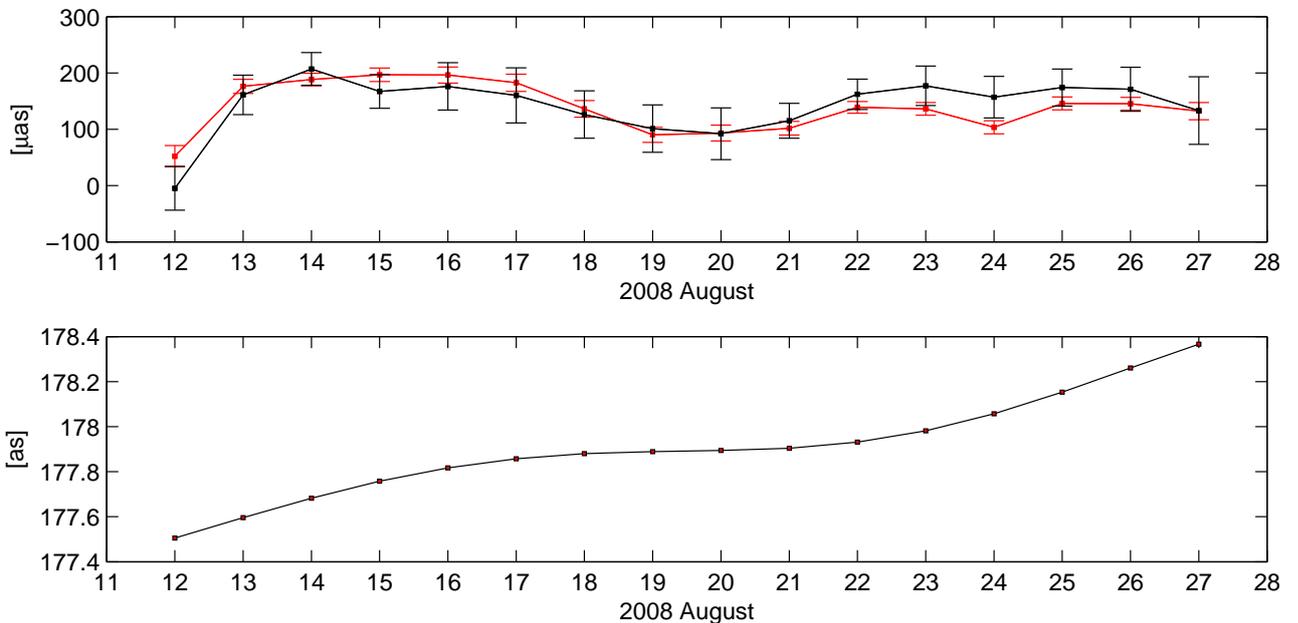
Figure 8.10.: In the upper plot, VieVS daily CPWLO of nutation dX estimates at epochs 0:00 UTC with their formal errors during IVS-CONT08 are shown in red. The daily ΔX_{IERS} at epochs 0:00 UTC and their formal errors are shown in black. In the lower plot, $X_{IAU2000A}$ values at epochs 0:00 UTC are shown. The VieVS analysis options are given in Table 8.2 and 8.3.

The Earth's rotation axis traces a counter clock-wise quasi-circular, quasi-periodic path on the crust (w.r.t. an Earth-fixed reference system) approximately 20 m in diameter called polar motion (terrestrial (crust fixed) motion of the CIP). The main long periods of polar motion are composed of one period of approximately 430 days, called Chandler wobble, and an annual period. The short periods of polar motion include all terms outside the retrograde (polar motion opposite to Earth's rotation direction) diurnal band in the ITRS (frequencies lower than -1.5
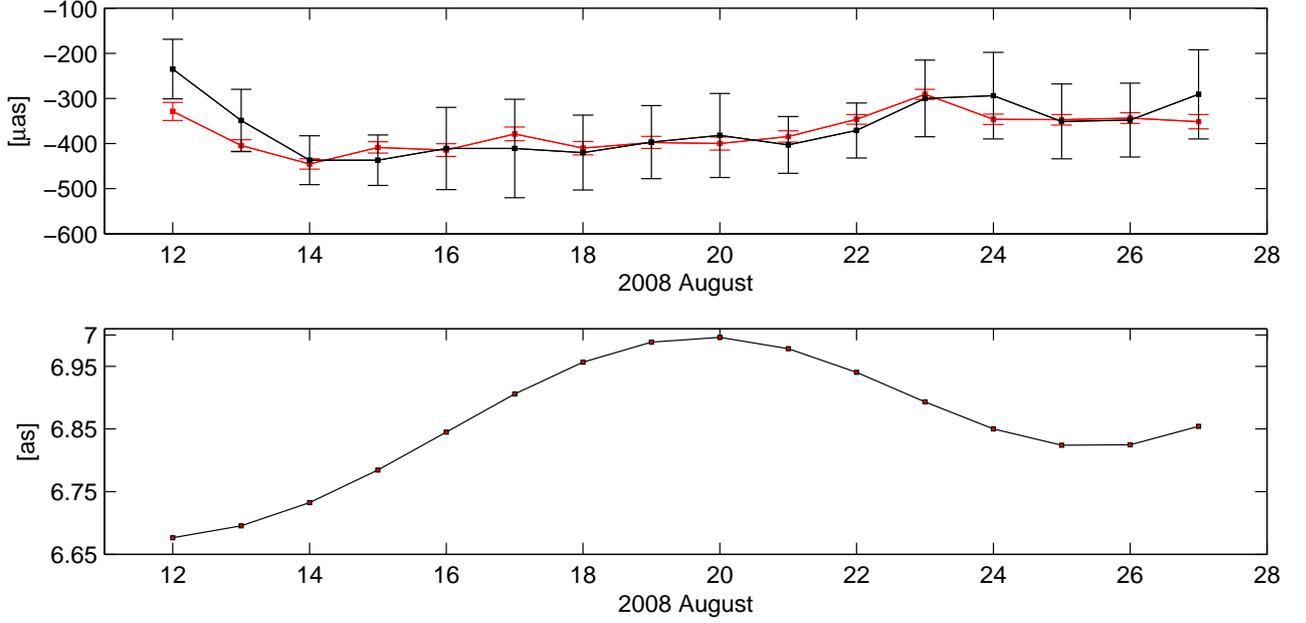
Figure 8.11.: In the upper plot, VieVS daily CPWLO of nutation dY at epochs 0:00 UTC with their formal errors during IVS-CONT08 are shown in red. The daily ΔY_{IERS} at epochs 0:00 UTC and their formal errors are shown in black. In the lower plot, $X_{IAU2000A}$ values at epochs 0:00 UTC are shown. The VieVS analysis options are given in Table 8.2 and 8.3.

cpsd and greater than -0.5 cpsd). Earth rotation parameters (ERP) are typically given as daily values (e.g. IERS 05 C04) and the sub-diurnal parts are calculated from models:

$$(x_p, y_p) = (x_p, y_p)_{predicted} + (\Delta x, \Delta y)_{HF-ERP} \tag{8.4}$$

and

$$\Delta UT1 = \Delta UT1_{predicted} + \Delta UT1_{HF-ERP}, \tag{8.5}$$

where $(x_p, y_p)_{predicted}$ are the daily TRF coordinates of the rotation pole and $\Delta UT1_{predicted}$ are the daily values of the Earth phase of rotation e.g. distributed with the IERS 05 C04 combined daily EOP series. $(\Delta x, \Delta y)_{HF-ERP}$ and $\Delta UT1_{HF-ERP}$ are the diurnal and semi-diurnal ERP variations which can be computed from the sum of high-frequency ERP models (HF-ERP) e.g. ocean tides (Ray et al., 1994); (McCarthy and Petit (2004), Chapter 8.2 and Chapter 5.5.1) and libration due to the external torque (mainly luni-solar) on the non-axisymmetric part of the Earth (Earth's triaxiality) (McCarthy and Petit (2004), Chapter 5.5.1). Detailed information on EOP can be found in Moritz and Mueller (1987); Souchay and Kinoshita (1997); Sovers et al. (1998); Roosbeek (1999); Bizouard et al. (2000, 2001); Mathews et al. (2002); Mathews and Bretagnon (2003); Brzeziński and Capitaine (2003); McCarthy and Petit (2004); Dehant and Mathews (2009); Gross (2009).

Hourly CPWLO dx_p and dy_p estimates at UTC integer hours from VieVS analysis during IVS-CONT08 are compared with the HF-ERP models (McCarthy and Petit (2004), Chapter 5 and 8). In the analysis, a priori nutation offsets were fixed to IAU2000A precession-nutation model plus IERS 05 C04 corrections. ERP were estimated at integer UTC hours without any constraints imposed. A priori ERP values before the parameter estimation are provided by a linear interpolation of the IERS 05 C04 daily combined ERP series to the epochs of observations and HF-ERP models were not added. The detailed VieVS parametrization is given in Tables 8.2 and 8.4.

Table 8.4.: Parametrization for the estimation of hourly CPWLO ERP with VieVS during IVS-CONT08 to analyze on HF-ERP.

a priori ERP	IERS 05 C04 series.
a priori nutation offsets	IAU2000A precession-nutation model plus
	IERS 05 C04 corrections (McCarthy and Petit, 2004).
Earth orientation parameters	Nutation offsets were fixed to their a priori values.
	CPWLO of ERP were estimated for 60 minutes interval.
	Neither absolute nor loose constraints were used between
	the CPWLO of ERP.

The formal errors of the hourly CPWLO estimates of ERP during IVS-CONT08 from VLBI and GPS (Steigenberger et al., 2006), mean and standard deviations of the differences between the estimates and the values from the HF-ERP models are calculated. The formal errors of hourly CPWLO ERP estimates from VLBI during IVS-CONT08 are within [59,155] μas for dx_p , for dy_p [64,174] μas, and for $dUT1$ [3,9] μs. The formal errors of hourly polar motion estimates from GPS during IVS-CONT08 are within [15,20] μas for dx_p, [17,21] μas for dy_p (Figure 8.13, 8.14, and 8.15). The formal errors of GPS ERP estimates are smaller than the VLBI ERP formal errors. This is due to the number of GPS observations per estimation interval being more than those of VLBI (higher sampling, more stations $\sim$ 100).

The standard deviation of the differences between the hourly VLBI dx_p estimates and the hourly computed values of HF-ERP models is 224.5 μas and the mean value of the difference vector (estimate minus model) is -52.8 μas (Figure 8.13). The standard deviation of the differences between the hourly GPS estimates, dx_p and the hourly computed values from HF-ERP models is 122.05 μas and the mean value of the difference vector (estimate minus model) is 54.1 μas.
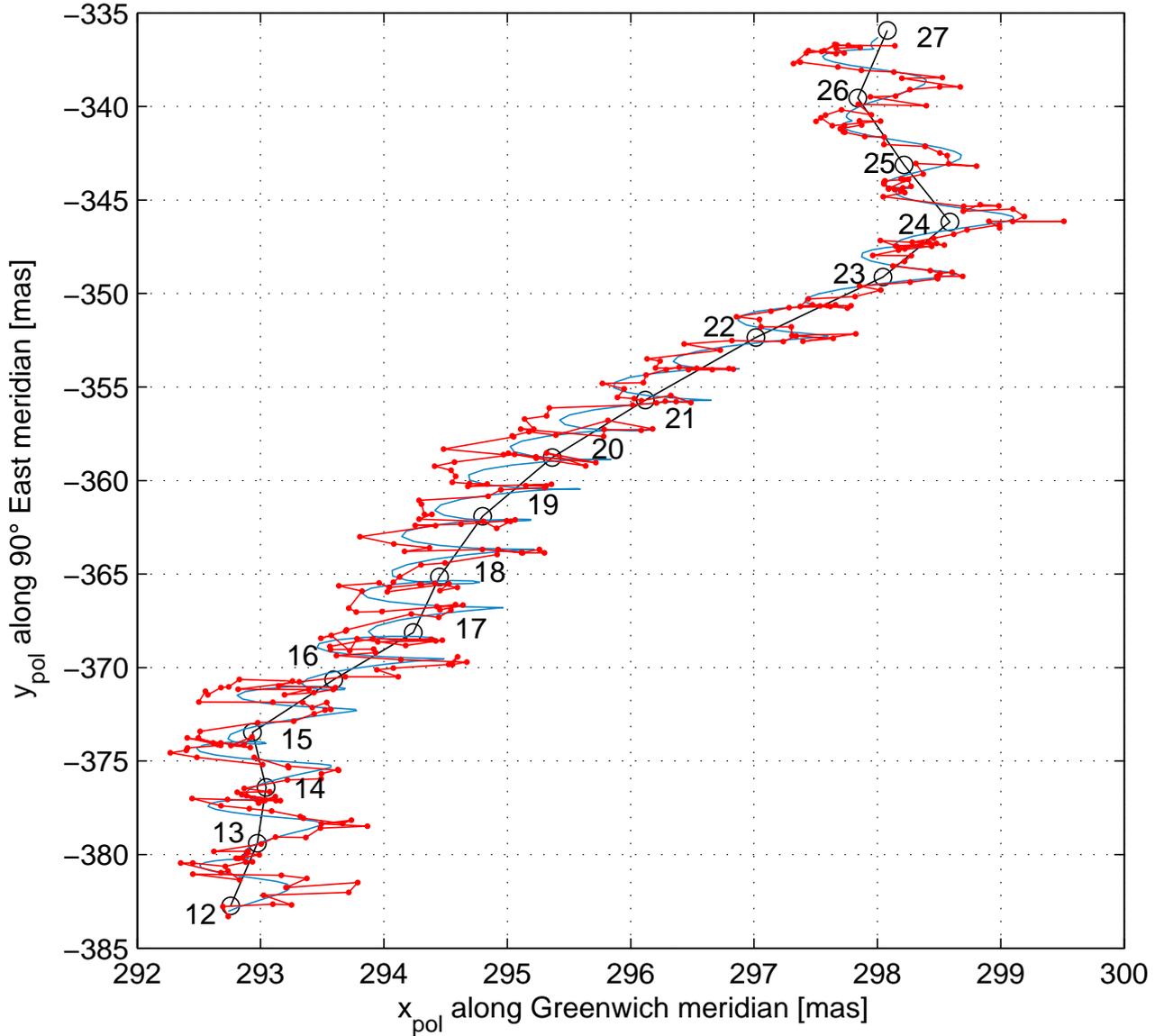
Figure 8.12.: The red dotted line shows the hourly CPWLO dx_p, and dy_p estimates of VieVS during IVS-CONT08 in addition to linearly interpolated a priori $(x_p, y_p)_{IERS}$. A priori to the parameter estimation corrections from HF-ERP models were not added to IERS 05 C04 daily combined ERP series. The corrections from the HF-ERP models $((\Delta x, \Delta y)_{ocean\ tides}$ plus $(\Delta x, \Delta y)_{libration})$ in addition to linearly interpolated $(x_p, y_p)_{IERS}$ are shown in the same plot in blue. Black circles show the daily $(x_p, y_p)_{IERS}$ at epochs 0:00 UTC and the assigned numbers to the black circles denote the dates of August 2008. The VieVS analysis options are given in Table 8.2 and 8.4.

The standard deviation of the differences between the hourly dy_p estimates and the hourly computed values of HF-ERP models is 187.2 μas and the mean value of the difference vector (estimates minus model) is 58.1 μas (Figure 8.14). On the other hand, the standard deviation of the differences between the hourly GPS dy_p estimates and the hourly computed values of HF-

ERP models is 139.25 μas and the mean value of the difference vector (estimate minus model) is -57.5 μas.

The standard deviation of the polar motion coordinates difference vector of VLBI minus model is larger than GPS minus model. This could be due to the constraints on the estimated ERP offsets. In VLBI analysis neither relative nor absolute constraints on the ERP estimates were introduced (see Table 8.4).

The standard deviation of the differences between the hourly $dUT1$ estimates and the hourly computed values of HF-ERP models is 22.9 μs and the mean value of the difference vector (estimate minus model) is 6.6 μs (Figure 8.15).
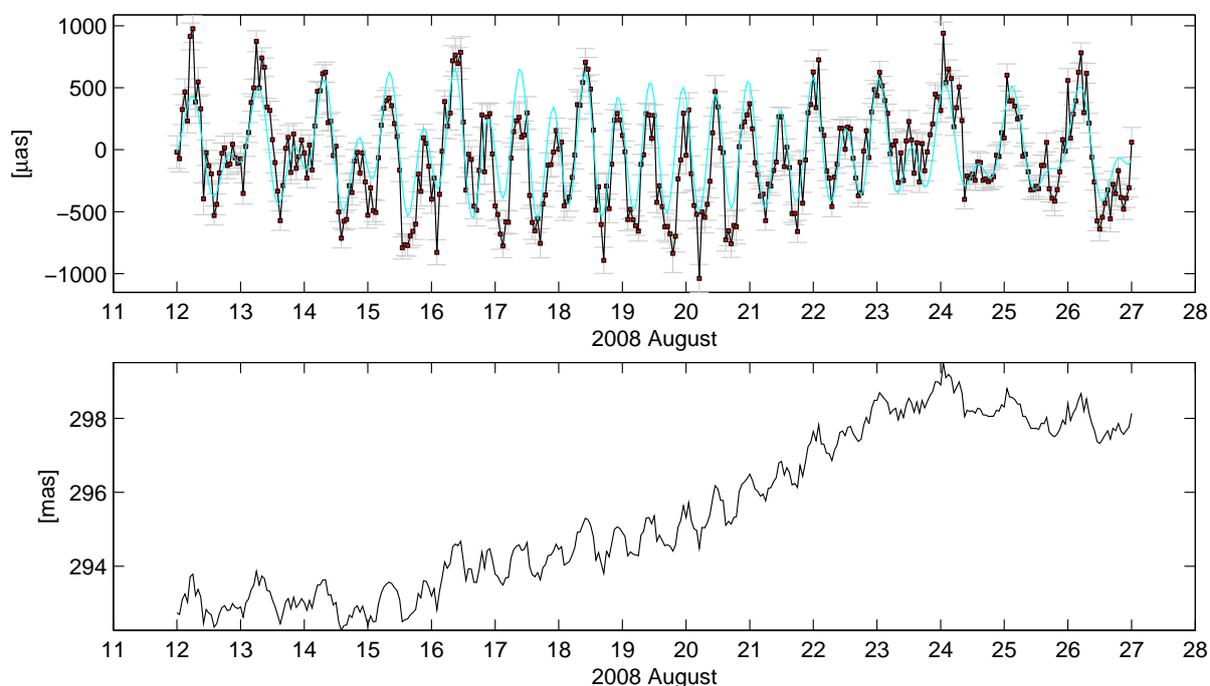
Figure 8.13.: In the upper figure, grey bars show the VieVS hourly (at UTC integer hours) CPWLO dx_p estimates with their formal errors during IVS-CONT08. The total hourly Δx values of the HF-ERP models are shown in the same plot in cyan. In the lower plot, linearly interpolated $(x_p)_{IERS}$ plus VieVS hourly CPWLO dx_p estimates are shown. The VieVS analysis options are given in Tables 8.2 and 8.4.

The Fourier spectra amplitudes of the hourly VLBI and GPS ERP estimates and the HF-ERP models during IVS-CONT08 are in a good agreement at prograde and retrograde 12 hours both for LOD and polar motion (Figure 8.18). However, at 24 hours prograde polar motion the amplitude from GPS is larger by about 100 μas than VLBI and larger by about 160 μas than HF-ERP models. The VLBI, VieVS LOD and polar motion estimates are more noisy than from
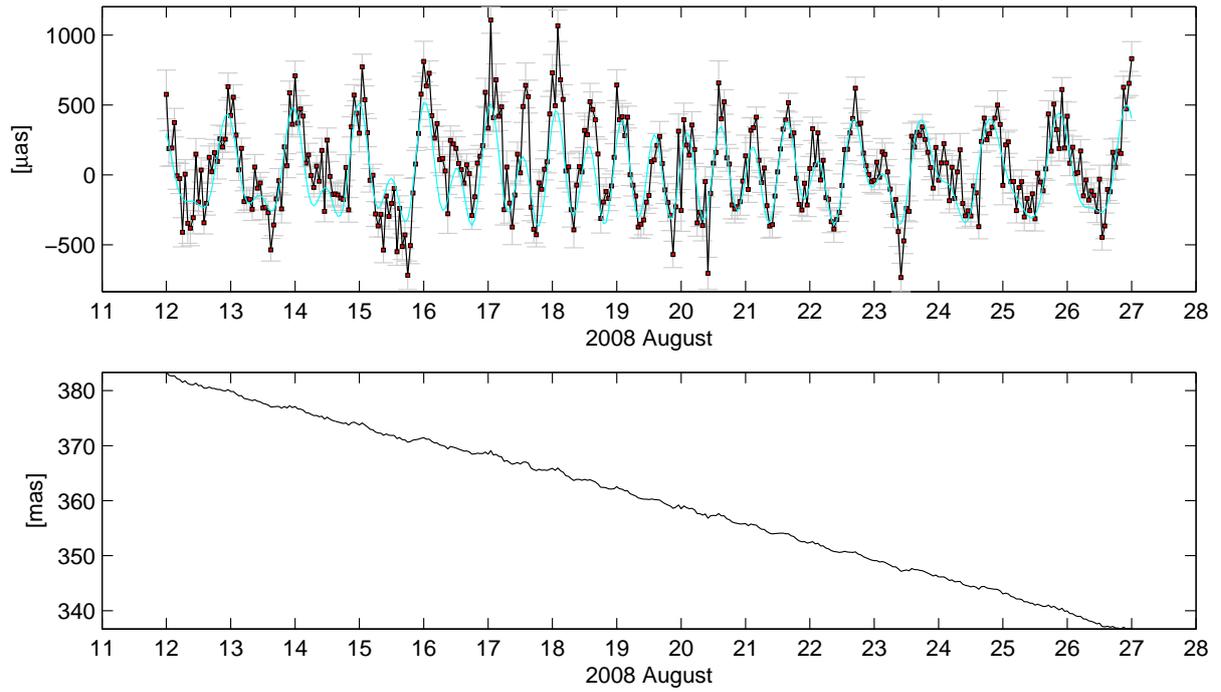
Figure 8.14.: In the upper figure, grey bars show the VieVS hourly (at UTC integer hours) CPWLO dy_p estimates with their formal errors during IVS-CONT08. The total hourly Δy values of the HF-ERP models are shown in the same plot in cyan. In the lower plot, linearly interpolated $(y_p)_{IERS}$ plus VieVS hourly CPWLO dy_p estimates are shown. The VieVS analysis options are given in Tables 8.2 and 8.4.

GPS. This may be due to the fact that relative constraints between the CPWLO ERP estimates in VLBI analysis were not introduced. The Fourier spectra of the IVS-CONT08 hourly polar motion and hourly LOD estimates given in Figure 8.18 reveal a good agreement with those of the results from Nilsson et al. (2010).
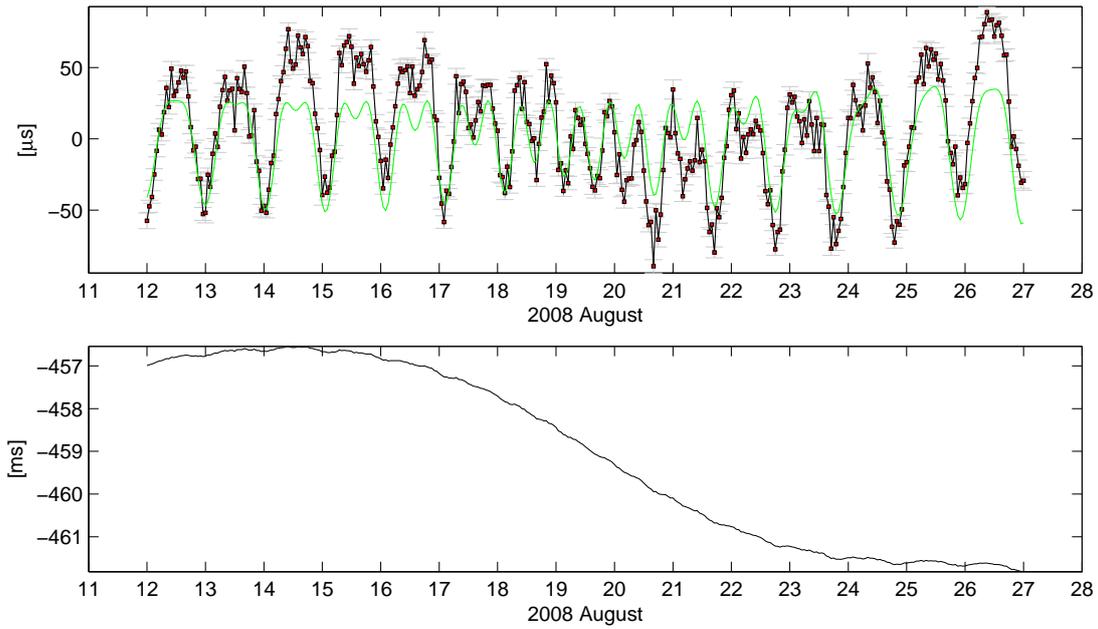
Figure 8.15.: In the upper figure, grey bars show the VieVS hourly (at UTC integer hours) CPWLO $dUT1$ estimates with their formal errors during IVS-CONT08. The total hourly $\Delta UT1$ values of the HF-ERP models are shown in the same plot in green. In the lower plot, linearly interpolated $\Delta UT1_{IERS}$ plus VieVS hourly CPWLO $dUT1$ estimates are shown. The VieVS analysis options are given in Tables 8.2 and 8.4.
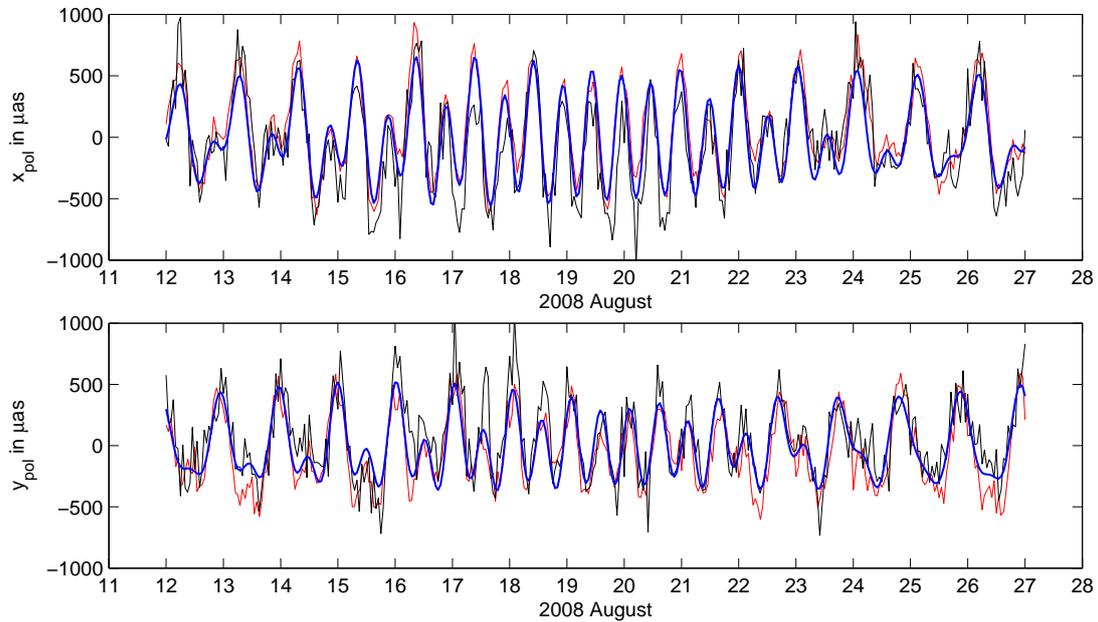
Figure 8.16.: In both upper and lower plots the blue line shows the hourly $(\Delta x, \Delta y)$ values of HF-ERP models. The red line shows GPS hourly (dx_p, dy_p) estimates (Steigenberger et al., 2006) (after linearly interpolated $(x_p, y_p)_{IERS}$ are reduced from the total estimates). The black line shows the VLBI, VieVS hourly CPWLO estimates of (dx_p, dy_p). The VieVS analysis options are given in Tables 8.2 and 8.4.
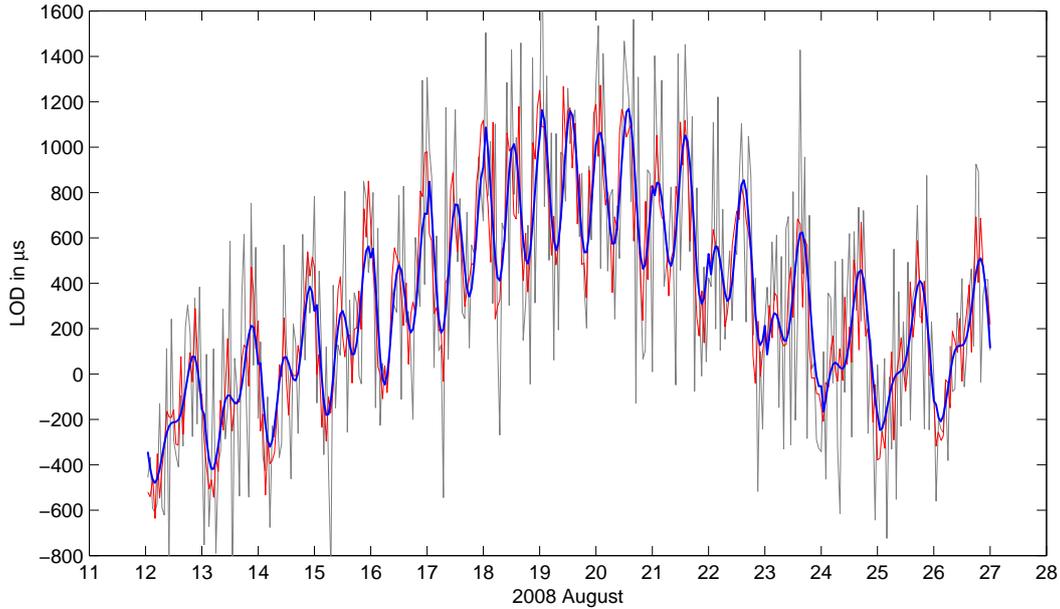
Figure 8.17.: The blue line shows the hourly length of day (LOD) variations derived from HF-ERP models. The red line shows the GPS hourly LOD estimates (Steigenberger et al., 2006). The black line shows the VLBI, VieVS hourly LOD estimates. The LOD were calculated from $\Delta UT1$ offsets of HF-ERP models and $dUT1$ CPWLO estimates of VieVS. The VieVS analysis options are given in Tables 8.2 and 8.4.
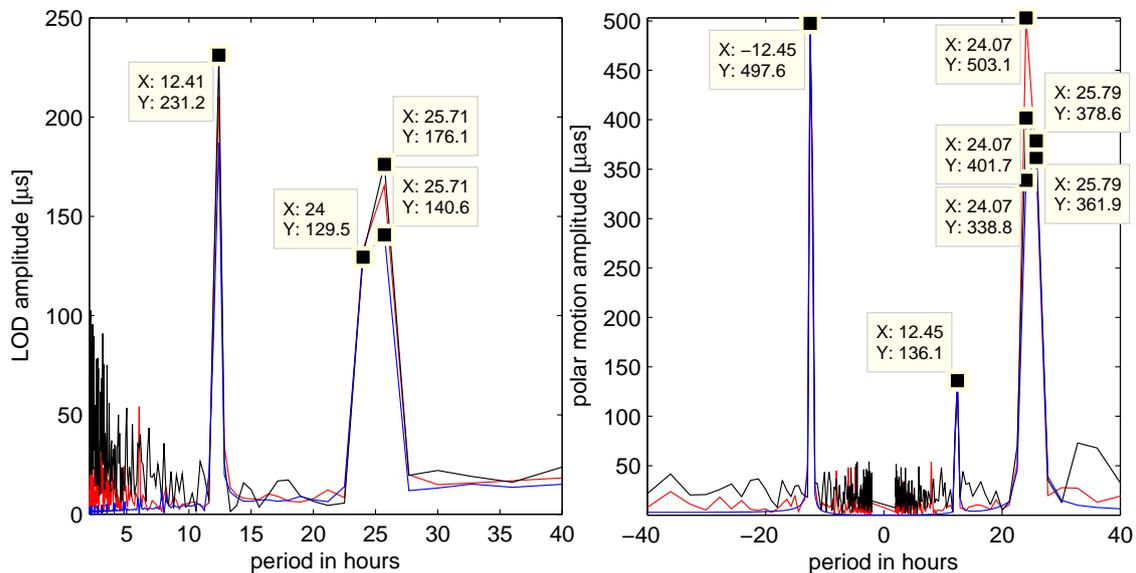
Figure 8.18.: Fourier spectra plots of LOD and polar motion. The blue line shows the spectra of the hourly ERP values from HF-ERP models. The red line shows the spectra of the hourly ERP estimates from GPS. The black line shows the spectra of the hourly ERP estimates from VLBI (VieVS). The LOD were calculated from the time derivatives of $\Delta UT1$ values of HF-ERP models and $dUT1$ estimates of VieVS. The VieVS analysis options are given in Tables 8.2 and 8.4.

8.3. Analyses of the sub-daily coordinate time series of several defining sources in ICRF2 during IVS-CONT08

In this chapter, hourly CPWLO coordinate estimates from VieVS of four sources: 1803+784, 1357+769, 1606+106, and 1749+096 are investigated during IVS-CONT08. The aim is to investigate the effects of different EOP parametrization on hourly source coordinates. The reasons of analyzing these four sources are to figure out if the long term stable sources have sub-daily harmonic coordinate variations, and if the sub-daily CPWLO source coordinate estimates are sensitive to EOP parametrization. Since, source positions do not have any motion this part of the study is just a kind of 'abstract test' without real implication. Only two source coordinates are estimated in each run while the others are fixed to ICRF2. Structure indices of all four investigated sources are one or two at both S-band (2 GHz) and X-band (8 GHz), which means that all them are point like (structure indices: 1-3) sources. The other structure indices are resolved (3-10), extended (10-30), and very extended (>30). 1803+784, 1357+769, 1606+106, and 1749+096 are stable over time. These sources are among the 259 defining sources of ICRF2. It should be noted that defining sources are the sources of which ICRF2 coordinates will be used for the next ICRF realization as datum sources. ICRF2 has a noise floor of 40 μas and an axis stability of 10 μas. ICRF2 was aligned to ICRF1 with 138 stable sources also included in ICRF-Ext2 (Fey et al., 2009; McCarthy and Petit, 2004).

Two of the sources 1357+769 and 1803+784, (first group) were selected among the sources which are close to celestial north pole and the other two 1606+106, and 1747+096, (second group) were selected close to the celestial equator. Hourly CPWLO CRF coordinates (right ascension, α and declination, δ) of the sources in a group were estimated from the IVS-CONT08 data and the coordinates of the other sources were fixed to ICRF2. 1357+769 and 1803+784 are close to the celestial north pole and have the maximum number of observations per session relative to other sources during IVS-CONT08. The solution options are the same for both groups. The relative constraints between source coordinates were selected as 1250 μas/hour. Troposphere total gradients were estimated with 3 hours intervals and loose constraints were introduced as 0.25 mm/3hours. The parametrization of the analysis of IVS-CONT08 sessions are given in Table 8.8.

Three different IVS-CONT08 solutions were carried out to find out the effects of the EOP parametrization on the hourly CRF coordinates of the sources. Common parametrization of

all the solutions are given in Table 8.8. In the first solution (referred as Solution1) all EOP were estimated as CPWLO with 1 day estimation interval. Tight constraints (10^{-4} m(a)s) were introduced between EOP estimates. Results are given in Table 8.5 and and the coordinate time series are plotted in black line in Figure 8.21.

Table 8.5.: Median of the hourly CPWLO estimates ($\bar{\alpha}$ and $\bar{\delta}$) and of their formal errors ($m_{\bar{\alpha}}$ and $m_{\bar{\delta}}$) during IVS-CONT08 from Solution1.

Source	α_{ICRF2} in degrees	δ_{ICRF2} in degrees	$\bar{\alpha} \pm m_{\bar{\alpha}}$ in μas	$\bar{\delta} \pm m_{\bar{\delta}}$ in μas
1357+769	209.4807	76.7225	220 ± 324	46 ± 131
1803+784	270.1903	78.4678	201 ± 333	2 ± 122
1606+106	242.1925	10.4855	-61 ± 493	4 ± 687
1749+096	267.8867	9.6502	-58 ± 495	2 ± 764

In the second solution, Solution2, all EOP were fixed to their a priori values (the other parametrizations are given in Table 8.8). The results are given in Table 8.6 and the coordinate time series are plotted in green line in Figure 8.21.

Table 8.6.: Median of the hourly CPWLO estimates ($\bar{\alpha}$ and $\bar{\delta}$) and of their formal errors ($m_{\bar{\alpha}}$ and $m_{\bar{\delta}}$) during IVS-CONT08 from Solution2.

Source	α_{ICRF2} in degrees	δ_{ICRF2} in degrees	$\bar{\alpha} \pm m_{\bar{\alpha}}$ in μas	$\bar{\delta} \pm m_{\bar{\delta}}$ in μas
1357+769	209.4807	76.7225	204 ± 324	37 ± 132
1803+784	270.1903	78.4678	87 ± 331	10 ± 122
1606+106	242.1925	10.4855	-103 ± 495	62 ± 694
1749+096	267.8867	9.6502	-79 ± 495	-12 ± 768

In the third solution, Solution3, nutation offsets were fixed to their a priori values and ERP were estimated at UTC hours. Loose constraints (30 mas/day = 1250 μas after one hour for polar motion and 2 ms/day = 83 μs after one hour for $UT1 - UTC$) were introduced (the other parameterizations are given in Table 8.8). The results are given in Table 8.7 and the coordinate time series are plotted in red line in Figure 8.21.

Table 8.7.: Median of the hourly CPWLO estimates ($\bar{\alpha}$ and $\bar{\delta}$) and of their formal errors ($m_{\bar{\alpha}}$ and $m_{\bar{\delta}}$) during IVS-CONT08 from Solution3.

Source	α_{ICRF2} in degrees	δ_{ICRF2} in degrees	$\bar{\alpha} \pm m_{\bar{\alpha}}$ in μas	$\bar{\delta} \pm m_{\bar{\delta}}$ in μas
1357+769	209.4807	76.7225	210 ± 326	45 ± 132
1803+784	270.1903	78.4678	147 ± 340	-4 ± 124
1606+106	242.1925	10.4855	-87 ± 488	32 ± 678

1749+096	267.8867	9.6502	-74 ± 487	-10 ± 752

Table 8.8.: Parametrization for the estimation of hourly of CPWLO source coordinates with VieVS during IVS-CONT08.

a priori CRF	ICRF2 (except two sources the others were fixed).
a priori TRF	VTRF2008 (NNT and NNR conditions were applied on the coordinate estimates with a priori coordinates from VTRF2008.).
a priori ERP	IERS 05 C04 ERP series plus HF-ERP models* (*ocean tides and libration (McCarthy and Petit (2004), Chapter 5 and 8)).
a priori nutation offsets	IAU2000A precession-nutation model plus IERS 05 C04 corrections (McCarthy and Petit, 2004).
corrections to the	
antenna TRF coordinates	Solid Earth tides (McCarthy and Petit (2004), Chapter 7.1.1), ocean tidal loading (FES 2004, Lyard et al. (2006)), tidal and non-tidal atmosphere loading (Petrov and Boy, 2004), pole tide (McCarthy and Petit (2004), Chapter 7.1.4).
corrections to the baselines	Thermal deformation of the antennas (Nothnagel, 2009). Antenna axis offset correction.
Troposphere MF	Vienna Mapping Functions1 (VMF1) (Böhm et al., 2006).
handling observations	Outliers ($v_i \geq 3m_{v_i}$) were eliminated. No down-weighting of the observations was introduced. No cut-off elevation angle to the observations was introduced.
Estimated parameters	
Clocks	Quadratic clock function coefficients (first LS). Hourly CPWLO of clocks plus rate and quadratic term (second LS). Loose constraints were used between the hourly CPWLO of clocks (0.5 $ps^2/s = 13$ mm after one hour).
zenith wet delays	CPWLO of ZWD for 30 minutes intervals. Loose constraints were used between ZWD. (0.7 $ps^2/s = 10.6$ mm after 30 minutes).
troposphere gradients	CPWLO of troposphere total gradients for 3 hours intervals. Loose constraints were used between gradients. 2 mm/day = 0.25 mm after 3 hours.
Earth orientation parameters	Options are explained in the following parts of this section.
antenna TRF coordinates	One offset estimate per session (day). Condition equations were introduced to the normal equation system providing the new TRF of the estimated coordinates have NNT and NNR w.r.t. VTRF2008.

The median formal errors ($m_{\bar{\alpha}}$ and $m_{\bar{\delta}}$) only change slightly between different solutions. Dominantly, the number of observations per estimation interval determines the magnitude of the formal errors. The total number of observations carried out per session for each source during IVS-CONT08 is given in Table 8.9. The median of hourly α estimates ($\bar{\alpha}$) differs from one solution to another by up to 114 μas for the source 1803+784. For the other sources $\bar{\alpha}$ differs by not more than 42 μas. The median of hourly δ estimates ($\bar{\delta}$) differs from one solution to another by up to 58 μas.
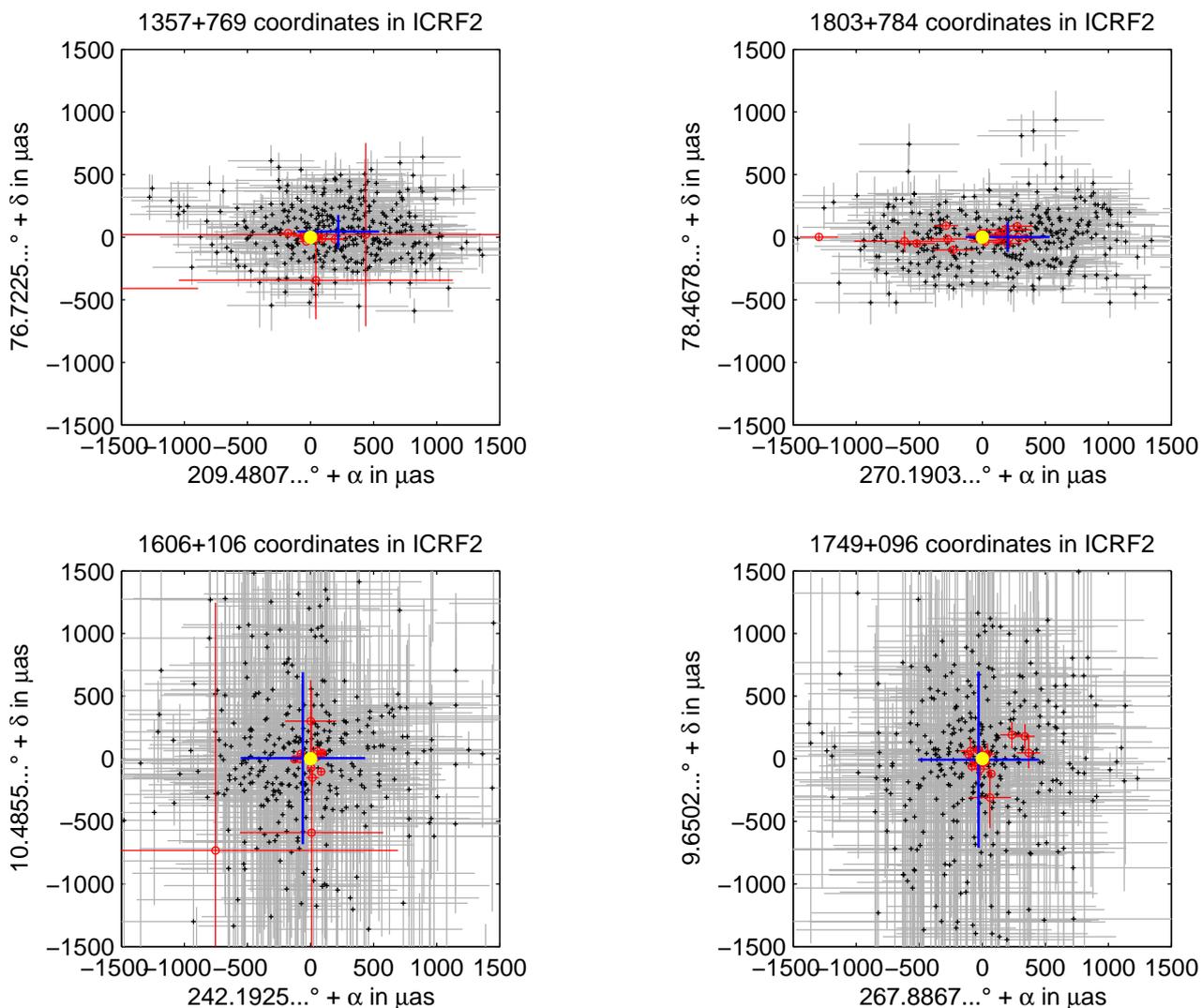
Figure 8.19.: Black dots show the hourly positions of the sources in ICRF2 during IVS-CONT08 with their formal errors in grey error bars. All EOP were estimated once per day (Solution1). The blue dot with error bar shows the median of hourly CPWLO source positions and their median of formal errors, respectively. The yellow dot is the ICRF2 catalogue coordinate. Red error bars show the yearly coordinates and formal errors from IERS solution taken from the official web site where the time stabilities of sources are shown. All analysis options are given in Table 8.8.

The dispersion of hourly CPWLO α is about three times larger than the dispersion of δ for the polar sources. On the other hand, this is not the case for the sources close to equator. This is the result of not scaling α with $\cos \delta$.

Table 8.9.: Total number of observations per source during IVS-CONT08.

Day of August	12	13	14	15	16	17	18	19	20	21	22	23	24	25	26
1357+769	873	1049	861	865	807	702	798	766	831	782	820	945	751	916	826
1803+784	871	699	909	815	855	927	754	846	829	786	809	874	608	848	981
1606+106	193	260	182	253	195	187	207	252	197	210	290	193	182	263	174
1749+096	212	249	207	215	232	156	235	180	164	257	166	169	181	122	177

When we compare the three solutions, the following results can be drawn;

- The formal errors do not change significantly from one solution to another. The magnitude of the formal errors depends on the number of observations to the source per estimation interval.

- The $\bar{\alpha}$ and $\bar{\delta}$ are smaller than their formal errors, thus the biases between the medians and the ICRF2 catalogue coordinates (corresponding to zero in the Figures 8.19, 8.20, and 8.21) are insignificant.

- When the variation of the hourly α and δ CPWLO estimates are between the aforementioned three solutions considered, only small changes are visible in the time series and in the Fourier spectra.

The significant peaks in the spectra of α and δ for such a small sampling interval for source coordinates (i.e. hour) are most likely caused by un-modelled effects (e.g. errors in troposphere modelling or source structure effects) in observations that propagate to hourly source coordinates.

From the investigations on the time series of the hourly source positions and on the spectra of the time series, the following results can be concluded:

- The hourly CPWLO coordinates of all three solutions are in a good agreement in time domain (Figure 8.21) and in frequency domain (Figure 8.22).
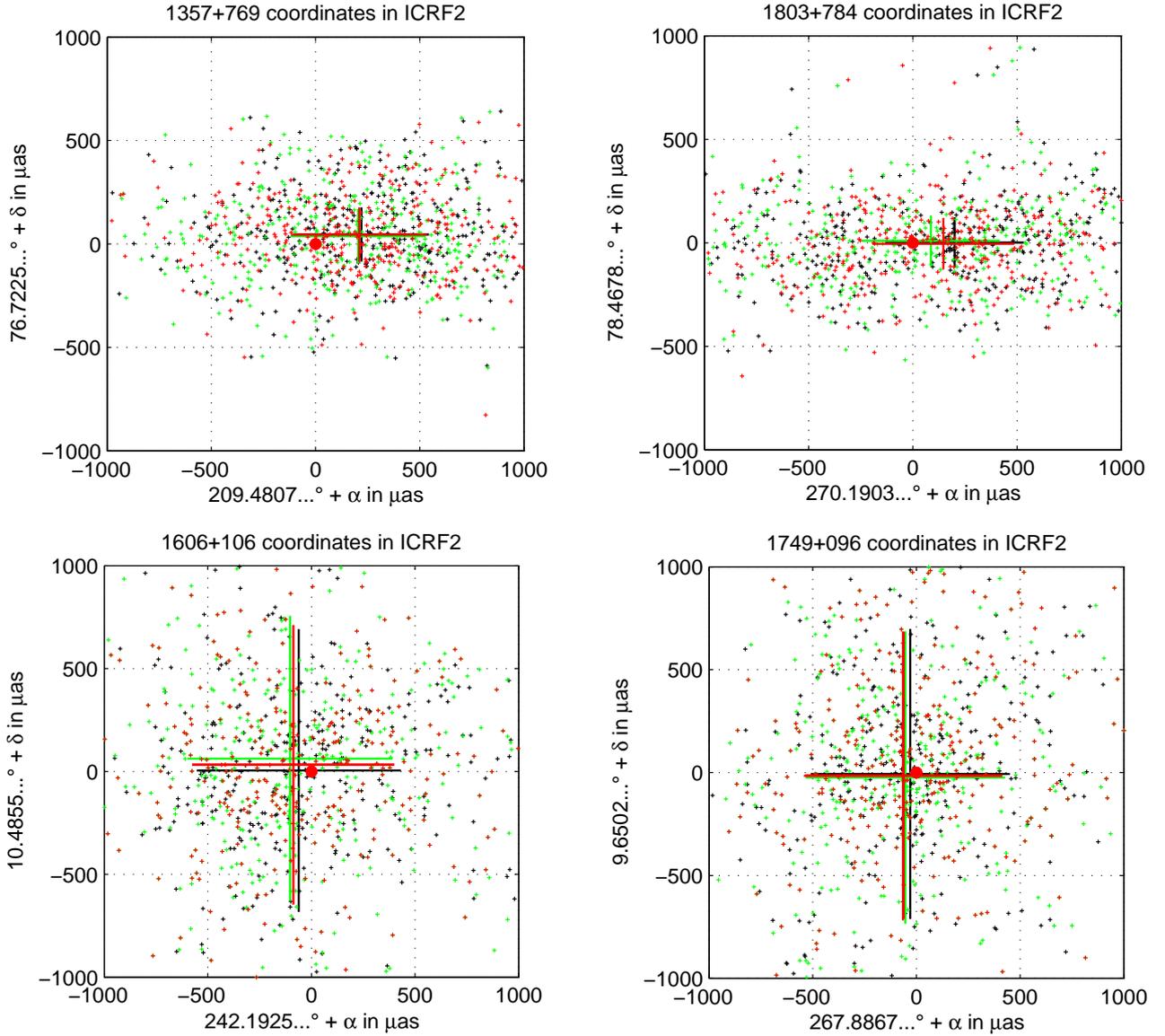
Figure 8.20.: Black dots show the hourly position estimates of the sources during IVS-CONT08 when all EOP were estimated once per day (Solution1). Green dots show the estimates when all EOP were fixed to their a priori values (Solution2). Red dots show the estimates when all ERP were estimated hourly and nutation offsets were fixed (Solution3). Black, green and red error bars illustrate the median of hourly coordinate estimates and their formal errors. Other analysis options which are the same for these three solutions are given in Table 8.8.

- As long as hourly CPWLO coordinates of two sources are estimated and the remaining sources are fixed to their a priori CRF, EOP parametrization is not critical.
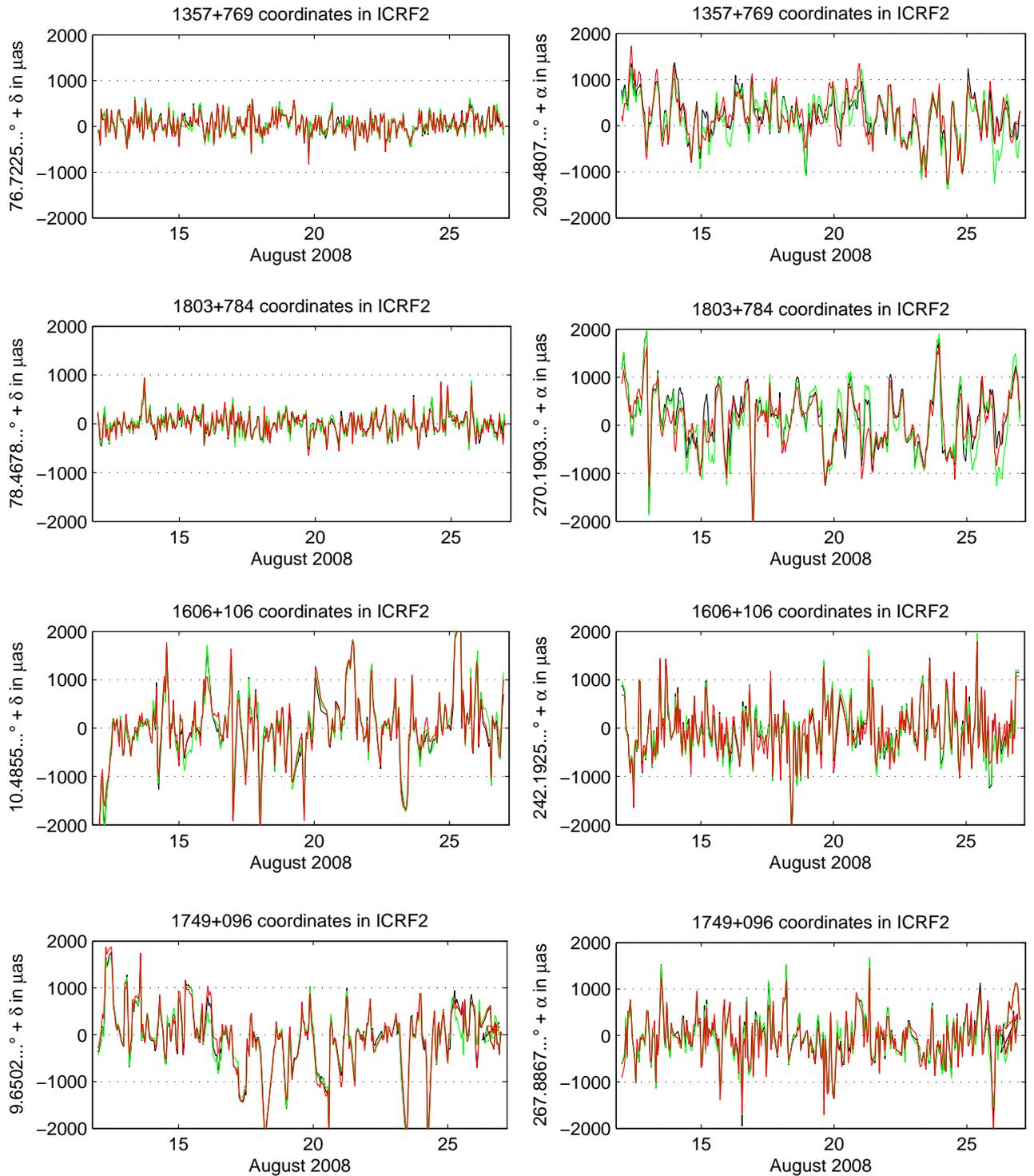
Figure 8.21.: Time series of the hourly CPWLO coordinate estimates in ICRF2 during IVS-CONT08 of the sources: $1357 + 769$, $1803 + 784$, $1606 + 106$ and $1749 + 096$. Black lines show the series when all EOP are estimated once per day (Solution1). Green lines show the series when all EOP are fixed to their a priori values (Solution2). Red lines show the series when all ERP are estimated hourly and nutation offsets are fixed (Solution3). Other analysis options which are the same for these three cases as given in Table 8.8.
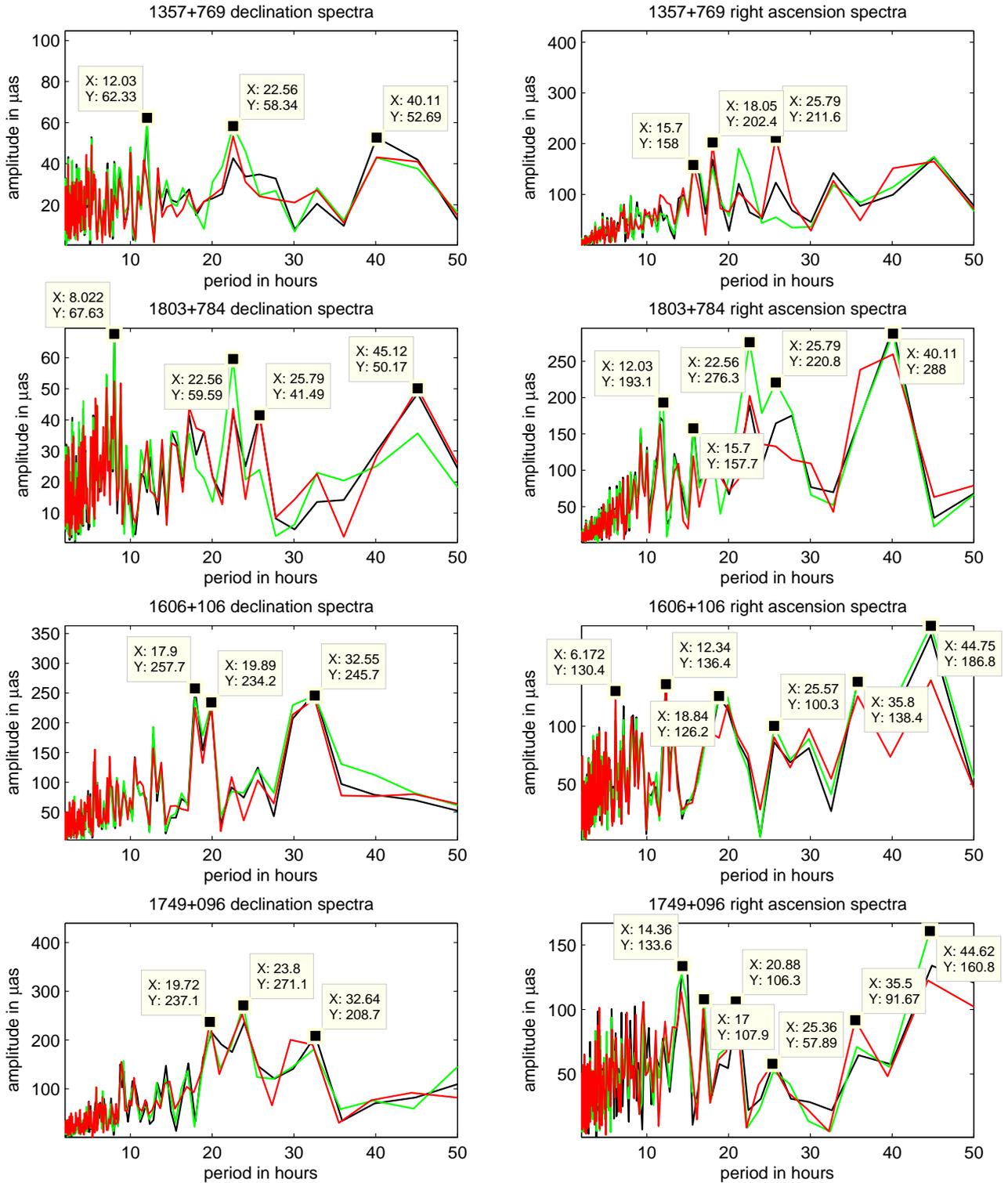
Figure 8.22.: Spectra of the hourly CPWLO CRF coordinate estimates during IVS-CONT08 of the sources: $1357 + 769$, $1803 + 784$, $1606 + 106$ and $1749 + 096$. Black lines show the spectra when all EOP are estimated once per day (Solution1). Green lines show the spectra when all EOP are fixed (Solution2). Red lines show the spectra when all ERP are estimated hourly and nutation offsets are fixed (Solution3). Other analysis options which are the same for these three cases are given in Table 8.8. In the plots, X values refer to the periods in hours and Y refer to the amplitudes in μas of the hourly source coordinate time series Fourier spectra.

9. Conclusions and Outlook

A new VLBI analysis software called Vienna VLBI Software (VieVS) (Böhm et al., 2010) was developed at the Institute of Geodesy and Geophysics of the Vienna University of Technology (in MATLAB programming language). VieVS is designed to meet the analysis related requirements of VLBI in the future, in particular the huge amount of observations compared to the present status.

The LS parameter estimation module of VieVS is named, vie_lsm. In vie_lsm, most of the parameters to be estimated are basically modelled with continuous piece-wise linear offset (CPWLO) functions where offsets are estimated at integer hours, integer fractions or at integer multiples of integer hours. These parameters are:

- CPWLO of clocks (plus rate and quadratic terms of the clocks polynomials),

- CPWLO of zenith wet delays,

- CPWLO of troposphere north and east gradients,

- CPWLO of polar motion coordinates in TRF along the Greenwich meridian, (x_p) and along the 270° east meridian (y_p),

- CPWLO of Earth's rotation phase $(\Delta UT1)$,

- CPWLO of celestial intermediate pole (CIP) coordinates in CRF (X, Y),

- CPWLO of right ascensions and declinations of sources in CRF,

- CPWLO of VLBI antenna cartesian coordinates in TRF (or of one offset (optional)).

It has been shown that hourly CPWLO of these parameters can be calculated reliably with VieVS. This allows e.g. the comparison of hourly station coordinates with tidal models of station displacements. For IVS-CONT05 there are radial amplitudes of about 7 mm at Kokee and 9 mm at HartRAO at semi-diurnal periods when all the tidal models are reduced from the observations a priori to the adjustment. In the case of diurnal periods, clear spectral peaks can be seen at the VLBI sites Gilcreek (6 mm), Kokee (6 mm), Westford (7 mm), and HartRAO (8 mm).

The comparison of hourly ERP during IVS-CONT08 yields good agreement with hourly ERP from GPS (standard deviations of dx_p and dy_p differences between VLBI and GPS are about 200 μas) and with high frequency ERP (HF-ERP) models (ocean tides and libration terms). The standard deviations of the dx_p and dy_p differences between VLBI and HF-ERP models are 224 and 187 μas, respectively.

The estimation of hourly source coordinates was rather intended as test study. More investigations on this issue need to be carried out in future, e.g. a lot can be learned from correlations between hourly source coordinates and observation geometry.

With VLBI2010, many more observations will be available so that the parameters can be estimated with even smaller estimation intervals, e.g. 10 minutes. This will allow the validation and improvement of many existing models, e.g. ocean loading models, if a good distribution of VLBI sites is available.

From the comparisons of troposphere ZTD and gradients with other techniques the following results are found: Space geodetic techniques generally agree at the sub-centimeter level during IVS-CONT08 and, as expected, the best agreement is found for intra-technique comparisons: VieVS with the combined IVS solutions as well as the Center for Orbit Determination in Bern (CODE) solution with an IGS Kalman filter series; both intra-technique comparisons show standard deviations of about 3 to 6 mm. The best inter space geodetic technique agreement of ZTDs during IVS-CONT08 is found between the combined IVS and the IGS solutions with a mean standard deviation of about 6 mm over all sites, whereas the agreement with numerical weather models is between 6 and 20 mm. The standard deviations are generally larger at low latitude sites because of higher humidity, and the latter is also the reason why the standard deviations are larger at northern hemisphere stations during IVS-CONT08 in comparison to IVS-CONT02 which was observed in October 2002. The assessment of the troposphere gradients from the

different techniques is not as clear because of different time intervals, different estimation properties, or different observables. However, the best inter-technique agreement is found between the IVS combined gradients and a GPS solutions with standard deviations between 0.2 mm and 0.7 mm.

References

Allan, D. and J. Barnes (1981). A Modified Allan Variance with Increased Oscillator Characterization Ability. In *Proc. 35th Annual Freq. Control Symp.*, pp. 470–474.

Altamimi, Z., X. Collilieux, J. Legrand, B. Garayt, and C. Boucher (2007). ITRF2005, A new release of the International Terrestrial Reference Frame based on time series of station positions and Earth orientation parameters. *J Geophys Res 112(B9)*(B09401).

Behrend, D., L. Cucurull, J. Vila, and R. Haas (2000). An inter-comparision study to estimate zenith wet delays using VLBI, GPS, and NWP models. *Earth Planets Space 52*, 691–694.

Behrend, D., R. Haas, D. Pino, L. Gradinarsky, S. Keihm, W. Schwarz, L. Cucurull, and A. Rius (2002). MM5 derived ZWDs compared to observational results from VLBI, GPS and WVR. *Physics and Chemistry of the Earth 27*, 3301–3308.

Bevis, M., S. Businger, S. Chiswell, T. Herring, R. Anthes, C. Rocken, and R. Ware (1994). GPS meteorology: mapping zenith wet delays onto precipitable water. *J Applied Meteorology 33*(3), 379–386.

Bizouard, C., M. Folgueira, and J. Souchay (2000). Comparison of the short period rigid Earth nutation series. In S. Dick, D. McCarthy, and B. Luzum (Eds.), *IAU Colloquium 178*, Volume 208 of *Publications of the Astron. Soc. Pac. Conf. Ser.*, pp. 613–617.

Bizouard, C., M. Folgueira, and J. Souchay (2001). Short period nutations: comparison between series and influence on polar motion. In N. Capitaine (Ed.), *Journèes 2000-Systèmes de Rèfèrence Spatio-Temporels*, pp. 260–265. Observatoire de Paris.

Bizouard, C. and D. Gambis (2009). The combined solution C04 for Earth orientation parameters consistent with International Terrestrial Reference Frame. In H. Drewes (Ed.), *Geodetic reference frames*, Volume 134 of *IAG symp*, pp. 265–270.

Böhm, J. (2004). Troposphrische Laufzeitverzgerungen in der VLBI. *Schriftenreihe der Studienrichtung Vermessung und Geoinformation, Technische Universitt Wien 68*.

Böhm, J. (2009, October). *Atmospheric Effects in Geodesy* (Lecture Notes ed.). Vienna, Aus-

tria: Institute of Geodesy and Geophysics, Vienna University of Technology.

Böhm, J., S. Böhm, T. Nilsson, A. Pany, L. Plank, H. Spicakova, K. Teke, and H. Schuh (2010). The new Vienna VLBI Software VieVS. In *IAG Symposia Series*, Buenos Aires. in press.

Böhm, J., R. Heinkelmann, J. Cerveria, A. Pany, and H. Schuh (2009). Atmospheric loading corrections at the observation level in VLBI analysis. *J Geod 83*, 1107–1113.

Böhm, J. and H. Schuh (2007). Troposphere gradients from the ECMWF in VLBI analysis. *J of Geod 81*, 403–408.

Böhm, J., B. Werl, and H. Schuh (2006). Troposphere mapping functions for GPS and Very Long Baseline Interferometry from European Center for Medium-Range Weather Forecasts operational analysis data. *J Geophys Res 111*(B02406).

Brockmann, E. (1997). Combination of solutions for geodetic and geodynamic applications of the Global Positioning System (GPS). Technical Report 55, Geodätisch Geophysikalische Arbeiten in der Schweiz, Schweizerische Geodätische Kommission.

Brunner, F. and J. Rüeger (1992). Theory of the local scale parameter method for EDM. *Bulletin Géodésique 66*, 355–364.

Brzeziński, A. and N. Capitaine (2003). Lunisolar perturbations in Earth rotation due to the triaxial figure of the Earth: geophysical aspects. In N. Capitaine (Ed.), *Journèes 2001-Systèmes de Rèfèrence Spatio-Temporels*, pp. 51–58. Observatoire de Paris.

Byun, S. and Y. Bar-Server (2009). A new type of troposphere zenith path delay product of the international GNSS service. *J Geod 83*(3-4), 1–7.

Campbell, J. (1979). *Die Radiointerferometrie auf langen Basen als geodätisches Messprinzip hoher Genauigkeit*. Number Heft 314 in Reihe C. München: DGK.

Campbell, J. (2000). From Quasar to Benchmarks: VLBI Links Heaven and Earth. In N. Vandenberg and K. Baver (Eds.), *International VLBI Service for Geodesy and Astrometry,*, Volume NASA/CP-2000 of *General Meeting Proceedings*.

Capitaine, N., D. Gambis, D. McCarthy, G. Petit, J. Ray, B. Richter, M. Rothacher, M. Standish, and J. Vondrak (2002). Proceedings of the IERS Workshop on the Implementation of the New IAU Resolutions. IERS Technical Note 29, Verlag des Bundesamts für Kartographie und Geodäsie, Frankfurt am Main.

Capitaine, N., B. Guinot, and D. McCarthy (2000). Definition of the Celestial Ephemeris origin and of UT1 in the International Celestial Reference Frame. *Astron. Astrophys. 335*(1), 398–405.

Capitaine, N., B. Guinot, and J. Souchay (1986). A Non-rotating Origin on the Instantaneous

Equator: Definition, Properties and Use. *Celest. Mech. 39*(3), 283–307.

Cartwright, D. and A. Edden (1973). Corrected tables of tidal harmonics. *Geophys. J. Roy. astr. Soc. 33*(3), 253–264.

Cartwright, D. and R. Tayler (1971). New computations of the tide-generating potential. *Geophys. J. Roy. astr. Soc. 23*(1), 45–74.

Chao, B., D. Dong, H. Liu, and T. Herring (1991). Libration in the Earth's rotation. *Geophys. Res. Letters 18*(11), 2007–2010.

Chen, G. and T. Herring (1997). Effects of atmospheric azimuthal asymmetry on the analysis from space geodetic data. *J Geophys Res 102*(B9), 20489–20502.

Claude, A. and G. Bernard (2001). *The measuremet of time - time, frequency and the atomic clock*. Cambridge University Press. Originally published in French, translated by Stephen Lyle.

Cucurull, L., B. Navascues, G. Ruffini, P. Elosegui, A. Rius, and J. Vila (2000). The use of GPS to validate NWP systems: the HIRLAM model. *J Atmospheric and Oceanic Technology 17*(6), 773–787.

Cucurull, L. and F. Vandenberghe (1999). Comparision of PW estimated from MM5 and GPS data. In *MM5 workshop '99'*, Boulder, Colorado, U.S.A.

Dach, R., E. Brockmann, S. Schaer, G. Beutler, M. Meindl, L. Prange, H. Bock, A. Jäggi, and L. Ostini (2009). GNSS processing at CODE: status report. *J Geod 83*, 353–365.

Dach, R., U. Hugentobler, P. Fridez, and M. Meindl (2007). *Bernese GPS Software Version 5.0*. Switzerland: Astronomical Institute, University of Bern.

Davis, J., G. Elgered, A. Niell, and K. C.E. (1993). Ground-based measurements of gradients in the "wet" radio refractivity of air. *Radio Sci 28*(6), 1003–1018.

Davis, J., T. Herring, and I. Shapiro (1991). Effects of atmospheric modeling errors on determinations of baseline vectors from VLBI. *J Geophys Res 96*(B1), 643–650.

Davis, J., T. Herring, I. Shapiro, A. Rogers, and G. Elgered (1985). Geodesy by radio interferometry: effects of atmospheric modeling errors on estimates of baseline length. *Radio Sci 20*(6), 1593–1607.

Dehant, V. and P. Mathews (2009). *Geodesy*, Volume 3, Chapter Earth Rotation Variations, pp. 295–349. Amsterdam, Boston, Heidelberg, London, New York, Tokyo: Elsevier.

Elgered, G. (1993). *Atmospheric remote sensing by microwave radiometry*, Chapter Tropospheric radio path delay from ground-based microwave radiometry, pp. 215–258. Wiley, NewYork.

Elgered, G. and P. Jarlemark (1998). Ground-based microwave radiometry and long-term

observations of atmospheric water vapor. *Radio Sci 33*(3), 707–717.

Emardson, T., G. Elgered, and J. Johansson (1998). Three months of continuous monitoring of atmospheric water vapor with a network of Global Positioning System receivers. *J Geophys Res 103*(D2), 1807–1820.

Eubanks, T. (Ed.) (1991). *Proceedings of the U. S. Naval Observatory Workshop on Relativistic Models for Use in Space Geodesy*. U. S. Naval Observatory, Washington, D.C.

Fey, A., D. Gordon, and C. Jacobs (2009). The Second Realization of the International Celestial Reference Frame by Very Long Baseline Interferometry. IERS Technical Note 35, Frankfurt am Main: Verlag des Bundesamts für Kartographie und Geodäsie.

Förstner, W. (1979). Ein Verfahren zur Schtzung von Varianz- und Kovarianzkomponenten. *Allg. Vermess. Nachr 11-12*(446-453).

Gambis, D. (2004). Monitoring Earth orientation using space geodetic techniques: State-of-the-art and prospective. *J Geod 78*(4-5), 295–303.

Gobinddass, M., P. Willis, M. Menvielle, and M. Diament (2010). Refining DORIS atmospheric drag in preparation of ITRF2008. *Adv Space Res*. in press.

Gobinddass, M. L., P. Willis, A. Sibthorpe, N. P. Zelensky, F. G. Lemoine, J. C. Ries, R. Ferland, and Y. E. Bar-Sever (2009). Improving DORIS geocenter time series using an empirical rescaling of solar radiation pressure models. *Adv Space res 44*(11), 1279–1287.

Gradinarsky, L., R. Haas, G. Elgered, and J. Johansson (2000). Wet path delay and delay gradients inferred from microwave radiometer, GPS and VLBI observations. *Earth Planets Space 52*(10), 695–698.

Gross, R. (2009). *Geodesy*, Volume 3, Chapter Earth Rotation Variations - Long Period, pp. 239–294. Amsterdam, Boston, Heidelberg, London, New York, Tokyo: Elsevier.

Haas, R., L. Gradinarsky, J. Johansson, and G. Elgered (1999). The atmospheric propagation delay: a common error source for collocated space techniques of VLBI and GPS. In *Proceedings of International Workshop "Geod. Meas. Coll. Spac. Tech. Earth" (GEMSTONE)*, Koganei, Tokyo, pp. 230–234.

Hartmann, T. and H. Wenzel (1995). The HW95 tidal potential catalogue. *Geophysical Research Letters 22*(24), 3553–3556.

Heinkelmann, R., J. Böhm, S. Bolotin, G. Engelhardt, R. Haas, D. MacMillan, M. Negusini, H. Schuh, E. Skurikhina, and O. Titov (2011). Analysis and model noise assessment of VLBI derived tropospheric parameters during CONT08. *J Geod*. in press.

Heinkelmann, R., J. Böhm, H. Schuh, S. Bolotin, G. Engelhardt, D. MacMillan, M. Negusini, E. Skurikhina, V. Tesmer, and O. Titov (2007). Combination of long time series of

troposphere zenith delays observed by VLBI. *J Geod 81*, 483–501.

Heinkelmann, R., J. Freymueller, and H. Schuh (2008). A postseismic relaxation model for the 2002 Denali earthquake from GPS deformation analysis applied to VLBI data. In A. Finkelstein and D. Behrend (Eds.), *5th IVS General Meeting Proceedings*, St. Petersburg, Russia, pp. 178–182.

Helmert, F. (1872). *Die Ausgleichungsrechnung nach der Methode der kleinsten Quadrate.* Teubner, Leipzig.

Herring, T. (1986). Precision of vertical estimates from very long baseline interferometry. *J Geophys Res 91*(B9), 9177–9182.

Herring, T., J. Davis, and I. Shapiro (1990). Geodesy by Radio Interferometry: The Application of Kalman Filtering to the Analysis of Very Long Baseline Interferometry Data. *Journal of Geophysical Research 95*(B8), 12561–12581.

Hirvonen, R. (1971). *Adjustment by least squares in geodesy and photogrammetry.* Frederick Ungar Publishing Co. Inc., New York.

Hobiger, T., R. Ichikawa, Y. Koyama, and T. Kondo (2008). Fast and accurate ray-tracing algorithms for real-time space geodetic applications using numerical weather models. *J Geophys Res 113:D20302*.

Hobiger, T., R. Ichikawa, T. Takasu, Y. Koyama, and T. Kondo (2008). Ray-traced troposphere slant delays for precise point positioning. *Earth Planets Space 60*(5).

Hobiger, T., S. Shimada, S. Shimizu, R. Ichikawa, Y. Koyama, and T. Kondo (2010). Improving GPS positioning estimates during extreme weather situations by the help of fine-mesh numerical weather models. *J Atmosph Solar-Terrestr Phys 72*(2-3), 262–270.

Holman, K. (2005). *Distribution of an Ultrastable Frequency Reference Using Optical Frequency Combs.* Phd thesis, University of Colorado, Department of Physics.

Ishikawa, Y. (2001). Development of a mesoscale 4-dimensional variational data assimilation (4D-Var) system at JMA. In *Proceedings of the 81st Annual Meeting of the AMS: Precipitation Extremes: Prediction,Impacts and Responses*, Volume P2.45.

Kaplan, G. (1981). *The IAU Resolutions on Astronomical Constants, Time Scales, and the Fundemental Reference Frame.* Number 163. United States Naval Observatory Circular.

Koch, K. (1988). *Parameter estimation and hypothesis testing in linear models.* Springer, Berlin Heidelberg New York.

Koch, K. (1997). *Parameterschatzung und Hypothesentests.* 3rd edn. Dmmler, Bonn.

Kopeikin, S. (1990). Theory of relativity in observational radio astronomy. *Sov. Astron. 34*(1), 5–10.

Kopeikin, S. and G. Schafer (1999). Lorentz covariant theory of light propagation in gravitational fields of arbitrary-moving bodies. *Physical Review D 60*(12), 124002/1–44.

Kouba, J. (2009). Testing of global pressure/temperature (GPT) model and global mapping function (GMF) in GPS analyses. *J Geod 83*, 199–208.

Kutterer, H. (2003). The role of parameter constraints in VLBI Analysis. In W. Schwegmann and V. Thorandt (Eds.), *Proc. 16th Working Meeting on European VLBI for Geodesy and Astrometry*, pp. 171–180. Bundesamt für Kartographie und Geodäsie, Frankfurt/Leipzig.

Lambert, S. and C. Bizouard (2002). Positioning the Terrestrial Ephemeris Origin in the International Terrestrial Reference Frame. *Astron. Astrophys. 394*(1), 317–321.

Leick, A. (1990). *GPS Satellite Surveying*. New York, Chichester, Brisbane, Toronto, Singapore: Willey Inter Science.

Lyard, F., F. Lefevre, T. Lettelier, and O. Francis (2006). Modelling the global ocean tides, Modern insightths from FES2004. *Ocean Dyn 56*(6), 394–415.

MacMillan, D. (1995). Atmospheric gradients from very long baseline interferometry observations. *Geophys Res Lett 22*(9), 1041–1044.

MacMillan, D. and C. Ma (1994). Evaluation of very long baseline interferometry atmospheric modeling improvements. *J Geophys Res 99*(B1), 637–651.

MacMillan, D. and C. Ma (1997). Atmospheric gradients and the VLBI terrestrial and celestial reference frames. *Geophys Res Lett 24*(4), 453–456.

Malkin, Z. (2008). Influence of the Cut-off Elevation Angle and Elevation-Dependent Weighting on Parameter Estimates: A Case of CONT05. In A. Finkelstein and D. Behrend (Eds.), *5th IVS General Meeting Proceedings*, St. Petersburg, Russia, pp. 178–182.

Marini, J. (1972). Correction of satellite tracking data for an arbitrary tropospheric profile. *Radio Sci 7*(2), 223–231.

Mathews, P. (2009). *Geodesy* (First ed.), Volume 3 of *Treatise on Geophysics*, Chapter Earth Rotation Variations, pp. 295–350. New York: Elsevier.

Mathews, P. and P. Bretagnon (2003). High frequency nutation. In N. Capitaine (Ed.), *Journèes 2001-Systèmes de Rèfèrence Spatio-Temporels*, pp. 28–33. Observatoire de Paris.

Mathews, P., T. Herring, and B. Buffet (2002). Modelling of nutation and precession: New nutation series for nonrigid Earth, and insights into the Earth's Interior. *J. Geophys. Res. 107*(B4).

McCarthy, D. and G. Petit (2004). *IERS Conventions 2003*, Chapter IERS Techn. Note 32.

Frankfurt am Main, Germany: Verlag des Bundesamts für Kartographie und Geodäsie.

Moritz, H. and I. Mueller (1987). *Earth Rotation Theory and Observation*. 370 Lexington Avenue, New York, NY 10017: The Ungar Publiching Company.

Niell, A. (1996). Global mapping functions for the atmosphere delay at radio wavelengths. *J Geophys Res 101* (B2), 3227–3246.

Niell, A. (2000). Improved atmospheric mapping functions for VLBI and GPS. *Earth Planets Space 52*, 699–702.

Niell, A. (2006). Baseline Length Repeatability. Technical report, MIT Haystack Observatory.

Niell, A., A. Coster, F. Solheim, V. Mendes, P. Toor, R. Langley, and C. Upham (2001). Comparision of measurements of atmospheric wet delay by radiosonde, water vapor radiometer, GPS, and VLBI. *J Atmos Oceanic Technol 18*, 830–850.

Niell, A. and L. Petrov (2003). Using a Numerical Weather Model to Improve Geodesy. In T. van Dam and O. Francis (Eds.), *The State of GPS Vertical Positioning Precision: Separation of Earth Processes by Space Geodesy*. European Center for Geophysics and Seismology, Luxembourg, Belgium.

Niemeier, W. (2002). *Ausgleichungsrechnung*. Verlag de Gruyter, Berlin New York.

Nilsson, T., J. Böhm, and H. Schuh (2010). Sub-Diurnal Earth Rotation Variations Observed by VLBI. *Artificial Satellites 45* (2), 49–55.

Nothnagel, A. (2009). Conventions on thermal expansion modelling of radio telescopes for geodetic and astrometric VLBI. *J. Geod. 83* (8), 787–792.

Nothnagel, A. and C. Steinforth (2002). IVS analysis coordination. *CSTG Bulletin, Progress Report 2001*, 84–90.

Owens, J. (1967). Optical refractive index of air: Dependence on pressure, temperature and composition. *Applied Optics 6*, 51–58.

Öztürk, E. and M. Serbetçi (1989). Dengeleme hesabı, cilt 2.

Öztürk, E. and M. Serbetçi (1992). *Dengeleme hesabı, cilt 3*. Karadeniz Technical University, Trabzon.

Pany, A., J. Wresnik, and B. J. (2008). VLBI2010 analysis strategies tested with the PPP Simulator. Memorandum, International VLBI Service for Geodesy and Astrometry.

Pelzer, H. (1974). Zur Behandlung singulaerer Ausgleichungsaufgaben. *ZfV*, 181–194.

Petrachenko, B., A. Niell, D. Behrend, B. Corey, J. Böhm, P. Charlot, A. Collioud, J. Gipson, R. Haas, T. Hobiger, Y. Koyama, D. MacMillan, Z. Malkin, T. Nilsson, A. Pany, G. Tuccari, W. A., and J. Wresnik (2009). Design Aspects of the VLBI2010 System. Progress Report of the IVS VLBI2010 Committee NASA/TM-2009-214180, Interna-

tional VLBI Service for Geodesy and Astrometry.

Petrov, L. and J. Boy (2004). Study of the atmospheric pressure loading signal in Very Long Baseline Interferometry observations. *J. Geophys. Res. 109(B3):B03405.*

Prongle, P. and A. Rayner (1971). *Generalized invers matrices with applications to statistics.* Griffin, London.

Rabbel, W. and H. Schuh (1986). The influence of atmospheric loading on VLBI-experiments. *J. Geophys. 59*, 164–170.

Rao, C. and S. Mitra (1971). *Generalized Inverse of Matrices and Its Applications.* New York: Wiley.

Ray, R. and R. Ponte (2003). Barometric tides from ECMWF operational analyses. *Ann Geophys 21*(8), 1897–1910.

Ray, R., D. Steinberg, B. Chao, and D. Cartwright (1994). Diurnal and semi-diurnal variations in the Earth's rotation rate induced by oceanic tides. *Science 264*(5160), 830–832.

Rocken, C., S. Sokolovskij, J. Johnson, and D. Hunt (2001). Improved mapping of tropospheric delays. *J Atmos Oceanic Technol 18*(7), 1205–1213.

Roosbeek, F. (1999). Diurnal and sub-diurnal terms in RDAN97 series. *Celest. Mech. Dyn. Astr. 74*(4), 243–252.

Rüeger, J. (2002). Refractive Index Formulae for Radio Waves. FIG XXII International Congress, Washington, D.C. USA.

Rummel, R., M. Rothacher, and G. Beutler (2005). Integrated Global Geodetic Observing System (IGGOS)-science rationale. *Journal of Geodynamics 40*(4-5), 357–362.

Saastamoinen, J. (1972). *The use of artificial satellites for geodesy*, Chapter Atmospheric correction for the troposphere and stratosphere in radio ranging of satellites, pp. 247–251. Geophys. Monogr. Ser. 15, American Geophysical Union.

Saastamoinen, J. (1973). Contributions to the theory of atmospheric refraction (in three parts). *Bull. Geod. 105, 106, 107*, 279–298, 383–397, 13–34.

Schervish, M. (1996). P Values: What They Are and What They Are Not. *The American Statistician 50*(3), 203–206.

Schlüter, W. and D. Behrend (2007). The International VLBI Service for Geodesy and Astrometry (IVS): current capabilities and future prospects. *Journal of Geodesy 81*(6-8), 379–387.

Schuh, H. (1987). *Die Radiointerferometrie auf langen Basen zur Bestimmung von Punktverschiebungen und Erdrotationsparametern.* DGK Reihe C, Heft 328, Verlag der Bayerischen Akademie der Wissenchaften.

Schuh, H. and D. Behrend (2009). *Report of the International Association of Geodesy 2007-2009*, Volume 36, Chapter International VLBI Service for Geodesy and Astrometry (IVS), pp. 297–306. Travaux de l'Association Internationale de Géodésie.

Schuh, H. and J. Böhm (2003). Status Report of the IVS pilot project-tropospheric parameters. In N. Vandenberg and K. Baver (Eds.), *International VLBI Service for Geodesy and Astrometry 2002 Annual Report*, NASA/TP-2003-211619. Goddard Space Flight Center, Maryland: Goddard Space Flight Center, Maryland.

Schuh, H., C. Ma, and A. Nothnagel (2007). Preface. *Journal of Geodesy 81*(6-8), 377–378.

Seeber, G. (1993). *Satellite Geodesy: Foundations, methods, and applications.* Berlin, New York: Walter de Gruyter.

Snajdrova, K., J. Böhm, P. Willis, R. Haas, and H. Schuh (2006). Multi-technique comparison of tropospheric zenith delays derived during the CONT02 campaign. *J Geod 79*(613-623), 613–623.

Soffel, M., J. Mller, X. Wu, and C. Xu (1991). Consistent relativistic VLBI theory with picosecond accuracy. *Astron. J. 101*(6), 2306–2310.

Souchay, J. and H. Kinoshita (1997). Corrections and new developments in rigid-Earth nutation theory. II. Influence of second-order geopotential and direct planetary effect. *Astron Astrphys. 318*, 639–652.

Sovers, O., J. Fanselow, and C. Jacobs (1998). Astrometry and geodesy with radio interferometry: experiments, models, results. *Reviews of Modern Physics 70*(4), 1393–1453.

Sovers, O. and C. Jacobs (1994). *Observation model and parameter partials for the JPL VLBI parameter estimation software "MODEST" - 1994*, Volume 83-39 of *Rev. 5.* Pasedana, California: Jet Propulsion Laboratory.

Steigenberger, P., M. Rothacher, R. Dietrich, M. Fritsche, A. Rülke, and S. Vey (2006). Reprocessing of a global GPS network. *J Geophys Res 111*(B05402).

Steigenberger, P., V. Tesmer, M. Krügel, D. Thaller, R. Schmid, S. Vey, and M. Rothacher (2007). Comparisons of homogeneously reprocessed GPS and VLBI long time-series of troposphere zenith delays and gradients. *J Geod 81*(6-8), 503–514.

Stein, S. (1985). *Precision Frequency Control*, Volume 2, Chapter Frequency and Time: Their Measurement and Characterization, pp. 191–232. Academic Press.

Tamura, Y. (1987). A harmonic development of the tide-generating potential. *Bull. d'Inform. Marees Terr. 99*, 6813–6855.

Tesmer, V., J. Böhm, R. Heinkelmann, and H. Schuh (2007). Effect of different tropospheric mapping functions on the TRF, CRF and position time-series estimated from VLBI.

J of Geodesy 81, 409–421.

Thaller, D. (2008). Inter-technique combination based on homogeneous normal equation systems including station coordinates, Earth orientation and troposphere parameters. Scientific technical report str08/15, Fakultät für Bauingenieur- und Vermessungswesen der Technischen Universität München.

Titov, O., V. Tesmer, and J. Boehm (2004). OCCAM v.6.0 Software for VLBI Data Analysis. In N. Vandenberg and K. Baver (Eds.), *International VLBI Service for Geodesy and Astrometry 2004 General Meeting Proceedings*, NASA/CP-2004-212255.

Treuhaft, R. and J. Thomas (1991). Incorporating atmospheric delay into the relativistic VLBI time delay. IOM 335 6-91-016, JPL Technical Memorandum.

Tsuboki, K. and A. Sakakibara (2002). Large-scale parallel computing of Cloud Resolving Storm Simulator: High Performance Computing. In G. Goos, J. Hartmanis, and V. Leeuwen (Eds.), *Lecture notes in computer science*, Volume 2327, pp. 243–259.

Undén, P., L. Rontu, H. Järvinen, P. Lynch, J. Calvo, G. Cats, J. Cuxart, K. Eerola, C. Fortelius, J. Garcia-Moya, C. Jones, G. Lenderlink, A. McDonald, R. McGrath, B. Navascues, N. Woetman, V. Ødegaard, E. Rodriguez, M. Rummukainen, R. Rõõm, K. Sattler, S. Hansen, H. Savijärvi, S. Wichers, R. Sigg, H. The, and A. Tijm (2002). HIRLAM-5 Scientific documentation. Technical report, Swedish Meteorological and Hyrdological Institute, Norrköping. 144 pages.

vanDam, T. and T. Herring (1994). Detection of atmospheric pressure loading using very long baseline Interferometry measurements. *J. Geophys. Res. 99*, 4505–4517.

Wahr, J. (1981). Body tides on an elliptical, rotating, elastic, and oceanless Earth. *Geophys. J. Roy. astr. Soc. 64*(3), 677–703.

Webb, F. and J. Zumberge (1993). An introduction to GIPSY/ OASIS-II. Publication d-11088, JPL, Pasadena, CA.

Willis, P., C. Boucher, H. Fagard, B. Garayt, and M. Gobinddass (2010). Contributions of the French Institut Géographique National (IGN) to the International DORIS Service. *Adv Space Res 45*(12), 1470–1480.

Willis, P., P. Ferrage, F. Lemoine, C. Noll, R. Noomen, M. Otten, J. Ries, M. Rothacher, L. Soudarin, G. Tavernier, and J. Valette (2010). The International DORIS Service: Toward maturity. *Adv Space Res 45*(12), 1408–1420.

Wolf, P. and C. Ghilani (1997). *Adjustment Computations Statistics and Least Squares in Surveying and GIS*. John Wiley and Sons Inc. New York.

Zumberge, J., M. Heflin, D. Jefferson, M. Watkins, and F. Web (1997). Precise point position-

ing for the efficient and robust analysis of GPS data from large networks. *J Geophys Res 102*, 5005–5017.

Curriculum vitae

30.01.1979	Born in Ankara, Turkey
1997-2001	Bachelor studies at the Department of Geomatics Engineering, Karadeniz Technical University, Trabzon, Turkey
2001-2004	Master of Science (MSc) studies at the Geodesy program of the Institute of Natural and Applied Sciences, Karadeniz Technical University, Trabzon, Turkey
2001-2007	Research Assistant at the Department of Geomatics Engineering, Karadeniz Technical University, Trabzon, Turkey
2005-2006	Guest researcher at Middle East Technical University, Ankara, Turkey
2006-2007	Guest researcher at the Institute of Geodesy and Geophysics, Vienna University of Technology, Vienna, Austria, in the scope of the Erasmus student mobility program
2007-	Doctoral studies at the Institute of Geodesy and Geophysics, Vienna University of Technology, Vienna, Austria
2008-	Research Assistant at the Department of Geomatics Engineering, Hacettepe University, Ankara, Turkey

A. Appendices

A.1. Rotation matrices and partial derivatives

Rotations between two cartesian coordinate systems are expressed in terms of rotation matrices. The transformation of the position of a point P from a first cartesian system x_p^1 to second x_p^2 with identical origin can be carried out by the matrix operation,

$$x_p^2 = R_1(\alpha)R_2(\beta)R_3(\gamma)x_p^1 \tag{A.1.1}$$

where the rotation around the third axis (z-axis) by the angle γ and partial derivative w.r.t. γ is

$$R_3(\gamma) = \begin{bmatrix} \cos\gamma & \sin\gamma & 0 \\ -\sin\gamma & \cos\gamma & 0 \\ 0 & 0 & 1 \end{bmatrix} \quad ; \quad \frac{\partial R_3(\gamma)}{\partial \gamma} = \begin{bmatrix} -\sin\gamma & \cos\gamma & 0 \\ -\cos\gamma & -\sin\gamma & 0 \\ 0 & 0 & 0 \end{bmatrix}, \tag{A.1.2}$$

the rotation around the second axis (y-axis) by the angle β and partial derivative w.r.t. β is

$$R_2(\beta) = \begin{bmatrix} cos\beta & 0 & -sin\beta \\ 0 & 1 & 0 \\ sin\beta & 0 & cos\beta \end{bmatrix} \quad ; \quad \frac{\partial R_2(\beta)}{\partial \beta} = \begin{bmatrix} -\sin\beta & 0 & -\cos\beta \\ 0 & 0 & 0 \\ \cos\beta & 0 & -\sin\beta \end{bmatrix}, \tag{A.1.3}$$

and the rotation around the first axis (x-axis) by the angle α and partial derivative w.r.t. α is

$$R_1(\alpha) = \begin{bmatrix} 1 & 0 & 0 \\ 0 & cos\alpha & sin\alpha \\ 0 & -sin\alpha & cos\alpha \end{bmatrix} \quad ; \quad \frac{\partial R_1(\alpha)}{\partial \alpha} = \begin{bmatrix} 0 & 0 & 0 \\ 0 & -\sin\alpha & \cos\alpha \\ 0 & -\cos\alpha & -\sin\alpha \end{bmatrix}. \tag{A.1.4}$$

The representation is valid for a right-handed coordinate system. As viewed from the positive end of the axis about which the rotation takes place, for a counter clock-wise rotation: the rotation angle is positive.

A.2. Time systems

Sidereal time is related to the rotation of the Earth where equal intervals of angular motion correspond to equal intervals of sidereal time. The fundamental unit of sidereal time is the mean sidereal day. Mean sidereal day is conventionally divided into hours, minutes, and seconds. Mean sidereal day is defined as the interval between two successive transits of the mean vernal equinox across the meridian. However, due to the position change of the mean vernal equinox caused by the precession, Earth does not revolve around itself completely within one sidereal day. Sidereal day is shorter about 0.0084 seconds than one complete revolution.

Hour angle is the counter clock-wise angle from the true/mean vernal equinox at an epoch through the true/mean celestial equator to the i.e. observer's true/mean astronomical meridian or to the quasar's true/mean hour circle. Since, the true hour angle of the observer's meridian is equal to the true right ascension of a celestial object (e.g. sun, quasar) at the instant of the upper transit across the observer's astronomical meridian, the sidereal time can be determined by observing transits of celestial objects. The local hour angle of the true (i.e. affected by precession and nutation) vernal equinox is termed apparent sidereal time (AST), while that of the mean (i.e. affected by precession only) vernal equinox is termed mean sidereal time (MST). If the hour angle is measured/calculated to the true/mean Greenwich astronomical meridian it is called as *Greenwich apparent (true)* or *Greenwich mean sidereal time* (GAST and GMST) (Figure A.2.1). The difference between the AST-MST refer to CIP and AST1-MST1 refer to the CTP is termed by *Equation of Equinoxes Eq.E*) as follows (see Figure A.2.1),

$$Eq.E = AST - MST = \Delta\psi \, cos\varepsilon,$$
$$Eq.E = AST1 - MST1$$

(A.2.1)

where AST1 and MST1 are the reduced sidereal times from CIP to CTP due to the polar motion $(x_p \, , y_p)$,

$$AST1 = AST + (\Lambda_{CTP} - \Lambda_{CIP}),$$
$$AST1 = AST - (y_p cos\Lambda_{CIP} + x_p sin\Lambda_{CIP})tan\Phi.$$

(A.2.2)

where Λ and Φ are the astronomical longitude and latitude of the observer. The astronomical longitude of the observer meridian (Λ_L) and the sidereal time relation can be formulated as,

$$\Lambda_L = LMST - GMST = LAST - GAST.$$

(A.2.3)

Mean solar day is defined as the interval between two successive transits of the mean sun (sun

145

is assumed to move without any declination from ecliptic (or from celestial equator since both assumptions are true for this case) plane and with a constant velocity) across the meridian of the observer. The length of the mean solar day is a function of the motion of the mean sun and the mean vernal equinox. Mean solar day is $3^m\,55.909^s$ longer than mean sidereal day due to the diurnal motion of the Earth in its orbit.
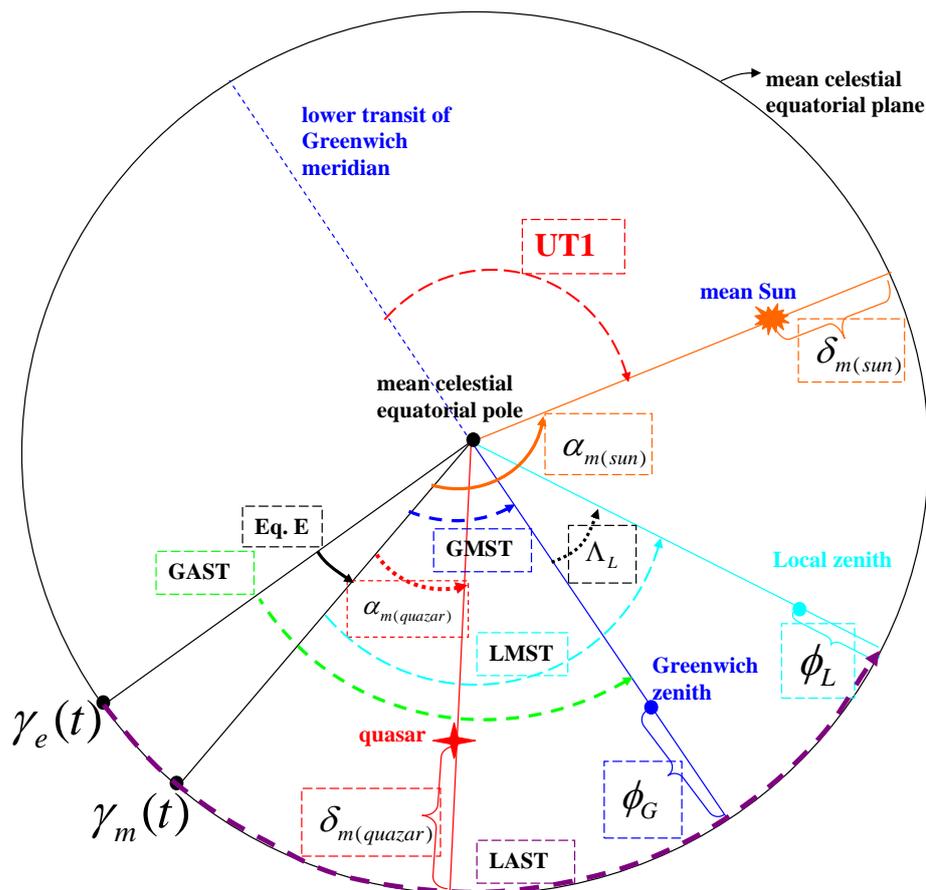
Figure A.2.1.: The illustration of the relation between sidereal times.

Universal Time (UT) is defined as the Greenwich hour angle of the mean sun. UT1 measures the true (actual) angular rotation of the earth as corrected for the rotational component induced by polar motion. In other words, UT1 gives the measure of the rotation as if the earth were rotating around the CTP. This means UT1 defines the actual rotation of conventional reference system w.r.t. space (Figure A.2.1). Mathematical relation between sidereal and universal time

is as follows (Kaplan, 1981):

$$UT1 = GMST - \alpha_m(sun) + 12^h \tag{A.2.4}$$

with the right ascension of mean sun, $\alpha_m(sun)$ is

$$\alpha_m(sun) = 18^h41^m50.54841^s + 8640184.812866^sT_u + 0.093104T_u^2 - 6.2^s \times T_u^3 \tag{A.2.5}$$

where T_u is the time from 2000 January, 12^h UT1 to the epoch, u in Julian Date, JD_u counted in Julian centuries ($36525days$),

$$T_u = (JD_u - 2451545.0)/36525, \tag{A.2.6}$$

conversion of any Gregorian calender date (Y: year, M: month, D:day) to *Julian Date* (JD) used in the above equation can be done with the equation below,

$$JD = 367 * Y - 7 * [Y + (M + 9)/12]/4 + 275 * M/9 + D + 1721014, \tag{A.2.7}$$

while the above expression is valid for dates since March 1900. In order to use small numbers *Modified Julian Date* is defined as

$$MJD = JD - 2400000.5. \tag{A.2.8}$$

The *Dynamical Time* is a uniform time scale derived from the equations of orbital motions of celestial bodies based on the law of gravitation and the relativity. Predecessor of the Dynamical Time is the Ephemeris Time (ET). The Ephemeris Time had been derived from lunar observations without relativistic considerations. Dynamical Time can be distinguished between two parts: If the equation of motions refer to the barycenter of the solar system the appropriate time scale is *Barycentric Dynamical Time* (Temps Dynamique Barycentrique, TDB), and the Terrestrial Dynamical Time (Temps Dynamique Terrestre, TDT) refers to the geocenter. TDB and TDT differ only by small periodic terms. For the sake of continuity TDB was set equal to ET at the beginning of January 1, 1984 and Dynamical Time has been used as the argument for astronomical ephemerides since this time.

In 1967, first international atomic definition of the second succeeded and replaced the previously used astronomical (celestial) time definition by the 13th Conference of the International Committee of Weights and Measures. After several years later, in 1971, the existence of the *atomic time scale* (Temps Atomique International, TAI) for the management of the world affairs was officially recognized at the 14th General Conference on Weights and Measures. The unit TAI

second was selected in such a way that it equals the duration of the ephemeris second defined as "The second is the duration of 9 192 631 770 periods of the radiation corresponding to the transition between the two hyperfine levels of the ground state of the Cesium 133 atom". The international atomic time scale is maintained by the Time Section of the International Bureau of Weights and Measures (Bureau International des Poids et Mesures, BIPM) in Paris, based on the weighted mean of the readings of a large number of non-moving atomic clocks in various laboratories at sea level. The epoch of TAI agreed with the epoch of UT1 on January 1, 1958. By definition $TDT - TAI$ is 32.184 seconds. For the time arguments used to obtain precession and nutation, or refer to the solar system ephemerides TDB is used. TDB is related to TDT as follows,

$$TDB = TDT + 0.001658 \, sin[g + 0.0167 \, sin(g)], \tag{A.2.9}$$

where

$$g = 2\pi(357.528 + 35999.050 \, T)/360, \tag{A.2.10}$$

is the mean anomaly of the Earth in its orbit, and T denotes to the interval measured in Julian centuries of TDB between $J2000.0$ and the epoch given in Equation(A.2.6).

For the best possible adaptation of atomic time, TAI to earth rotational time, UT1, a hybrid time scale (TAI added an offset due to the slowing down of the rotation of the earth relatively to atomic time), *Coordinated Universal Time* (UTC) was introduced. UTC and TAI differ by an integer number of seconds, so called *leap seconds* in order to keep the difference in,

$$UT1 - UTC = \Delta UT1 \, \leq \, 0.9 \, seconds. \tag{A.2.11}$$

UTC is also referred to the basis of daily civilian timing requirements (Kaplan, 1981; Moritz and Mueller, 1987; Leick, 1990; Seeber, 1993; Sovers et al., 1998; Claude and Bernard, 2001). For more information on time conventions see e.g. McCarthy and Petit (2004).

A.3. VieVS variables saved as structure arrays

Table A.3.1.: "multi_lsmopt.m" and "vie_setup.m" options for multi session process, saved in "/DATA/LEVEL1/" named as "session_name_parameter.mat".

parameter.lsmopt

VARIABLE	DEFAULT	UNIT	DESCRIPTION
.diropt:	'YOURDIR-A'	*character*	directory named by the user where the session
			option files are stored in:
			$/DATA/OPT/$**YOURDIR-A**$/YEAR/$
.dirs.name:	'DEFAULT',		session-wise option files stored in:
	'IGG08R01', ...	*struct.*	$/DATA/OPT/$**DEFAULT**$/YEAR/$
.dirout:	'YOURDIR-B'	*character*	directory named by the user where
			the outlier files are read and/or written in:
			$/DATA/OUTLIER/$**YOURDIR-B**$/YEAR$
			when it is left empty $/DATA/OUTLIER/YEAR$
			is used
.ref:	0 (1)	*logical*	no reference clock is selected as default
			for multi session process
.first:	1 (0)	*logical*	a first basic solution will be carried out
			including only clock error model
.firstclock:	2 (0,1)	*logical*	in the first basic solution one offset, one rate and
			one quadratic term per clock is estimated
.treat_breaks:	1 (0)	*logical*	in the first basic solution separate clock functions
			are formed defined by the epoch of break
.second:	1 (0)	*logical*	main solution is carried out
.pw_clk:	3 (0,1,2)	*logical*	in the main solution a quadratic term is estimated
			in addition to rate and PWLOs of clock functions
.coef_clk:	0.1	$\frac{picosec^2}{sec}$	coefficients of the weights of clock constrain equations
			which renders PWLO estimates loose or tight
.int_clk:	60 (20, 30)	*minutes*	clocks PWLO estimation interval
.constr_clk:	1 (0)	*logical*	introduce relative constraints as pseudo observations
			on clocks PWLO estimates
.pw_zwd:	1 (0)	*logical*	estimate zenith wet delays (ZWDs) as PWLOs
.constr_zwd:	1 (0)	*logical*	introduce relative constraints as pseudo observations
			on zenith wet delay PWLO estimates
.coef_zwd:	0.7	$\frac{picosec^2}{sec}$	coefficients of the weights of ZWD constrain equations
			which renders PWLO estimates loose or tight

.int_zwd:	30 (20, 60)	*minutes*	ZWD PWLO estimation interval
.pw_ngr:	1 (0)	*logical*	estimate troposphere north gradients as PWLOs
.constr_rel_ngr:	1 (0)	*logical*	introduce relative constraints on PWLO estimates of troposphere north gradients
.constr_abs_ngr:	0 (1)	*logical*	do not introduce absolute constraints on PWLO estimates of troposphere north gradients
.coef_rel_ngr:	2 (0.01)	$\frac{mm}{day}$	coefficients of the weights of north gradients relative constraints
.coef_abs_ngr:	1 (0.001)	*mm*	coefficients of the weights of north gradients absolute constrain equations
.int_ngr:	360	*minutes*	north gradients PWLOs estimation interval
.pw_egr:	1 (0)	*logical*	estimate troposphere east gradients as PWLOs
.constr_rel_egr:	1 (0)	*logical*	introduce relative constraints on PWLO estimates of troposphere east gradients
.constr_abs_egr:	0 (1)	*logical*	do not introduce absolute constraints on PWLO estimates of troposphere east gradients
.coef_rel_egr:	2 (0.01)	$\frac{mm}{day}$	coefficients of the weights of east gradients relative constraints
.coef_abs_egr:	1 (0.001)	*mm*	coefficients of the weights of east gradients absolute constrain equations
.int_egr:	360	*minutes*	east gradients PWLOs estimation interval
.stc:	1 (0)	*logical*	estimate antenna TRF coordinates
.pw_stc:	0 (1)	*logical*	do not estimate antenna TRF coordinates as PWLO (or estimate as one offset for one session)
.constr_xyz:	1 (0)	*logical*	introduce constraints between PWLO estimates of antenna coordinates (only if PWLO)
.coef_xyz:	100	$\frac{mm}{day}$	coefficients of the weights of antenna coordinates relative constraints
.int_xyz:	360	*minutes*	antenna TRF coordinates PWLOs estimation interval (only if PWLO)
.nnt_stc:	1 (0)	*logical*	introduce NNT condition equations for antenna TRF coordinates to NEQ matrix
.nnr_stc:	1 (0)	*logical*	introduce NNR condition equations for antenna TRF coordinates to NEQ matrix
.sca_stc:	0 (1)	*logical*	do not introduce scale condition equations for antenna TRF coordinates to NEQ matrix
.pw_sou:	0 (1)	*logical*	do not estimate sources CRF coordinates as PWLOs

			(do not estimate any source coordinates)
.constr_sou:	0 (1)	*logical*	do not introduce relative constraints on PWLO estimates of source coordinates
.sour_coef_rade:	0.0001 (1)	$\frac{mas}{day}$	weight coefficients of relative constraints on PWLO source coordinates estimates (0.0001:tight)
.sour_int_rade:	1440 (30,60)	*minutes*	estimation interval of PWLO source coordinates estimates
.global_solve:	0 (1)	*logical*	do not prepare TRF datum free N and b for a global solution
.est_love:	0 (1)	*logical*	do not prepare sub-N and -b for a global solution to estimate 77 different parameters of Love Numbers
.est_shida:	0 (1)	*logical*	do not prepare sub-N and -b for a global solution to estimate 79 different parameters of Shida Numbers
.est_vel:	0 (1)	*logical*	do not prepare sub-N and -b for a global solution to estimate velocities of TRF coordinates of antennas
.est_source:	0 (1)	*logical*	do not prepare CRF datum free sub-N and -b for a global solution to estimate source coordinates
.xpol:	1x1	*struct.*	parametrization for polar motion, xpol PWLO estimates see Table A.3.2
.ypol:	1x1	*struct.*	parametrization for polar motion, ypol PWLO estimates see Table A.3.2
.dUT1:	1x1	*struct.*	parametrization for polar motion, dUT1 PWLO estimates see Table A.3.2
.nutdx:	1x1	*struct.*	parametrization for celestial pole offset dx PWLO estimates see Table A.3.2
.nutdy:	1x1	*struct.*	parametrization for celestial pole offset dy PWLO estimates see Table A.3.2
.par_outlier:	5 (3)	*unitless*	outlier test boundary: par_outlier x m_0 or par_outlier x m_v
.simple_outlier:	0 (1)	*logical*	do not apply: par_outlier x m_0
.basic_outlier:	1 (0)	*logical*	apply: par_outlier x m_v
.control_gui_vie_lsm:	1 (0)	*logical*	allow session-wise parametrization through GUIs

Table A.3.2.: "multi_lsmopt.m" and "vie_setup.m", EOP options for multi sessions process, saved in "/DATA/LEVEL1/" named as "session_name_parameter.mat".

parameter.lsmopt.xpol, **parameter.lsmopt.ypol**, **parameter.lsmopt.dut1**

parameter.lsmopt.nutdx, **parameter.lsmopt.nutdy**

VARIABLE	DEFAULT	*UNIT*	DESCRIPTION
.model:	1 (0)	*logical*	estimate EOP PWLOs in LS parameter estimation
.int:	1440	*minutes*	estimation interval of the EOP PWLOs
.constrain:	1 (0)	*logical*	introduce relative constraints on the EOP PWLO estimates
.coef:	0.0001	$\frac{mas}{day}$	coefficient of the weight of relative constraints on the EOP PWLO estimates (0.0001 is loose)

Table A.3.3.: "vie_lsm" options for single session process, saved in "/DATA/LEVEL3/" named as "opt_session_name.mat". The below variables of single session process are added to the ones given in Table A.3.1.

opt_

VARIABLE	DEFAULT	UNIT	DESCRIPTION
.first_scan:	52563.7501736111	*MJD*	epoch of the first scan of the session
.last_scan:	52564.7334027778	*MJD*	epoch of the last scan of the session
.stat:	1 x num_of_antennas	*struct.*	station-wise parametrization of the session see Table A.3.4
.source:	1 x num_of_sources after outliers eliminated	*struct.*	source-wise parametrization of the session see Table A.3.5
.limit_num_obs_sou:	246	*integer*	maximum number of observations to a source (this information is not directly related to LS)
.ref_first_clk:	1	*integer*	the number of the fixed clock in the session
.scans_total:	467	*integer*	total number of scans in the session
.midnight:	52564	*MJD*	midnight of the session
$.s_0$:	1.189	*unitless*	a priori standard deviation of unit weight
.fixed_clock:	WETTZELL	*character*	clock Wettzell is fixed
.fixed_station:	'none'	*character*	the station of which TRF coordinates are fixed to their a priori values
.total_obs:	3017	*integer*	total number of observations in a session
$.m_0$:	0.790	*unitless*	a posteriori standard deviation of unit weight
totalest	[0 175 189 580 620 ...]	*integer*	total number of estimates after each model

Table A.3.4.: "vie_lsm" station-wise options for single session process saved in "/DATA/LEVEL2/" named as "opt_session_name.mat".

opt_.stat(1)

VARIABLE	DEFAULT	UNIT	DESCRIPTION
.name:	WESTFORD	*character*	name of the station
.zwd_inc:	1 (0)	*logical*	estimate zenith wet delays of this station
.ngr_inc:	1 (0)	*logical*	estimate troposphere north gradients of this station
.egr_inc:	1 (0)	*logical*	estimate troposphere east gradients of this station
.xyz_inc:	1 (0)	*logical*	estimate antenna TRF coordinates of this station
.coef_clk:	0.1	$\frac{picosec^2}{sec}$	coefficient of the weight of relative constraints clock PWLO estimates of this station (0.1 is loose)
.coef_zwd:	0.7	$\frac{picosec^2}{sec}$	coefficient of the weight of realtive constrain equations on ZWD PWLO estimates of this station (0.7 is loose)
.coef_rel_ngr:	2	$\frac{mm}{day}$	coefficient of the weight of relative constraints on tropo. north gradient PWLO estimates of this station (2 is loose)
.coef_rel_egr:	2	$\frac{mm}{day}$	coefficient of the weight of relative constraints tropo. east gradient PWLO estimates of this station (2 is loose)
.coef_abs_ngr:	1	*mm*	coefficient of the weight of absolute constrain equations on tropo. north gradient PWLO estimates of this station (1 is loose)
.coef_abs_egr:	1	*mm*	coefficient of the weight of absolute constrain equations on tropo. east gradient PWLO estimates of this station (1 is loose)
.coef_xyz	100	*mm*	coefficient of the weight of absolute constrain equations on TRF antenna coor. PWLO estimates of this station (100 is loose) (only if opt_.stat(1).nnt_inc = 0)
.int_clk	60 (30)	*minutes*	PWLOs estimation interval of this station clock
.int_zwd	30	*minutes*	ZWD PWLOs estimation interval of this station
.int_ngr	360 (180)	*minutes*	tropo. north gradient PWLOs estimation interval of this station
.int_egr	360 (180)	*minutes*	tropo. east gradient PWLOs estimation interval of this station
.int_xyz	360 (180)	*minutes*	PWLOs estimation interval of this antenna TRF coordinates (only if opt_.stat(1).nnt_inc = 0)
.ref	1 (0)	*logical*	fix clock of this station
.nnt_inc	1 (0)	*logical*	include this station's NNT condition equation in NEQ system
.nnr_inc	1 (0)	*logical*	include this station's NNR condition equation in NEQ system
.nns_inc	1 (0)	*logical*	do not include this station's NNS (no-net-scale) condition equation in NEQ system
.clkbreak	[ ]	*MJD*	no clock break information in this session for this station
.delete	0 (1)	*logical*	this station is not excluded from the session for the analysis

Table A.3.5.: "vie_lsm" source-wise options and EOP options for single session process saved in "/DATA/LEVEL3/" named as "opt_session_name.mat".

opt_.source(1)

VARIABLE	DEFAULT	UNIT	DESCRIPTION
.total_obs:	49	*integer*	total number of observations made to the source within the session
.name:	1741-038	*character*	source name
.coef_rade:	0.0001	$\frac{mas}{day}$	coefficient of the weight of constrain equations on this source's CRF PWLO coordinate estimates (0.0001 is tight)
.int_rade:	1440	*minutes*	estimation interval of this source's CRF PWLO coordinate estimates
.rade_inc:	0 (1)	*logical*	do not estimate PWLO CRF coordinates of this source
.de:	-0.066926...	*radians*	a priori (from almanac) declination of this source
.ra:	4.6424926...	*radians*	a priori (from almanac) right ascension of this source

opt_.xpol; opt_.ypol; opt_.dut1; opt_.nutdx; opt_.nutdy;

VARIABLE	DEFAULT	UNIT	DESCRIPTION
.model:	1 (0)	*logical*	include corresponding EOP model in the analysis
.int:	1440	*minutes*	estimation interval of corresponding EOP model PWLO estimates
.constrain:	1 (0)	*logical*	introduce relative constraints on the corresponding EOP PWLO estimates
.coef:	$\frac{mas}{day}$	*logical*	coefficients of the weights of relative constraints on the corresponding EOP PWLO estimates (also for dUT1 : $\frac{mas}{day}$)

Table A.3.6.: "vie_lsm" single session solution results, e.g. IVS-CONT08 first session, saved in "/DATA/LEVEL3/" named as "x_session_name.mat" e.g. for the antenna, ZELENCHUKSKAYA.

x_

VARIABLE	DEFAULT	UNIT	DESCRIPTION
.pwclk(4).first_mjd:	54690.000115	*MJD*	epochs of the first scan, break, last scan
	54690.406	*MJD*	of the antenna in the session
	54690.995914	*MJD*	
.pwclk(4).first_val:	786178.032	*cm*	the first treatment of clock: two offsets of clock
	785918.502	*cm*	function at the epochs of first scan and clock break
.pwclk(4).first_mx:	0.80	*cm*	the first treatment of the clock: formal errors of the
	1.17	*cm*	function offsets at first scan and at the clock break
.pwclk(4).val:	[1 x 25]	*cm*	PWLO clock estimates of this station
.pwclk(4).mx:	[1 x 25]	*cm*	standard deviations of PWLO clock estimates of
			this station
.pwclk(4).mjd:	[1 x 25]	*mjd*	estimation epochs of PWLO clock estimates of
			this station
.pwclk(4).col:	[1 x 25]	*integer*	column and row numbers of PWLO clock estimates of this
			station in NEQ system matrix N, and vector, b
.rclk(4).first_mjd:	54690.000115	*MJD*	first scan, break, and last scan mjd
	54690.406	*MJD*	of this antenna in the session
	54690.995914	*MJD*	
.rclk(4).first_val:	-756.887	$\frac{cm}{day}$	the first treatment of this clock: rates of first
	-867.003	$\frac{cm}{day}$	and second quadratic functions
.rclk(4).first_mx:	1.86	$\frac{cm}{day}$	the first treatment of this clock: std. dev. of rates
	7.14	$\frac{cm}{day}$	of first and second quadratic functions
.qclk(4).first_mjd:	54690.000115	*MJD*	first scan, break, and last scan mjd
	54690.406	*MJD*	of this antenna in the session
	54690.995914	*MJD*	
.qclk(4).first_val:	16.006	$\frac{cm}{day^2}$	first treatment of this clock: quadratic terms
	78.314	$\frac{cm}{day^2}$	of first and second quadratic functions
.qclk(4).first_mx:	2.05	$\frac{cm}{day^2}$	the first treatment of this clock: std. dev. of rates
	1.83	$\frac{cm}{day^2}$	of first and second quadratic functions
.rqclk(4).val:	43.538	$\frac{cm}{day}$	main solution: rate of the clock function
	-37.231	$\frac{cm}{day^2}$	main solution: quad. term of the clock function
.rqclk(4).mx:	6.348	$\frac{cm}{day}$	main solution: std. dev. of the clock func. rate
	5.678	$\frac{cm}{day^2}$	main solution: std. dev. of the clock func. quad. term
.rqclk(4).col:	243	*integer*	column and row number of clock rate in N and b

	244	*integer*	column and row numbers of clock quad. term in N and b
.antenna(4).name:	ZELENCHK	*character*	name of the fourth antenna within the session
.zwd(4).val:	[1 x 49]	*cm*	PWLO estimates of ZWDs
.zwd(4).mx:	[1 x 49]	*cm*	standard deviations of ZWD PWLO estimates
.zwd(4).mjd:	[1 x 49]	*MJD*	estimation epochs of ZWD PWLO estimates
.zwd(4).col:	[1 x 49]	*integer*	column and row numbers of ZWD PWLO estimates in N and b
.ngr(4).val:	[1 x 5]	*cm*	PWLO estimates of troposphere north gradients
.ngr(4).mx:	[1 x 5]	*cm*	standard deviations of troposphere north gradients PWLO estimates
.ngr(4).mjd:	[1 x 5]	*MJD*	estimation epochs of troposphere north gradients PWLO estimates
.ngr(4).col:	[1 x 5]	*integer*	column and row numbers of troposphere north gradients PWLO estimates in N and b
.egr(4).val:	[1 x 5]	*cm*	PWLO estimates of troposphere east gradients
.egr(4).mx:	[1 x 5]	*cm*	standard deviations of troposphere east gradients PWLO estimates
.egr(4).mjd:	[1 x 5]	*MJD*	estimation epochs of troposphere east gradients PWLO estimates
.egr(4).col:	[1 x 5]	*integer*	column and row numbers of troposphere east gradients PWLO estimates in N and b
.xpol.val:	[1 x 2]	*mas*	PWLO estimates of polar motion xpol coordinates
.xpol.mx:	[1 x 2]	*mas*	st. dev. of PWLO xpol coordinate estimates
.xpol.mjd:	[1 x 2]	*MJD*	estimation epochs of PWLO xpol coordinate estimates
.xpol.col:	[1 x 2]	*integer*	column and row numbers of PWLO xpol coordinate estimates in N and b
.ypol.val:	[1 x 2]	*mas*	PWLO estimates of polar motion ypol coordinates
.ypol.mx:	[1 x 2]	*mas*	st. dev. of PWLO ypol coordinate estimates
.ypol.mjd:	[1 x 2]	*MJD*	estimation epochs of PWLO ypol coordinate estimates
.ypol.col:	[1 x 2]	*integer*	column and row numbers of PWLO ypol coordinate estimates in N and b
.dut1.val:	[1 x 2]	*ms*	PWLO estimates of dUT1
.dut1.mx:	[1 x 2]	*ms*	st. dev. of PWLO dUT1 estimates
.dut1.mjd:	[1 x 2]	*MJD*	estimation epochs of PWLO Earth rotation angle rate estimates
.dut1.col:	[1 x 2]	*integer*	column and row numbers of PWLO Earth rotation angle rate estimates in N and b
.nutdx.val:	[1 x 2]	*mas*	PWLO estimates of celestial pole dX coordinate

.nutdx.mx:	[1 x 2]	*mas*	st. dev. of PWLO celestial pole dX coordinate estimates
.nutdx.mjd:	[1 x 2]	*MJD*	estimation epochs of PWLO celestial pole dX coordinate estimates
.nutdx.col:	[1 x 2]	*integer*	column and row numbers of PWLO celestial pole dX coordinate estimates in N and b
.nutdy.val:	[1 x 2]	*mas*	PWLO estimates of celestial pole dY coordinate
.nutdy.mx:	[1 x 2]	*mas*	st. dev. of PWLO celestial pole dY coordinate estimates
.nutdy.mjd:	[1 x 2]	*MJD*	estimation epochs of PWLO celestial pole dY coordinate estimates
.nutdy.col:	[1 x 2]	*integer*	column and row numbers of PWLO celestial pole dY coordinate estimates in N and b
.soura(1).name:	0133+476	*character*	name of the source of which CRF coordinates are estimated as PWLOs
.soura(1).val:	[1 x 2]	*mas*	PWLO estimates of right ascension of the source
.soura(1).mjd:	[1 x 2]	*MJD*	epochs of right ascension coor. PWLO estimates
.soura(1).mx:	[1 x 2]	*mas*	st. dev. of right ascension coor. PWLO estimates
.soura(1).col:	[1 x 2]	*integer*	column and row numbers of right ascension coor. PWLO estimates in N and b
.soude(1).name:	0133+476	*character*	name of the source of which CRF coordinates are estimated as PWLOs
.soude(1).val:	[1 x 2]	*mas*	PWLO estimates of declination of the source
.soude(1).mjd:	[1 x 2]	*MJD*	epochs of declination coor. PWLO estimates
.soude(1).mx:	[1 x 2]	*mas*	st. dev. of declination coor. PWLO estimates
.soude(1).col:	[1 x 2]	*integer*	column and row numbers of declination coor. PWLO estimates in N and b
.coorx(4).val:	[1 x 1]	*cm*	one offset TRF-X coordinate estimate of this antenna
.coorx(4).mx:	[1 x 1]	*cm*	st. dev. of the estimated TRF-X coordinate offset
.coorx(4).mjd:	[1 x 1]	*MJD*	estimation epoch of the TRF-X coordinate offset
.coorx(4).col:	[1 x 1]	*integer*	column and row number the antenna's TRF-X coordinate offset estimate in N and b
.coory(4).val:	[1 x 1]	*cm*	one offset TRF-Y coordinate estimate of this antenna
.coory(4).mx:	[1 x 1]	*cm*	st. dev. of the estimated TRF-Y coordinate offset
.coory(4).mjd:	[1 x 1]	*MJD*	estimation epoch of the TRF-Y coordinate offset
.coory(4).col:	[1 x 1]	*unitless*	column and row number the antenna's TRF-Y coordinate offset estimate in N and b

.coorz(4).val:	[1 x 1]	*cm*	one offset TRF-Z coordinate estimate of this antenna
.coorz(4).mx:	[1 x 1]	*cm*	st. dev. of the estimated TRF-Z coordinate offset
.coorz(4).mjd:	[1 x 1]	*MJD*	estimation epoch of the TRF-Z coordinate offset
.coorz(4).col:	[1 x 1]	*integer*	column and row number the antenna's TRF-Z coordinate offset estimate in N and b

Table A.3.7.: "vie_lsm" single session solution results of NEQ system, e.g. IVS-CONT08 first session, structure array "atpa_.mat" saved in "/DATA/LEVEL3/" named as "atpa_session_name.mat" and "atpl_.vec" saved in "/DATA/LEVEL3/" named as "atpl_session_name.mat".

VARIABLE	DEFAULT	UNIT	DESCRIPTION
.atpa_.mat:	[955 x 955]	*various*	NEQ system coefficients matrix with 6 NNT/NNR condition eq.
.atpl_.vec:	[955 x 1]	*various*	NEQ system right hand side vector with 6 NNT/NNR condition eq.

Table A.3.8.: "vie_lsm" single session solution results for being input of global solution, e.g. IVS-CONT08 first session, structure array "glob1.an" saved in "/DATA/LEVEL2/" named as "session_name_an_glob.mat".

glob1.an

VARIABLE	DEFAULT	UNIT	DESCRIPTION
.name:	TSUKUB32...	*character*	all antenna names in the session
.in_trf:	[1 x 11]	*logical*	stations that are included in NNT/NNR condition eq.s
.x:	[1 x 11]	*meter*	a priori TRF-X coordinate of the antenna
.y:	[1 x 11]	*meter*	a priori TRF-Y coordinate of the antenna
.z:	[1 x 11]	*meter*	a priori TRF-Z coordinate of the antenna
.vx:	[1 x 11]	*meter/year*	a priori TRF-X velocity of the antenna
.vy:	[1 x 11]	*meter/year*	a priori TRF-Y velocity of the antenna
.vz:	[1 x 11]	*meter/year*	a priori TRF-Z velocity of the antenna
.epoch:	[1 x 11]	*MJD*	reference epoch of the a priori TRF of each station

Table A.3.9.: "vie_lsm" single session solution results for being input of global solution, e.g. IVS-CONT08 first session, structure array "glob2.x" saved in "/DATA/LEVEL2/" named as "session_name_par_glob.mat". Addition to the variables shown in Table A.3.6

glob2.x

VARIABLE	DEFAULT	*UNIT*	DESCRIPTION
.col_love:	[1 x 77]	*unitless*	column and row numbers corresponding to Love numbers estimates in N and b for global solution
.col_shida:	[1 x 79]	*integer*	column and row numbers corresponding to Shida numbers estimates in N and b for global solution
.col_soura:	[1 x 0]	*integer*	column and row numbers corresponding to sources' right ascension estimates in N and b for global solution
.col_soude:	[1 x 0]	*integer*	column and row numbers corresponding to sources' declination estimates in N and b for global solution
.col_vx:	[1 x 11]	*integer*	column and row numbers corresponding to antennas' TRF-X velocity estimates in N and b for global solution
.col_vy:	[1 x 11]	*integer*	column and row numbers corresponding to antennas' TRF-Y velocity estimates in N and b for global solution
.col_vz:	[1 x 11]	*integer*	column and row numbers corresponding to antennas' TRF-Z velocity estimates in N and b for global solution

Table A.3.10.: "vie_lsm" single session solution results for being input of global solution, e.g. IVS-CONT08 first session, structure array "glob2.opt" saved in "/DATA/LEVEL2/" named as "session_name_par_glob.mat". Addition to the variables shown in Tables A.3.1, A.3.3, A.3.4, A.3.5

glob2.opt

VARIABLE	DEFAULT	*UNIT*	DESCRIPTION
.nconstr:	834	*integer*	number of absolute and relative constraints on the unknown PWLO estimates
.lTPl:	17225029.83	*unitless*	the weighted square sum of the vector "observed minus computed"

Table A.3.11.: "vie_lsm" single session solution results for being input of global solution, e.g. IVS-CONT08 first session, structure array "glob3.opt" saved in "/DATA/LEVEL2/" named as "session_name_Nb_glob.mat".

glob3

VARIABLE	DEFAULT	*UNIT*	DESCRIPTION
.N:	[1138 x 1138]	*various*	TRF and CRF datum free NEQ system coefficients matrix (N)
.b:	[1138 x 1]	*various*	TRF and CRF datum free NEQ system right hand side vector (b)

Table A.3.12.: "vie_mod" multi session solution options.

parameter.vie_mod

VARIABLE	DEFAULT	*UNIT*	DESCRIPTION
.eph:	jpl_405	*character*	ephemerides for celestial bodies
.planets:	yes	*character*	include gravitational bending due to planets
.EOPfile:	C04 05	*character*	introduce IERS 05 C04 EOP series,
			one for each day at 0.00 UTC
.tidalUT:	1 (0)	*logical*	reduce long term tidal variations from UT1 values
			of EOP series before interpolation
.linear:	0 (1)	*logical*	use lagrange interpolation to the obs. epochs
			over the values of EOP series
.eopoc:	eop_eanes.m	*character*	include Eanes model (Effect of ocean tides on high
			frequency polar motion) in a priori values
.tri_pxpy:	1 (0)	*logical*	include effect of triaxiality on polar motion
			in a priori values
.tri_ut:	0 (1)	*logical*	do not include effect of triaxiality on UT1
.dXdY:	1 (0)	*logical*	include nutation offsets from EOP series in
			a priori values
.nutmod:	IAU_2000A	*character*	calculate a priori nutation offsets with IAU_2000A
			precession-nutation model
.cts:	1 (0)	*logical*	introduce corrections to a priori TRF station coordinates
			due to solid Earth tides
.cto:	1 (0)	*logical*	introduce corrections to a priori TRF station coordinates
			due to tidal ocean loading
.cnta:	1 (0)	*logical*	introduce corrections to a priori TRF station coordinates
			due to non-tidal atmosphere loading
.ctp:	1 (0)	*logical*	introduce corrections to a priori TRF station coordinates
			due to pole tide
.therm:	1 (0)	*logical*	introduce corrections to a priori TRF station coordinates
			due to thermal deformation of the antenna
.mf:	VM1	*character*	use VMF1, when introducing a priori hydrostatic slant
			delays and when estimating ZWDs and tropo. gradients
.ocm:	FES2004.mat	*character*	introduce this tidal ocean loading model when including
			tides on the TRF a priori station coordinates
.ctam:	s12_cm ...	*character*	introduce this tidal atmosphere loading model
			on TRF a priori station coordinates
.eophf:	1 (0)	*logical*	include high frequency EOP in a priori polar motion

Table A.3.13.: "vie_mod" multi session solution options of EOP.

parameter.eop

VARIABLE	DEFAULT	*UNIT*	DESCRIPTION
.mjd:	[12 x 1]	*MJD*	epochs of the EOP offsets from IERS 05 C04 combined EOP series (12 a priori values are for interpolation)
.xp:	[12 x 1]	*arcsecond*	polar motion x coordinate offsets
.yp:	[12 x 1]	*arcsecond*	polar motion y coordinate offsets
.ut1:	[12 x 1]	*second*	dUT1 offsets
.dX:	[12 x 1]	*arcsecond*	celestial pole offset dX coordinates
.dY:	[12 x 1]	*arcsecond*	celestial pole offset dY coordinates

Table A.3.14.: "vie_init" multi session solution options.

parameter.vie_init

VARIABLE	DEFAULT	UNIT	DESCRIPTION
.diropt:	**DEFAULT**	character	session-wise option files stored in: $/DATA/OPT/$**DEFAULT**$/YEAR/$
.dirout:	**YOURDIR-B**	*character*	the outlier files read and/or written in: $/DATA/OUTLIER/$**YOURDIR-B**$/YEAR$ when its left empty $/DATA/OUTLIER/YEAR$ is used
.rm_outlier:	1 (0)	*logical*	remove outliers stored in session-wise ASCII files: $/DATA/OUTLIER/$**YOURDIR-B**$/YEAR$
trf:	../TRF/VTRF2008	*character*	path of the selected TRF catalog "*.mat" file
crf:	../CRF/ICRF2	*character*	path of the selected CRF catalog "*.mat" file
sta_info:	../TRF/STAT_INFO	*character*	path of the station based auxiliary information "*.mat" file
min_elev:	0 (3,5,7,...)	*arcdegree*	observations below this elevation angle are excluded

Table A.3.15.: antenna based parametrization and auxiliary information.

antenna(2)

VARIABLE	DEFAULT	*UNIT*	DESCRIPTION
.name:	WETTZELL	character	antenna name
.in_trf:	1 (0)	*logical*	antenna TRF coordinates are taken from catalog
			(if 0 then this station is not included in NNT/NNR)
.x:	4075539.835	*meters*	antenna TRF-X coordinate from catalog
.y:	931735.314	*meters*	antenna TRF-Y coordinate from catalog
.z:	4801629.401	*meters*	antenna TRF-Z coordinate from catalog
.vx:	-0.0157	$\frac{m}{year}$	antenna TRF-X coordinate velocity from catalog
.vy:	0.017	$\frac{m}{year}$	antenna TRF-Y coordinate velocity from catalog
.vz:	0.0103	$\frac{m}{year}$	antenna TRF-Z coordinate velocity from catalog
.epoch:	51544	*MJD*	reference estimation epoch of the catalog coordinates
.x_sigma:	[ ]	*meters*	std. dev. of the TRF-X coor. estimate of the catalogue
.y_sigma:	[ ]	*meters*	std. dev. of the TRF-Y coor. estimate of the catalogue
.z_sigma:	[ ]	meters	std. dev. of the TRF-Z coor. estimate of the catalogue
.vx_sigma:	[ ]	$\frac{m}{year}$	std. dev. of the TRF-X velocity estimate of the catalogue
.vy_sigma:	[ ]	$\frac{m}{year}$	std. dev. of the TRF-Y velocity estimate of the catalogue
.vz_sigma:	[ ]	$\frac{m}{year}$	std. dev. of the TRF-Z velocity estimate of the catalogue
.gptpres:	0 (1)	*logical*	surface pressure values of this station is not derived
			from GPT model (taken from NGS file)
.gpttemp:	0 (1)	*logical*	surface temperature values of this station is not derived
			from GPT model (taken from NGS file)
.cto:	[6x11]	*meters*, [°C]	tidal ocean loading amplitudes and phases for the station
			in REN coordinate system
			column order: M2 S2 N2 K2 K1 O1 P1 Q1 MF MM SSA
			row order: amplitudes (m) [1 : 3] - phases (degrees) [4 : 6]
.cta:	[1x15]	*mm*	[1x3] latitude, longitude, height of the antenna
			[4x15] cos, sin component of S1 and S2 atmosphere
			tidal wave in Up, North, East system
.cnta_dx:	[44x4]	*meters*	non-tidal atmosphere loading on this station
			epoch [MJD], station displacements [dx, dy, dz] in meters
.thermal:	[1x1]	*struct.*	structure array for antenna thermal deformation
			data from THERMAL.DEF
.vm1:	[44x3]	*unitless*	epoch [MJD], hydrostatic VMF "a" coefficient,
			wet VMF "a" coef.
.numobs:	2288	*integer*	total num. of observation of this station in the session
.axtyp:	AZEL	*character*	case of an azimuth-elevation mounting

			(EQUA) case of an equatorial antenna
			(X-Y1) case of an X/Y-fixed N-S axis antenna
			(X-Y2) or (X-YE) or (XYEA) case of an
			X/Y-fixed E-W axis antenna
.axtyp:	-0.0001	*meters*	axis offset of the antenna
.info:	[1x1]	*struct.*	antenna auxiliary information
.ecc:	[1x3]	*meters*	NEU or XYZ eccentricity vector of the antenna
.ecctype	XYZ (NEU)	*character*	coordinate system of the eccentricity vector
.ngsfile:	[ ]	*character*	name of the ngs file entry only in antenna(1).ngsfile 2008/08AUG12XA_N0004
.session:	[ ]	*character*	session name entry only in antenna(1).session 08AUG12XA_N0004
.c_ecc:	[1x3]	*meters*	XYZ eccentricity vector introduced to the a priori antenna TRF coordinates

Table A.3.16.: antenna auxiliary information.

antenna(2).info

VARIABLE	DEFAULT	*UNIT*	DESCRIPTION
.focus:	FO_SECN	*character*	focus type: FO_PRIM – primary
			FO_SECN – secondary
.mount:	MO_AZEL	*character*	mounting type: MO_AZEL – azimuthal
			MO_EQUA – equatorial
			MO_XYNO – XY north
			MO_XYEA – XY east
			MO_RICH – misplaced equatorial RICHMOND
.flag:	RA_NO	*character*	flag: whether the station has radome: RA_NO or RA_YES
.measuretype:	ME_COMP	*character*	measurement type: ME_COMP (complete),
			ME_INCM (incomplete), ME_ROUGH (rough)
.reftemp:	7.8	°C	reference temperature
.reftemp_sin:	0	°C	sin amplitude of annual temperature variations w.r.t.
			the J2000.0 epoch
.reftemp_cos:	0	°C	cos amplitude of annual temperature variations w.r.t.
			the J2000.0 epoch
.refpres:	943.9	*hPa*	reference pressure
.diam:	20	*meters*	antenna diameter
.found_h:	8	*meters*	height of foundation
.found_d:	0	*meters*	depth of foundation
.found_texp:	1e-005	$\frac{1}{Kelvin}$	foundation thermal expansion coefficient
.fixedaxis:	4	*meters*	length of the fixed axis
.fixedaxis_texp:	1.2e-005	$\frac{1}{Kelvin}$	fixed axis thermal expansion coefficient
.axis_offset:	-0.0001	*meters*	length of the axis offset
.axis_offset_texp:	1.2e-005	$\frac{1}{Kelvin}$	axis offset thermal expansion coefficient
.avertex:	3.7	*meters*	distance from the movable axis to the antenna vertex
.avertextexp:	1.2e-005	$\frac{1}{Kelvin}$	thermal expansion coefficient of the structure from
			the movable axis to the antenna vertex
.subref_h:	7.9	*meters*	height of the sub-reflector above the vertex
.subref_h_texp:	1.2e-005	$\frac{1}{Kelvin}$	sub-reflector mounting legs thermal expansion coefficient

Table A.3.17.: scan-wise station variables saved in "DATA/LEVEL1/" named as "session_name_scan.mat".

scan(1).stat(1)

VARIABLE	DEFAULT	*UNIT*	DESCRIPTION
.x:	[1x3]	*meters*	corrected station TRF coordinates (velocity and tidal corrections introduced)
.temp:	27.895	°C	measured temperature at the site
.pres:	1010.5	*hPa*	total surface pressure
.az:	4.6639...	*radians*	azimuth of observation
.zd:	0.9976...	*radians*	zenith distance of observation
.zdry:	2.302...	*m*	zenith hydrostatic delay of the site at observation epoch
.cab:	0.03586	*nanoseconds*	cable delay (correction)
.axkt:	[1x2]	*seconds*	correction to the delay due to axis offset of the antenna
.therm:	-2.687e-12	*seconds*	correction to the delay due to thermal deformation of the antenna
.pantd:	[3x1]	*unitless*	partial derivatives of delay w.r.t. antenna coordinates
.xcrs:	[3x1]	*m*	corrected station positions in GCRS
.mfh:	1.838...	*unitless*	hydrostatic MF at the epoch of the scan and of the zenith distance for the station (VMF1 or GMF)
.mfw:	1.841...	*unitless*	wet MF at the epoch of the scan and of the zenith distance for the station (VMF1 or GMF)
.pLove:	[1x77]	*cm*	partial derivatives of the delay w.r.t. the Love number coefficients
.pShida:	[1x79]	*cm*	partial derivatives of the delay w.r.t. the Shida number coefficients

Table A.3.18.: scan-wise observation variables saved in ”DATA/LEVEL1/” named as ”session_name_scan.mat”.

scan(1).obs(1)

VARIABLE	DEFAULT	*UNIT*	DESCRIPTION
.i1:	6	*integer*	number of the station in the session (first station of the observation)
.i2:	11	*integer*	number of the station in the session (second station of the observation)
.obs:	0.001...	*seconds*	observed delay
.sig:	4.84e-12	*seconds*	standard deviation of the observed delay
.com:	0.001...	*seconds*	computed delay
.iso:	14	*integer*	observed source number within the scan
.q_code:	0 (1-9)	*integer*	quality code of the delay observation
.q_code_ion:	0 (1-9)	*integer*	quality code for ionosphere correction
.psou:	[pra,pde]	$\frac{cm}{mas}$	partial derivatives of the delay w.r.t. source coordinates
.pnut:	[pdX,pdY]	$\frac{sec}{rad}$	partial derivatives of the delay w.r.t. celestial pole offsets
.ppol:	[pdx,pdy,put]	$\frac{sec}{rad}$	partial derivatives of the delay w.r.t. Earth rotation parameters (polar motion)
.pstat1:	[1x3]	*unitless*	partial derivatives of the delay w.r.t. station1
.pstat2:	[1x3]	*unitless*	partial derivatives of the delay w.r.t. station2
.pLove:	[1x77]	*cm*	partial derivatives of the delay w.r.t. the Love number coefficients
.pShida:	[1x79]	*cm*	partial derivatives of the delay w.r.t. the Shida number coefficients

Table A.3.19.: scan-wise space variables saved in "DATA/LEVEL1/" named as "session_name_scan.mat".

scan(1).space			
VARIABLE	**DEFAULT**	*UNIT*	**DESCRIPTION**
.source:	[1x3]	*radians*	unit vector to the observed source (catalogue system)
.xp:	1.4192...	*radians*	pole coordinate - x (interpolated to the epoch and high frequency variations added)
.yp:	1.8569...	*radians*	pole coordinate - y (interpolated to the epoch and high frequency variations added)
.xnut:	0.0008...	*radians*	celestial pole X (nutation model + interpolated EOP series correction)
.ynut:	3.2366...	*radians*	celestial pole Y (nutation model + interpolated EOP series correction)
.t2c:	[3x3]	*unitless*	rotation matrix from terrestrial to celestial

Table A.3.20.: variables of sources saved in "DATA/LEVEL1/" named as "session_name_sources.mat".

source(2)

VARIABLE	DEFAULT	*UNIT*	DESCRIPTION
.name:	1334-127	*character*	source name
.ra2000:	3.5677...	*radians*	right ascension from catalogue
.de2000:	-0.226...	*radians*	declination from catalogue
.ra_sigma:	2.03e-10	*radians*	standard deviation of right ascension from catalogue
.de_sigma:	2.07e-10	*radians*	standard deviation of declination from catalogue
.corr:	-0.018		from catalogue
.in_crf:	1 (0)	*logical*	the source coor. are in selected CRF catalogue, if 0 then the source coor. will be taken from NGS file
.def:	1 (0)	*logical*	defining source, 0 is not defining source
.numobs:	182	*integer*	number of observations to the source carried out within the session

A.4. Multi-session analysis options of VieVS through Graphical User Interfaces
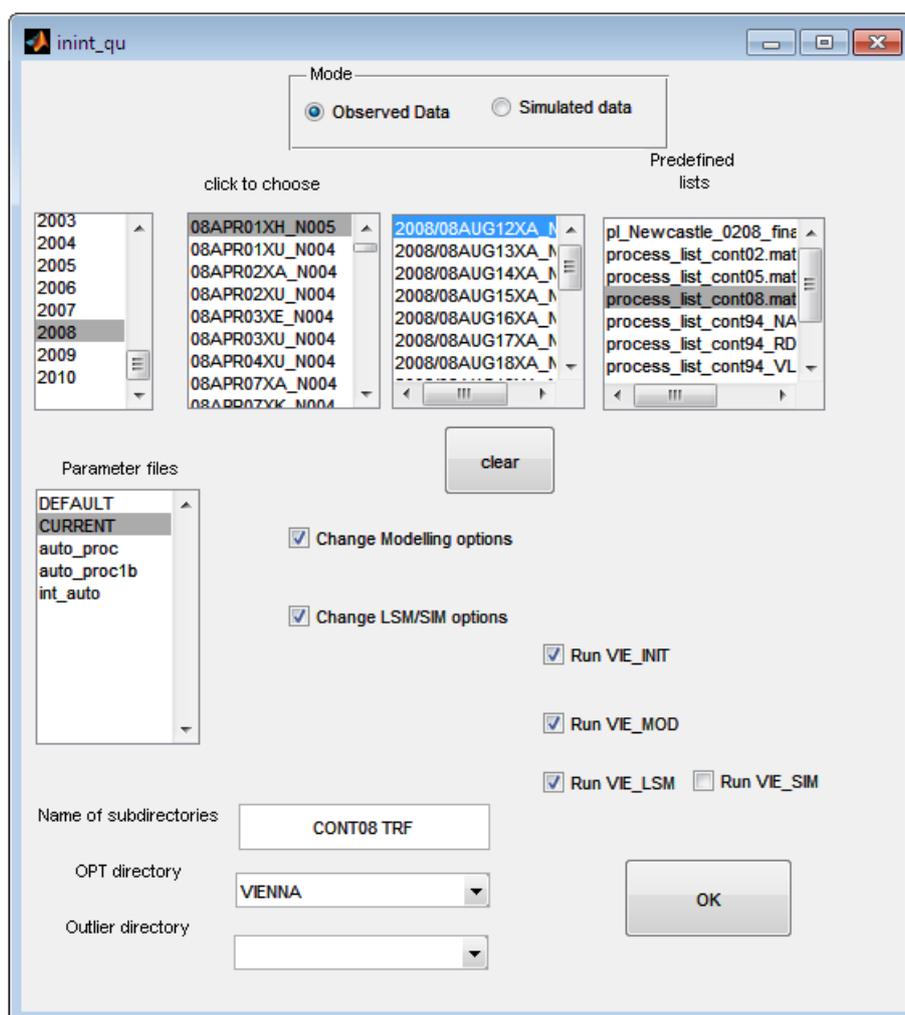
Figure A.4.1.: VieVS GUI, *inint_qu.fig* : determining on the sessions to analyze, on the option and outlier directories to use, on the pre-defined parametrization files to use, selecting module/s of VieVS to run and naming output directory.

Mode (Figure A.4.1): In case, *observed data* is selected, real observation files will be used, stored in the directory: /DATA/NGS, for analyzing or simulated NGS files will be created on the baselines of these real NGS files (these NGS files will be used as template for creating simulated NGS files). In case, *simulated data* is selected, simulated files will be used, stored in the directory: /DATA/SIM, for analyzing.

Predefined lists (Figure A.4.1): These lists are including the group of sessions. The process lists files are stored in WORK/PROCESSLIST directory. The process lists can be created

by selecting sessions in this GUI and after analyzing the sessions the process_list can be found in the WORK directory or "mk_list" function can be used in WORK directory.

Parameter files (Figure A.4.1): DEFAULT: Default vie_mod and vie_lsm parameterizations will be used. Default parameterizations are changed in the file: /VIE_SETUP_V1d/multi_lsmopt.m. CURRENT: The parameterizations of last process are used. User defined parameter files can be created and stored in /WORK/PARAMETERS as mat files by copying the DATA/LEVEL1/sessionname_parameter.mat or DATA/LEVEL0/sessionname_parameter.mat file in to the directory, /WORK/PARAMETERS.

Change Modelling options (Figure A.4.1): This option is activated when CURRENT is selected which allows to change the modelling options.

Change LSM options (Figure A.4.1): This option is activated when CURRENT is selected which allows to change least-squares adjustment parameterizations.

Run VIE_INIT (Figure A.4.1): Only runs vie_init module of VieVS.

Run VIE_MOD (Figure A.4.1): Only runs vie_mod module of VieVS.

Run VIE_LSM (Figure A.4.1): Only runs vie_lsm module of VieVS.

Run VIE_SIM (Figure A.4.1): When vie_sim is selected instead of parameter estimation simulated NGS files (VLBI measurement files) are created. The computed delay is derived from vie_init and vie_mod. In vie_sim in addition to the computed delay, simulated clock, ZWD, and white noise are added and written to NGS file/s as observed delay.

Name of subdirectories (Figure A.4.1): The results is stored in /DATA/LEVEL1 to 3/user_directory, if the user do not specify a directory name then the results will be stored directly in /DATA/LEVEL1 to 3/.

OPT directory (Figure A.4.1): Select a directory where the OPT files are stored in. The OPT files contains the information: clock to be fixed, clock breaks, stations, sources, baselines to be excluded. In order to analyze a session option files are not needed. However, option files are formed in order to fix the clock breaks or/and session specific errors e.g. a specific baseline or a specific antenna may have problems. For that reason, excluding the

177

corresponding baseline or antenna will improve the accuracy of the overall estimates.

Outlier directory (Figure A.4.1): Outliers are stored in DATA/OUTLIER/user_directory/YEAR. If no directory is seen in the list box, then the directory DATA/OUTLIER/YEAR is used if the analyst choose in the second GUI "use outliers".
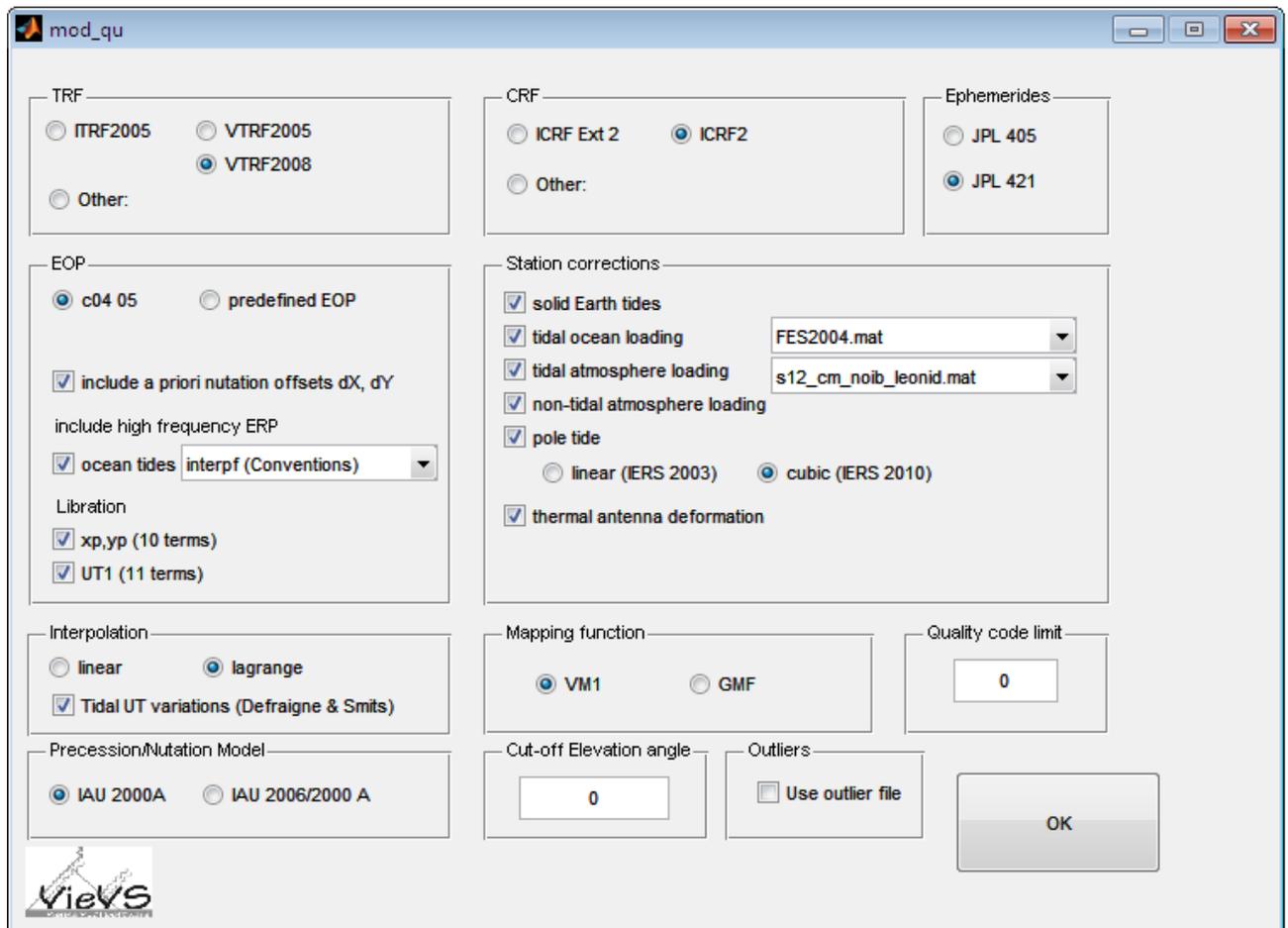
Figure A.4.2.: VieVS GUI, *mod_qu.fig*: vie_mod parameterizations (settings) of a priori models including the TRF, CRF, Ephemerides, troposphere mapping functions. The standard settings realize the IERS conventions.

TRF (Figure A.4.2): Station coordinates and velocities are read from the chosen TRF catalogue (e.g. VTRF2008) stored in VieVS/TRF directory. If a station is not found in the TRF catalogue, the coordinates are read from the NGS-header. To use your own TRF, a corresponding file *filename.txt* has to be created and put in TRF directory and *Other* should be selected.

CRF (Figure A.4.2): BCRS source coordinates are read from the chosen CRF catalogue (e.g. ICRF2) stored in VieVS/CRF directory. If a source is not found in the CRF catalogue, the coordinates are read from the NGS-header. To use your own CRF, a corresponding file *filename.txt* has to be created and put in CRF directory and *Other* should be selected.

Ephemerides (Figure A.4.2): Jet Propulsion Laboratory (JPL) ephemerides: JPL 405/421 are

available. Positions are calculated directly via interpolation of Chebychev polynomials. These information of the time dependent positions and velocities in BCRS of Sun, of Earth, and of other planets are due to e.g. computing gravitational corrections for each observation due to planets i.e. when this option is selected the ray path (in the delay model) is corrected for the gravitational influence of the SUN, EARTH, MOON, and the other planets in the solar system (as requested in the IERS Conventions Chapter 11).

EOP (Figure A.4.2): Predefined EOP lists can be used. They must be stored in VieVS/EOP and must be named like eop_filename.txt. By default C04 05 daily series from the IERS are interpolated to the observation epoch.

include a priori nutation offsets dX, dY (Figure A.4.2): Include corrections from the C04 05 IERS EOP series to the precession/nutation model. These mainly include the free core nutation.

Interpolation (Figure A.4.2): If Lagrange interpolation method is selected, long period tidal UT1 variations are removed from the C04 05 combined EOP IERS daily series. Then, UT1 is interpolated with 4 data points around the observation epoch with Lagrange interpolation. Afterwards, the long term tidal UT1 value of the corresponding observation epoch is added to the interpolated UT1 value. If linear is selected a linear interpolation between the midnight before and after the observation is carried out. For a 24 hour session from 18 : 00 to 18 : 00 this means there are two a priori lines and a break at midnight.

include high frequency ERP (Figure A.4.2): Includes ocean diurnal and semi-diurnal tidal terms (optional) and libration (optional) effect on polar motion and Earth's rotation speed (see Chapter 5.4.2 and Chapter 8 in McCarthy and Petit (2004)).

Station corrections (Figure A.4.2): Tide, load and antenna thermal deformation corrections of introduced to the TRF coordinates of the VLBI antennas a priori to the adjustment in addition to the TRF catalogue velocity corrections (all are w.r.t. the observation epoch) (see Chapter 7 in McCarthy and Petit (2004)).

Mapping function (Figure A.4.2): Vienna mapping functions 1 or Global mapping functions are available.

Use outlier file (Figure A.4.2): This option stands for eliminating pre-determined outliers that are stored in /DATA/OUTLIER/user_directory/YEAR/sessionname.out where user_directory is the directory includes pre-determined outliers. If this option is selected outlier observations are read from corresponding files and eliminated by vie_init.

Quality code limit (Figure A.4.2): Good quality observations have zero code. The observations of which quality code are smaller or equal to the *Quality code limit* are included in the analysis.

Cut-off Elevation angle (Figure A.4.2): Observations below this angle (degrees) are omitted.
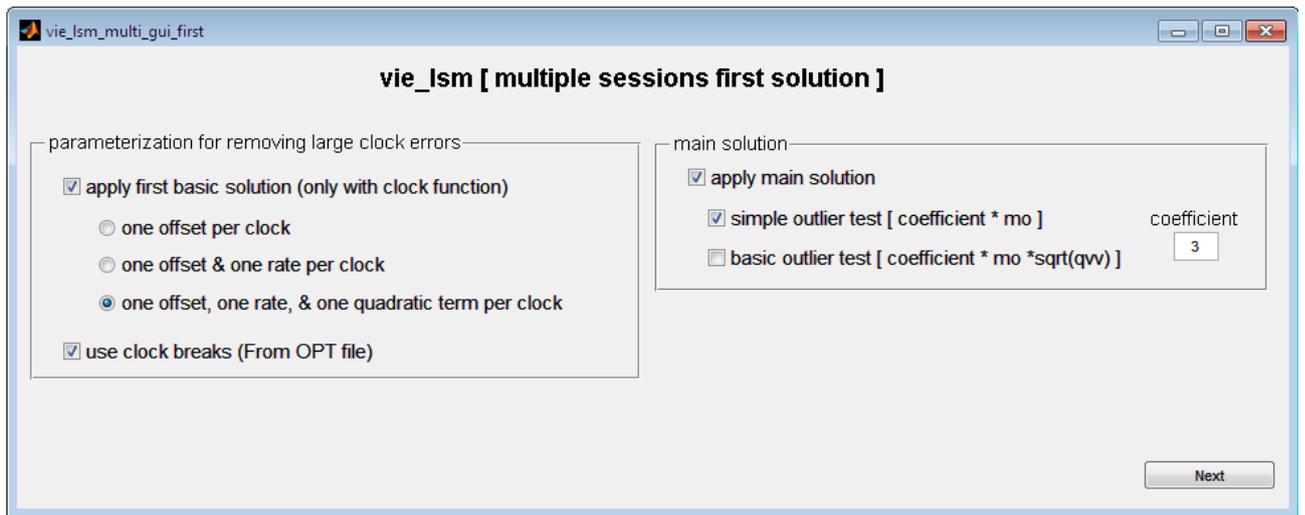
Figure A.4.3.: VieVS GUI, *vie_lsm_multi_gui_first.fig*: vie_lsm parameterizations of first solution including clock estimation and treatment of clock breaks for multiple sessions process.

apply first basic solution (Figure A.4.3): One offset, a linear or a quadratic polynomial (optional) are fitted for the clocks contributing to the session w.r.t. the reference clock, which is the first station in the NGS file or set in the OPT file. With the clock polynomial coefficients, one zenith delay offset for each station for the whole session is estimated. However, the effect of the estimated zenith delays on the observations are reduced in the first solution only for plotting purposes. The plots are station-wise post-fit observational residuals. This is because even minute $\sim$ 20 cm clock breaks can be detected from the plots without the zenith delay effects. If there is a clock break, a new clock polynomial is started at each clock break epoch. In case we deselect this option, only the main solution will be carried out. In the main solution, one rate, one quadratic term, and CPWLOs are estimated for all clocks w.r.t. reference clock, but in the main solution clock breaks are not considered. In other words, when we deselect this option, we must be sure that no clock break occurred at a station within the session.

one offset per clock (Figure A.4.3): If we select this option, only one offset per clock is estimated for each clock for the whole session.

one offset & one rate clock (see Figure A.4.3): If we select this option two clock parameters of the linear clock function are estimated for each clock for the whole session.

one offset, one rate & one quadratic term per clock (see Figure A.4.3): If we select this op-

tion three clock parameters of the quadratic clock function are estimated for each clock for the whole session.

use clock breaks (From OPT file) (Figure A.4.3): If we deselect this option no treatment for the clock breaks introduced. OPT files provide the information when (MJD) and at which clock the break/s occurred. These OPT files are saved in VieVS/DATA/OPT. In case two clock breaks occurred in a session at a clock, then for the corresponding clock three clock functions are formed. The first epoch of the first polynomial and the last epoch of the last polynomial are at the integer UTC hours before and after the first and the last observations, respectively. A clock with a clock break should not be fixed.

apply main solution (Figure A.4.3): By default this option is selected. If it is deselected then the main solution will not be performed but station-wise post-fit observational residuals after the first solution will show up. These plots are helpful for the determination of the epoch of clock breaks.

simple outlier test (coefficient × m0) (Figure A.4.3): An observation can be assumed as outlier if its residual is three times larger than the a posteriori standard deviation of unit weight of the adjustment. If selected, VieVS writes the corresponding outliers into an ASCII file in /VieVS/DATA/OUTLIER/user_directory/YEAR/session_name. The outliers are written in the format: from station, to station, epoch of the observation in MJD.

basic outlier test (coefficient × m0 × qvv) (Figure A.4.3): In this case the post-fit residuals of the observations are compared with the standard deviations of the residuals. If the residual is e.g. three (coefficient) times larger than its formal error, the observation is assumed to be an outlier. The basic difference between the two outlier tests is: The former uses the a posteriori standard deviation of unit weight, m_0 and the latter uses the formal error of the residuals, m_{v_i}.
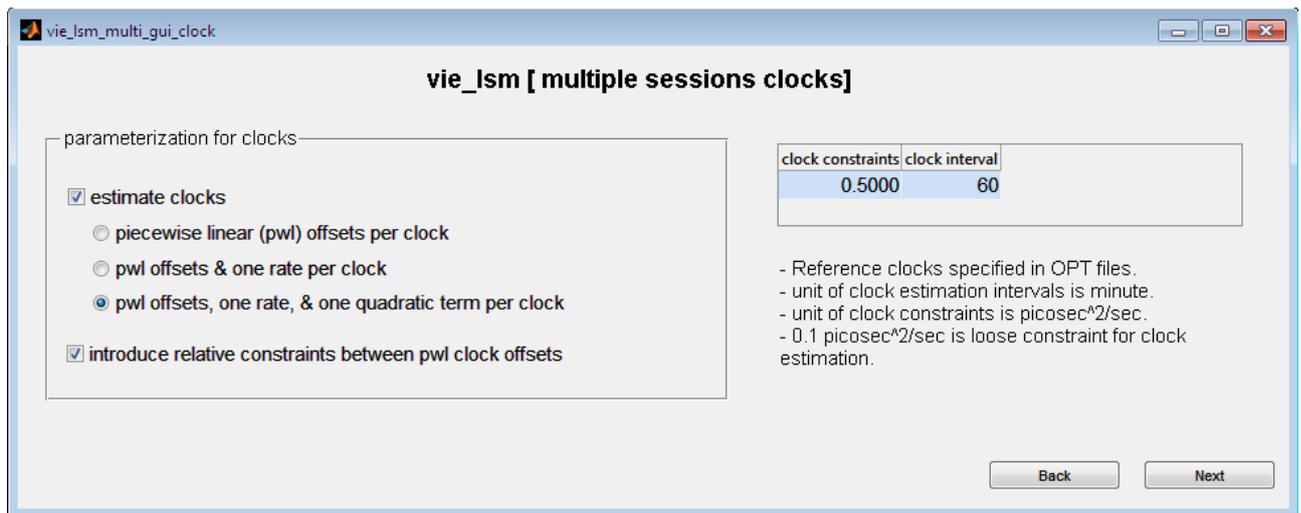
Figure A.4.4.: VieVS GUI, *vie_lsm_multi_gui_clock.fig*: vie_lsm parameterizations of the main solution clock estimation for multiple sessions process.

estimate clocks (Figure A.4.4): In case, we want to estimate clock in the main solution.

CPWLO per clock (Figure A.4.4): In case, we want to estimate only CPWL clock offsets for 60 minutes estimation intervals (at UTC integer hours) with $0.5ps^2/s$ variance rate. Variance rates are used to assign a weight to the constraints (pseudo-observations). Our time interval between CPWLOs is 60 minutes, i.e. we have a variance $1800ps^2$ after one hour equals to the standard deviation of 42 ps after one hour. This standard deviation equivalence is 13 mm after one hour.

pwl offsets & one rate per clock (Figure A.4.4): In case, we want to estimate one rate per clock in addition to CPWL clock offsets.

pwl offsets, one rate , & one quadratic term per clock (Figure A.4.4): In case, we want to estimate one rate and one quadratic term per clock in addition to CPWL clock offsets.

introduce relative constraints on pwl clock offsets (Figure A.4.4): In case, these constraints are not included by deselecting this option then if the estimation interval is too small (e.g. 10 minutes) most likely some estimation intervals might not include any observation which will result in singularity problem of the normal equation matrix.
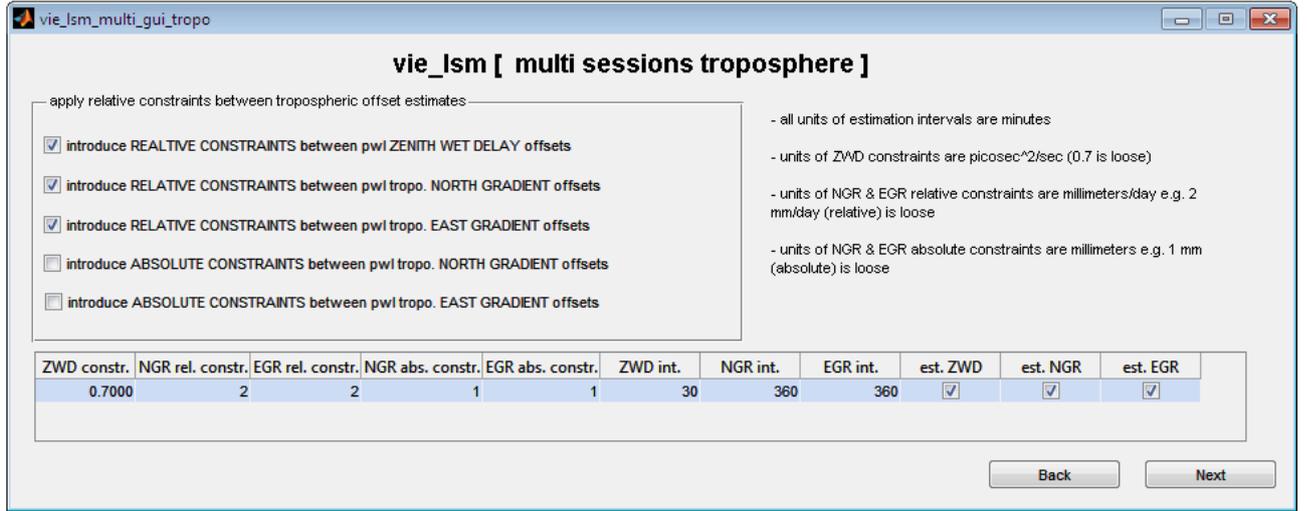
Figure A.4.5.: VieVS GUI, *vie_lsm_multi_gui_tropo.fig*: vie_lsm parameterizations of troposphere estimation for multiple sessions process.

est. ZWD (Figure A.4.5): In case we want to estimate zenith wet delays (ZWDs) as CPWLOs for all stations during the session.

ZWD constr. (Figure A.4.5): The constraint for the relative variation between ZWD estimates (assigning a standard deviation to the relative constraints, m_{zwd}). The relative constraints on parameters are introduced as:

$$ZWD_{EPOCH(i)} - ZWD_{EPOCH(i+1)} = 0 \pm m_{zwd}, \tag{A.4.1}$$

and the absolute constraints between parameters are introduced as:

$$ZWD_{EPOCH(i)} = 0 \pm m_{zwd}. \tag{A.4.2}$$

Pseudo-observation equations are added to the design matrix. The weights of the these pseudo-observations (constraints) are determined by the standard deviations assigned to them. In case we estimate gradients every 6 hours and the constraint is chosen as 2 mm/day in the GUI, the standard deviation in the pseudo observation equation is 0.5 mm. In case we estimate zenith wet delays every hour and the constraint (variance rate) chosen in the GUI is 0.7 ps^2/s, the variance of the pseudo-observation equation (constraint) is 0.7×3600 ps. Then, the standard deviation is 50 ps after one hour (loose) and is assigned for each constraint equation. This standard deviation equals to 15 mm after one hour.

ZWD int. (Figure A.4.5): Estimation intervals of ZWDs are specified in minutes.

est. NGR (Figure A.4.5): Deciding on estimating or not estimating troposphere north gradients as CPWLOs for all stations contributing to the session.

NGR rel. constr. (Figure A.4.5): The standard deviations of relative constraints on troposphere north gradients are assigned (by default: ± 2 mm after one day, relatively loose).

NGR abs. constr. (Figure A.4.5): The standard deviations of absolute constraints on troposphere north gradients are assigned (by default: ± 1) mm after one day. Constraints on the CPWLOs of troposphere gradients can be introduced as absolute or relative or both (absolute and relative).

EGR int (Figure A.4.5): Troposphere east gradients estimation interval is in minutes.
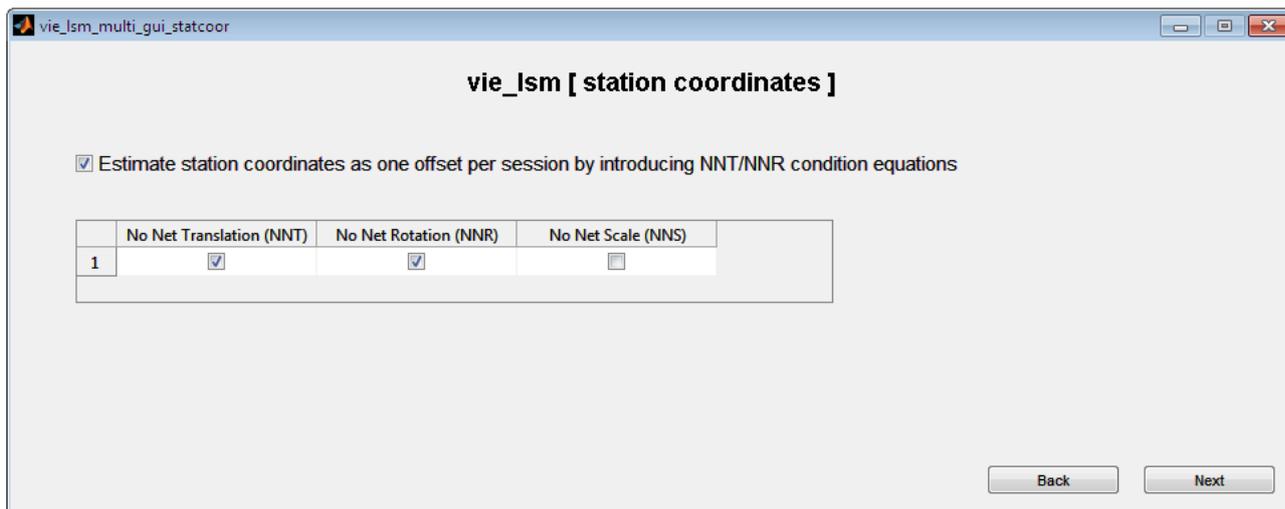
Figure A.4.6.: VieVS GUI, *vie_lsm_multi_gui_statcoor.fig*: vie_lsm parameterizations of antenna coordinate estimation in TRF for multiple sessions process.

Estimate station coordinates as one offset per session ... (Figure A.4.6): This option is for estimating antenna TRF coordinates. When estimating TRF, VieVS introduces condition equations for all stations (except for the stations of which coordinates are not in the TRF catalogue) to the normal equation matrix (N) of the session. For multiple session processes, the TRF is estimated only by NNT/NNR which is the only available option at present. When this option is deselected the station coordinates will be fixed to a priori coordinates from the catalogue.

No Net Translation (NNT) (Figure A.4.6): Providing the condition that the three translations will be zero between the a priori TRF and the estimated TRF of the session.

No Net Rotation (NNR) (Figure A.4.6): Providing the condition that the three rotations will be zero between the a priori TRF and the estimated TRF of the session.

No Net Scale (NNS) (Figure A.4.6): Providing the condition that the scale will be zero between the a priori TRF and the estimated TRF of the session. By default scale condition equation is not introduced. However, this condition also can be introduced on the new TRF in case the user select the option.
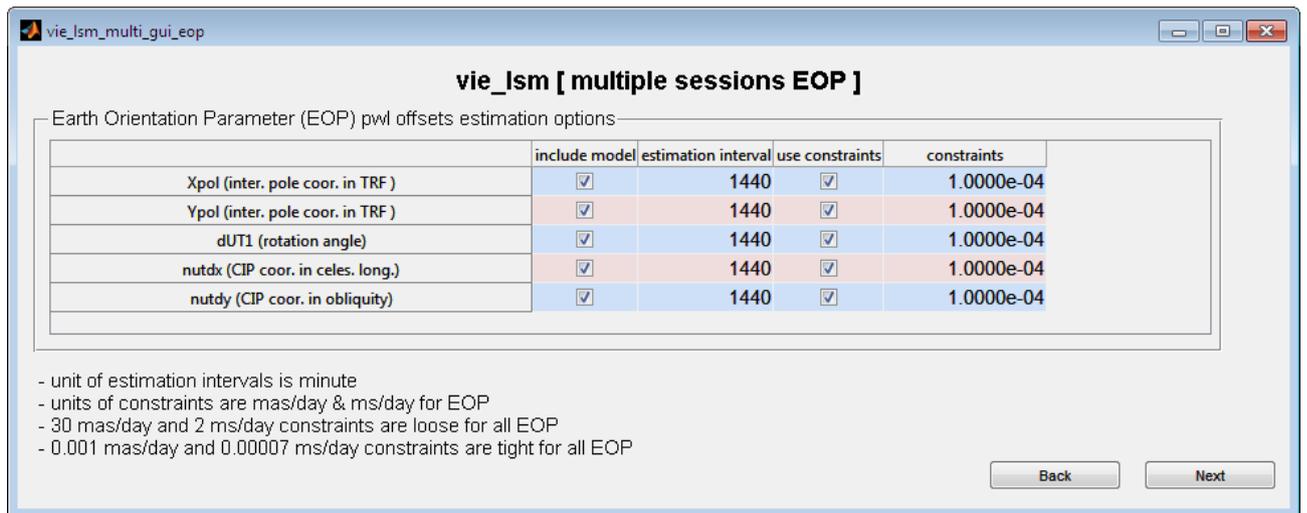
Figure A.4.7.: VieVS GUI, *vie_lsm_multi_gui_eop.fig*: vie_lsm parameterizations of Earth orientation parameters (EOP) estimation for multiple sessions process.

include model (Figure A.4.7): This option is for estimating Earth orientation parameters (EOP) in addition to their corresponding a priori values computed in vie_mod.

estimation interval (Figure A.4.7): Estimation interval of EOP CPWLOs in minutes.

use constraints (Figure A.4.7): If the relative constraints on the EOP CPWLO estimates are introduced.

constraints (Figure A.4.7): The standard deviations for relative constraints between EOP estimates. For nutation and polar motion units are mas/day, and for (UT1−UTC) ms/day. If the analyst wants to estimate one constant value per session, the recommendation is to set the parameterizations as shown in the Figure A.4.7. For example, if the session is from 18 UT to 18 UT then, three piece-wise linear offsets are set up for each EOP. (They are set up a midnight before the session, at midnight during the session, and at midnight after the session.) Very strong relative constraints of 1e-4 m(a)s/day take care that the estimates are the same over the session.
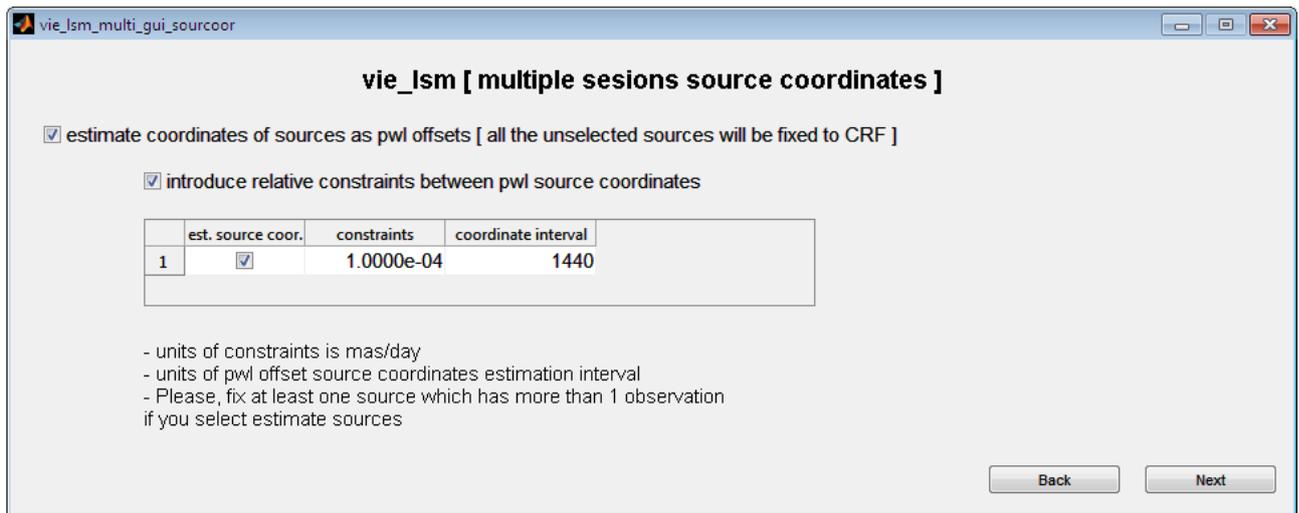
Figure A.4.8.: VieVS GUI, *vie_lsm_multi_gui_sourcoor.fig*: vie_lsm parameterizations for CPWLO source coordinates (right ascension and declination) estimation for multiple sessions process.

estimate coordinates of sources as pwl offsets ... (Figure A.4.8): This option is for estimating the CPWLOs of source coordinates. NNR solution is not available for single session analysis. In principle, if more than one source of which observations are more than one within the session when fixed to its CRF catalogue coordinates then the remaining coordinates of sources can be estimated without any datum deficiency (caused singularity) problem. In vie_lsm by default only one source of which number of observations in the session is maximum is estimated. All the other source coordinates are fixed to their a priori CRF catalogue coordinates. By applying a simple change in COMPILE/VIE_LSM_V1b/lsmopt.m file the sources that are to be estimated as pwl offsets can be chosen (e.g. sources of which number of observations are above 50 should be estimated or the ICRF2 defining sources should be fixed and remaining sources should be estimated, so on and so forth).

introduce relative constraints between pwl source coordinates (Figure A.4.8): This option is for introducing relative constraints between the estimated CPWLOs of source coordinates.

constraints (Figure A.4.8): The standard deviation assigned to the relative constraint equations between CPWLOs of source coordinates in units of mas/day.

coor. interval (Figure A.4.8): Estimation interval of CPWLOs of source coordinates. In case, the relative constraints are assigned very tight, regardless from the estimation interval all the offsets will take the same value and will be equal to one offset estimate. This is valid

189

for every kind of parameter that is estimated as CPWLOs.
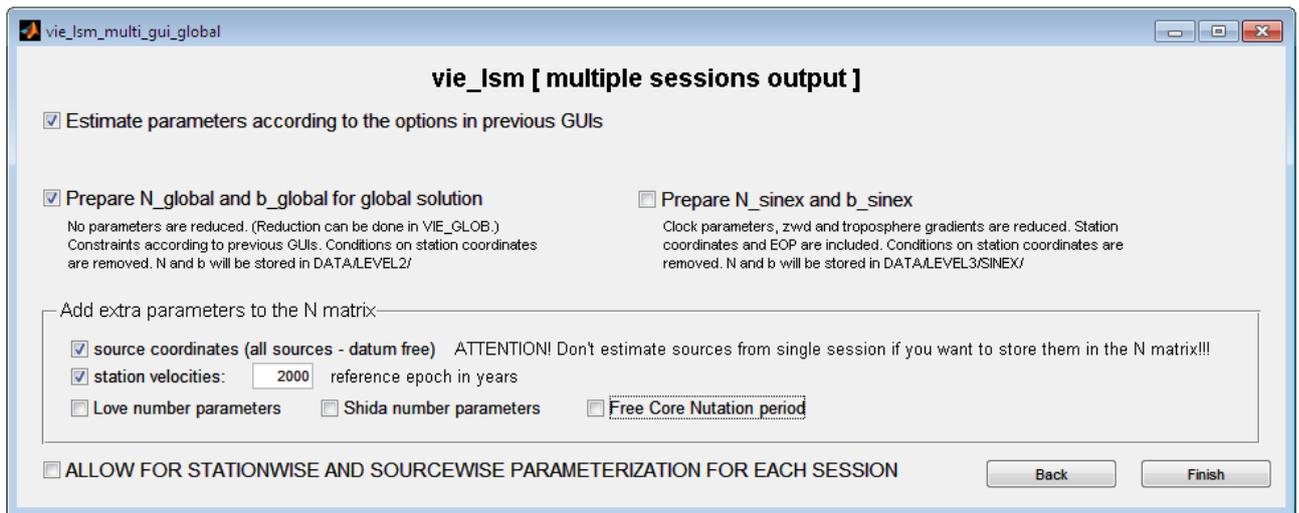
Figure A.4.9.: VieVS GUI, *vie_lsm_multi_gui_global.fig*: vie_lsm parameterizations of forming the reduced and not reduced datum free normal equations (N and b) for global solution.

Estimate parameters according to the options in the previous GUIs (Figure A.4.9): When we select this option, single session parameters will be estimated and stored in /LEVEL3/user_directory.

Prepare N_global and b_global for global solution (Figure A.4.9): When we select this option, datum free normal equation matrix (N_global) and right hand side vector (b_global) will be created and saved in /DATA/LEVEL2/user_directory directory. When we select this option and not select any option in the parameters menu named as "Add extra parameters to the N matrix" then the N_global and b_global will be formed for the parameters (optional): clocks, zenith wet delays, north and east gradients, antenna TRF coordinates, and EOP all as CPWLOs. No parameters are reduced in this option and absolute or relative continuity (soft) constraints are included.

Prepare N_sinex and b_sinex (Figure A.4.9): When this option is selected N_sinex, b_sinex are formed and stored in /DATA/LEVEL3/user_directory/SINEX. These normal equations include continuity (soft) constraints, but no TRF or CRF datum constraints the same as N_global and b_global. The difference is N_sinex, b_sinex are reduced normal equations. The reduced parameters are clocks, ZWDs, and troposphere gradients. The antenna TRF coordinates as one offset for one session, and EOP CPWLOs are included and source CRF coordinates as one offset for one session included as optional.

source coordinates (Figure A.4.9): Different from the single session solution (CPWLOs) pre-

pares N_global and b_global for all sources as one offset for one session. N_global and b_global are CRF datum free (CRF datum constraints are not included for the sources in N_global or b_global). It should be mentioned that in case CPWLO CRF coordinates of some sources are estimated in single session solution then source coordinates can not be prepared in N_global and b_global for global solution.

station velocities (Figure A.4.9): Concatenates three columns to the observation equations for each antenna $(v_x,\ v_y,\ v_z)$ as one offset for one session to form A_global. The partial derivatives of observations w.r.t. station coordinates are multiplied with

$$(\frac{mjd_{session} - mjd_{2000.0}}{36525}) \tag{A.4.3}$$

for each observation.

Love numbers (Figure A.4.9): When we select this option vie_lsm adds to N_global and b_global different types of frequency dependent Love numbers.

Shida number (all 79 columns) (Figure A.4.9): When we select this option vie_lsm adds to N_global and b_global different types of frequency dependent Shida numbers.

ALLOW FOR STATION-WISE AND SOURCE-WISE ... (Figure A.4.9): In case these option is selected: For each session, station and source specific parameters can be specified within "single session GUIs". For example:

- Clocks to be fixed for the first and the main solution can be changed separately.

- CPWLOs of station coordinates (sub-daily TRF antenna coordinates) can be estimated by fixing at least 3 VLBI antennas to any a priori TRF.

- When one antenna coordinate offset for one session is estimated on which coordinates of antennas NNT/NNR condition equations will be imposed can be selected.

- Which sources CRF coordinates as CPWLOs will be estimated (sub-daily CRF source coordinates) can be selected. The list of what can be done with the source and station specific parameterizations could be extended depending on the analyst requirements.

A.5. Single-session analysis options of VieVS through Graphical User Interfaces
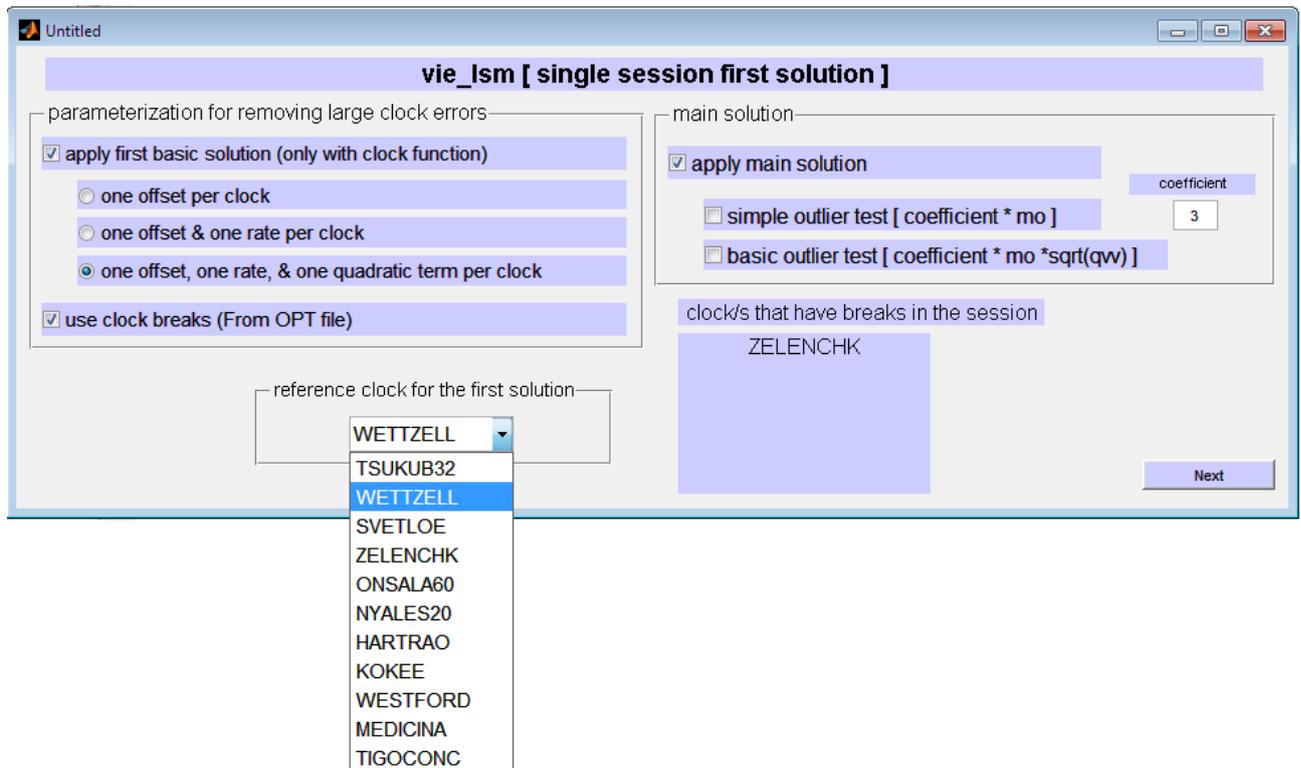
Figure A.5.1.: VieVS GUI, *single_session_first_sol.fig*: vie_lsm parameterizations for the first solution of single session process.

reference clock for the first solution (Figure A.5.1): If there is not an option file of a session clock to be fixed is chosen as the first VLBI antenna clock in the NGS file. In case, an OPT file exists in the directory /DATA/OPT/userdefined_filename/YEAR, then this specified clock. If there is not an option file of a session and the clock of the first VLBI site has a clock break then the clock of the second VLBI site in the NGS file is fixed. For the multi session process, same clock is fixed as default for the first and main solutions should be kept in mind. However, it is possible to change the clock to be fixed both for the first solution and the main solution in single session process.

clock/s that have breaks in the session (see Figure A.5.1): This static text box is for the user information. In case, in OPT file any clock break is reported then it is shown here in the GUI as to warn the user not to select the corresponding clock to fix.

Other options in the GUI (Figure A.5.1) are explained in Appendix **??** corresponding to the Figure A.4.3.
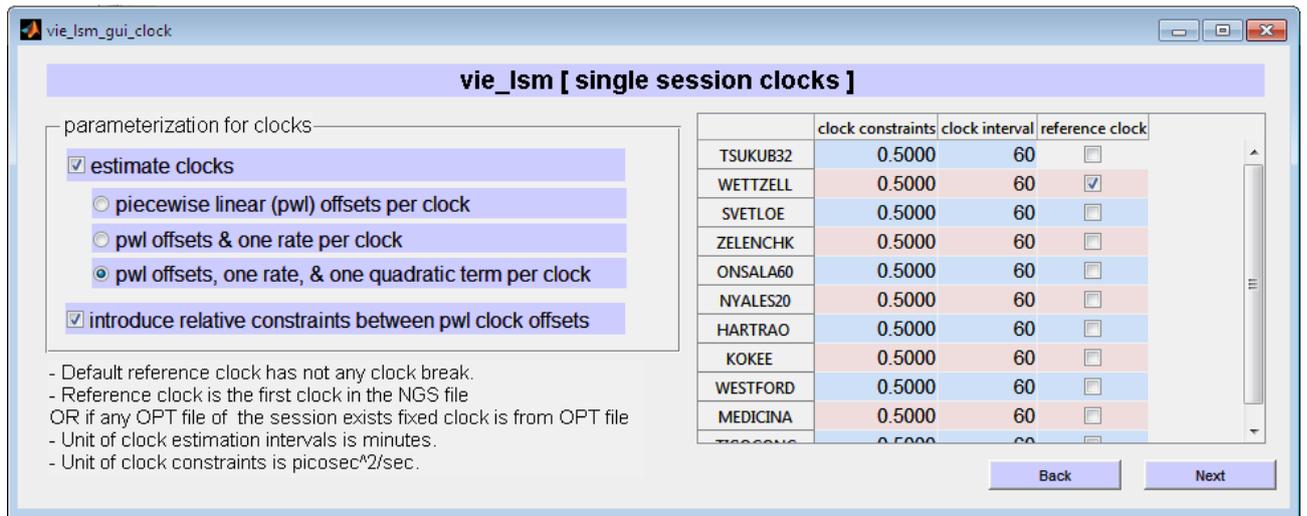
Figure A.5.2.: VieVS GUI, *single_session_clocks.fig*: vie_lsm parameterizations of the main solution pertaining to clocks of single session process.

In the main solution (Figure A.5.2) clock model parameters, their estimation intervals, and relative constraints between the CPWL clock offset estimates can be specified as station-wise independent from the first solution.
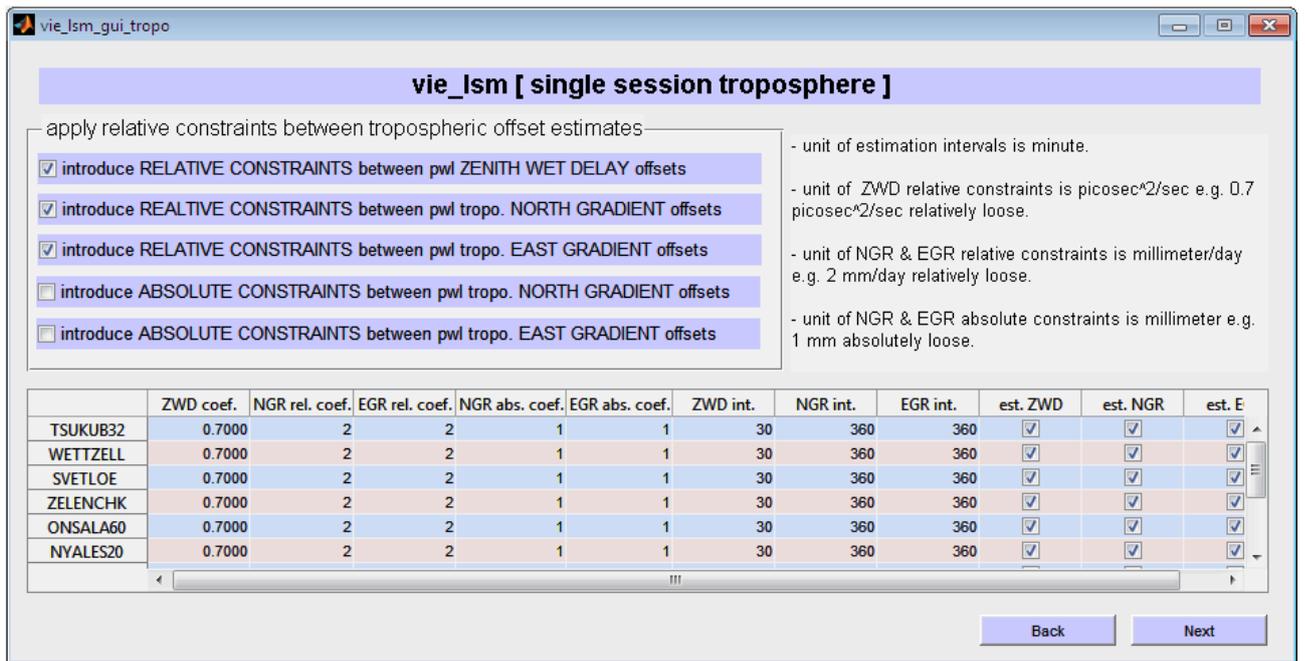
Figure A.5.3.: VieVS GUI, *single_session_troposphere.fig*: vie_lsm troposphere parameterizations of single session process.

Station-wise parameterizations can be done through the GUI given in Figure A.5.3. The settings of the Figure A.5.3 are explained in Appendix A.4 on the Figure A.4.5. It is worth to emphasize that the relative constraints between gradients and absolute constraints on gradients either can be introduced separately or together. In some cases, for instance, when the ray traced wet delays wanted to be introduced externally than the troposphere may not be estimated by deselecting the options: est. ZWD, est. NGR, and est. EGR.
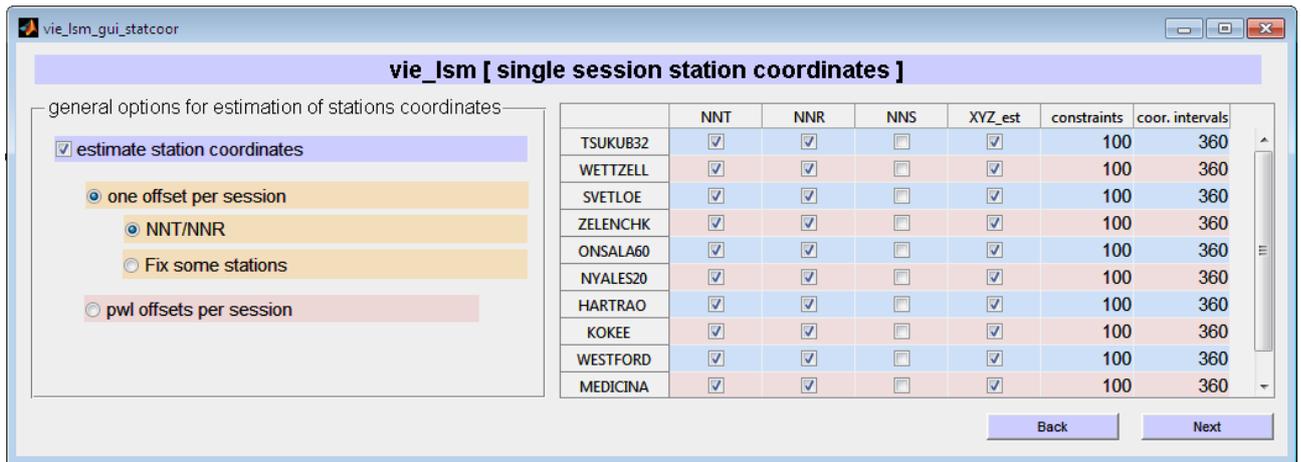
Figure A.5.4.: VieVS GUI, *single_session_statcoor.fig*: vie_lsm parameterizations for the estimation of station coordinates of single session process.

estimate station coordinates (Figure A.5.4): If the antenna coordinates will be estimated.

one offset per station (Figure A.5.4): To estimate one offset (dx, dy, dz) per session. In order to impose a TRF datum NNT/NNR solution and fixing to a priori coordinates are available for this type of parameter.

NNT/NNR (Figure A.5.4): The condition equations introduced to the normal equation matrix (N) providing the translation and rotation between the estimated and a priori TRF will be zero. Thus, the square sum of the antenna coordinate estimates is minimum. It should be noted that in VieVS if a station's TRF catalogue coordinates are not found, VieVS takes the a priori coordinates of the antenna from NGS file and do not allow the antenna to take part in the new TRF datum definition.

Fix some stations (Figure A.5.4): This option is only available for single session solution. In case, this option is selected than at least 3 antenna TRF coordinates should not be estimated (fixed to its a priori TRF coordinates) or if EOPs are not estimated then the rotation of the TRF will be fixed w.r.t. CRF catalogue and EOP models then fixing one antenna to its TRF catalogue coordinates (for translation) will be adequate for defining the TRF datum.

pwl offsets per session (Figure A.5.4): This option is only available for single session solution. In case, this option is selected at least 3 antennas TRF coordinates should be fixed to its

a priori coordinates and relative constraints should be introduced between the CPWLO estimates regardless from length of the estimation interval. The end results will be the sub-daily TRF coordinates of the antennas.
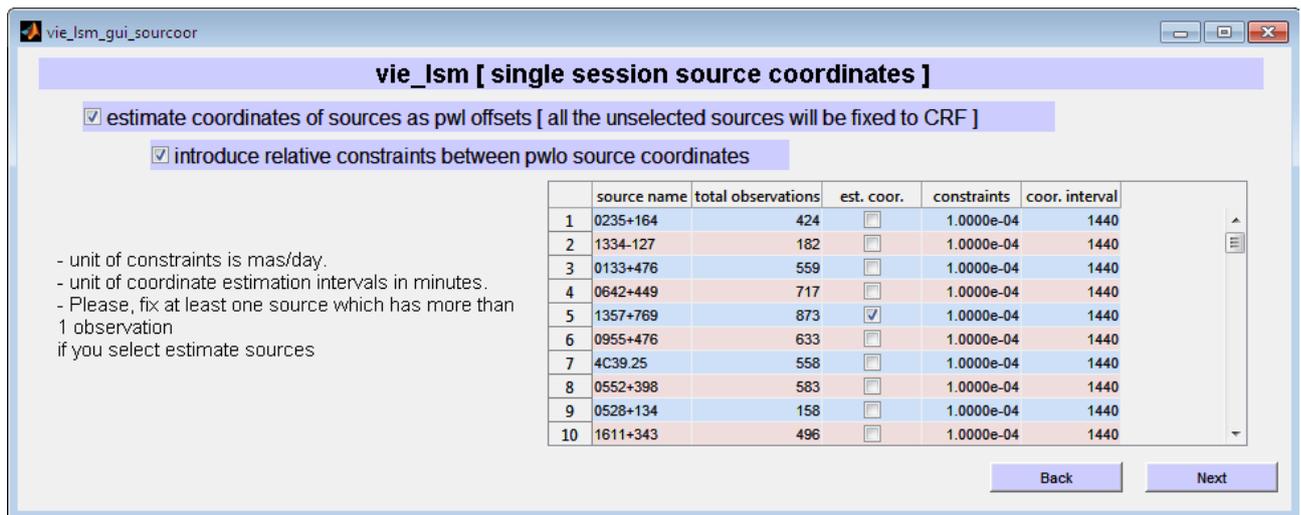
Figure A.5.5.: VieVS GUI, *single_session_sourcoor.fig*: vie_lsm parameterizations for the estimation of source coordinates during single session process.

total observations (Figure A.5.5): Number of total observations to the source carried out within the session (after outliers are eliminated).

est. coor. (Figure A.5.5): By default, VieVS estimates CRF coordinates as CPWLOs of the source of which total number of observations is maximum during the session. However, other sources coordinates can also be estimated as CPWLOs by selecting the corresponding source.

constraints (Figure A.5.5): Relative constraints between CPWLOs of coordinate estimates of sources in CRF in mas/day. If the relative constraints is selected as very tight then regardless from estimation interval length all the estimated offsets will be the same and equal to one offset estimate.

coor. interval (see Figure A.5.5): Estimation interval of the pwl offset estimates in minutes. In case, estimation interval is selected as 1440 minutes three estimates will be resulted in (one at the midnight before, one at the midnight of, and one at the midnight after the session). If this session is IVS-CONT08 for 1440 minutes two offsets will be estimated (one at the beginning and one at the end midnight).

A.6. Troposphere zenith total delays at co-located sites during IVS-CONT08
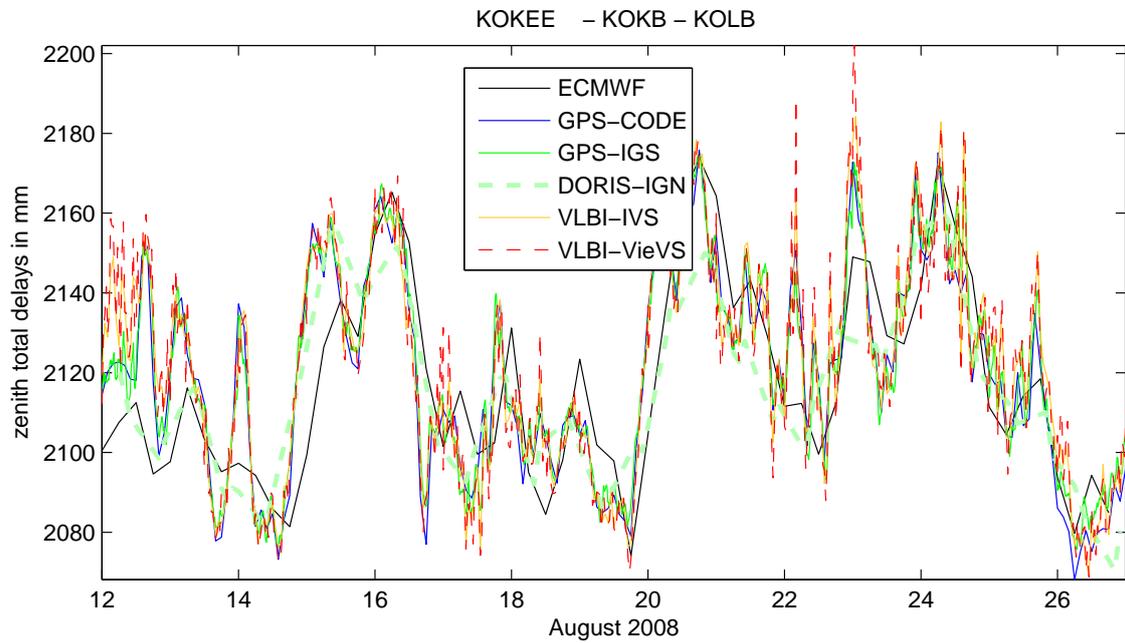
Figure A.6.1.: ZTDs at co-located site Kokee in USA during IVS-CONT08.
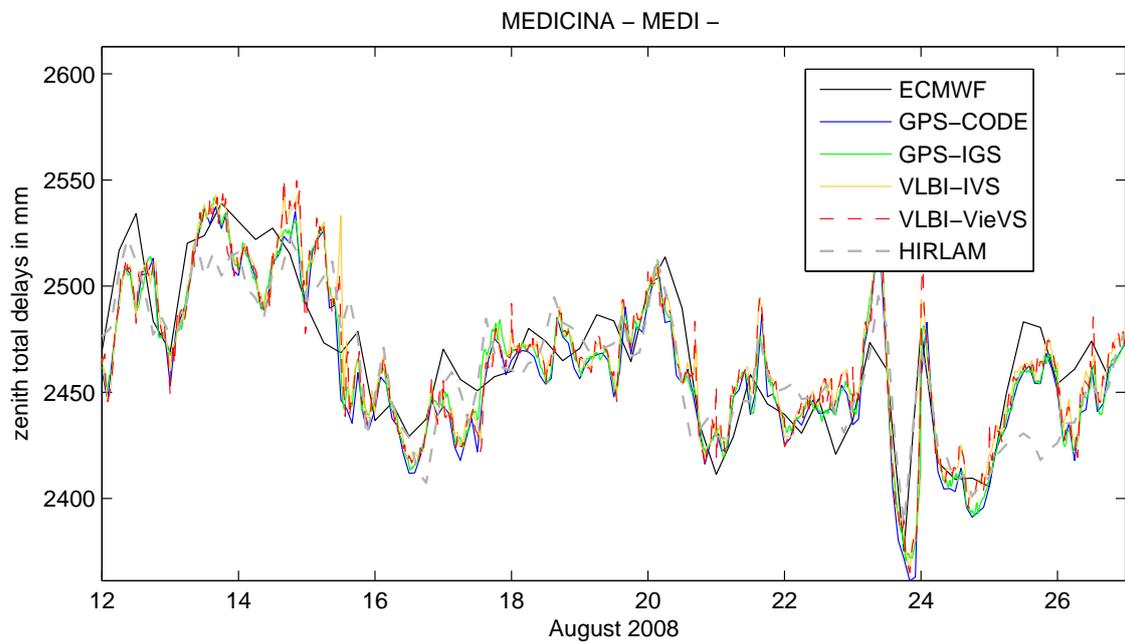
Figure A.6.2.: ZTDs at co-located site Medicina in Italy during IVS-CONT08.
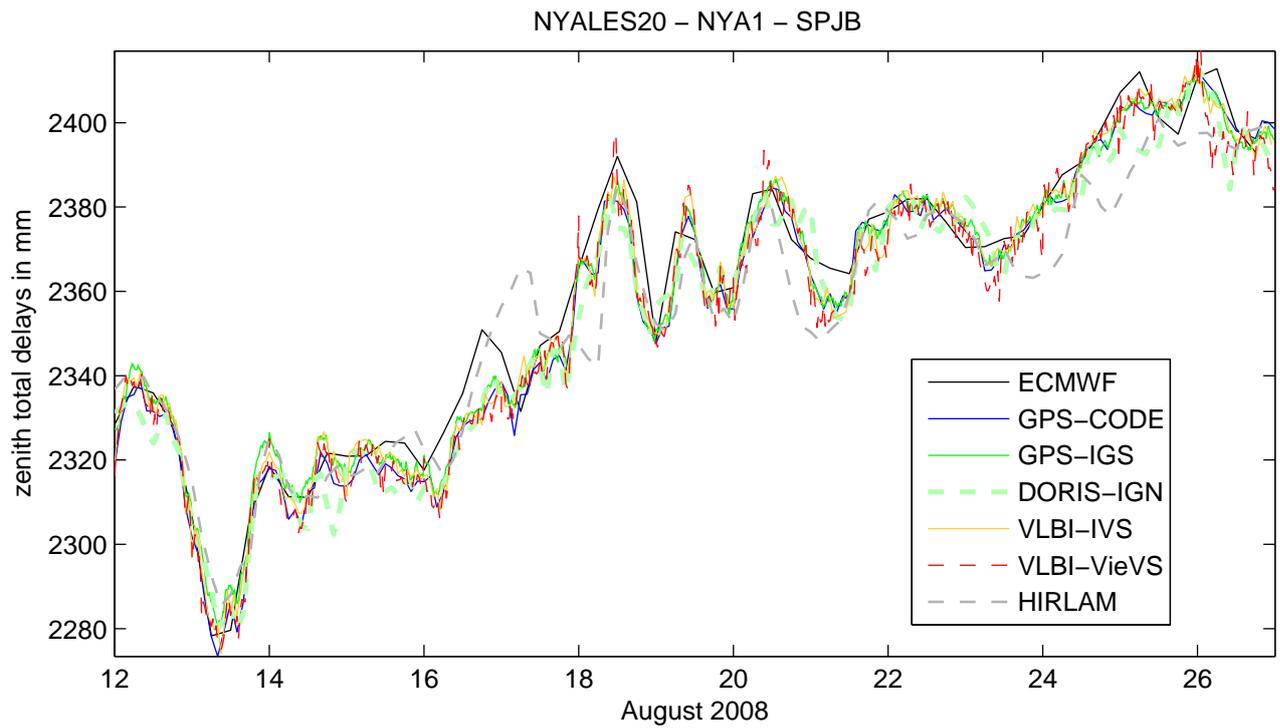
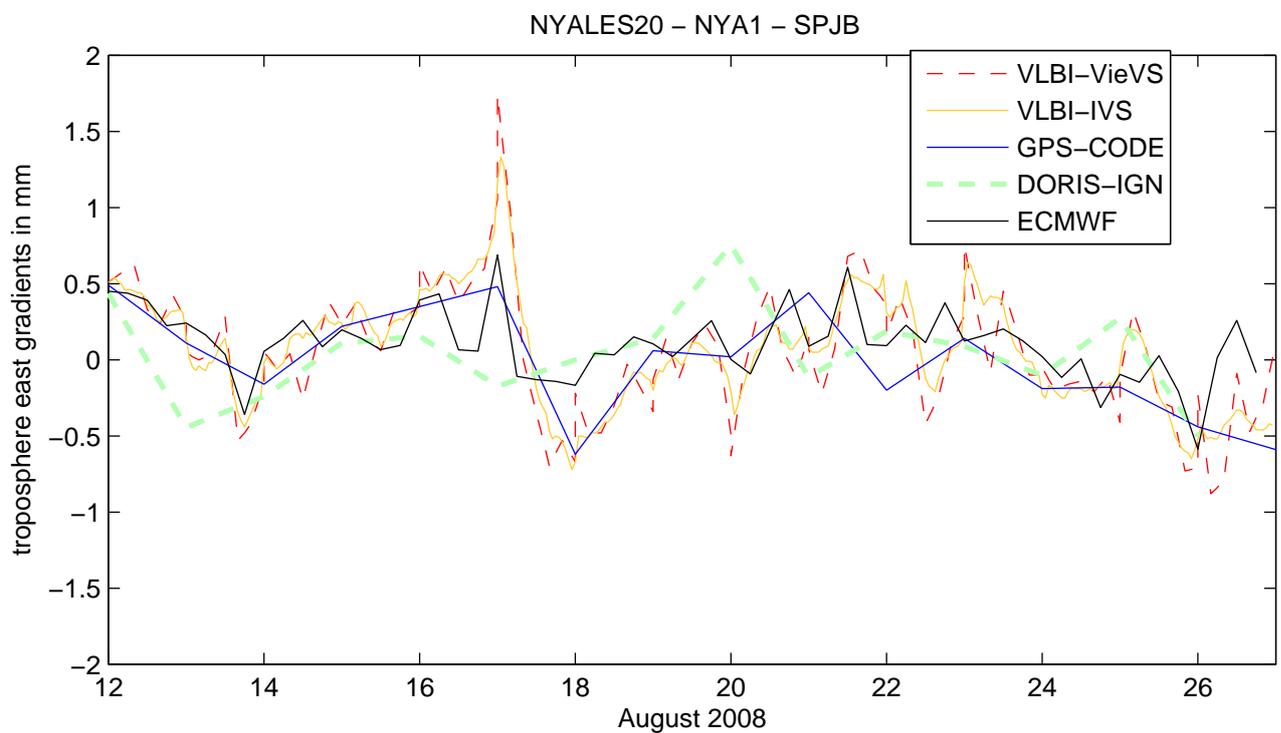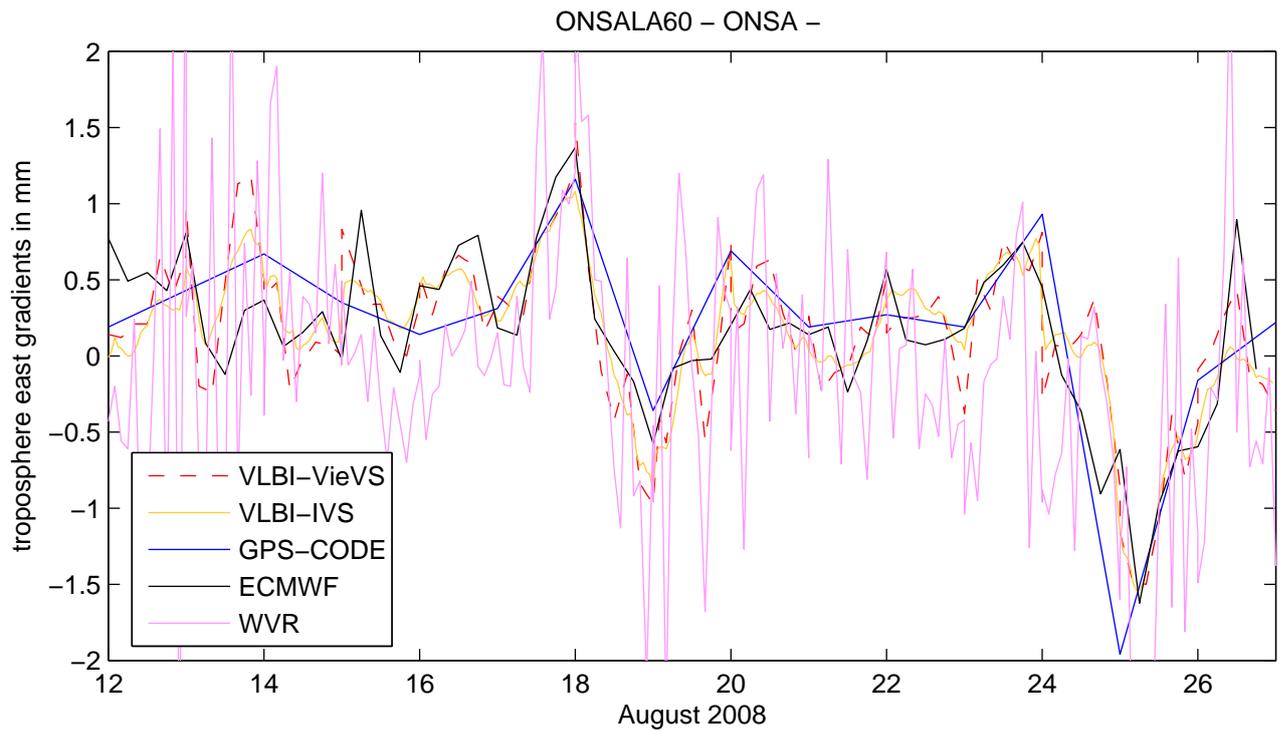Figure A.6.3.: ZTDs at co-located site Ny-Ålesund in Norway during IVS-CONT08.
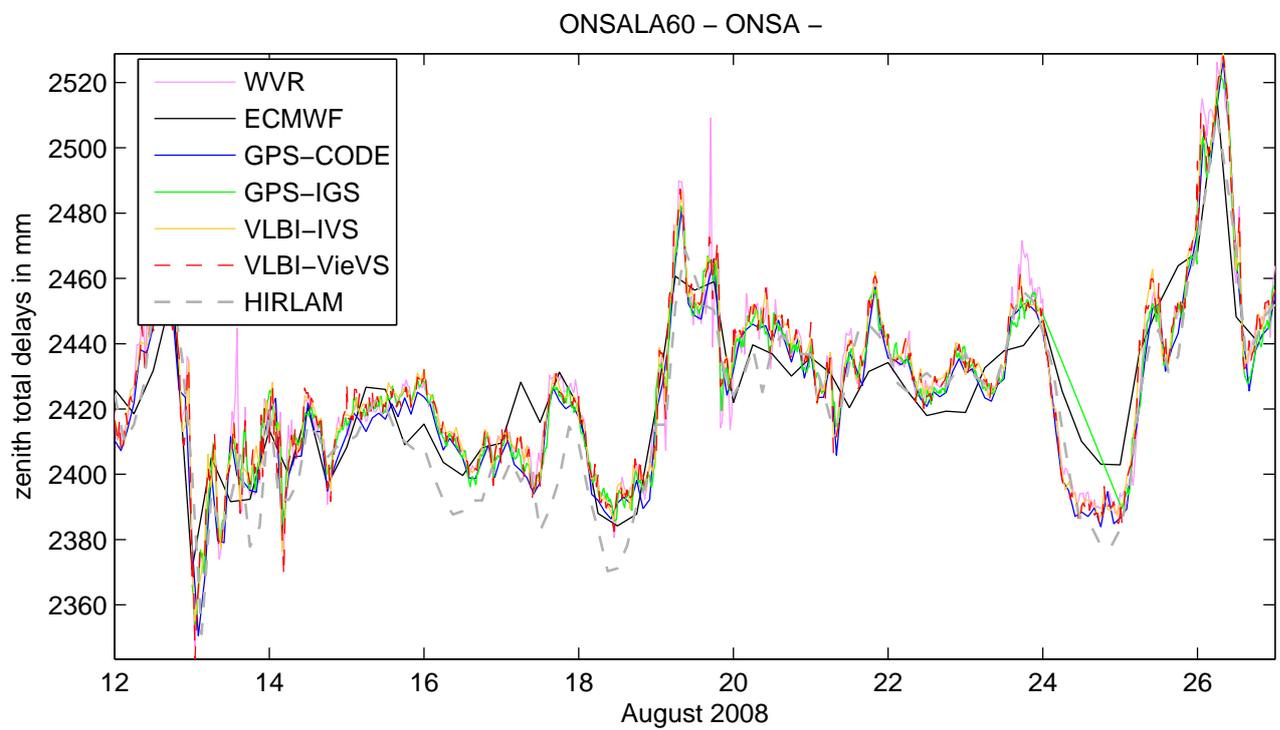
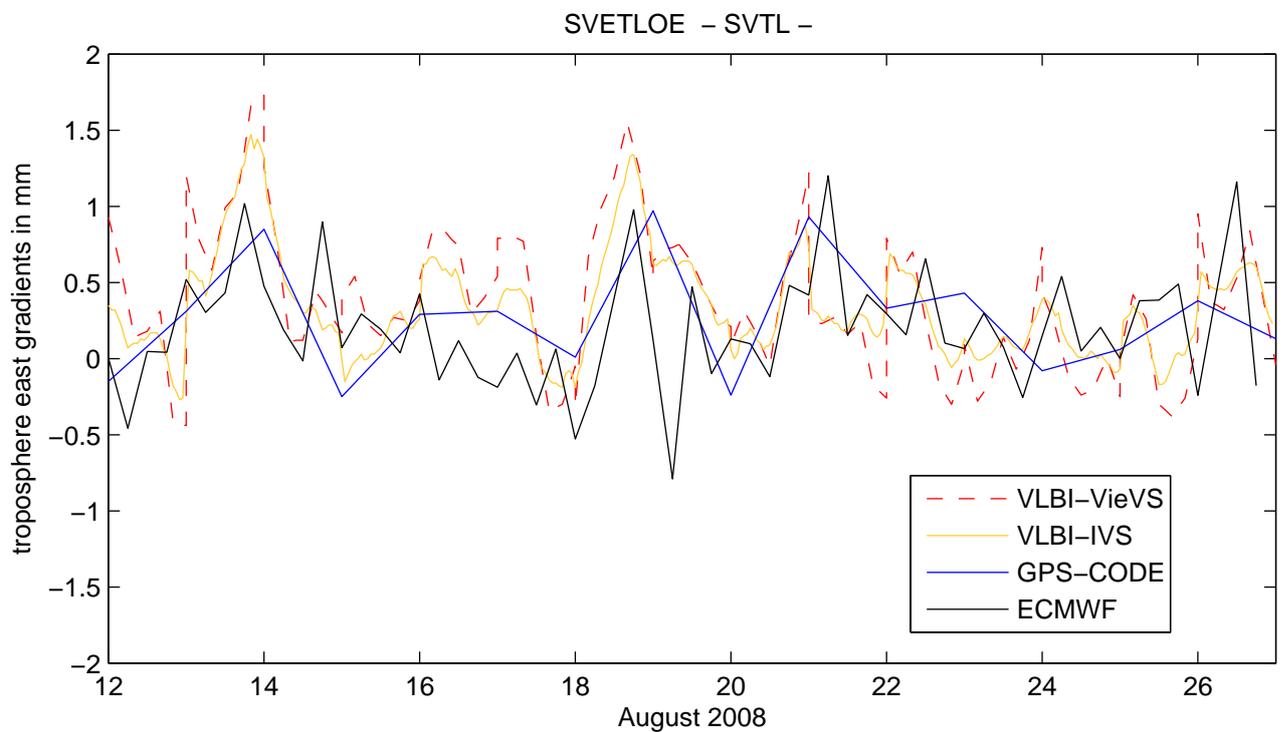Figure A.6.4.: ZTDs at co-located site Onsala in Sweden during IVS-CONT08.
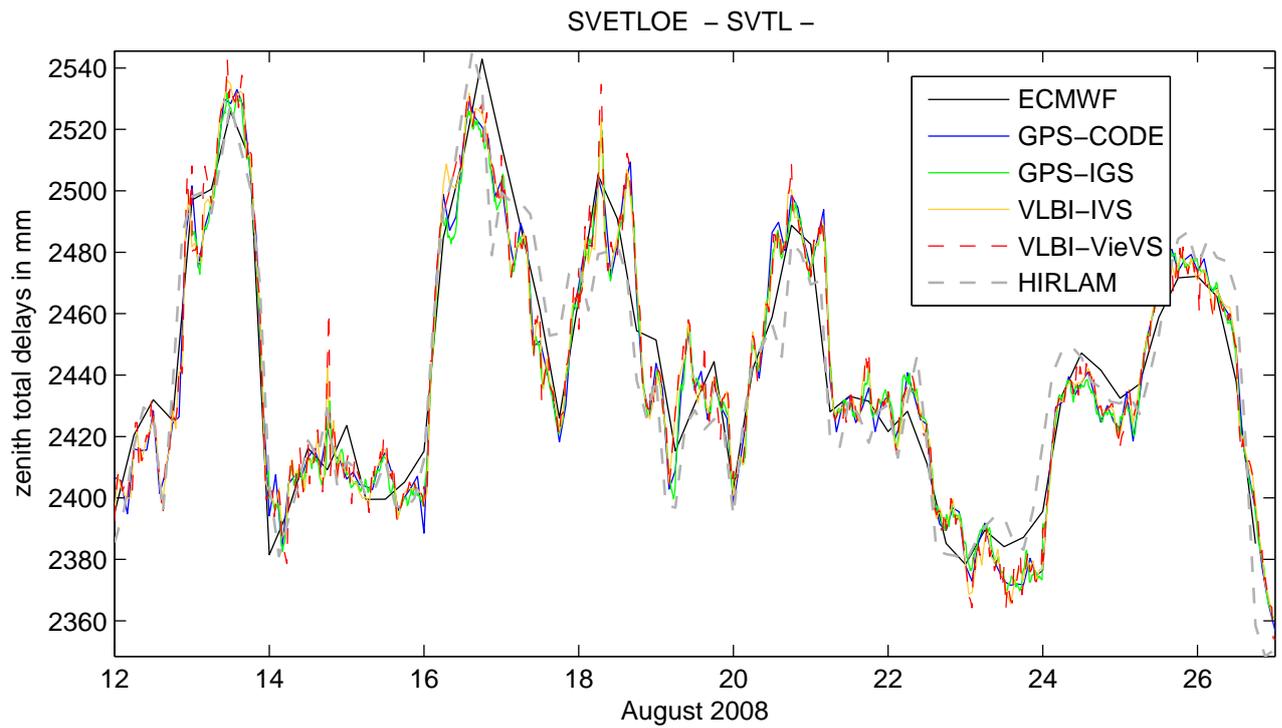
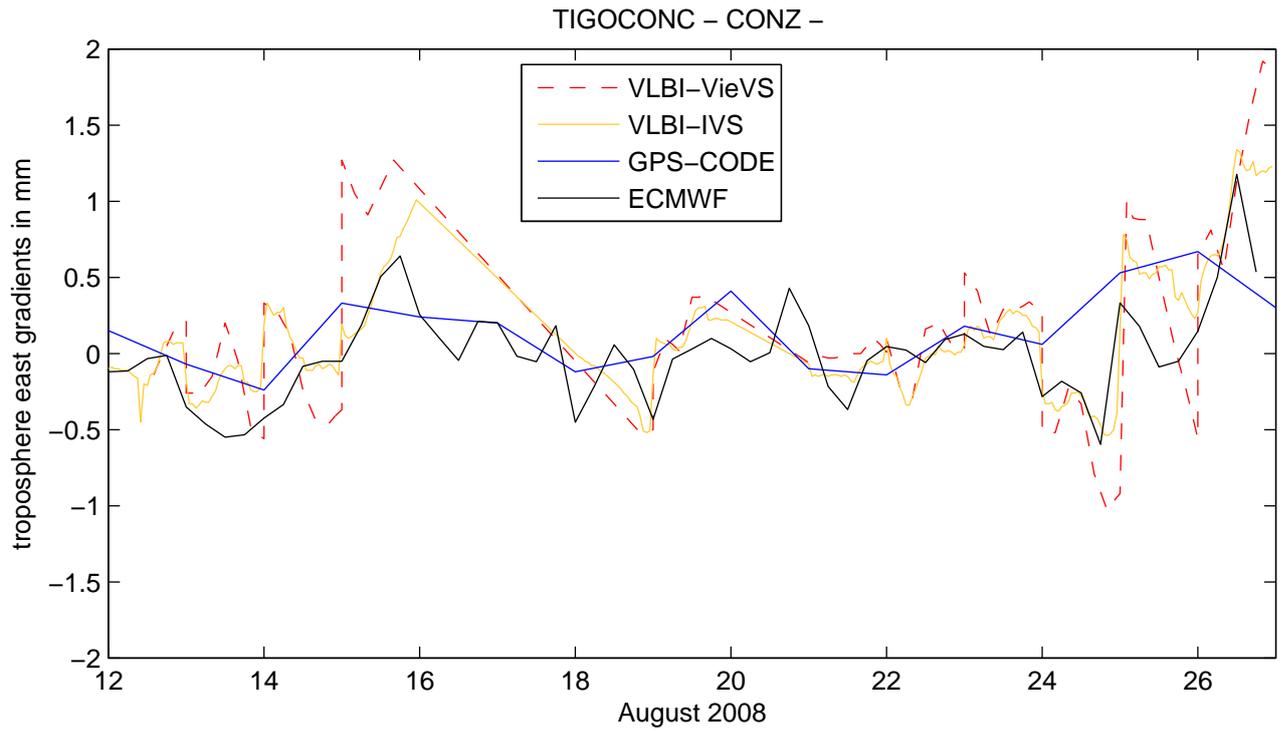Figure A.6.5.: ZTDs at co-located site Svetloe in Russia during IVS-CONT08.
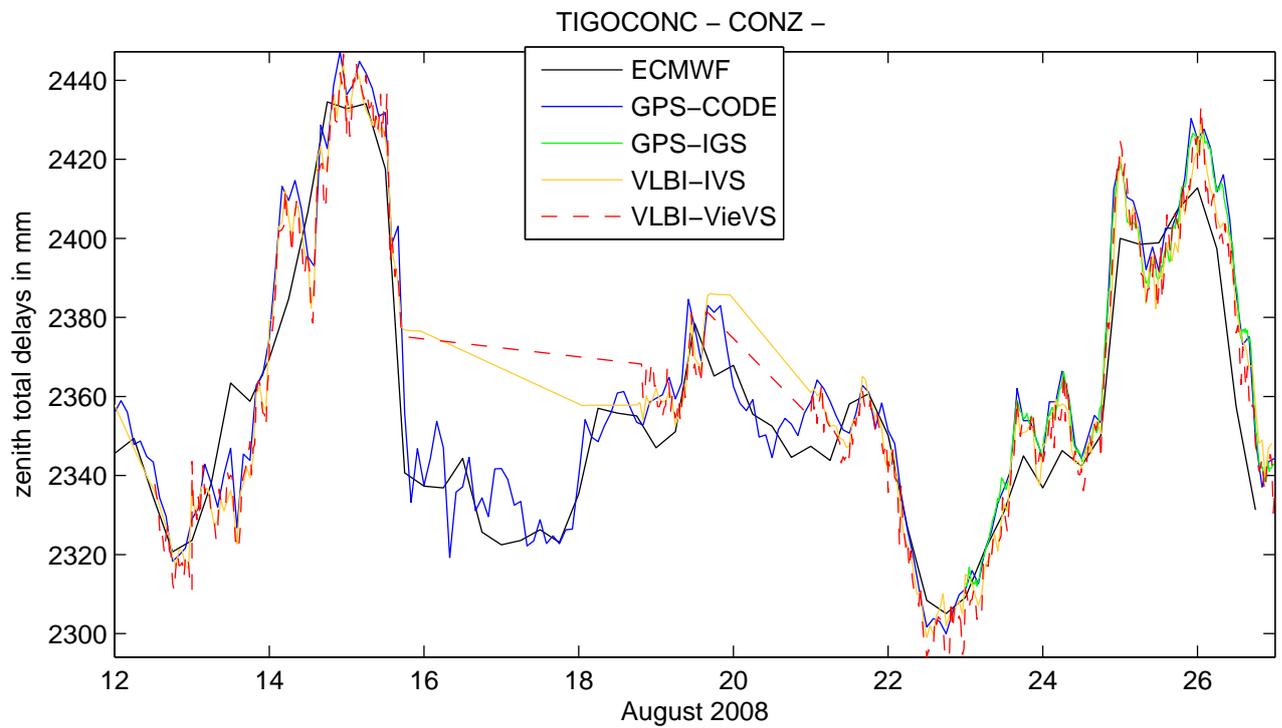
Figure A.6.6.: ZTDs at co-located site Tigo Concepcion in Chile during IVS-CONT08.
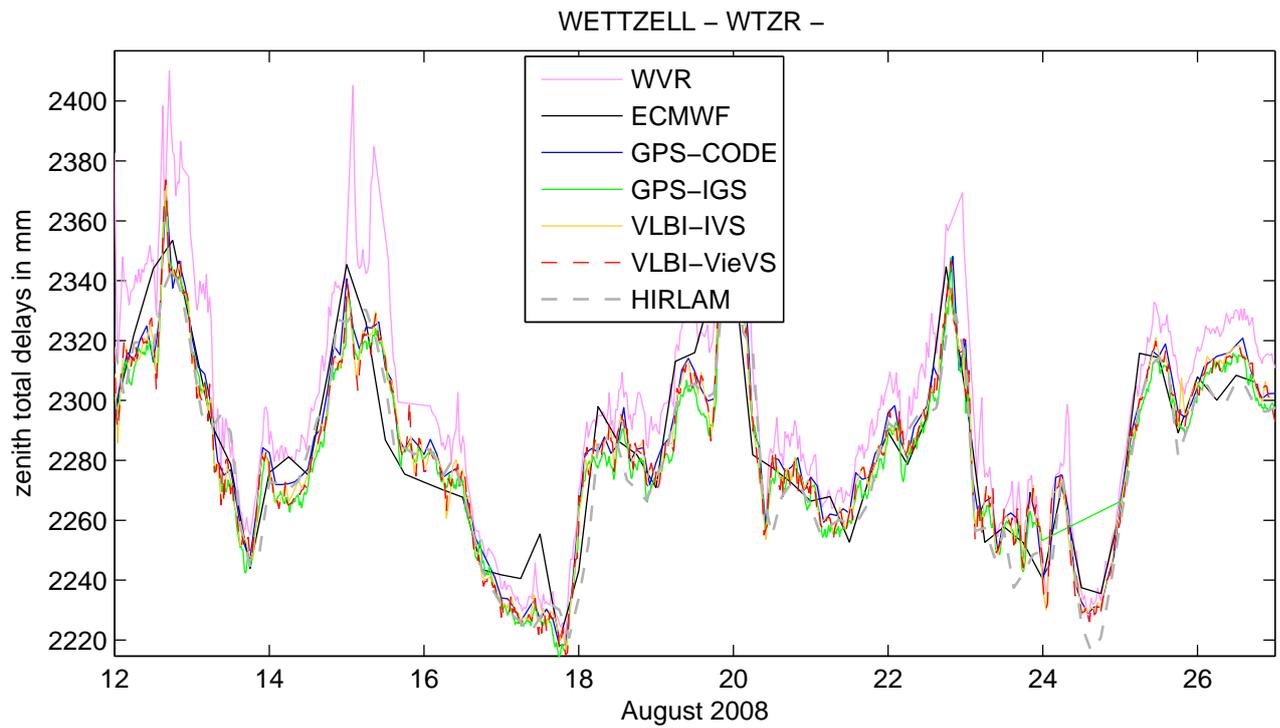
Figure A.6.7.: ZTDs at co-located site Wettzell in Germany during IVS-CONT08.
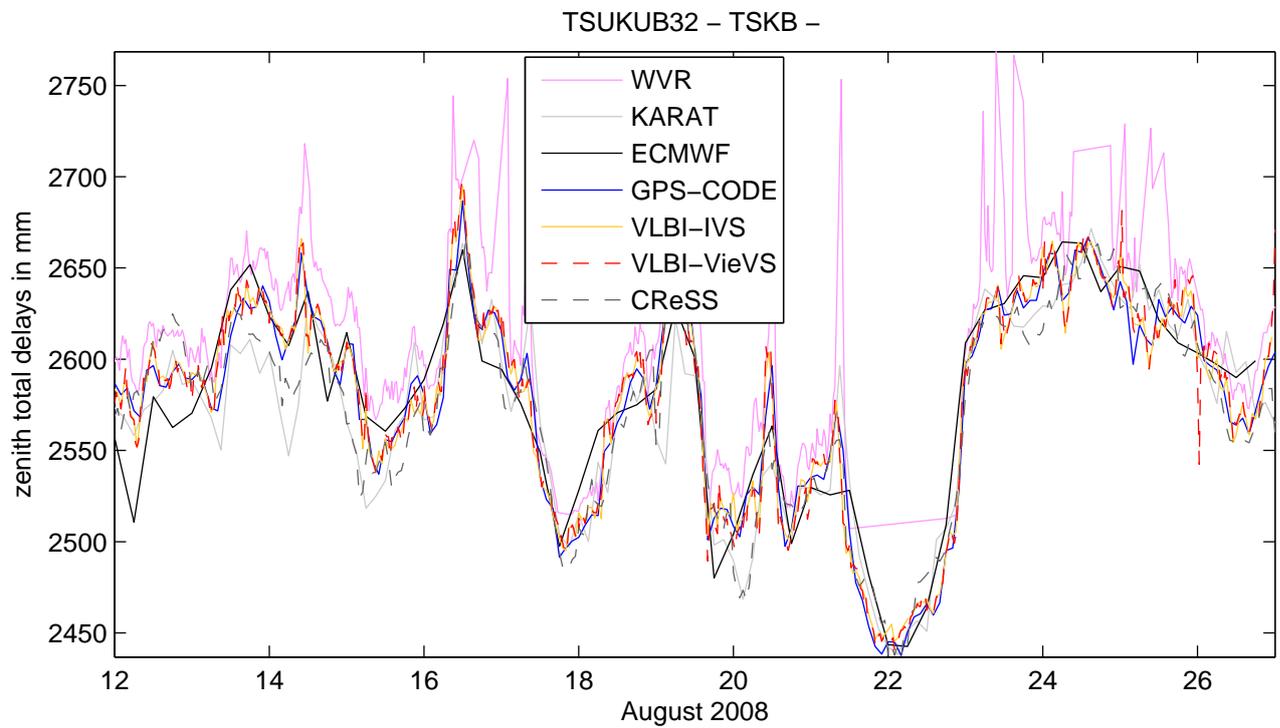
Figure A.6.8.: ZTDs at co-located site Tsukuba in Japan during IVS-CONT08.
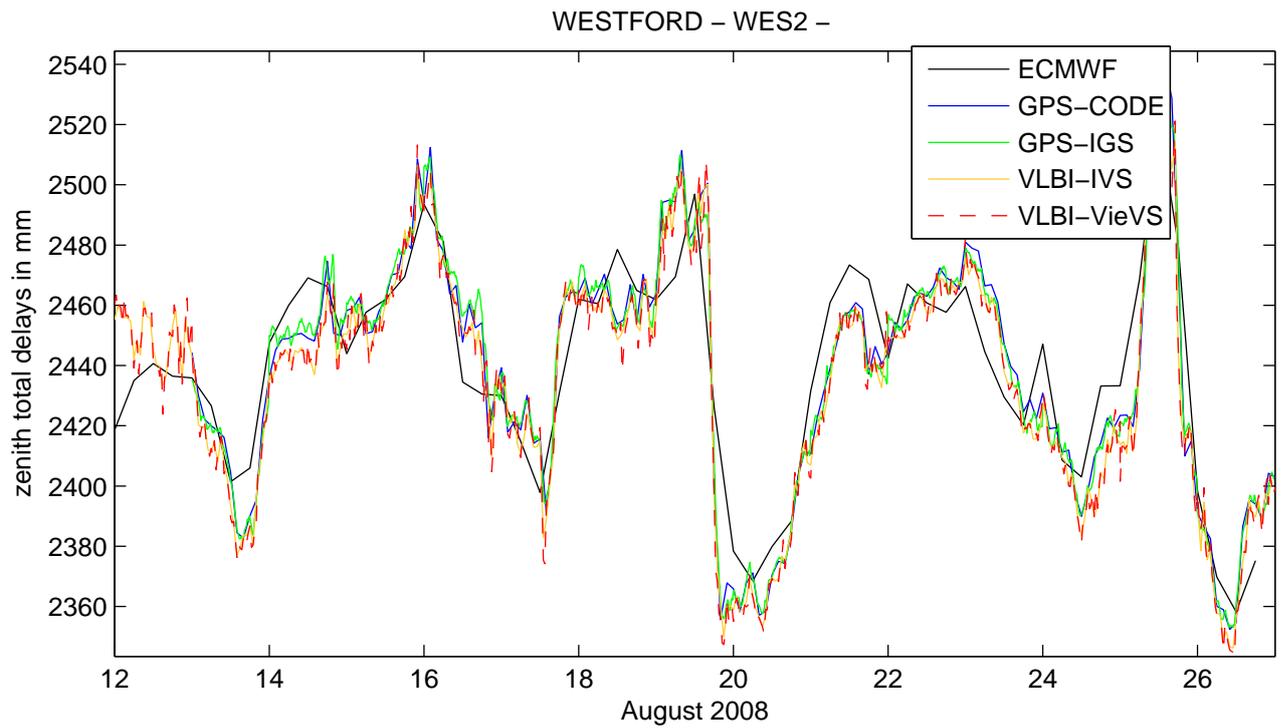
Figure A.6.9.: ZTDs at co-located site Westford in USA during IVS-CONT08.
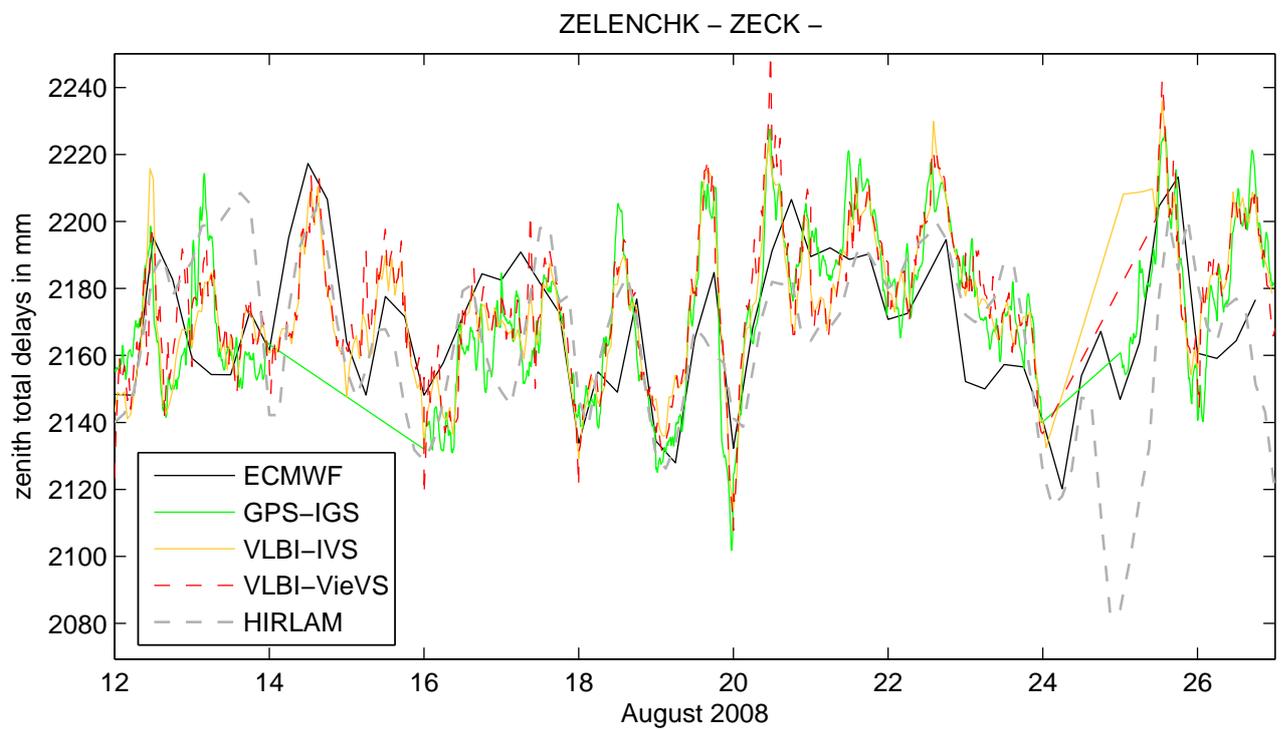
Figure A.6.10.: ZTDs at co-located site Zelenchukskaya in Russia during IVS-CONT08.

A.7. Troposphere gradients at co-located sites during IVS-CONT08

A.7.1. Troposphere north gradients
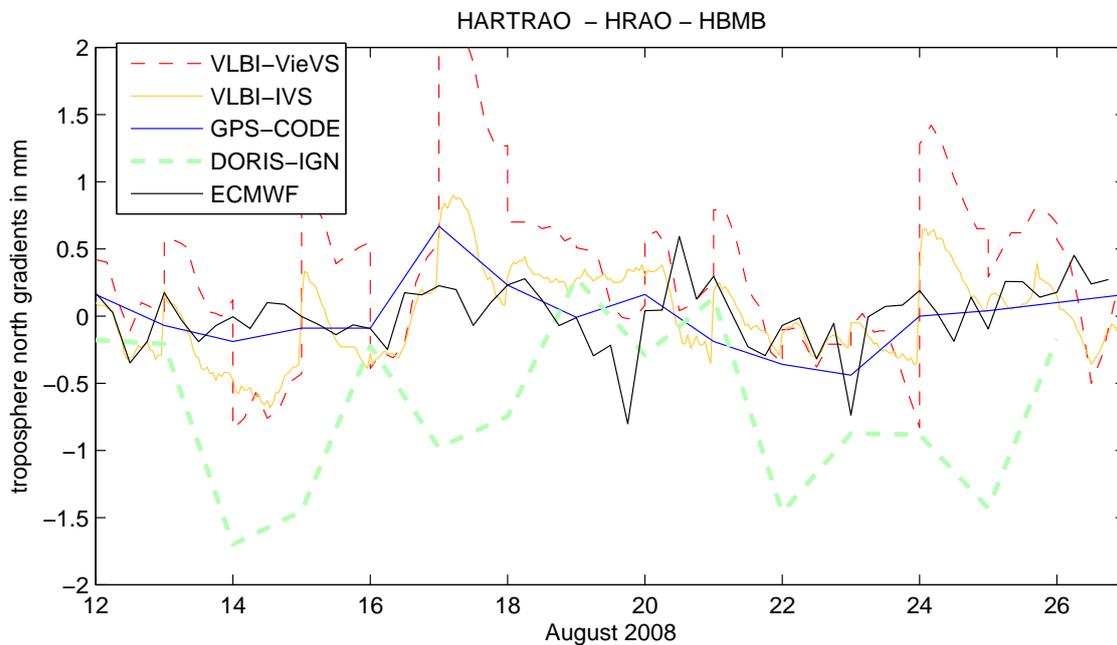
Figure A.7.1.: Troposphere north gradients at co-located site Hartebeesthoek in Republic of South Africa during IVS-CONT08.
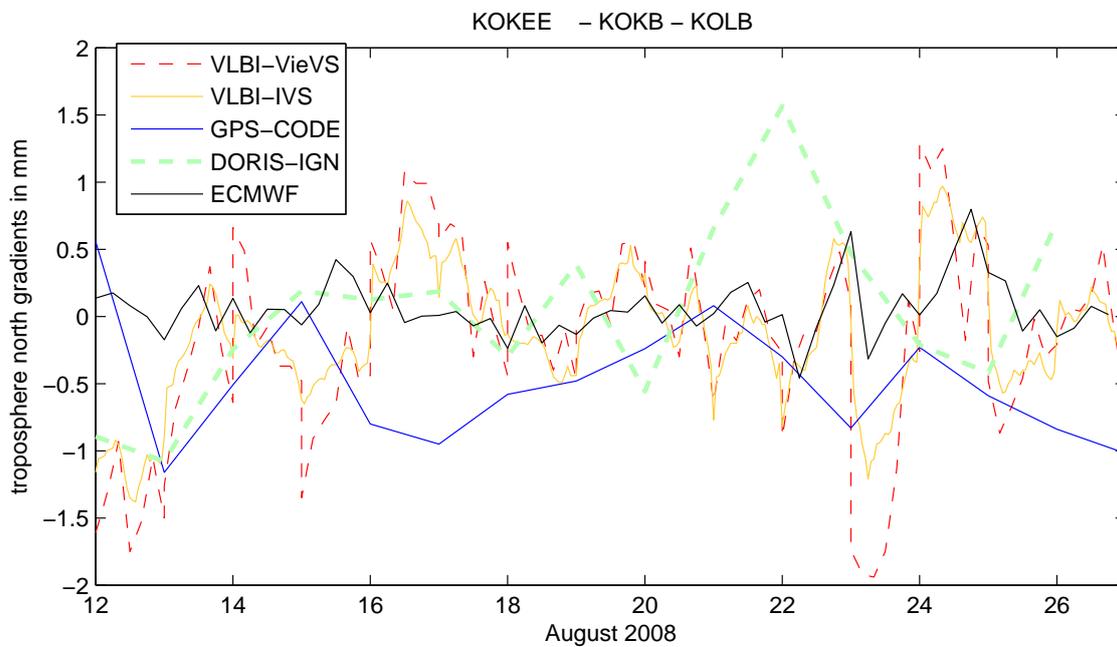
Figure A.7.2.: Troposphere north gradients at co-located site Kokee in USA during IVS-CONT08.
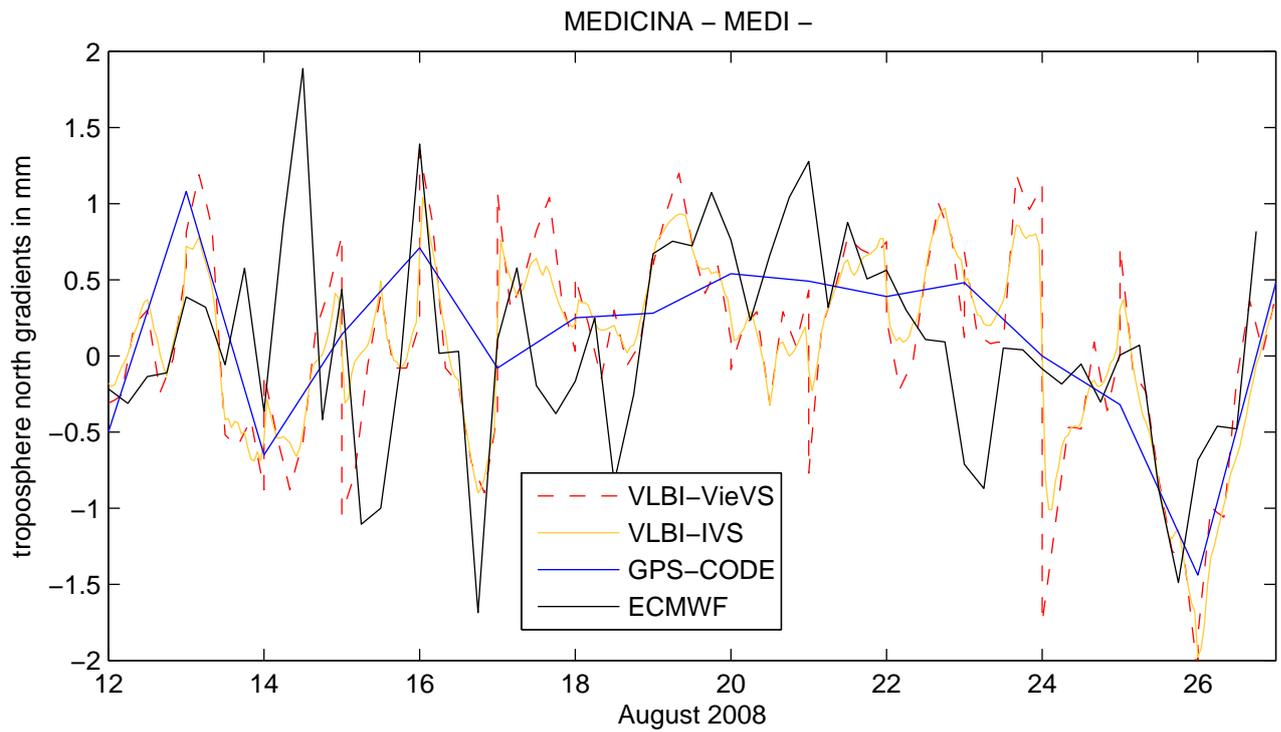
Figure A.7.3.: Troposphere north gradients at co-located site Medicina in Italy during IVS-CONT08.
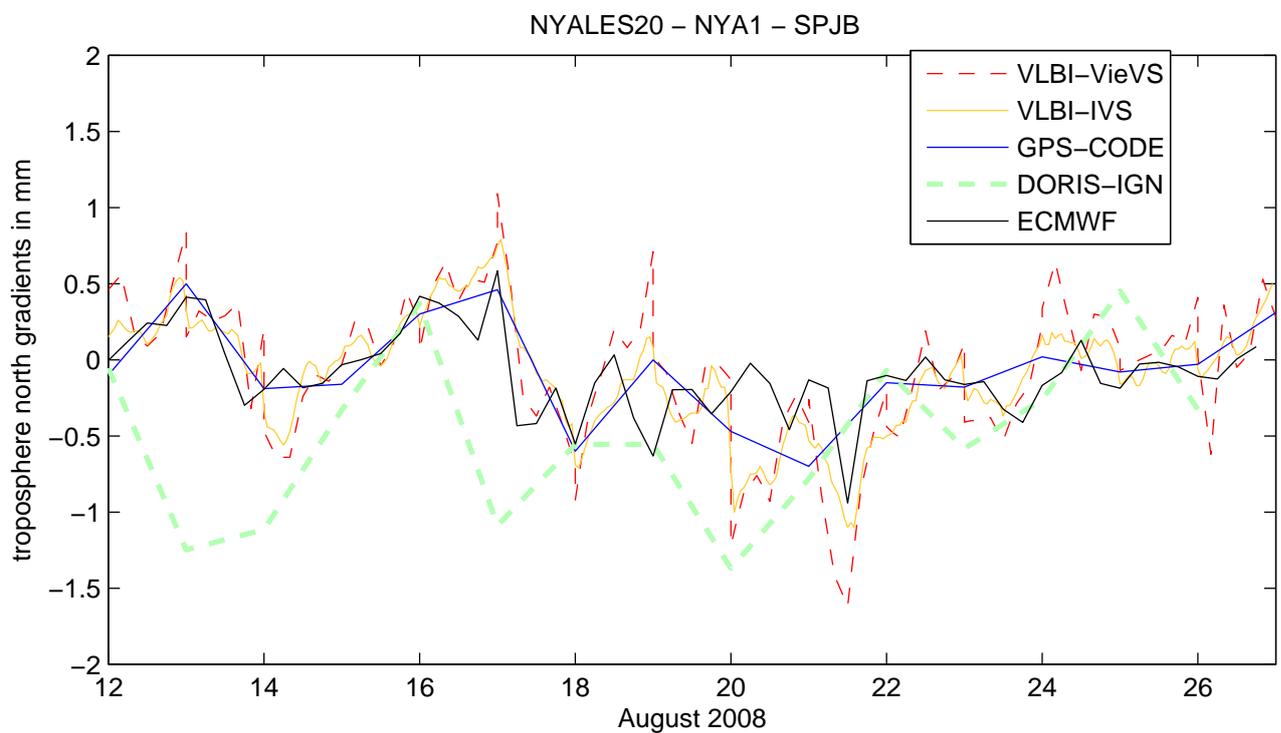
Figure A.7.4.: Troposphere north gradients at co-located site Ny-Ålesund in Norway during IVS-CONT08.
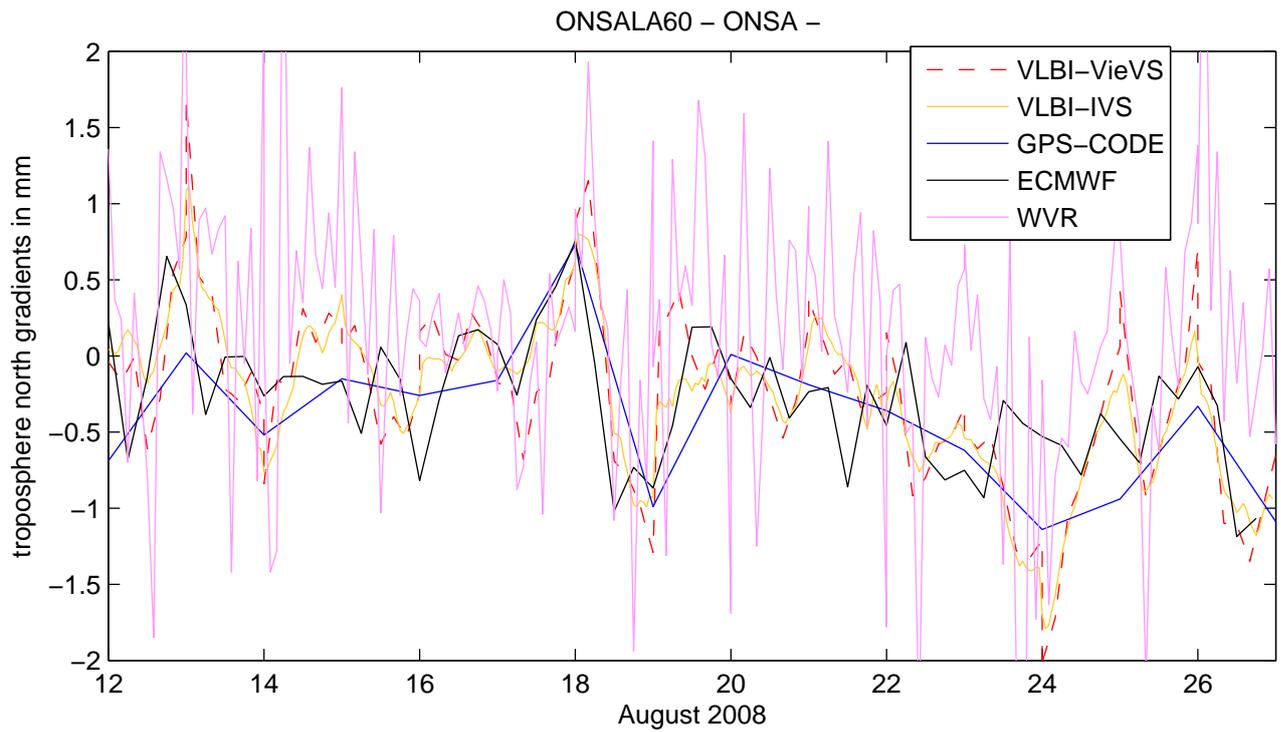
Figure A.7.5.: Troposphere north gradients at co-located site Onsala in Sweden during IVS-CONT08.
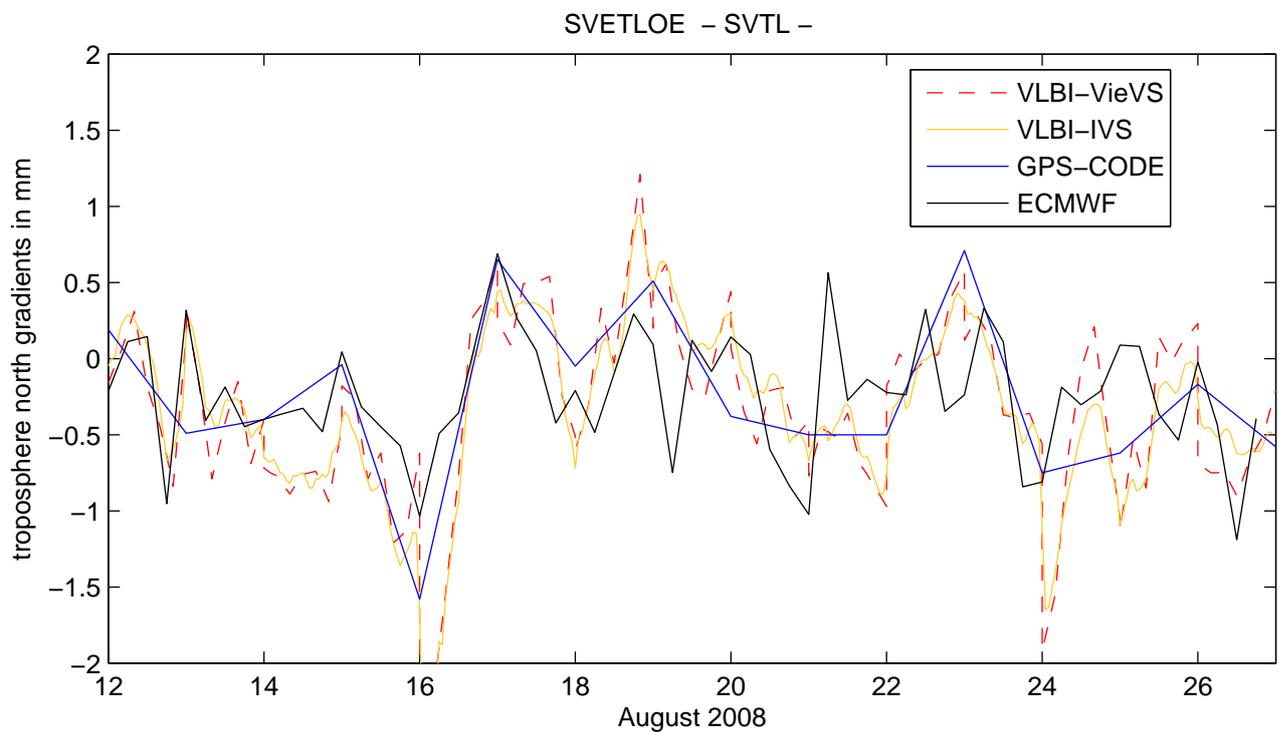
Figure A.7.6.: Troposphere north gradients at co-located site Svetloe in Russia during IVS-CONT08.
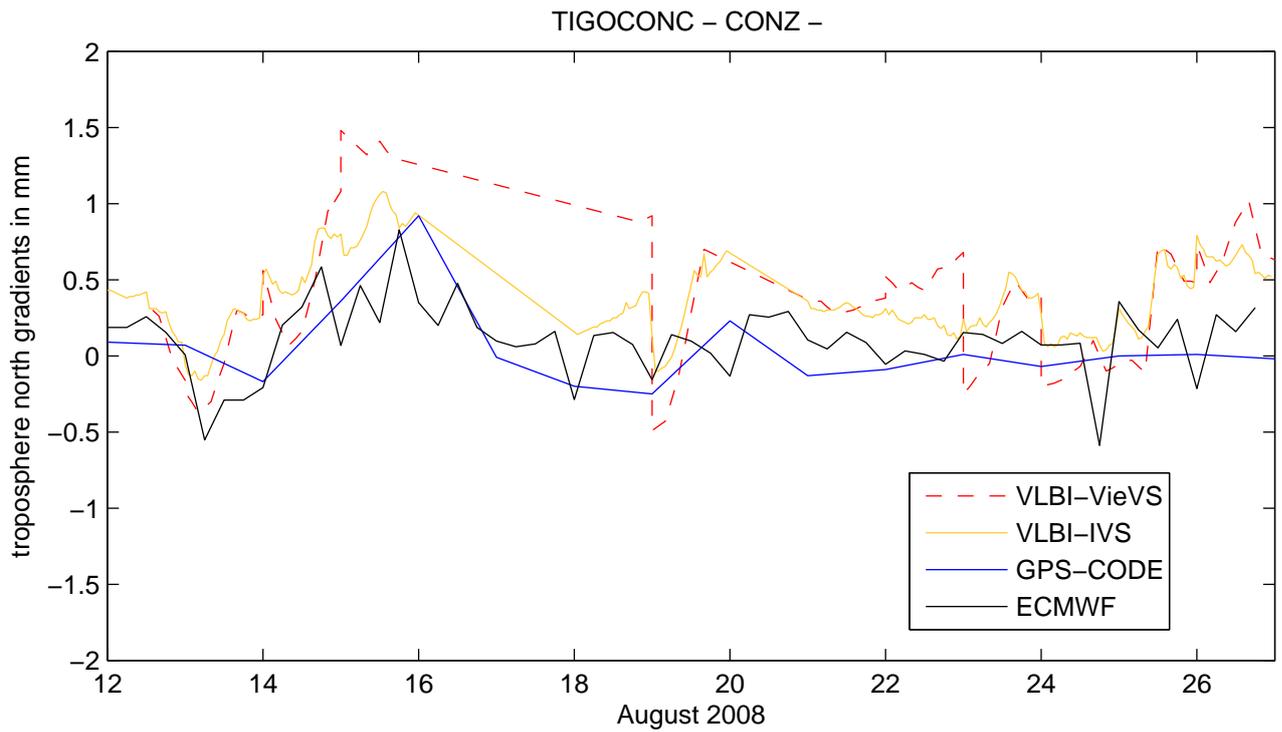
Figure A.7.7.: Troposphere north gradients at co-located site Tigo Concepcion in Chile during IVS-CONT08.
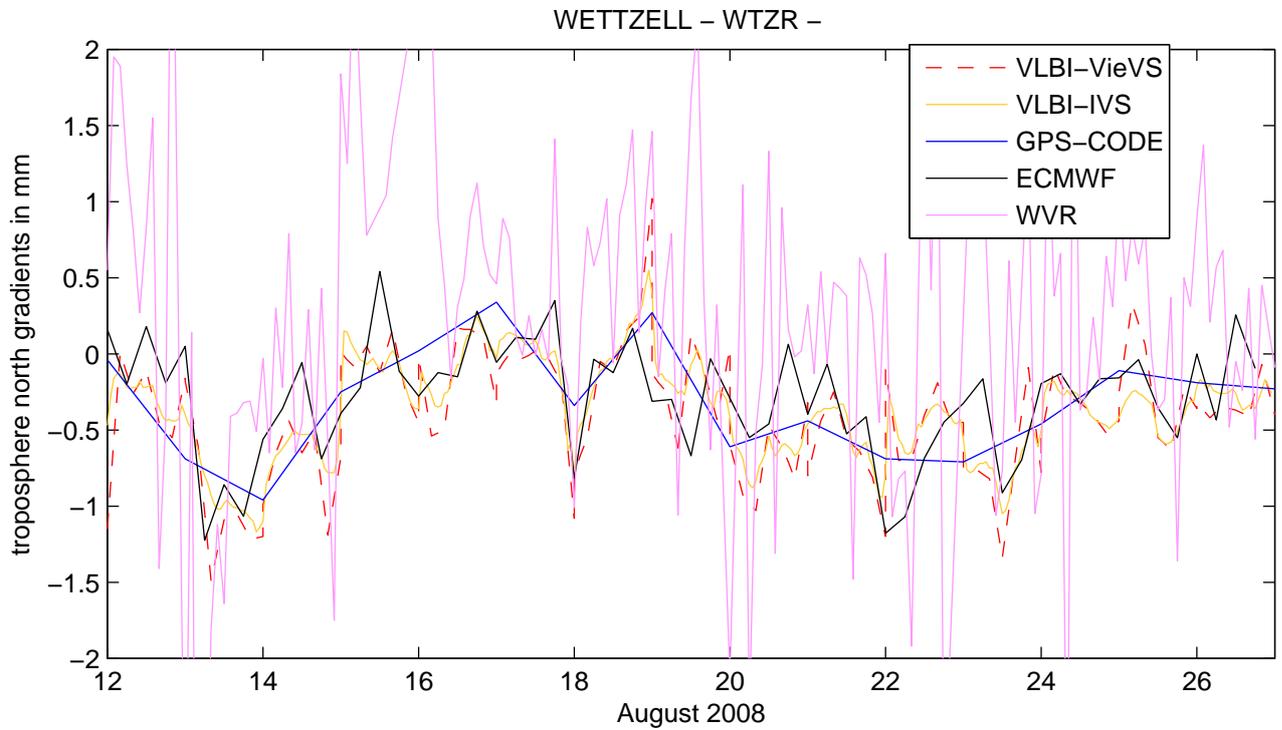
Figure A.7.8.: Troposphere north gradients at co-located site Wettzell in Germany during IVS-CONT08.
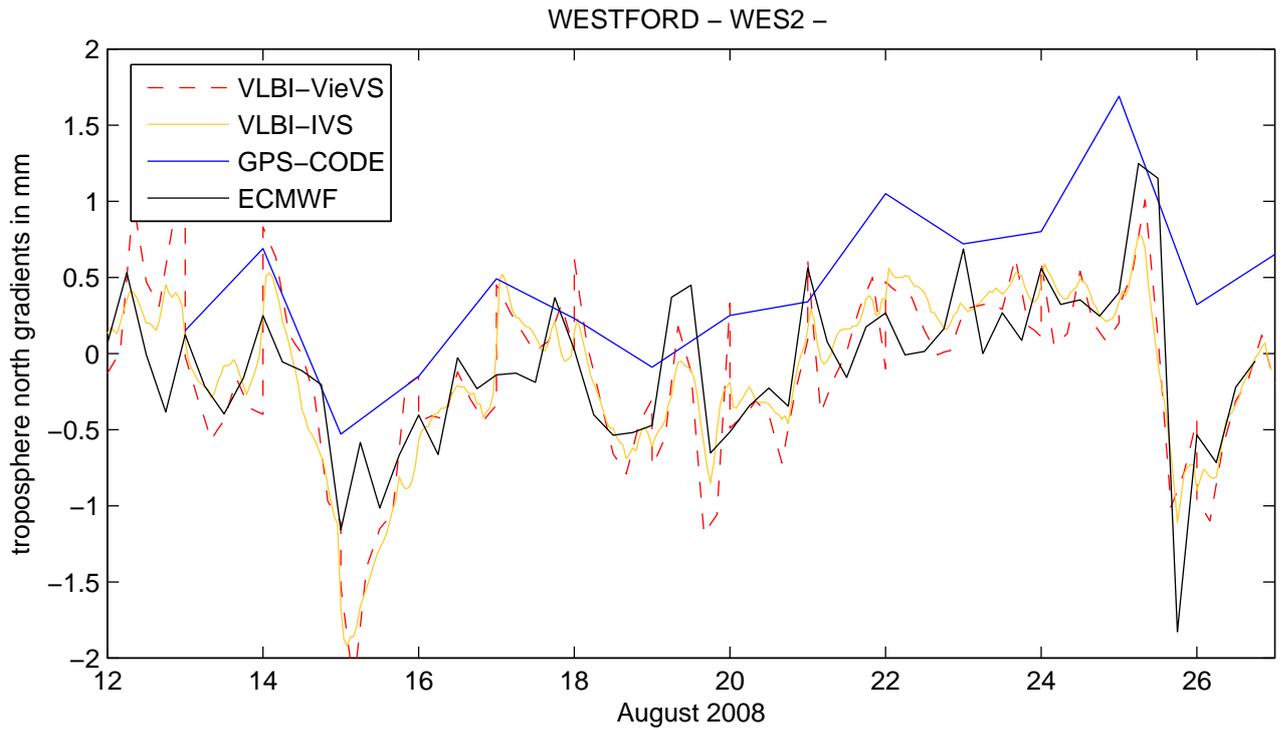
Figure A.7.9.: Troposphere north gradients at co-located site Westford in USA during IVS-CONT08 during IVS-CONT08.
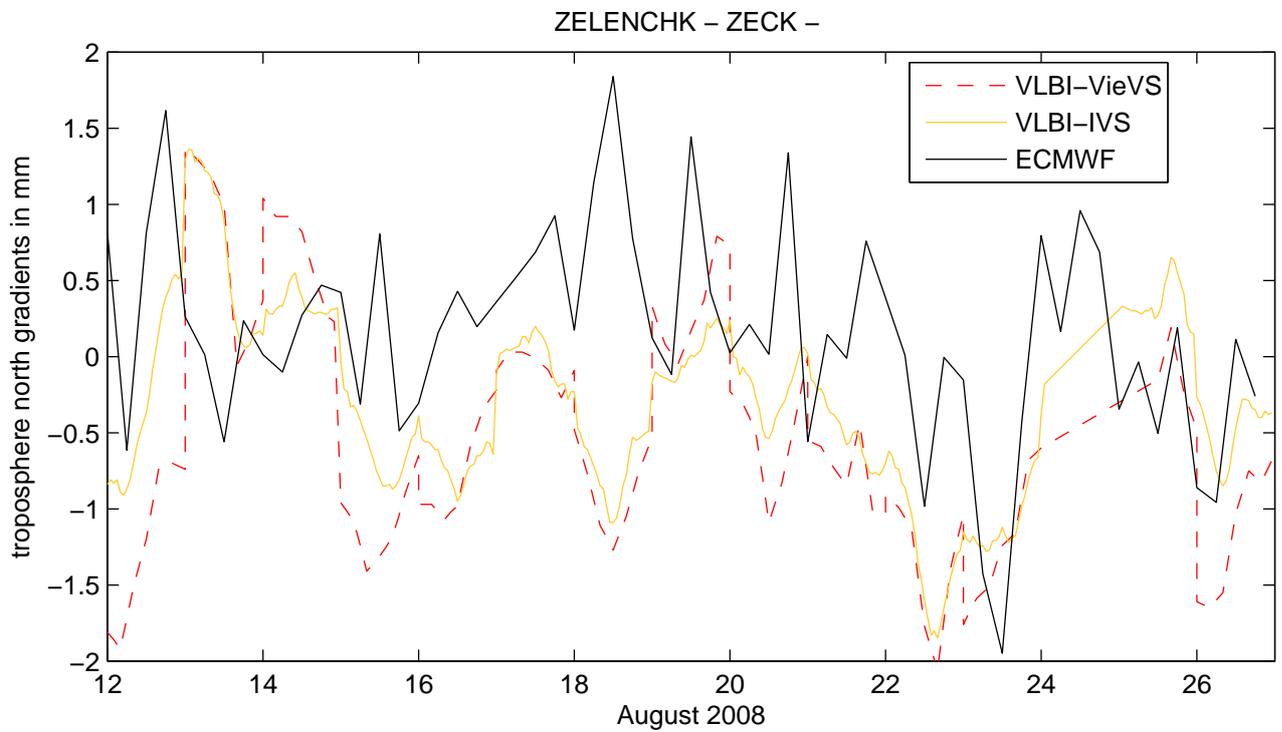
Figure A.7.10.: Troposphere north gradients at co-located site Zelenchukskaya in Russia during IVS-CONT08.

A.7.2. Troposphere east gradients
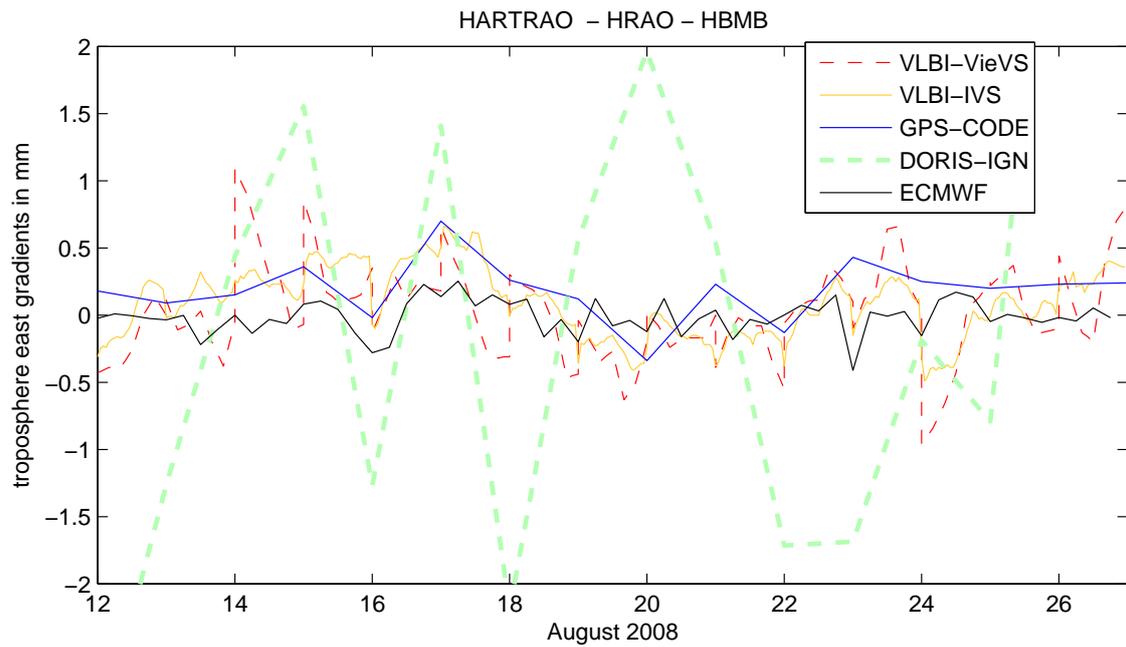
Figure A.7.11.: Troposphere east gradients at co-located site Hartebeesthoek in Republic of South Africa during IVS-CONT08.
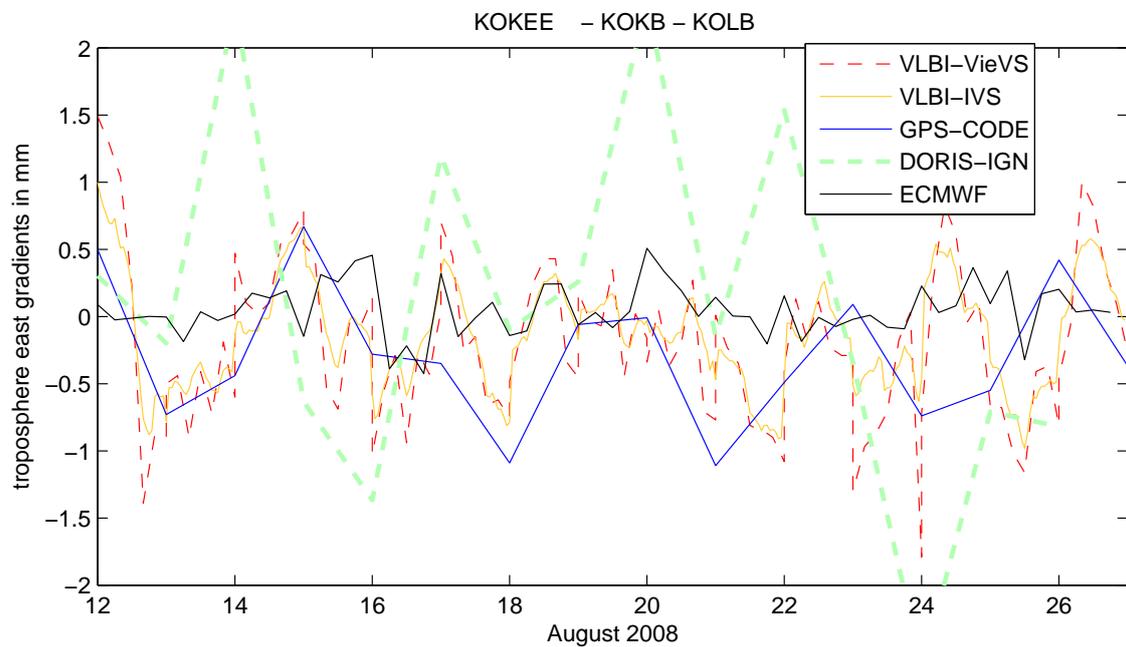
Figure A.7.12.: Troposphere east gradients at co-located site Kokee in USA during IVS-CONT08.
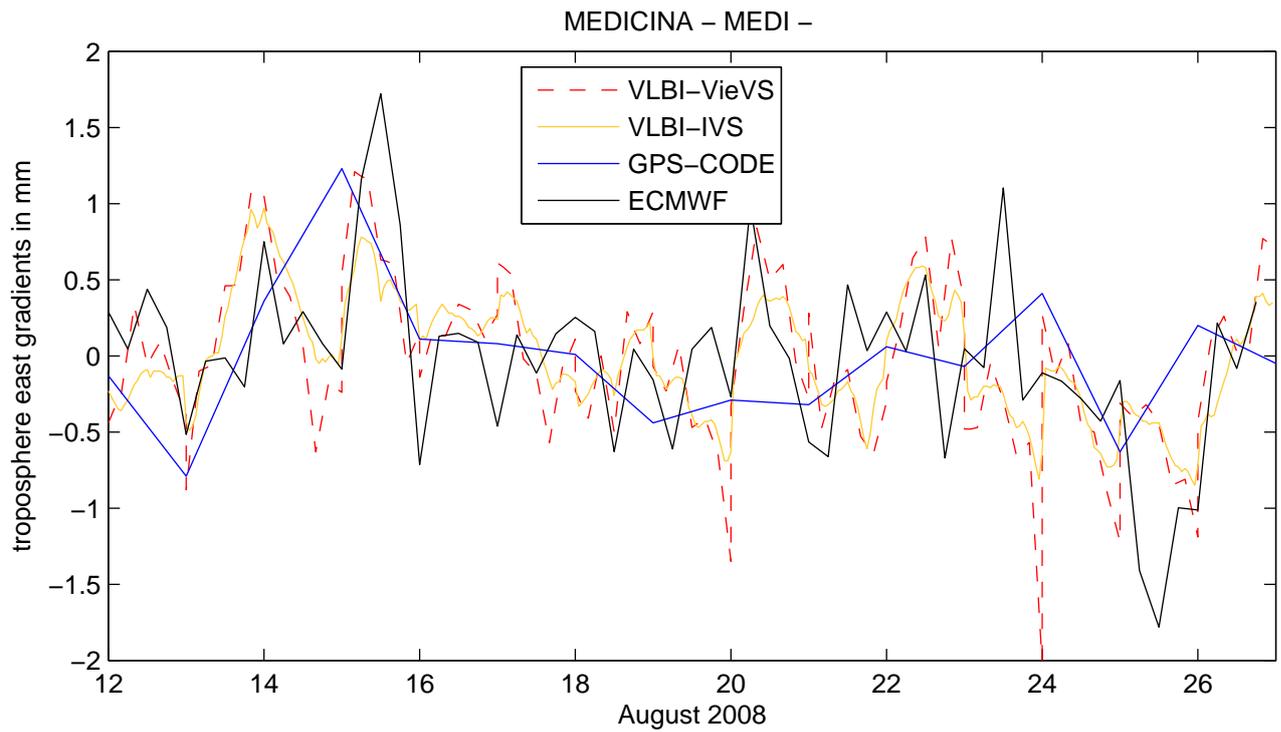
Figure A.7.13.: Troposphere east gradients at co-located site Medicina in Italy during IVS-CONT08.

Figure A.7.14.: Troposphere east gradients at co-located site Ny-Ålesund in Norway during IVS-CONT08.

Figure A.7.15.: Troposphere east gradients at co-located site Onsala in Sweden during IVS-CONT08.

Figure A.7.16.: Troposphere east gradients at co-located site Svetloe in Russia during IVS-CONT08.

Figure A.7.17.: Troposphere east gradients at co-located site Tigo Concepcion in Chile during IVS-CONT08.
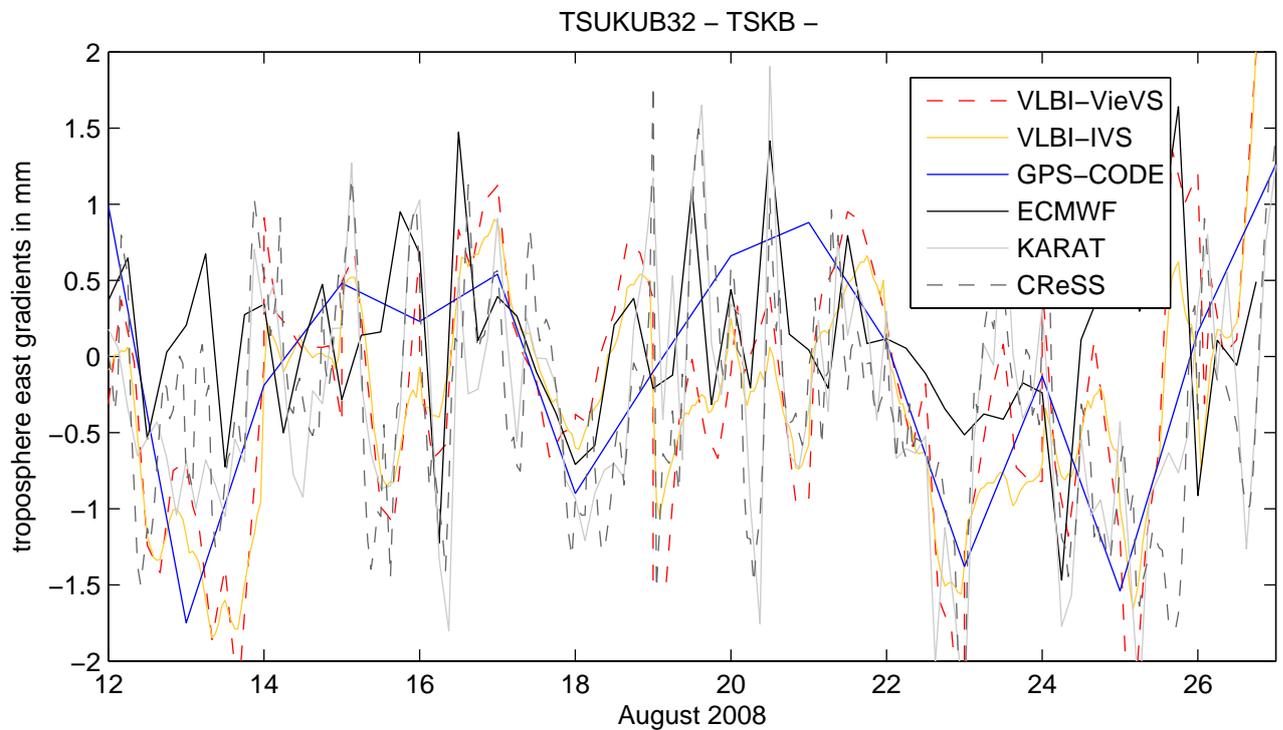
Figure A.7.18.: Troposphere east gradients at co-located site Tsukuba in Japan during IVS-CONT08 during IVS-CONT08.
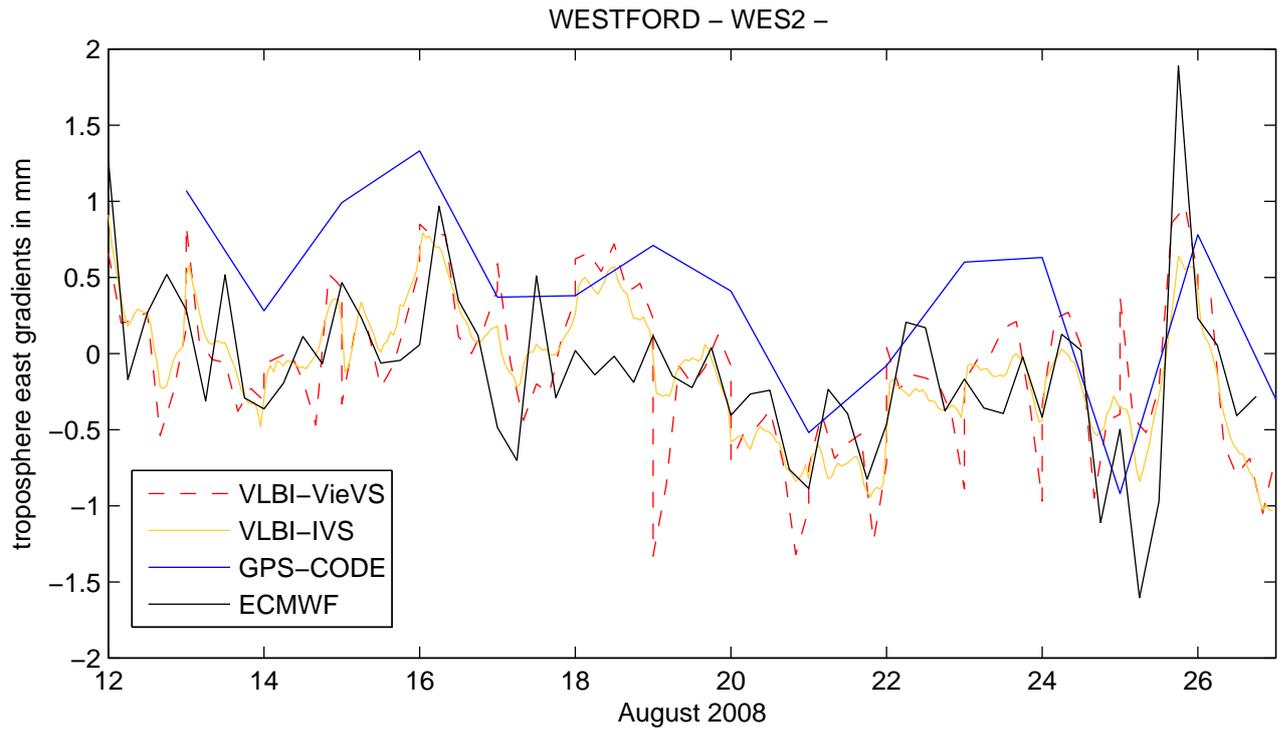
Figure A.7.19.: Troposphere east gradients at co-located site Westford in USA during IVS-CONT08 during IVS-CONT08.
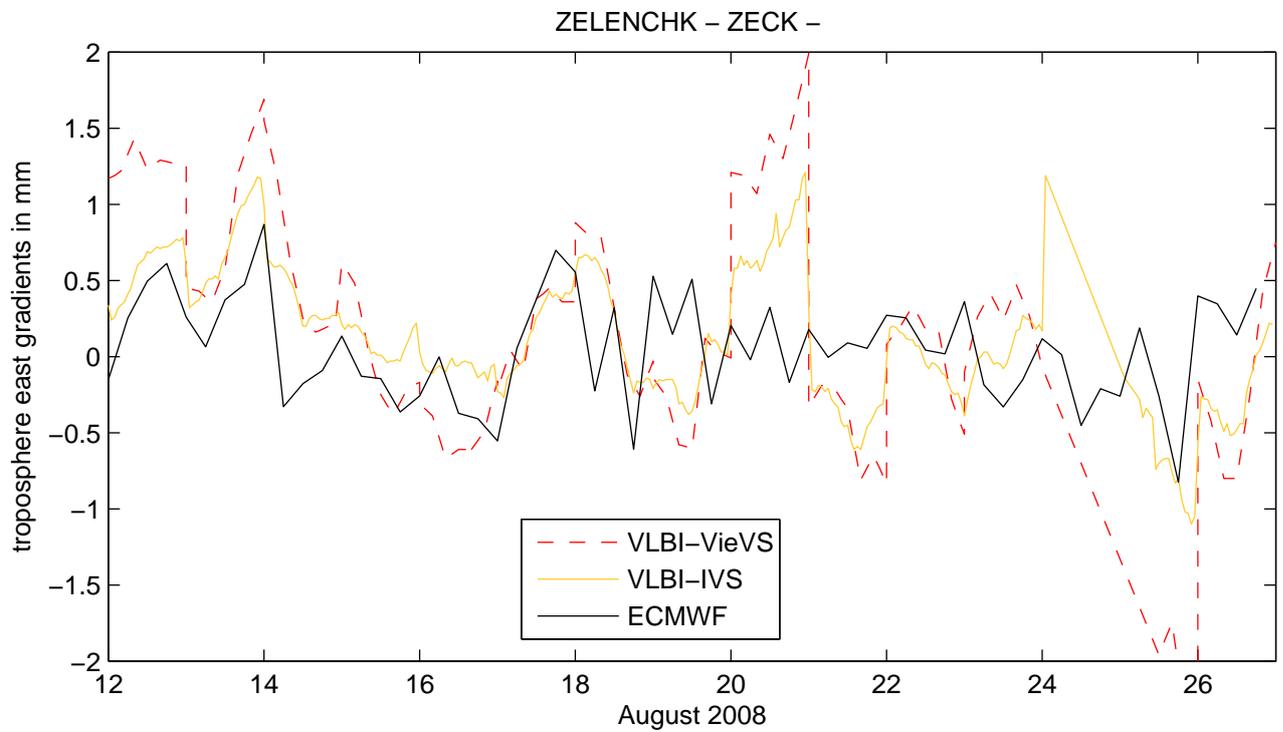
Figure A.7.20.: Troposphere east gradients at co-located site Zelenchukskaya in Russia during IVS-CONT08.

A.8. VieVS hourly CPWLO TRF coordinate estimates of all VLBI antennas contributing IVS-CONT05

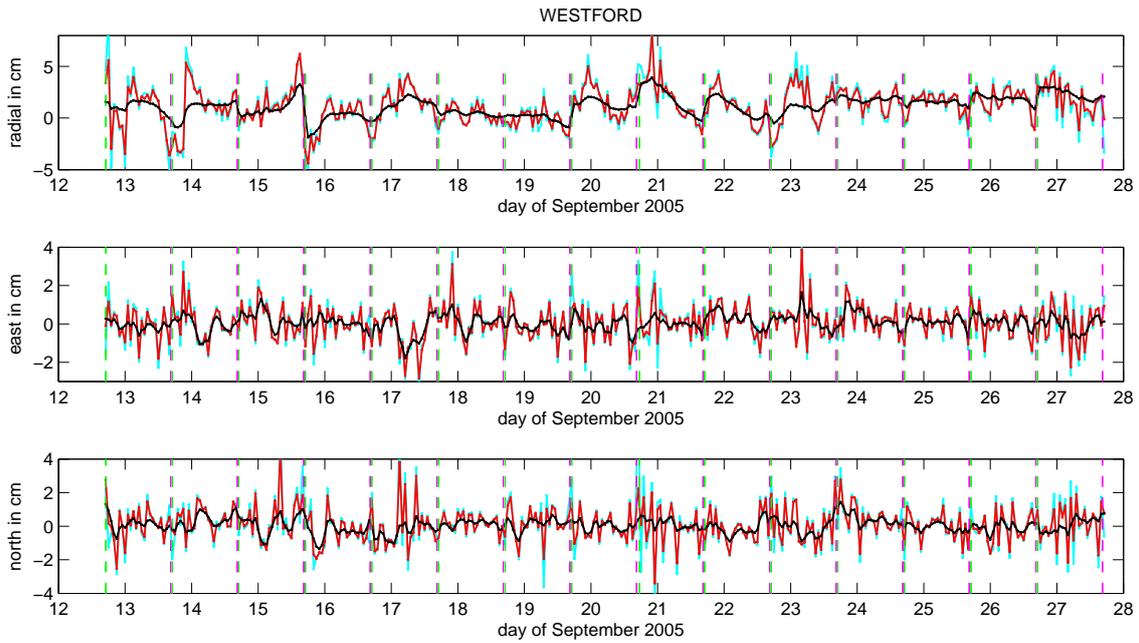In all the plots of this section: Black, red and cyan lines show VieVS, hourly (at UTC integer hours) CPWLO coordinate estimates of the VLBI antennas during IVS-CONT05. The coordinate estimates illustrated with black dotted lines when constraints of 4 mm/hour are used and red dotted lines are the series when loose constraints of 3 cm/hour are used and cyan dotted lines are the series when very loose constraints of 21 cm/hour are used. Zero ticks on the Y axes of the plots show the VTRF2008 coordinates of the antennas including all the model corrections introduced a priori to the parameter estimation. Vertical green dashed lines show the beginning of the sessions and vertical magenta dashed lines show the end of the sessions. The analysis options are shown in Table 8.1.
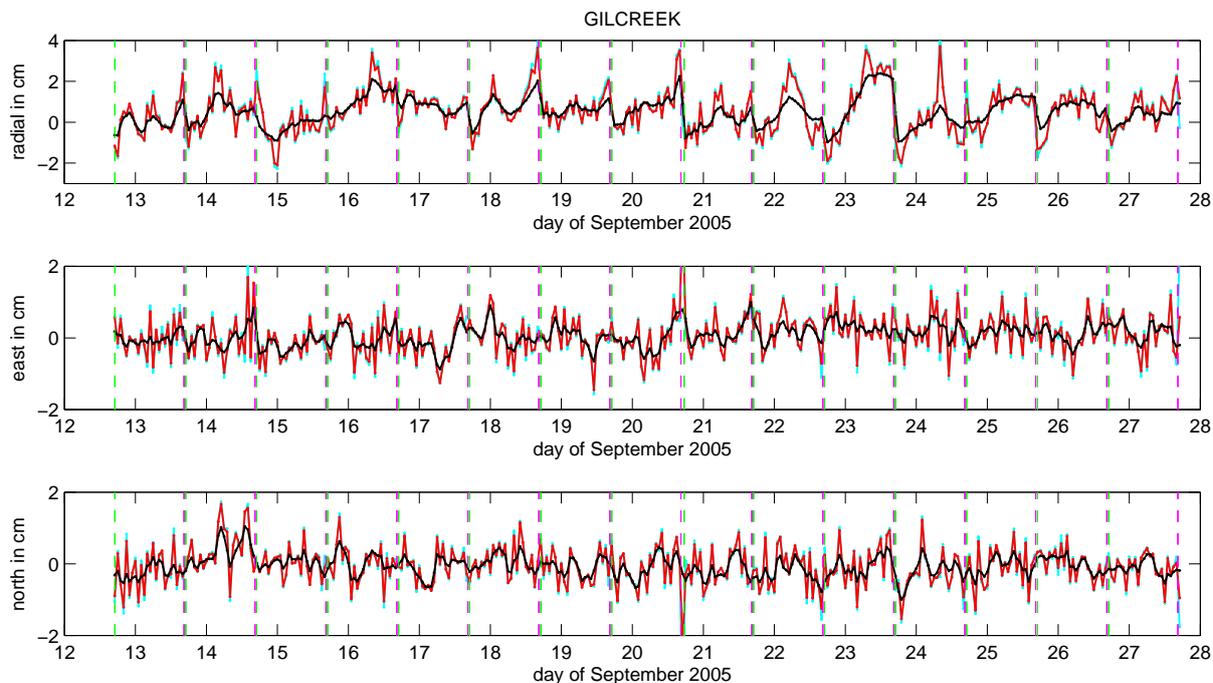
Figure A.8.1.: Black, red and cyan lines show VieVS, hourly (at UTC integer hours) CPWLO coordinate estimates of the VLBI antenna Gilcreek during IVS-CONT05 when loose constraints were applied on the hourly coordinate estimates as 4 mm/hour, 3 cm/hour, and 21 cm/hour, respectively.
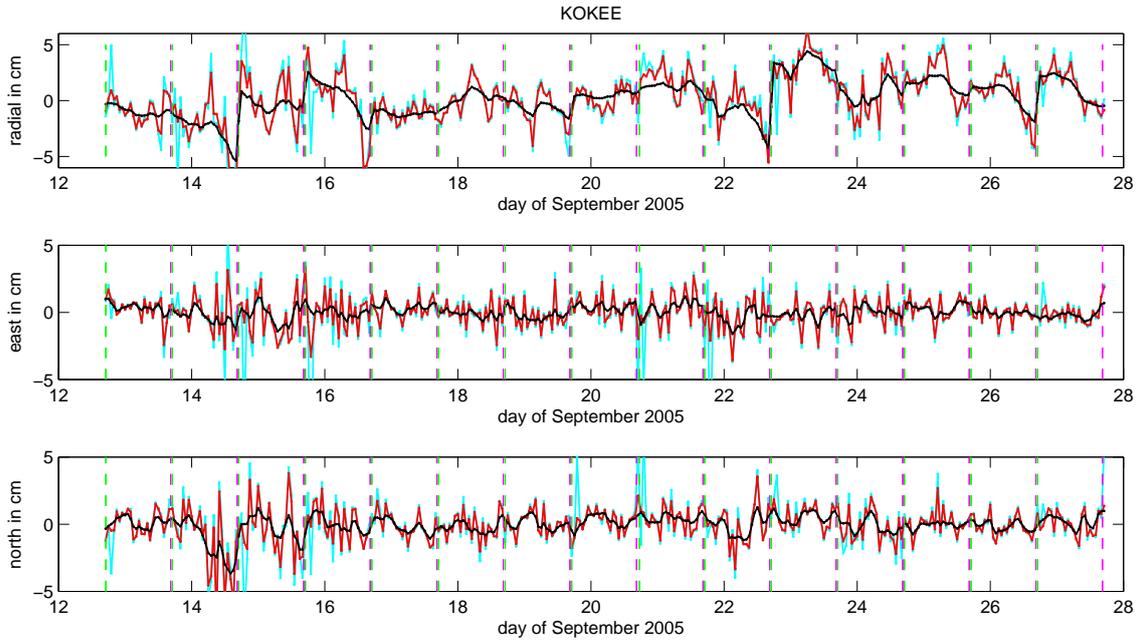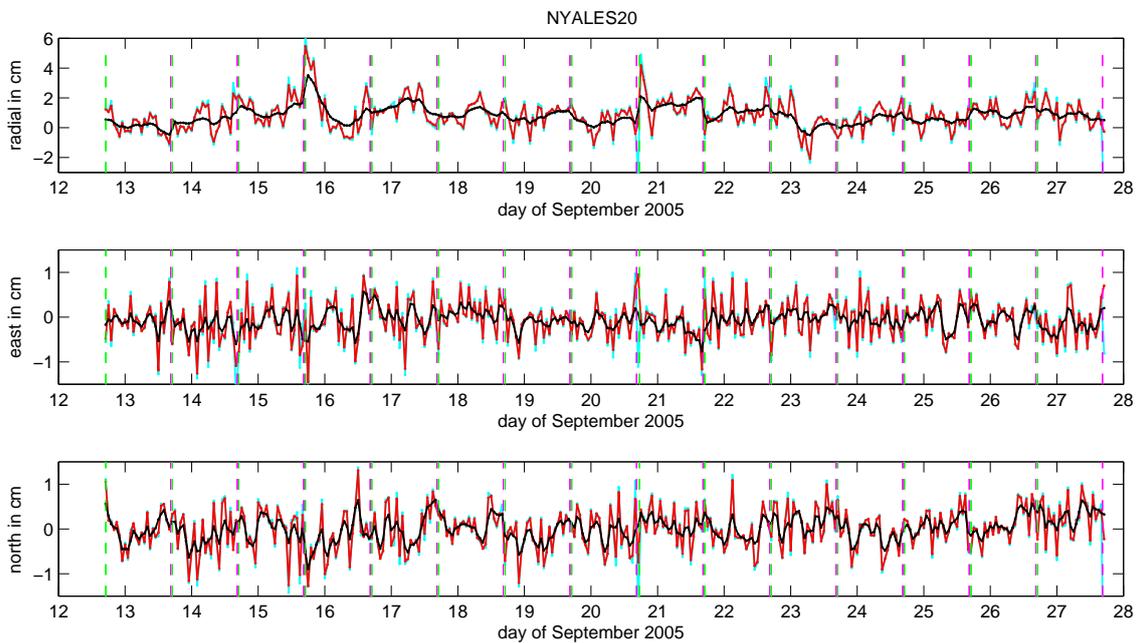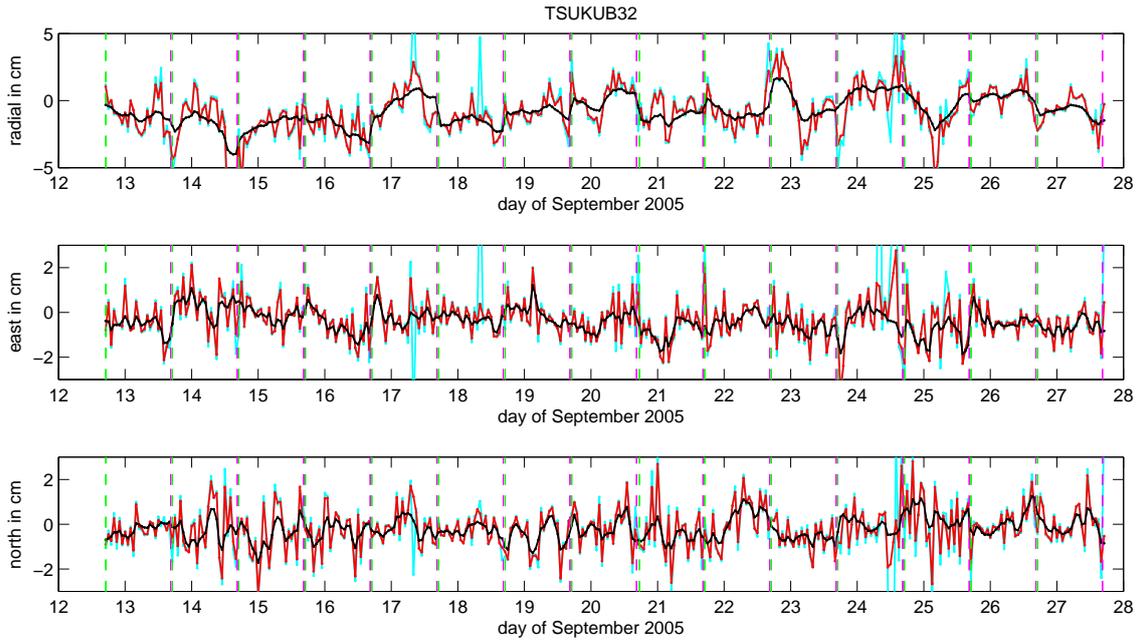
Figure A.8.2.: Black, red and cyan lines show VieVS, hourly (at UTC integer hours) CPWLO coordinate estimates of the VLBI antenna Kokee during IVS-CONT05 when loose constraints were applied on the hourly coordinate estimates as 4 mm/hour, 3 cm/hour, and 21 cm/hour, respectively.
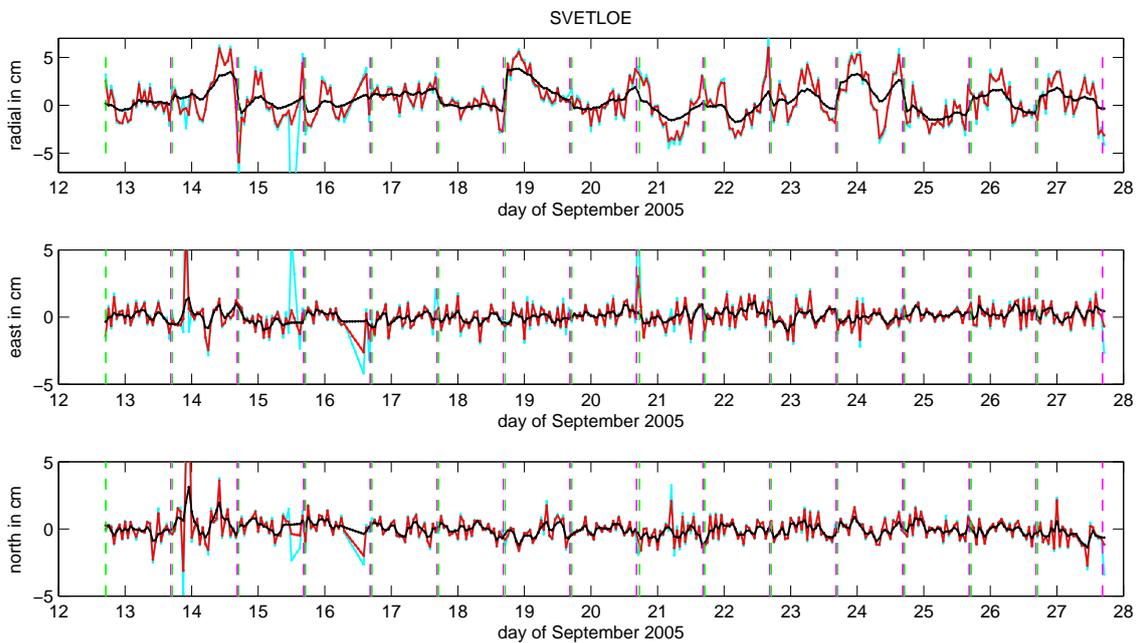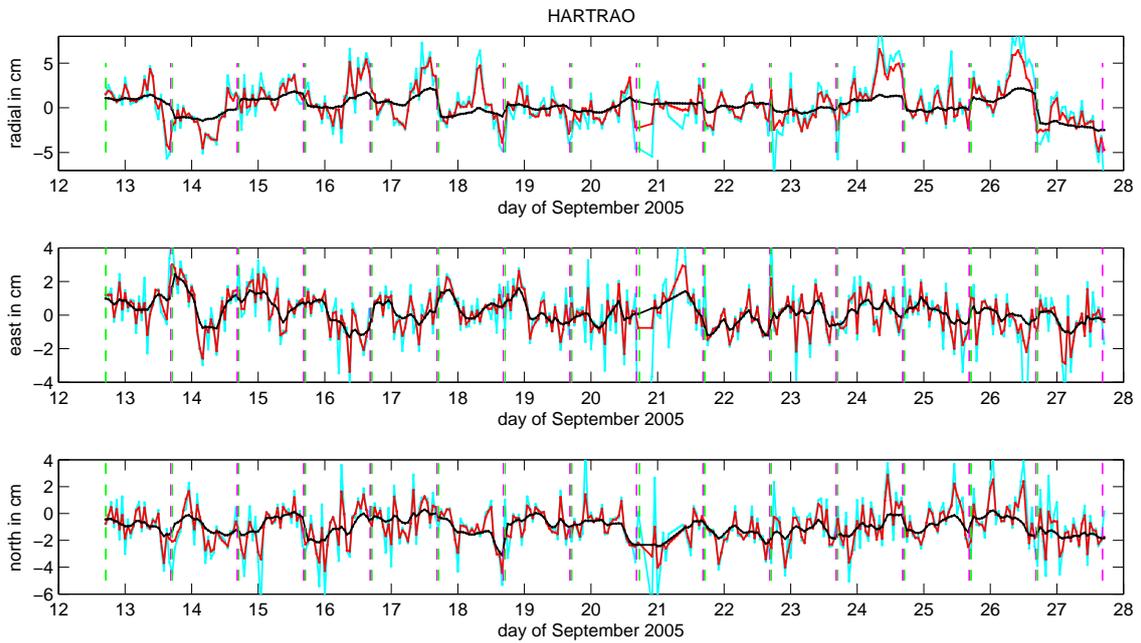

Figure A.8.3.: Black, red and cyan lines show VieVS, hourly (at UTC integer hours) CPWLO coordinate estimates of the VLBI antenna Svetloe during IVS-CONT05 when loose constraints were applied on the hourly coordinate estimates as 4 mm/hour, 3 cm/hour, and 21 cm/hour, respectively.
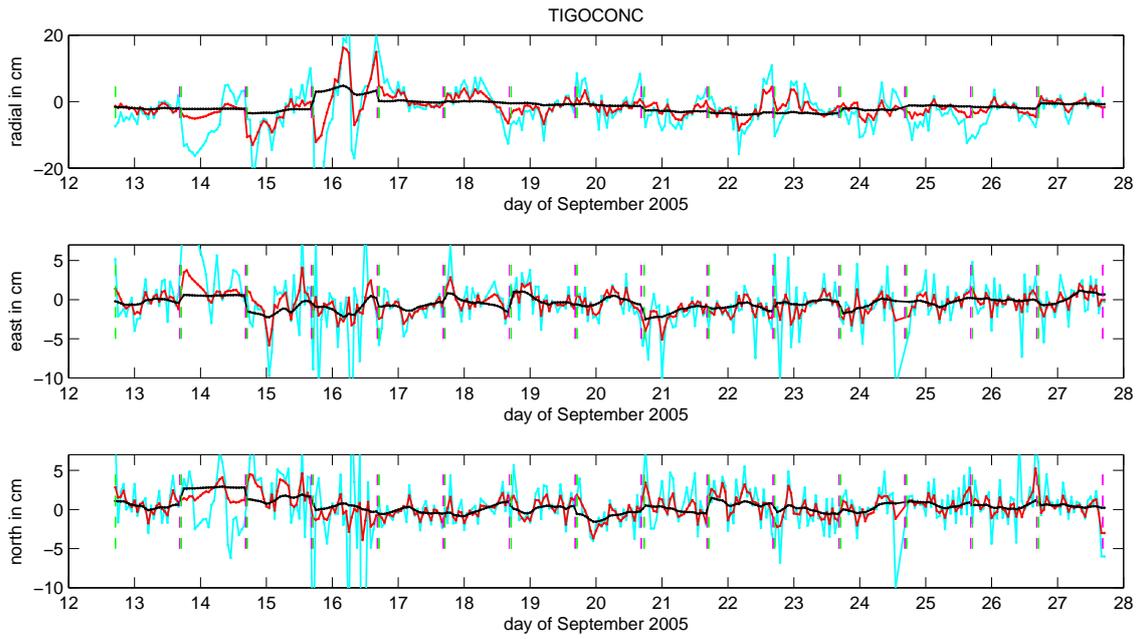
Figure A.8.4.: Black, red and cyan lines show VieVS, hourly (at UTC integer hours) CPWLO coordinate estimates of the VLBI antenna Westford during IVS-CONT05 when loose constraints were applied on the hourly coordinate estimates as 4 mm/hour, 3 cm/hour, and 21 cm/hour, respectively.

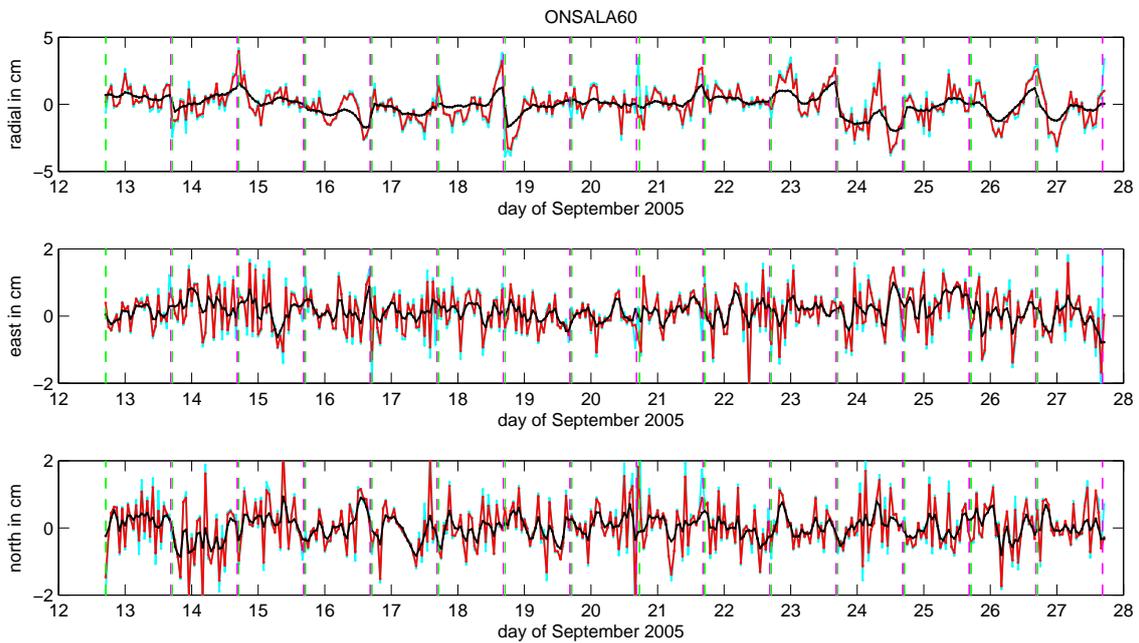Figure A.8.5.: Black, red and cyan lines show VieVS, hourly (at UTC integer hours) CPWLO coordinate estimates of the VLBI antenna Nyales20 during IVS-CONT05 when loose constraints were applied on the hourly coordinate estimates as 4 mm/hour, 3 cm/hour, and 21 cm/hour, respectively.

217

Figure A.8.6.: Black, red and cyan lines show VieVS, hourly (at UTC integer hours) CPWLO coordinate estimates of the VLBI antenna Tsukub32 during IVS-CONT05 when loose constraints were applied on the hourly coordinate estimates as 4 mm/hour, 3 cm/hour, and 21 cm/hour, respectively.

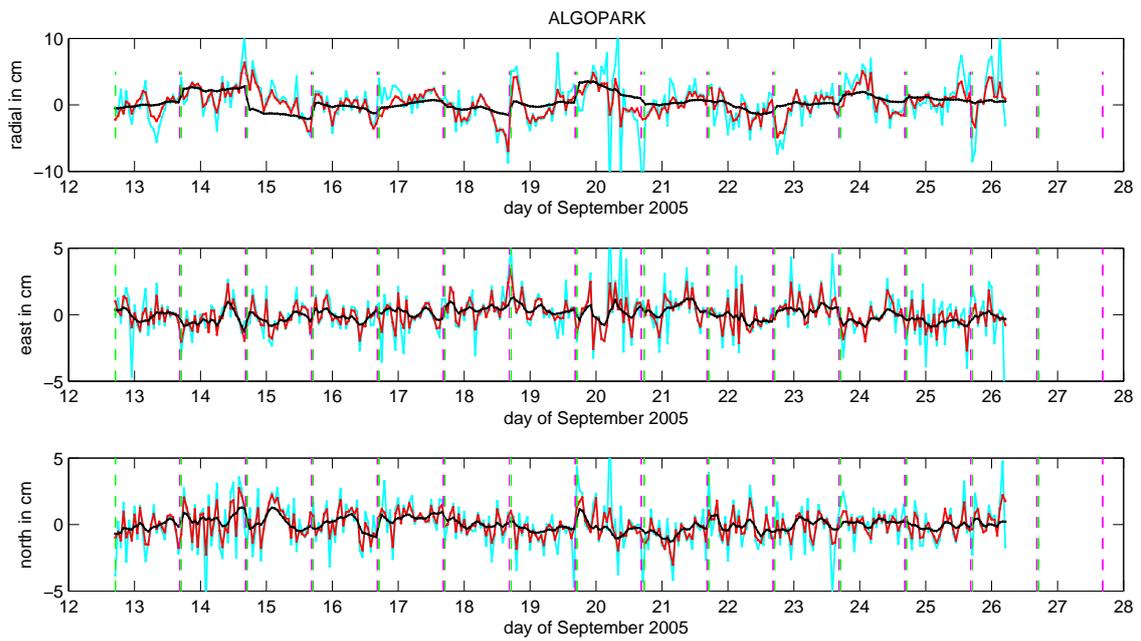Figure A.8.7.: Black, red and cyan lines show VieVS, hourly (at UTC integer hours) CPWLO coordinate estimates of the VLBI antenna HartRAO during IVS-CONT05 when loose constraints were applied on the hourly coordinate estimates as 4 mm/hour, 3 cm/hour, and 21 cm/hour, respectively.
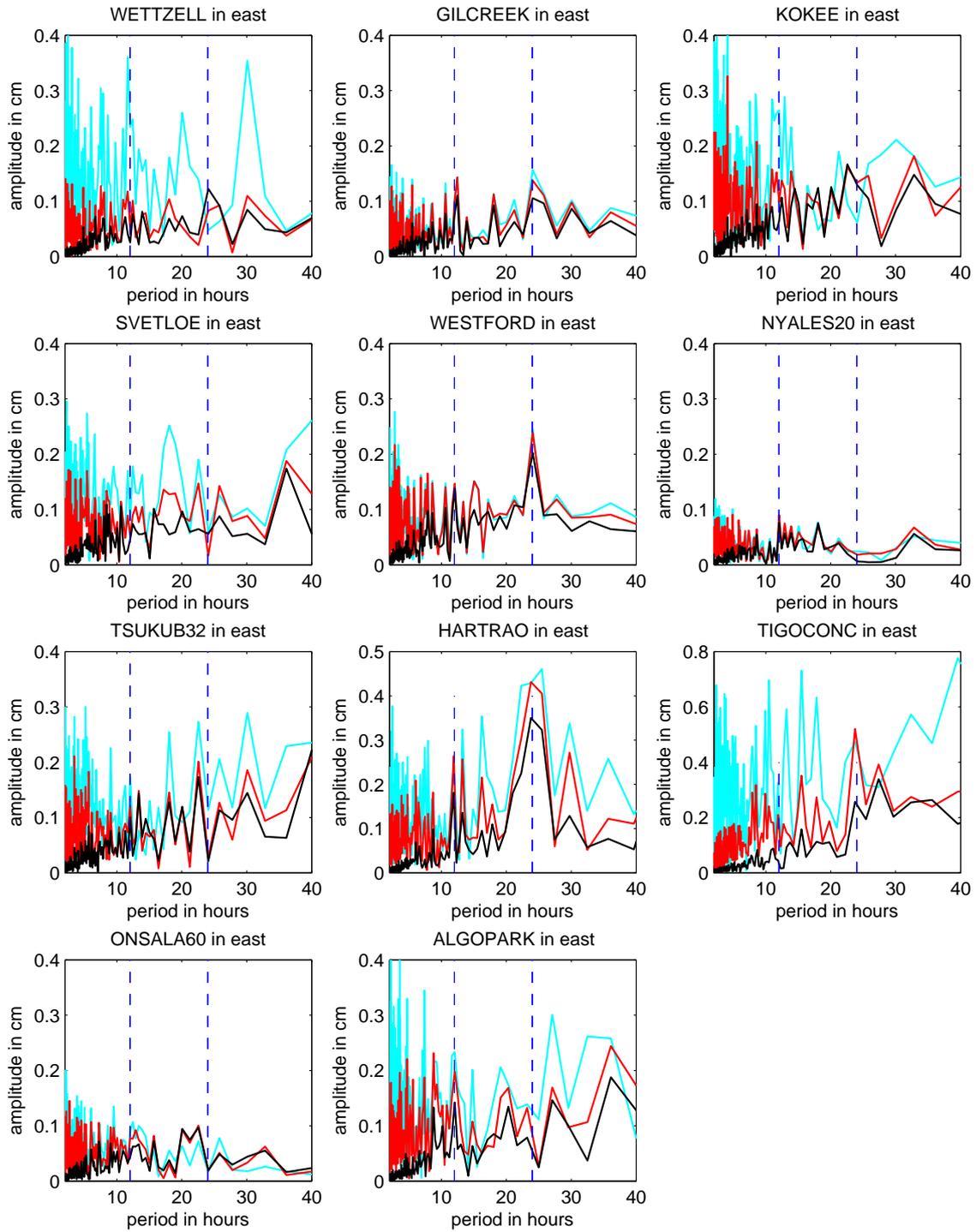
Figure A.8.8.: Black, red and cyan lines show VieVS, hourly (at UTC integer hours) CPWLO coordinate estimates of the VLBI antenna Tigoconc during IVS-CONT05 when loose constraints were applied on the hourly coordinate estimates as 4 mm/hour, 3 cm/hour, and 21 cm/hour, respectively.

Figure A.8.9.: Black, red and cyan lines show VieVS, hourly (at UTC integer hours) CPWLO coordinate estimates of the VLBI antenna Onsala60 during IVS-CONT05 when loose constraints were applied on the hourly coordinate estimates as 4 mm/hour, 3 cm/hour, and 21 cm/hour, respectively.

Figure A.8.10.: Black, red and cyan lines show VieVS, hourly (at UTC integer hours) CPWLO coordinate estimates of the VLBI antenna Algopark during IVS-CONT05 when loose constraints were applied on the hourly coordinate estimates as 4 mm/hour, 3 cm/hour, and 21 cm/hour, respectively.
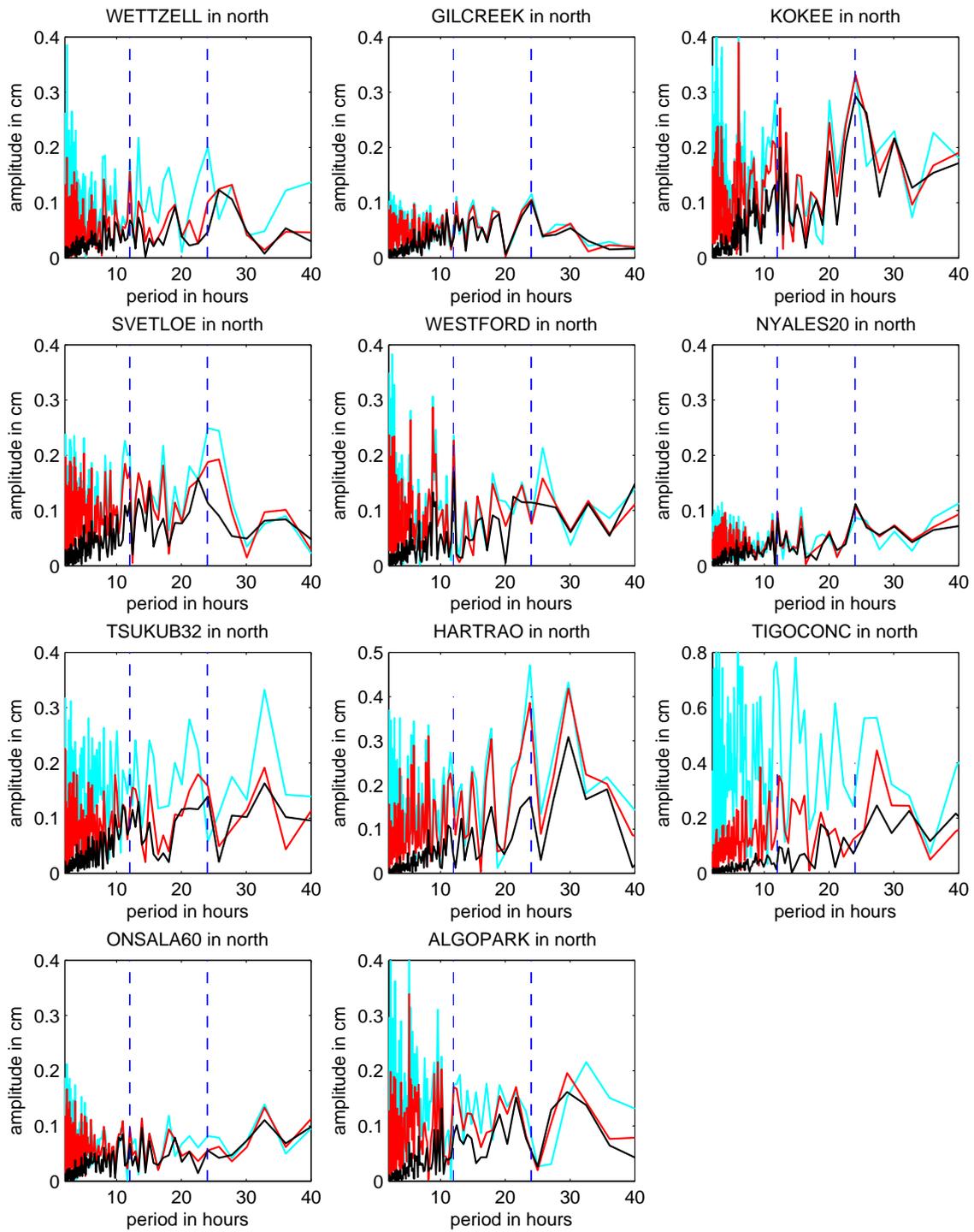
Figure A.8.11.: Spectra of the east components of the hourly CPWLO coordinate estimates during IVS-CONT05 when all the tidal models were reduced from the observations a priori to the adjustment during IVS-CONT05. Black, red, and cyan lines show the spectra of the hourly CPWLO coordinate estimates when constraints of 4 mm/hour, 3 cm/hour, and 21 cm/hour are applied, respectively.

Figure A.8.12.: Spectra of the north components of the hourly CPWLO coordinate estimates during IVS-CONT05 when all the tidal models were reduced from the observations a priori to the adjustment during IVS-CONT05. Black, red, and cyan lines show the spectra of the hourly CPWLO coordinate estimates when constraints of 4 mm/hour, 3 cm/hour, and 21 cm/hour are applied, respectively.

A.9. Hourly tidal motions at VLBI antennas during IVS-CONT05: VieVS CPWLO antenna coordinate estimates versus models at the Wettzell, HartRAO, and Kokee VLBI antennas
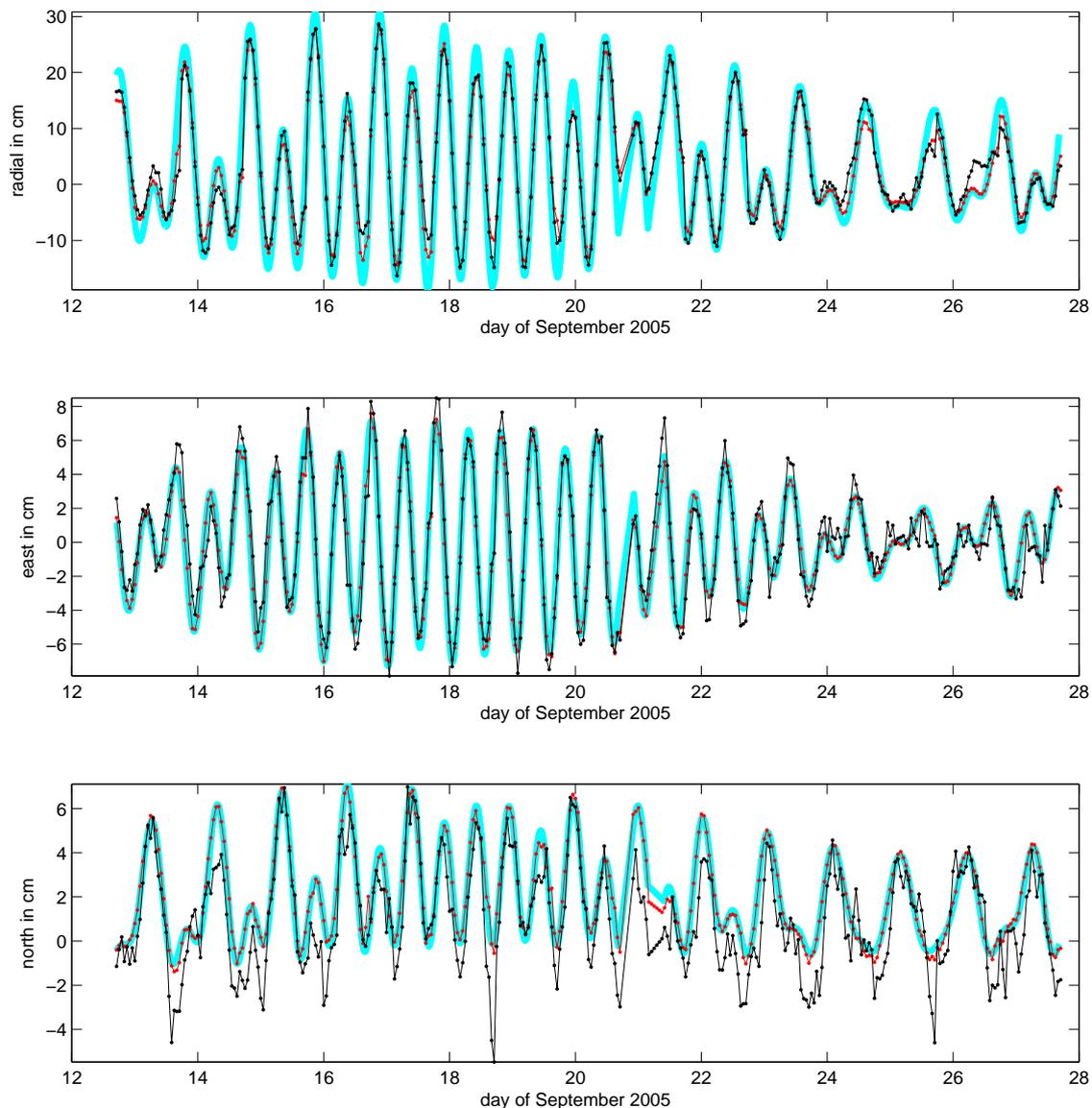
Figure A.9.1.: The cyan line shows the *solid Earth tide* model (McCarthy and Petit (2004), Chapter 7.1.1) at *Hartebeesthoek (Republic of South Africa)*. Red and black dotted line are the hourly CPWLO TRF coordinate estimates of VieVS when the solid Earth tide model for HartRAO is not reduced from the observations a priori to the adjustment. Observed vector of the black line consists of real observations. Observed vector of the red line is calculated from the models ($\tau_{computed}$) without clock errors, and troposphere wet delays. Zeros on Y axes of the plots show the VTRF2008 coordinates of the antennas including the corrections of tidal motions except solid Earth tide. The analysis options for IVS-CONT05 sessions are shown in Table 8.1.
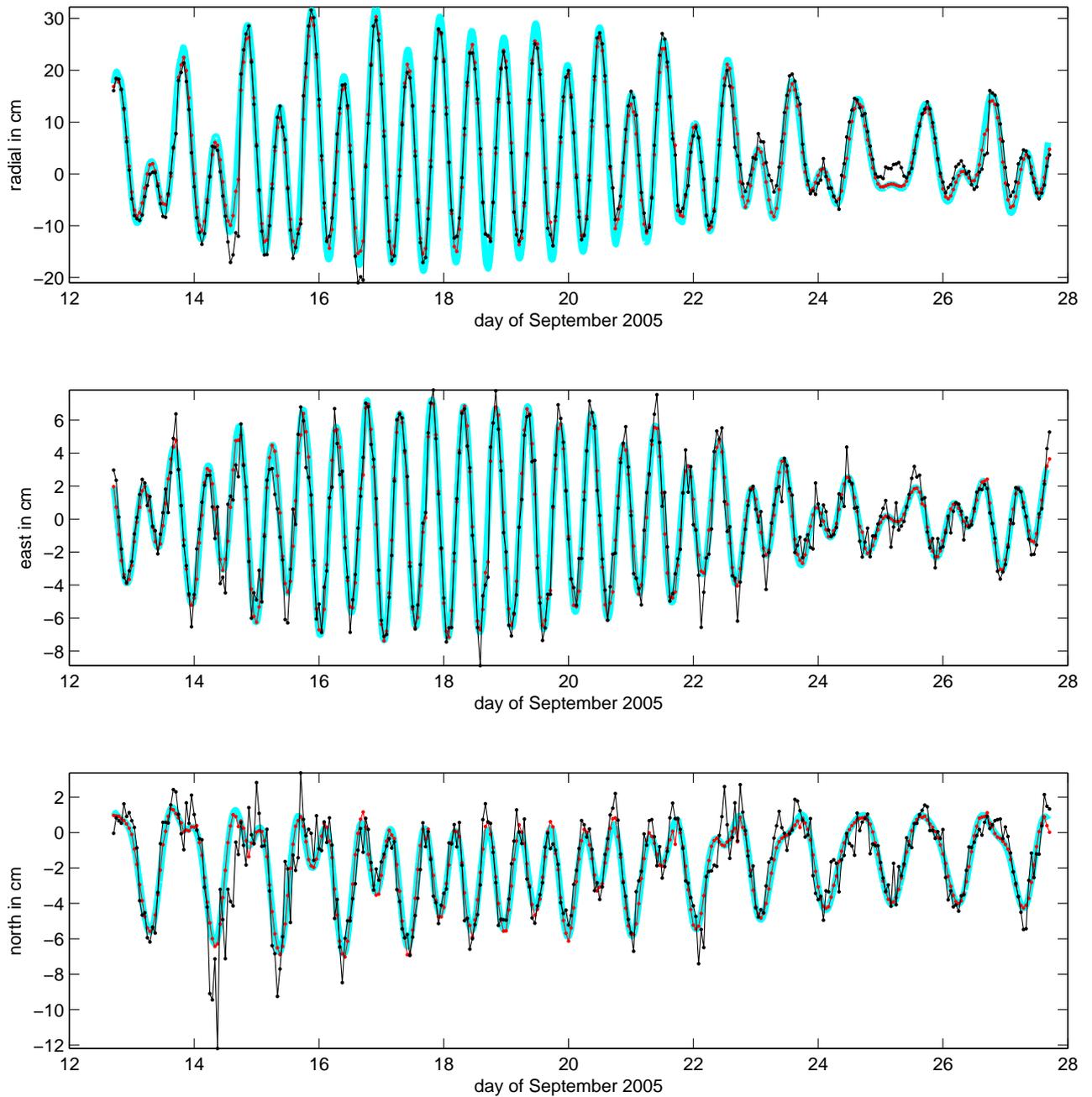
Figure A.9.2.: The cyan line shows the *solid Earth tide* model (McCarthy and Petit (2004), Chapter 7.1.1) at *Kokee (Hawaii, USA)*. Red and black dotted line are the hourly CPWLOs TRF coordinate estimates of VieVS when the solid Earth tide model for Kokee is not reduced from the observations a priori to the adjustment. Observed vector of the black line consists of real observations. Observed vector of the red line is calculated from the models ($\tau_{computed}$) without clock errors, and troposphere wet delays. Zeros on Y axes of the plots show the VTRF2008 coordinates of the antennas including the corrections of tidal motions except solid Earth tide. The analysis options for IVS-CONT05 sessions are shown in Table 8.1.
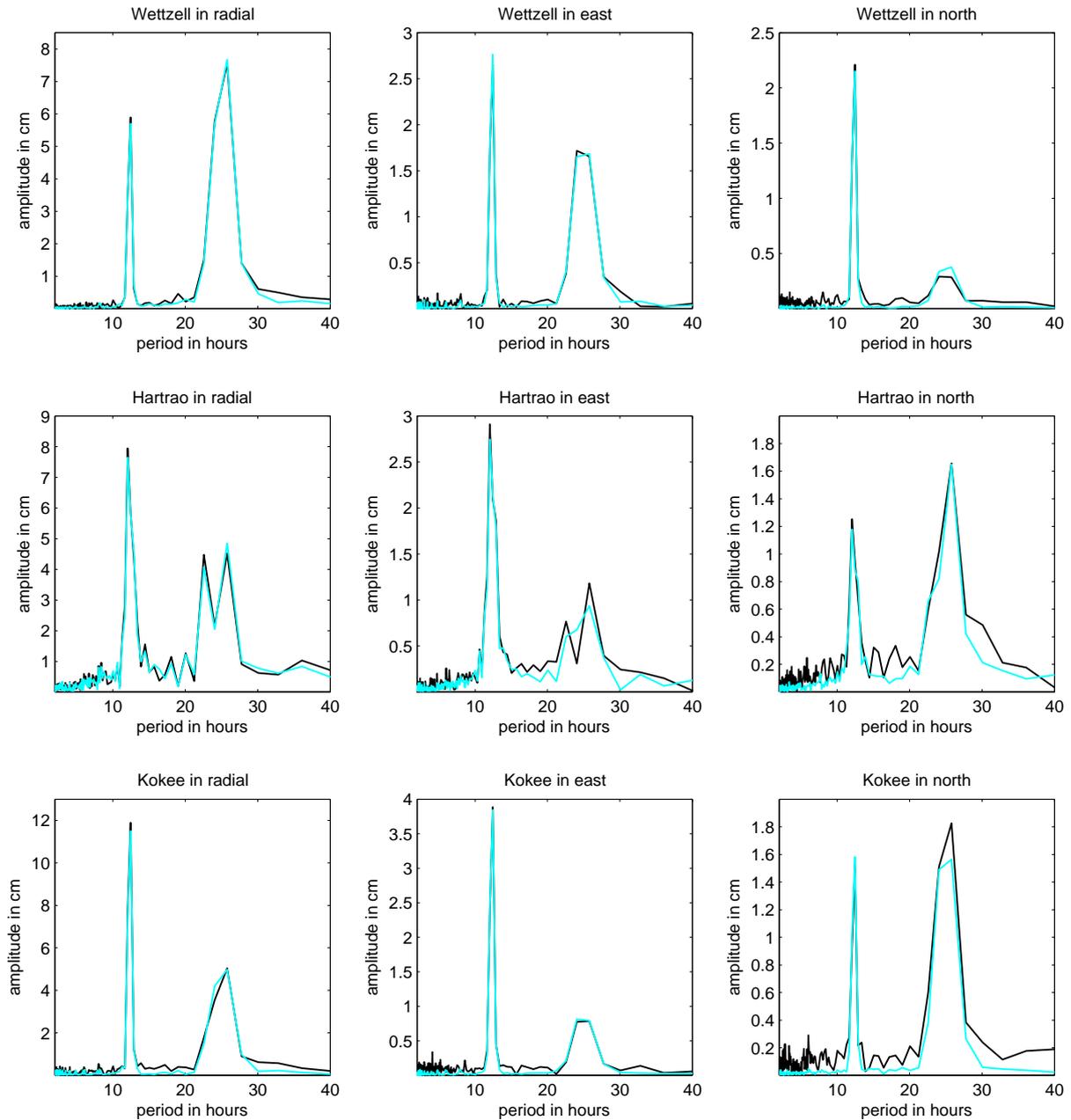
Figure A.9.3.: The cyan line shows the spectra of the hourly coordinate time series computed from the *solid Earth tide* model (McCarthy and Petit (2004), Chapter 7.1.1) during IVS-CONT05. Black line is the spectra of the CPWLO coordinate estimates of VieVS when the solid Earth tide model for the investigated station is not reduced from the observations a priori to the adjustment. It should be noted that both two series have the same epochs (evenly spaced and hourly). The analysis options for IVS-CONT05 sessions are shown in Table 8.1.
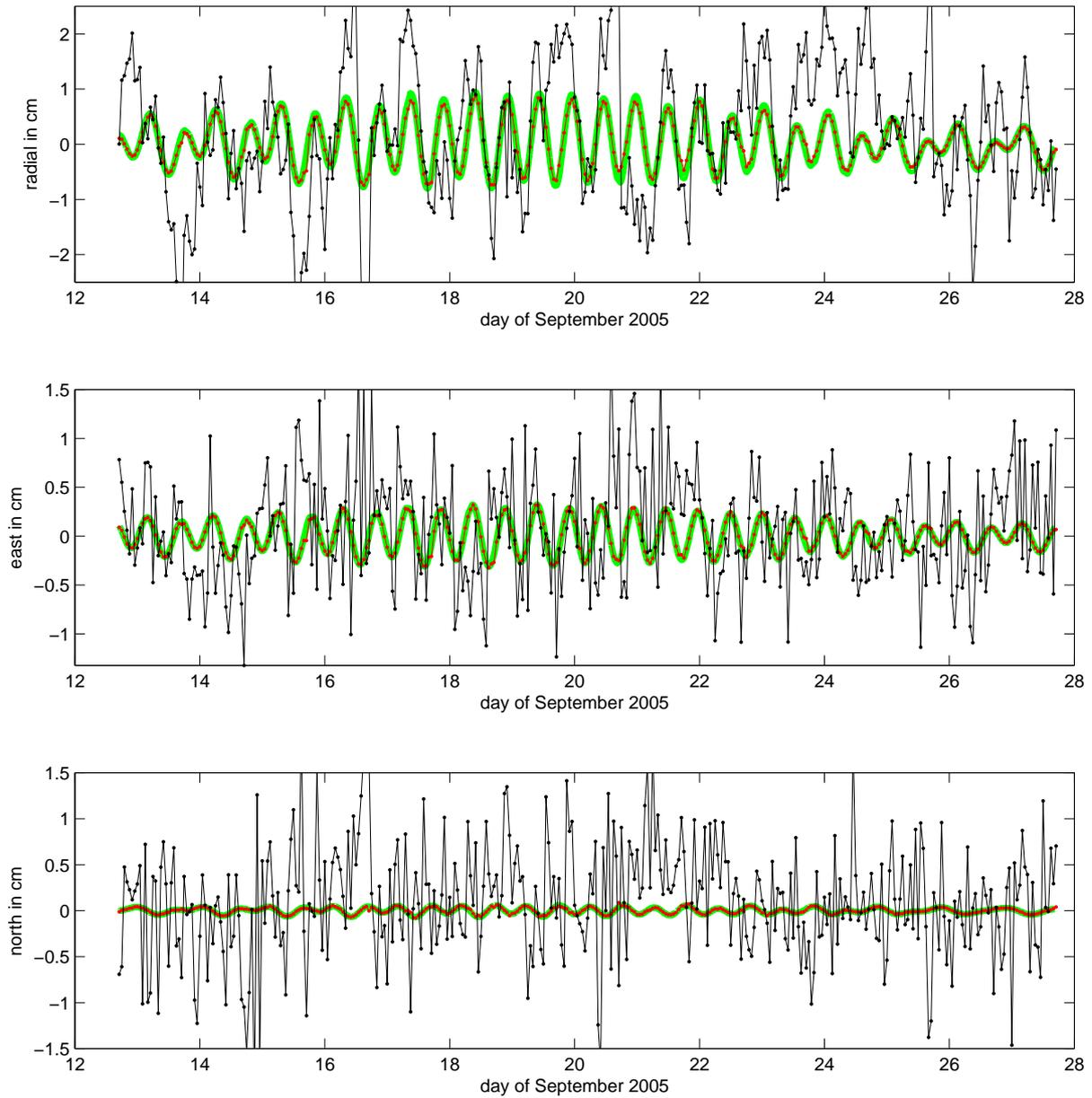
Figure A.9.4.: The green line shows the motions caused by *ocean tidal loading* computed from FES 2004, Lyard et al. (2006)) at *Wettzell (Germany)*. Red and black dotted line are the hourly CPWLOs TRF coordinate estimates of VieVS when the ocean tidal loading model for Wettzell is not reduced from the observations a priori to the adjustment. Observed vector of the black line consists of real observations. Observed vector of the red line is calculated from the models including ocean tidal loading but without clock errors, and troposphere wet delays. Zeros on Y axes of the plots show the VTRF2008 coordinates of the antennas including the corrections of tidal motions except ocean tidal loading. The analysis options for IVS-CONT05 sessions are shown in Table 8.1.
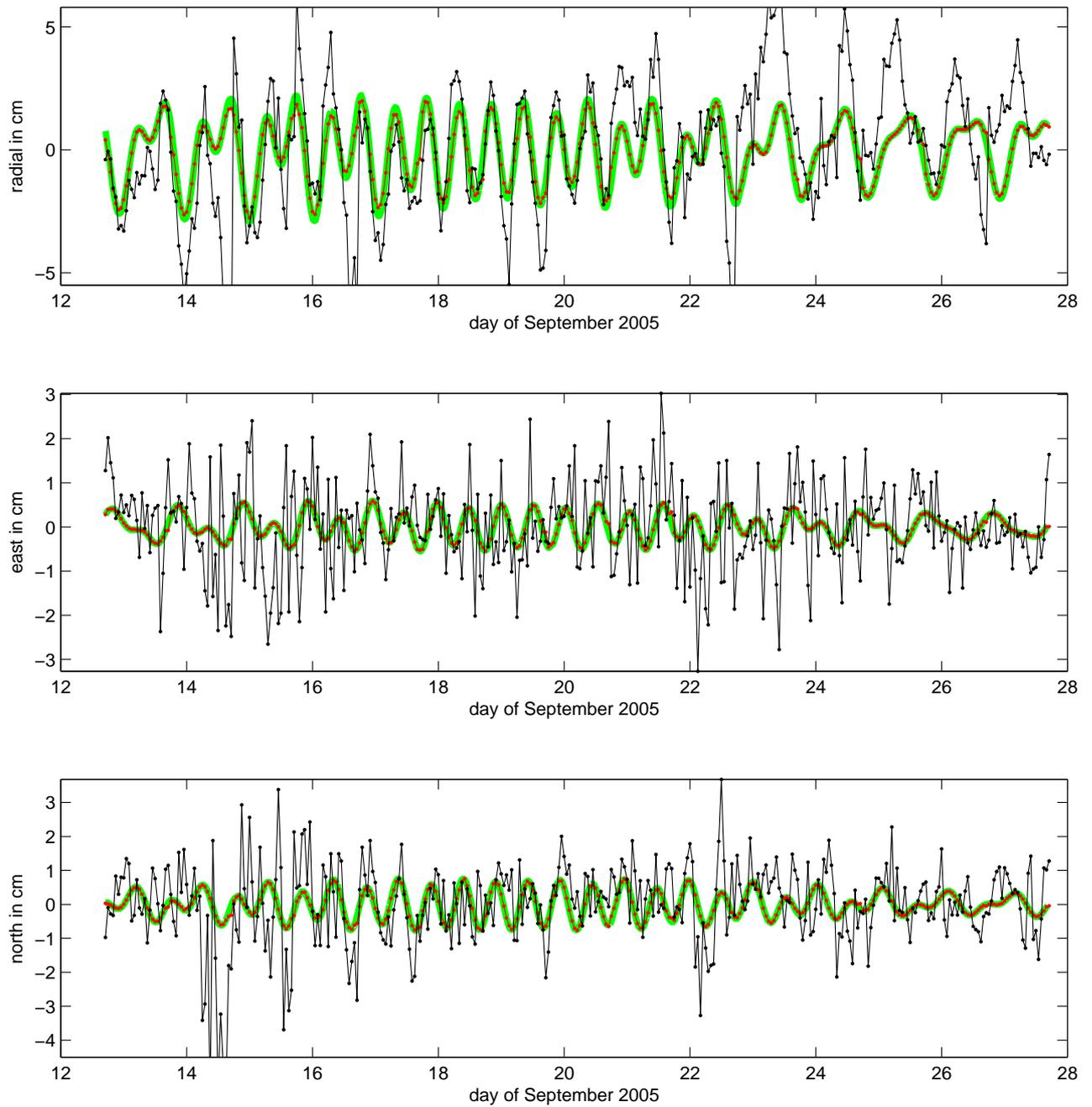
Figure A.9.5.: The green line shows the motions caused by *ocean tidal loading* computed from FES 2004, Lyard et al. (2006)) at *Kokee (Hawaii, USA)*. Red and black dotted line are the hourly CPWLOs TRF coordinate estimates of VieVS when the ocean tidal loading model for Kokee is not reduced from the observations a priori to the adjustment. Observed vector of the black line consists of real observations. Observed vector of the red line is calculated from the models ($\tau_{computed}$) without clock errors, and troposphere wet delays. Zeros on Y axes of the plots show the VTRF2008 coordinates of the antennas at the observation epochs including the corrections of velocity and tidal motions except ocean tidal loading. The analysis options for IVS-CONT05 sessions are shown in Table 8.1.
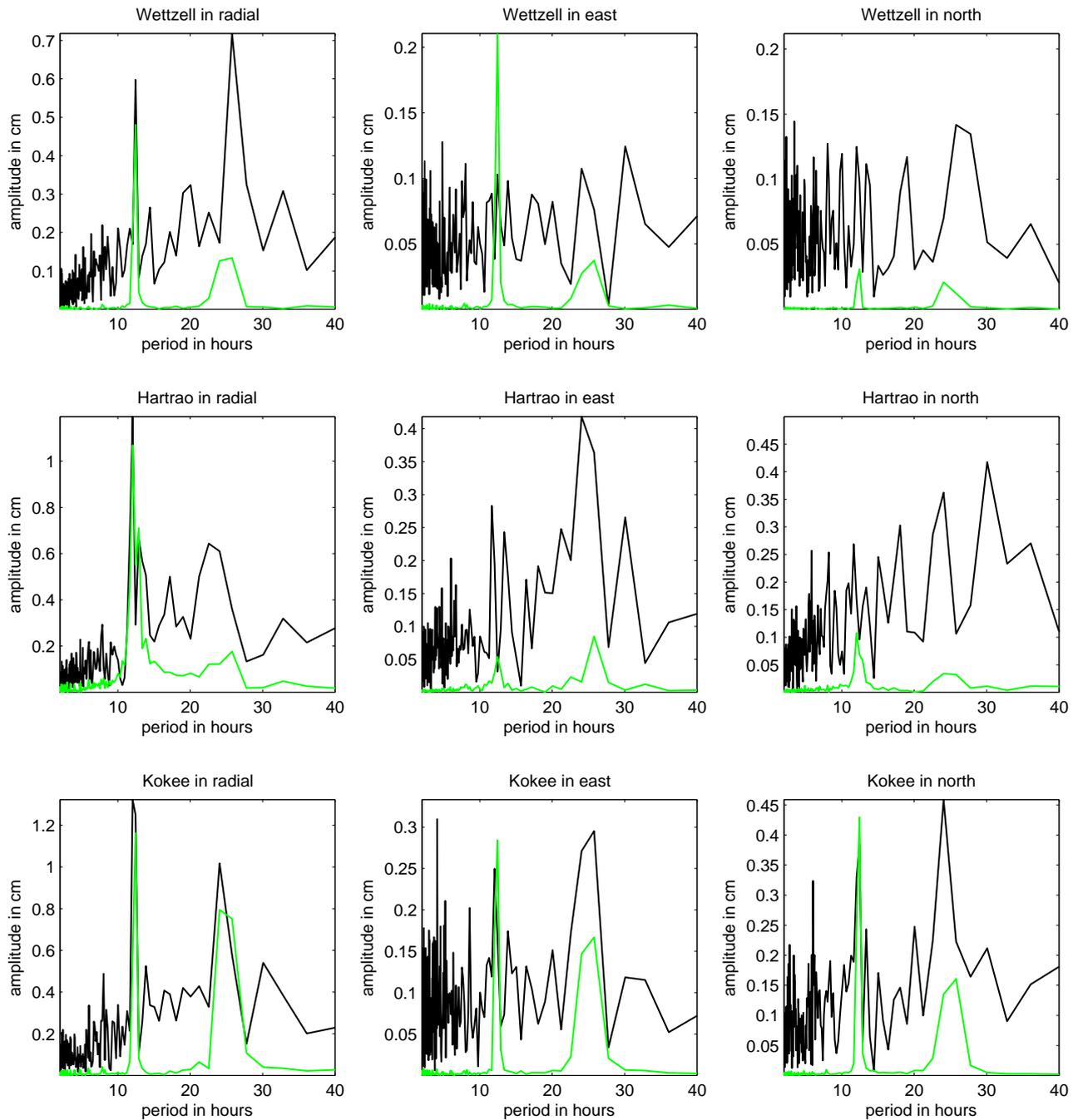
Figure A.9.6.: The green line shows the spectra of the hourly coordinate time series computed from the *ocean tidal loading* model (FES 2004, Lyard et al. (2006)) during IVS-CONT05. Black line shows the spectra of the CPWLO coordinate estimates of VieVS when the ocean tidal loading model for the investigated station is not reduced from the observations a priori to the adjustment. It should be noted that both two series have the same epochs (evenly spaced and hourly). The analysis options for IVS-CONT05 sessions are shown in Table 8.1.
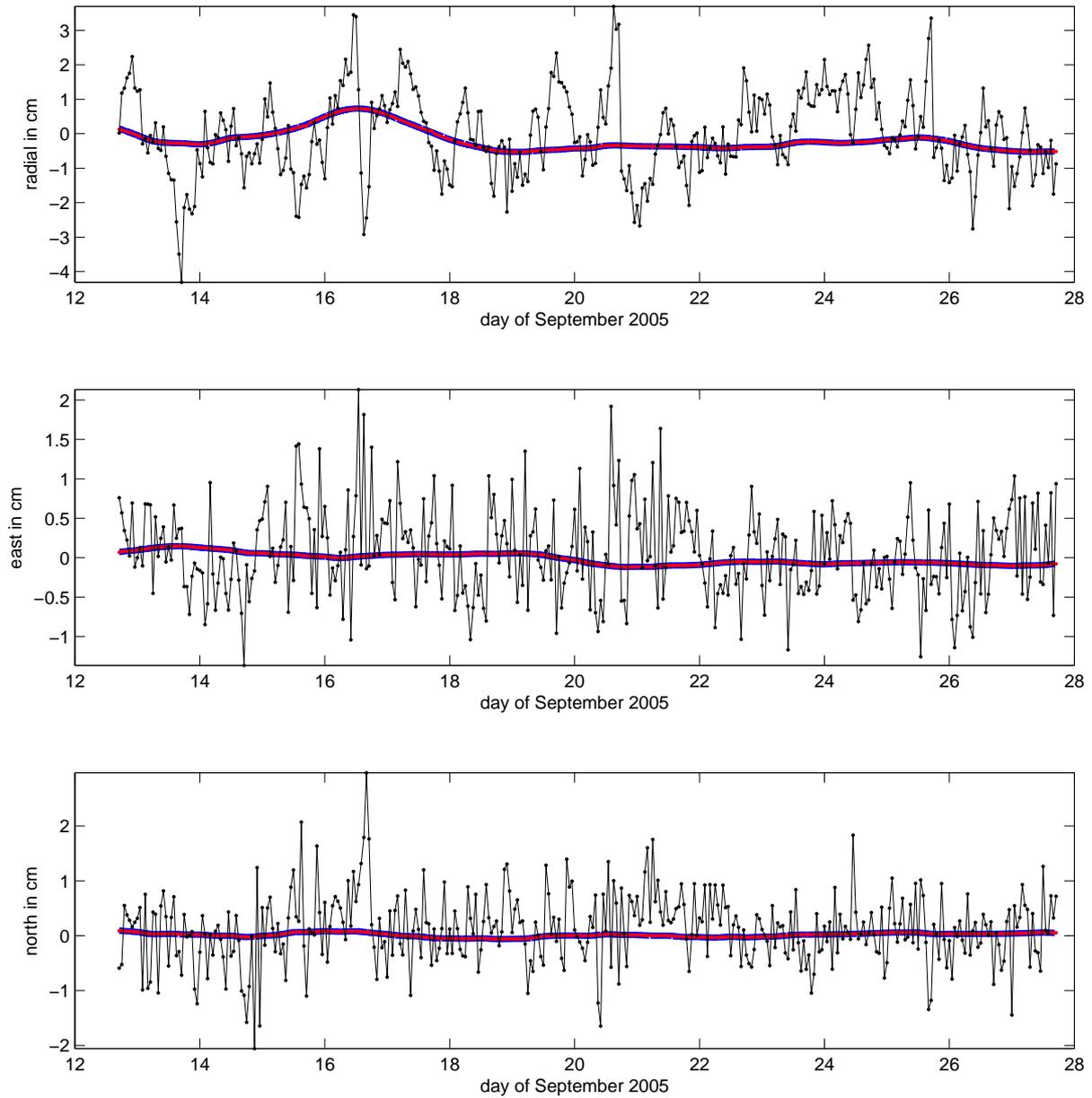
Figure A.9.7.: The blue line shows the motions caused by *atmosphere non-tidal loading* from model (Petrov and Boy, 2004) at *Wettzell (Germany)*. Red and black dotted line are the hourly CPWLOs TRF coordinate estimates of VieVS when the atmosphere non-tidal loading model for Wettzell is not reduced from the observations a priori to the adjustment. Observed vector of the black line consists of real observations. Observed vector of the red line is calculated from the models ($\tau_{computed}$) without clock errors, and troposphere wet delays. Zeros on Y axes of the plots show the VTRF2008 coordinates of the antennas including the corrections of velocity and tidal motions except atmosphere tidal loading. The analysis options for IVS-CONT05 sessions are shown in Table 8.1.
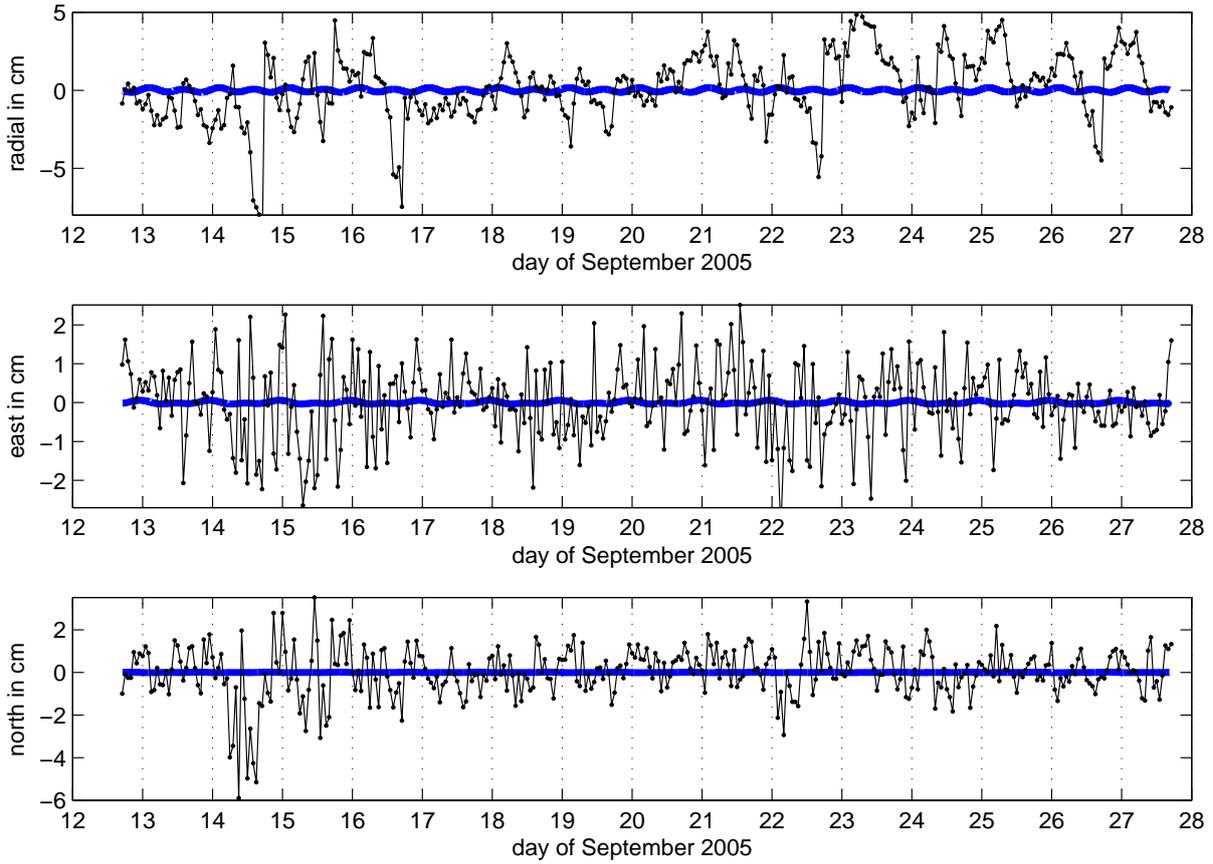
Figure A.9.8.: The blue line shows the *atmosphere tidal loading* model (Petrov and Boy, 2004) during IVS-CONT05 at the VLBI site Kokee. Black dotted line shows the hourly CPWLO coordinate estimates of VieVS when the atmosphere tidal loading model for Kokee is not reduced from the observations a priori to the adjustment. Zeros on Y axes of the plots show the VTRF2008 coordinates of the antennas including the corrections of tidal motions except atmosphere tidal loading. The analysis options for IVS-CONT05 sessions are shown in Table 8.1.
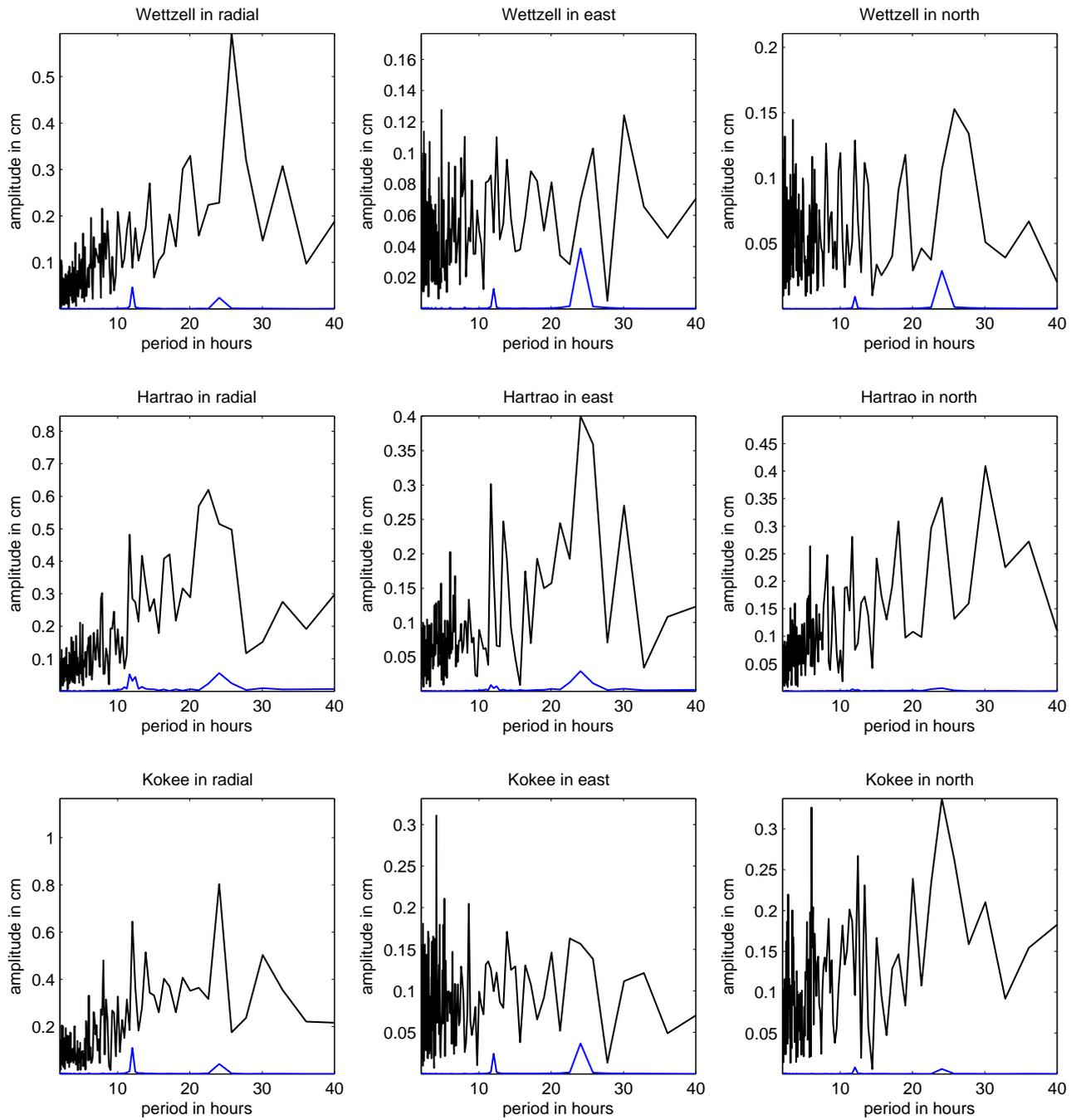
Figure A.9.9.: The blue line shows the spectra of the hourly coordinate time series computed from the *atmosphere tidal loading* model (Petrov and Boy, 2004). Black line is the spectra of the CPWLO coordinate estimates of VieVS when the atmosphere tidal loading model for the investigated station is not reduced from the observations during IVS-CONT05 a priori to the adjustment. It should be noted that both two series have the same epochs (evenly spaced and hourly). The analysis options for IVS-CONT05 sessions are shown in Table 8.1.
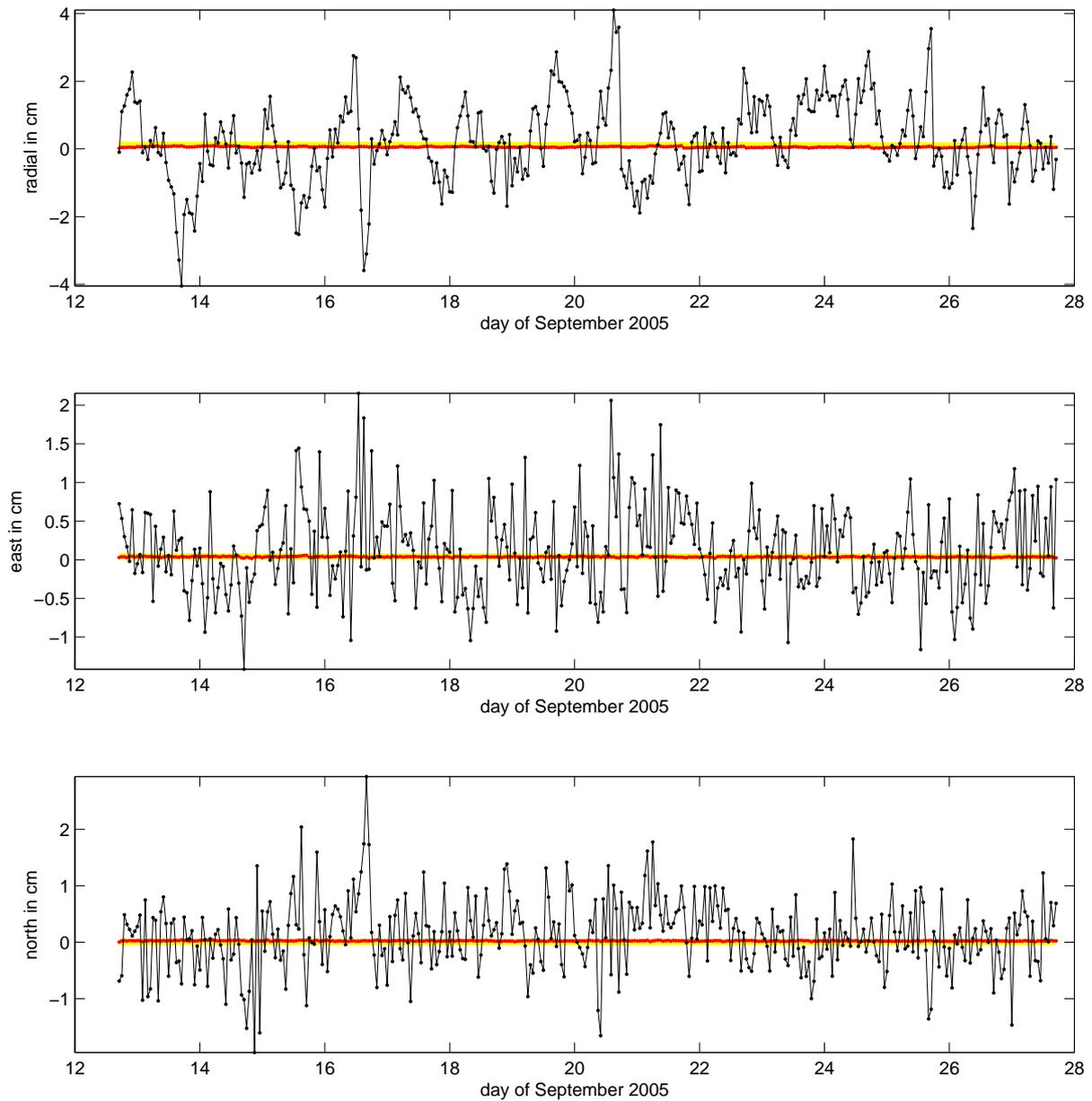
Figure A.9.10.: The blue line shows the motions caused by *pole tide* from model (McCarthy and Petit (2004), Chapter 7.1.4) at *Wettzell (Germany)*. Red and black dotted line are the hourly CPWLOs TRF coordinate estimates of VieVS when the pole tide model for Wettzell is not introduced reduced from the observations a priori to the adjustment. Observed vector of the black line consists of real observations. Observed vector of the red line is calculated from the models ($\tau_{computed}$) without clock errors, and troposphere wet delays. Zeros on Y axes of the plots show the VTRF2008 coordinates of the antennas including the corrections of velocity and tidal motions except pole tide. The analysis options for IVS-CONT05 sessions are shown in Table 8.1.